The Dissertation Committee for Kenneth Stephen Befus certifies that this is the approved version of the following dissertation:

Storage, ascent, and emplacement of rhyolite lavas

Committee:

James E. Gardner, Supervisor

Michael Manga

William D. Carlson

Mark Cloos

Marc Hesse

James Watkins

Storage, ascent, and emplacement of rhyolite lavas

by

Kenneth Stephen Befus, B.S.; M.S.

Dissertation

Presented to the Faculty of the Graduate School of
The University of Texas at Austin
in Partial Fulfillment
of the Requirements
for the Degree of

Doctor of Philosophy

The University of Texas at Austin
August 2014

Acknowledgements

I have treated each chapter like a publication-ready manuscript as much as possible. Although I do not list names of co-authors at the beginning of each chapter (told not appropriate for a dissertation), I can only refer to the work with “we” throughout this compilation. When it comes time to publish I will have many co-authors to each manuscript. So many people have helped me along the way. I was never isolated as a researcher or individual during my time at Texas. When my abilities were insufficient I was consistently uplifted by the encouragement and tangible scientific assistance of many people. I am indebted to each of you and I hope to return the favor for decades to come. Below, I deliberately acknowledge those who made my research possible. Each is a future a co-author and important partner.

Kevin Befus is my little brother who can dominate me at anything scientific. Thankfully, he instead loves to collaborate and has been the best scientific comrade as we work on our PhDs at Texas. Kevin’s guidance and patience helped me understand and employ fluid dynamics and Matlab computing to this dissertation.

Robert Zinke was an excellent undergraduate research assistant. He was my first assistant and together we learned how to attack the research. Zinke was indispensible on numerous ventures to the field. His contributions to this dissertation include sample preparation, and datasets on melt inclusions, microlite number density and microlite

orientation for Douglas Knob (Chapter 3). He is currently working on his PhD at USC (in Tectonics – frowny face) and I hope we can collaborate together again the future.

Matthew Williams was my second excellent undergraduate research assistant. Matt diligently worked for years on multiple projects and joined me on three trips to the field. Matt collected all of the microlite orientations and number densities for Northwest Coulee that I use in Chapter 2. Matt was also my “go to” and true champion for Mono Craters petrology and LIDAR projects that were not included in this dissertation. Matt is working on a MS in Volcanology at Buffalo, living the dream studying Colombian pyroclastic flows.

Jake Jordan is my mathematics and programming mercenary. He has been one of the best graduate student peers, always actively pursuing new ideas and collaboration. His insights and work were critical for both microlite and spherulite Matlab scripts.

Dominique Richard is a researcher in Germany I have never met. She graciously performed the differential scanning calorimetry on a sample of obsidian I sent her (Chapter 4). She taught me the basics on those techniques via email and was great to work alongside.

Other graduate students that deserve recognition include **Ethan Lake, Giovanni Sosa, Ben Byerly, John Singleton, and Brent Jackson**. During hallway and lunchtime discussions each of these peers provided guidance with open minds and careful thinking

Numerous faculty have had a positive impact on this project and my ability to perform research. Outside of my committee I must specifically thank **Luc Lavier** and **Jaime Barnes**. Both have been more significant to me than they realize. Luc was always so outwardly excited and invested as he taught me how to code. Jaime has been the encourager. Her guidance has gotten me interested in isotopic systems, and my fingers are crossed that the ideas we wrote up in our NSF proposal will be fruitful.

My PhD committee members were every bit the guides they needed to be. They taught me how to approach my research questions, and when I got stuck they were available to help. Beyond generalities I remember the specific thing each did. **Bill Carlson** realized I had never been forced to understand the details of diffusion. He fixed that. **Marc Hesse** found the flaw in my spherulite model, and showed me the mathematics to allow it to conserve mass. **Mark Cloos** was my shepherd during my first years here. Within the committee **Jim Gardner** (supervisor), **Michael Manga**, and **Jim Watkins** were my inner circle. Their help cannot be overstated. Each of them were instrumental in leading me to “my” ideas and then guiding me through the research to solve those problems. They enabled me at every turn. I thank them deeply.

Storage, ascent, and emplacement of rhyolite lavas

Kenneth Stephen Befus, Ph.D.
The University of Texas at Austin, 2014

Supervisor: James Gardner

The physical properties and dynamic processes that control effusions of rhyolitic lavas are poorly constrained because of a paucity of direct observations. To assess the pre-eruptive storage conditions, eruptive ascent, and subaerial emplacement for a suite of volumetrically diverse rhyolitic lavas, I studied 10 obsidian lavas from Yellowstone Caldera, Wyoming and Mono Craters, California. Storage, ascent, and emplacement of those lavas were quantitatively constrained using phenocryst compositions, high temperature experiments, microlite textures, and compositional gradients surrounding spherulites. Compositions of phenocrysts and quartz-hosted glass inclusions indicate the magmas at Yellowstone were stored at 750±25 °C in the shallow crust (<7 km), in agreement with phase equilibria experiments. Following the initiation of an eruption, magma leaves the chamber and ascends in a conduit. Microlite number density can be used to quantify eruptive ascent rates. To generate the observed microlite number densities ($10^{8.11\pm0.03}$ to $10^{9.45\pm0.15}$ cm^{-3}), the magmas decompressed at ~1 MPa $hour^{-1}$, equivalent to ascent rates of ~10 mm s^{-1}. Upon subaerial emplacement, microlites act as rigid particles in a deforming fluid (lava), and hence their 3D orientations could indicate flow direction and how strain accumulates in the fluid during flow. Microlites are strongly aligned in samples from all flows, but variations in alignment were found to be independent of flow volume or distance travelled. Together, those observations suggest that strains accumulated during subaerial transport must be small (<2). Instead, microlites most likely aligned in response to strain in the conduit, which can be generated by collapse and flattening. Upon reaching the surface, the cooling history and longevity of rhyolitic lavas are critical for developing models of emplacement and hazard assessment. Compositional gradients surrounding spherulites provide one method to assess such temporal characteristics. Spherulites, crystalline spheres of radiating quartz and feldspar, form by crystallization of obsidian glass in response to cooling. An advection-diffusion model was developed to simulate the growth of spherulites and compositional gradients that develop in the surrounding glass during spherulite growth. Observed gradients are consistent with spherulites growing between ~700 and ~400 °C, and cooling at rates of $10^{-5.2\pm0.3}$ °C s^{-1}.

Table of Contents

List of Tables

List of Figures

INTRODUCTION

High-silica rhyolites commonly erupt explosively, and have famously produced devastating “supervolcano” eruptions (e.g., those at Long Valley Caldera, Yellowstone Caldera). They erupt explosively because of their high melt viscosity and high pre-eruptive volatile content, but there are numerous examples of effusively-erupted rhyolite lavas in both modern and ancient volcanic systems. High-silica rhyolite lavas occur as small-volume (<1 km^3) domes and stubby flows, as well as large-volume (up to 70 km^3), low-aspect-ratio extrusions that extend kilometers from the vent. The mechanisms that control explosive versus effusive eruptive behavior remain poorly understood, as are the controls on effusive emplacement. To that end, I have focused my research on providing quantitative answers to the following research questions:

1. **What are the pre-eruptive storage conditions of rhyolite lavas at Yellowstone?**
2. **What are the ascent rates of effusive rhyolite lavas at Yellowstone and Mono Craters?**
3. **What are the emplacement conditions of rhyolite lavas at Yellowstone and Mono Craters?**

To address **(1)**, I use the composition of natural phenocryst assemblages and high temperature phase equilibria experiments to assess pre-eruptive magmatic storage conditions including pressure, temperature, and volatile content. Temperature and volatile content are the primary controls on melt viscosity. Pressure conditions control volatile contents and degassing behavior during ascent, which largely controls the explosivity of an eruption.

To address **(2)**, I compare natural microlite textures with those generated during continuous decompression experiments. Magmatic ascent rate dictates the degassing history of volatiles in the melt, which is the primary control on eruptive behavior. In general, effusive eruptions ascend at slow enough rates that gas is able to separate from the melt, and passively leave the system.

To address **(3),** I use compositional gradients surrounding spherulites and microlite orientations to understand the cooling history of lavas, and the mechanical aspects of transport such as rheology and strain. Timescales of emplacement and flow velocity depend upon mobility, which is directly controlled by how fast lavas cool. Microlite orientations can be used to infer the dominant directions of lava deformation and the accumulation of strain by the fluid during emplacement.

When I began this project, effusive rhyolitic eruptions had been largely absent from the historic record, requiring that our understanding be derived from studying past events. To that end, I spent 60 days in the field collecting ~150 obsidian samples at flow fronts and across traverses of high silica rhyolite lavas from Yellowstone caldera and Mono Craters, CA. Eruption volumes and flow distances of sampled lava flows range from 0.001 to 70 km^3 and 0.13 to 22 km. Rhyolitic effusions at Chaitén and Cordón Caulle volcanoes occurred in Chile in 2008-2009 and 2011-2012, respectively. Those eruptions have generated new interest in the magmatic conditions and conduit processes that control effusivity. Accordingly, my research project was fortuitously timed. As publications become available, results from my research can be contextualized with modern analogs, some with direct observational constraints.

This dissertation is a compilation of five stand alone manuscripts that will be, or have been, submitted for publication. Each chapter specifically addresses one or more of the aforementioned driving research questions. In **Chapter 1**, I constrain pre-eruptive conditions for volumetrically-diverse obsidian lava flows from Yellowstone caldera using geothermometry and high temperature phase equilibria. In that chapter, I also investigate eruptive ascent using comparisons between natural and experimental microtextures. In **Chapter 2**, I use microlite number density and microlite orientation to understand conduit dynamics, including ascent rate and deformation. **Chapter 3** provides a detailed treatment of pre-eruptive storage, ascent, and emplacement of Douglas Knob, a small-volume lava dome from Yellowstone caldera. In **Chapter 4**, I demonstrate how compositional gradients outside of spherulites can be used to obtain spherulite growth rates and the cooling rates of the host lava. **Chapter 5** describes a technique I developed to measure dissolved volatile contents in unexposed glass inclusions. In **Appendix 1**, I provide a list of all samples collected in the field, and brief field descriptions. In **Appendix 2**, I compile all microprobe analyses of natural samples and experiments.

CHAPTER 1:

MAGMATIC STORAGE CONDITIONS AND ERUPTIVE ASCENT OF CENTRAL PLATEAU MEMBER RHYOLITES, YELLOWSTONE VOLCANIC FIELD, USA

INTRODUCTION

Rhyolite magmas commonly erupt explosively, but they also erupt effusively generating lava flows and domes. Explosive and effusive eruptions of rhyolitic magma are capable of producing pyroclastic deposits and lava flows spanning a wide range of eruptive volumes from <0.01 km^3 to >1000 km^3 (Walker et al. 1973; Pyle 1989). Studies of those eruptive products have generated important insights to volcanic processes and associated hazards, but have also been used to understand how rhyolitic melts are formed, differentiated, stored, and mobilized in the crust (Bindeman and Valley 2000; Jellinek and DePaolo 2003; Bachmann and Bergantz 2004; Wark et al. 2007; Bachmann and Bergantz 2008; Huber et al. 2011).

Yellowstone caldera is one of the most productive rhyolitic systems over the past 2 million years (Hildreth et al. 1991; Gansecki et al. 1996; Christiansen 2001; Lanphere et al. 2002). Magmatism likely continues today, as evidenced by a vigorous geothermal system, dynamic surface deformation, elevated heat flow, seismic activity, and extensive low velocity zones in the shallow crust (Pelton and Smith 1979; Wicks et al. 2006; Chang et al. 2007; Christiansen et al. 2007; Farrell et al. 2009; Smith et al. 2009). Rhyolitic magmatism at Yellowstone caldera is most well known for producing the caldera-forming “supervolcano” eruptions of the Huckleberry Ridge, Mesa Falls, and Lava Creek tuffs (Christiansen and Blank 1972; Christiansen 2001; Lowenstern et al. 2006). The most recent volcanism at Yellowstone produced the Central Plateau Member Rhyolites, which consist of volumetrically minor to massive (0.01 to 70 km^3), effusive outpourings of high-silica rhyolite from 70 to 175 ka (Christiansen 2001; Christiansen et al. 2007). The cause and effect relationships that produce the style of rhyolitic eruptions remains largely unknown, but may be controlled by pre-eruptive storage conditions and timescales, as well as by eruptive ascent rates. Moreover, the magmatic storage conditions and eruption dynamics leading to eruptions of flood rhyolites and more typical lava flows and domes also remain unknown.

Because it has produced effusive and explosive eruptions, Yellowstone caldera provides a exceptional system in which to assess the storage and eruption of volumetrically-diverse rhyolitic magmas (Fig. 1). To help establish a comprehensive understanding of the effusive end member, we place quantitative constraints on pre-eruptive storage conditions and eruptive ascent rates of Central Plateau Member rhyolites. Specifically, we determine pre-eruptive storage conditions using petrographic observations, phenocryst compositions, and phase equilibria experiments. We constrain eruptive ascent rates by comparing natural microtextures with those generated by continuous decompression experiments. By defining storage pressure, temperature, and eruptive ascent rates we place constraints on the controls of rhyolite volcanism.

METHODS

Samples of rhyolitic obsidian were collected from outcrops from Trischmann Knob, Summit Lake, West Yellowstone, Pitchstone Plateau, and Solfatara Plateau (Table 1). Polished thin sections from each sample were prepared. For each flow, mineral separates of magnetite, fayalite, and clinopyroxene were hand-picked from crushed obsidian samples. In addition, a portion of sample Y82 from Solfatara Plateau was crushed to a ~50 μm powder to be used as starting material for experiments. That sample, considered to be compositionally representative of Central Plateau Member rhyolites, is composed of 5-10% phenocrysts of quartz, sanidine, clinopyroxene, fayalite, and magnetite that are hosted within a glassy rhyolite matrix. Mineral and glass compositions from natural samples and experiments were analyzed using the JEOL JXA-8200 electron microprobe at the University of Texas at Austin. All materials were analyzed using a 10 nA beam current with an 15 keV accelerating voltage. Magnetite, fayalite, and clinopyroxene were analyzed with a focused beam. To minimize Na migration during sanidine and glass analyses we used a 2 and 10 μm diameter defocused beam, respectively (Nielsen and Sigurdsson 1981). During glass analyses, Na migration was corrected using the Na-migration capability of *Probe for Windows*^{TM}. Working standards were analyzed repeatedly to monitor analytical quality and instrument drift. For crystals that were too small to analyze using wavelength-dispersive spectrometry (WDS), energy-dispersive spectra (EDS) were collected and used to identify those phases.

Phase equilibria experiments were prepared by partially filling 2-5 mm O.D. $Ag_{70}Pd_{30}$ capsules that were welded on one end with starting material powder and distilled water. Enough water was added to each capsule to ensure that each experiment was water-saturated at experimental conditions. The capsules were then welded shut on the other end. Reversal experiments used powders from previous experiments. Crystallization experiments used material run previously at hotter temperatures and/or higher pressures, whereas melting experiments were those that used material previously run at lower temperatures and/or pressures.

Experiments were performed by loading capsules and filler rods into externally-heated, cold-seal Nickel-based alloy pressure vessels, which were then placed within furnaces. Temperature was gauged in the vessel using K-type thermocouples that are precise to ±5 °C. Pressure was controlled with a hydraulic pressure system, and measured to ±0.1 MPa. Oxygen fugacity was largely controlled during experiments by the composition of the filler rod. Two sets of phase equilibria experiments were performed, the first used Ni filler rods to maintain an oxygen fugacity approximately one log unit above the Ni-NiO oxygen buffer (NNO+1) (e.g., Gardner et al. 1995). A second set of experiments used steel filler rods, which maintained oxygen fugacity at significantly more reduced conditions (≥3 log units). To ensure a controlled oxygen fugacity during those experiments, 2-3 mm O.D. experimental capsules were placed within 5 mm O.D. capsules that also contained a stoichiometric mixture of quartz, magnetite, and fayalite powders. When all phases remain present the oxygen fugacity is buffered at the quartz-magnetite-fayalite buffer (QFM).

Experimental runs typically 14 days, which is a sufficient duration for phases and rhyolite melt to at least begin to equilibrate experimentally. Following that time, samples were quenched in less than 5 minutes by removing the pressure vessels from the furnaces, and first blowing on the vessels with compressed air, and then submerging the vessels in water. Once cool, the experimental capsules were removed from the pressure vessels and weighed to check for leaks. We only consider experiments that did not lose water and thus remained water-saturated. The capsules were then opened, and the samples removed. A portion of each sample was mounted on glass slides and prepared for petrographic and microprobe analyses. In QFM-buffered experiments, a portion of the buffer powder was also prepared for analysis in order to verify each phase remained.

Continuous decompression experiments were prepared using starting material powders from crushed aliquots of past experiments and enough distilled water to ensure saturation. Three sets of decompression experiments were run isothermally at 720 °C, 750 °C, and 780 °C, respectively. Starting material powders were selected from experiments run at those temperatures, and at pressures such that the melt was a few degrees undercooled. The degree of undercooling was determined by phase equilibria experiments. Starting materials thus had sparse microlites in them, which were previously quantified so that the formation of new microlites could be determined. Decompressions were performed in rapid-quench, Ni-alloy pressure vessel assemblages as described in Carroll and Blank (1997). To control pressure we used an automated continuous decompression experimental design, modified from that described in Nowak et al. (2011). Briefly, a modified valve was equipped to control decompression using a *Eurotherm* process controller. The controller is able to receive an electronic signal from the pressure gauge and send voltages to a piezo stack ceramic motor in order to move a steel needle from open to closed positions. The amount of voltage sent to the motor controls the precise position of the needle. As the needle moves to the “open” position, pressure drops as water leaks from the system. The motor controls the decompression rate by switching from the closed to open positions at millisecond timescales. Decompressions are thus automated, and the system is responsive to pressure variations of less than 0.1 MPa.

Decompression experiments began after initially annealing the sample at the starting pressure and temperature for 20 minutes. Depressurization was then controlled by the automated continuous decompression system, with experiment durations lasting 6 to 72 hours (Fig. 2). Upon reaching the final pressure, samples were immediately quenched (≤ 5 seconds) by using a magnet to pull the sample out of the furnace and into the water-cooled area of the pressure vessel assemblage. After the pressure vessel cooled, the capsule was removed and checked for leaks. Last, the sample was removed, mounted in epoxy, and prepared for petrographic and microprobe analysis.

Microlite textures in experiments were quantified by counting microlites in rectangular prismatic sub-volumes of thin sections while continuously focusing through the transparent glass using a petrographic microscope. Rectangular volumes were generally 40 μm wide, 40 μm long, and 15 μm deep. Depth was measured using a petrographic microscope equipped with a linear encoder attached to the focusing drive. To ensure that a statistically significant number of microlites were counted in each analyzed thin section, microlites were counted at multiple positions across the sample. Number density counts include Fe-Ti oxide, clinopyroxene, and alkali feldspar microlites.

RESULTS

Phenocryst and glass composition

Glass and phenocryst compositions from the volumetrically diverse Central Plateau Member flows are remarkably homogenous (Table 2), and our results agree with and supplement previously published datasets (Christiansen 2001; Vazquez et al. 2009; Girard and Stix 2010). In each flow quartz occurs as euhedral to subhedral crystals, 500-2500 μm in diameter (Fig. 3a,b). Quartz crystals commonly contain glass inclusions, and some are embayed with reentrants. Sanidine occurs as euhedral to subhedral crystals and crystal fragments that reach up to 6 mm in size. They are compositionally indistinguishable between Central Plateau Member flows, and are unzoned from core to rim ($Or_{50\pm2}Ab_{47\pm2}An_{2\pm1}$). Plagioclase was never identified in Trischmann Knob, Summit Lake, West Yellowstone, or Pitchstone Plateau, but it was found in rare samples (<2%) from Solfatara Plateau and occurred as albitic cores ($Or_{9\pm1}Ab_{72\pm1}An_{19\pm1}$) within 1-3 sanidine phenocrysts in those samples. Magnetite occurs as euhedral, equant phenocrysts that are 50-500 μm across. It occurs as individual crystals or in glomerocrysts with clinopyroxene, fayalite, and trace phases (zircon, allanite). Magnetite is unzoned and compositionally similar between flows ($Mgt_{48\pm2}Usp_{52\pm2}$), although those in Pitchstone Plateau are richer in Fe by ~1 wt.%. Clinopyroxene occurs as euhedral, elongate crystals up to 1000 μm in size. They are compositionally unzoned ferroaugite ($En_{13\pm1}Fs_{46\pm1}Wo_{41\pm1}$), with those in Pitchstone Plateau having slightly higher Fe/Mg ratios relative to crystals in the other flows. Fayalite is the least common mafic phase in the lavas. It occurs as euhedral crystals 200 to 800 μm in diameter. As with the other mineral phases, it is also compositionally unzoned, but those in Pitchstone Plateau contain slightly higher Fe/Mg ratios ($Fa_{95\pm1}$) than those in other flows ($Fa_{92\pm1}$).

The high silica rhyolite glass of Central Plateau Member lavas contains abundant microlites of Fe-Ti oxide, clinopyroxene, and alkali feldspar. The average microlite number density of all phases combined in the target lavas varies from $10^{8.11\pm0.03}$ to $10^{9.45\pm0.15}$ cm^{-3} (Chapter 2). Fe-Ti oxides are present in all flows and are typically the most abundant microlite phase. They occur as either equidimensional crystals 1 to 2 μm in diameter, or as acicular rods 1 to 2 μm wide and 3 to 30 μm long. Clinopyroxene is the next most abundant phase, and is also present in each flow. Clinopyroxene occurs as prismatic crystals 1 to 10 μm wide and 2 to 20 μm long. Alkali feldspar is the only other microlite phase present. Alkali feldspar is generally absent, occurring only rarely in few samples from Pitchstone Plateau, Solfatara Plateau, Summit Lake, and West Yellowstone. It has not been found in Trischmann Knob. When present, alkali feldspar microlites are the least abundant phase, and occur as lath-shaped crystals 1 to 5 μm in width and 2 to 20 μm in length, commonly with swallowtail terminations.

Granophyre composed of intergrown, vermicular to micrographic quartz and sanidine ($Or_{46\pm6}Ab_{51\pm6}An_{2\pm1}$) was identified in some samples from Solfatara Plateau (Fig. 3). The granophyre occurs as overgrowths up to 1000 μm thick on sanidine and quartz phenocrysts, and as individual rounded clasts up to 1000 μm across. In some instances granophyre occurs as overgrowths that connect sanidine and quartz phenocrysts to form glomerocrysts. Discontinuous bands of sanidine and quartz fragments occur in samples with granophyre, and can sometimes be traced to the granophyre clasts. Such bands are not present in samples that do not contain granophyre. To understand the distribution of granophyre, we examined thin sections from samples collected across Solfatara Plateau. We found that granophyre was generally restricted to areas within 2 km of the flow front (Fig. 4). We searched for granophyre in samples collected across many of the other Central Plateau Member lavas. Granophyre was identified in one sample from the periphery of Pitchstone Plateau, but has not been identified in any other flow.

Phase equilibrium experiments

In both the NNO+1 and QFM buffered phase equilibria experiments magnetite was the liquidus phase, and was stable under all water pressure and temperature (P-T) conditions we investigated (Fig. 5a,b). Bubbles were also present in all experiments, demonstrating all experiments were water-saturated. At lower P-T conditions we identify mineral stability fields based on crystal morphology (e.g., anhedral, euhedral) and crystal content relative to starting material. Glass occurs in all samples above 725 °C.

In NNO+1 experiments, sanidine is the next phase to crystallize with decreasing temperature and/or water pressure (Fig. 5a). Sanidine first forms at ~750 °C at 150 MPa and at ~815 °C at 25 MPa. Next, clinopyroxene stabilizes at temperatures 5 to 20 °C cooler than sanidine at equivalent pressures. Quartz is the next phase to stabilize, and first crystallizes at 700±10 °C at 150 MPa and at 780±10 °C at 25 MPa. At lower temperatures those phases crystallize in unison until the solidus is reached at ~675 °C at 100 MPa and at ~710 °C at 25 MPa. At water pressures >100 MPa plagioclase was the final phase to stabilize. Plagioclase was only present at pressures >100 MPa and at temperatures ≤675 °C.

To test the effect of oxygen fugacity on phase equilibria, we performed QFM-buffered experiments at targeted P-T conditions (Fig. 5b). Overall, we find phase stabilities are similar, but some important differences exist. The reduced experiments contain much less magnetite than do oxidized runs at equivalent P-T conditions. They also contain fayalite, which was not observed in oxidized experiments. Sanidine, fayalite, and clinopyroxene first equilibrate at 750±10 °C at 150 MPa and at 825±15 °C at 25 MPa. Quartz joins the assemblage at 715±10 °C at 150 MPa and at 800±15 °C at 25 MPa, temperatures 5 to 20 degrees hotter than in NNO+1 experiments. Plagioclase was not stabilized in QFM experiments.

To further evaluate P-T space we estimated the proportion of glass and analyzed the composition of glass and stable mineral phases in most of the experiments. Glass abundance gradually decreases from ~100% glass, in experiments above the sanidine in-curve, to ~80% glass only 20 °C above the solidus (Fig. 6). In the 20 °C interval above the solidus, the melt crystallized significantly, forming fine-grained intergrowths of sanidine and quartz crystals that are 1 to 5 μm in size. Glass composition changes systematically with changing abundance and temperature. Concentrations of SiO_2 increase with decreasing temperature, whereas K_2O and FeO decrease (Fig. 7). Sanidine compositions range from $Or_{66\pm5}Ab_{34\pm4}An_{1\pm1}$ to $Or_{44\pm4}Ab_{52\pm3}An_{3\pm1}$, and become more potassic at higher pressures. Clinopyroxene crystals were typically very small, often only 1 μm in diameter. Clinopyroxene was thus difficult to analyze quantitatively using WDS.

When WDS analyses were possible, compositions in NNO+1 buffered experiments are $En_{14\pm8}Fs_{40\pm7}Wo_{46\pm4}$ and become slightly more Fe-rich in lower temperature experiments. Clinopyroxene compositions in QFM buffered experiments are $En_{7\pm3}Fs_{52\pm4}Wo_{41\pm4}$. EDS analyses confirm the presence of Fe-rich clinopyroxene in samples in which quantitative WDS analyses were not possible. When present, plagioclase ($Or_{12\pm3}Ab_{81\pm2}An_{7\pm2}$) and fayalite ($Fa_{96\pm2}$) compositions are not sensitive to pressure or temperature conditions.

Decompression experiments

Continuous decompression experiments were performed at 720 °C, 750 °C, and 780 °C to explore decompression-induced crystallization in high-silica rhyolitic melts. At 720 °C, decompressions were performed at 1.7 to 20 MPa hr^{-1}. Each of those experiments nucleated quartz and sanidine. The fastest decompression rates nucleated rare quartz and acicular sanidine needles, whereas those at the slowest rates generated coarser intergrowths of sanidine and quartz that comprised ≥20% of the run products. Quartz microlites were not observed in the natural glasses, thus there is no need to evaluate the similarity between natural and experimental microlite textures. Experiments at 750 °C were performed at 0.9 and 2.7 MPa hr^{-1}. When compared to the microlite texture of the experimental starting material, alkali-feldspar was found to be sensitive to decompression rates. Alkali-feldspar abundance did not change during decompressions of 2.7 MPa hr^{-1}, with final products containing alkali feldspar microlite number densities within error of starting materials ($10^{8.4\pm0.5}$and $10^{8.2\pm0.2}$, respectively). Alkali feldspar number density increased during decompressions at 0.9 MPa hr^{-1} from $10^{8.2\pm0.2}$ to $10^{8.6-9.3}$ cm^{-3}.

Decompression rates of 0.8 to 7.0 MPa hr^{-1} were used in experiments at 780 °C. No microlites were formed in those experiments, even at rates as slow as 0.75 MPa hr^{-1}. In all decompression experiments clinopyroxene and magnetite textures were indistinguishable from starting materials, indicating they did not texturally evolve.

DISCUSSION

Storage

Volumetrically diverse Central Plateau Member rhyolites are nearly identical petrographically, containing a phenocryst assemblage of quartz, sanidine, magnetite, clinopyroxene, and fayalite, all set in a high-silica rhyolitic glass. Compositionally, glass and phenocryst phases are internally homogenous, and again are nearly indistinguishable between flows. The only recognizable compositional difference is in crystals of magnetite, clinopyroxene, and fayalite in Pitchstone Plateau that are all slightly enriched in Fe relative to Mg when compared those phases in other flows, consistent with compositional analyses performed by Christiansen (2001), Vazquez et al. (2009), and Girard and Stix (2010).

The phenocryst assemblage in Central Plateau Member rhyolites is generally reproduced by both NNO+1 and QFM-buffered phase equilibria experiments. Experiments run at an oxygen fugacity of NNO+1 generate sanidine, quartz, magnetite, clinopyroxene, and plagioclase (only <700 °C). Those experiments were too oxidized to stabilize fayalite. Fayalite joined the stable assemblage of sanidine, quartz, magnetite and clinopyroxene in QFM-buffered experiments. The only other effect of oxygen fugacity was that QFM experiments were found to stabilize phases at temperatures 5 to 20 degrees hotter than in NNO+1 experiments. Because phase equilibria are more tightly constrained in P-T space at NNO+1 we use it to evaluate the natural phase assemblage, but employ constraints from QFM experiments when possible. The natural phase assemblage is only stable at conditions below the quartz-in curve at 715±10 °C at 150 MPa and at 800±15 °C at 25 MPa, but above the solidus or plagioclase-in curve. Such constraints generate a ~75 °C stability window that narrows with increasing water pressure. Because sanidine becomes more potassic with increasing pressure, natural sanidine compositions ($Or_{50\pm2}Ab_{47\pm2}An_{2\pm1}$) are only similar to experimental products formed at less than 120 MPa.

To better constrain the storage conditions we apply the QUILF geothermometer using compositions of coexisting natural assemblages of unzoned quartz, fayalite, clinopyroxene, and magnetite (Andersen et al. 1993). Average phenocryst compositions in Trischmann Knob, West Yellowstone, Summit Lake, and Solfatara Plateau each yield temperatures of 755±20 °C, whereas those in Pitchstone Plateau provide an estimate of 745±15 °C. All flows return oxygen-fugacity values ranging 0.4 to 0.5 log units below the QFM buffer. When compared to the phase equilibria results, QUILF temperatures further constrain the storage conditions. To experimentally produce the natural phase assemblage at the estimated QUILF temperature for each flow, then water pressures were mostly likely less than 75 MPa.

Volatile contents in quartz-hosted glass inclusions from the Yellowstone caldera have been determined for few eruptions. Volatile contents in the Lava Creek Tuff range from 1.9 to 3.9 wt.% H_2O and 93 to 770 ppm CO_2, in the Tuff of Bluff Point they range from 1.6 to 2.6 wt.% H_2O and 114 to 585 ppm CO_2, and in Douglas Knob lava dome they range from 1.2 to 2.5 wt.% H_2O and 56 to 254 ppm CO_2 (Gansecki and Lowenstern 1995; Gansecki 1998; Befus et al. 2012; 2014). Importantly, those results fall along a trend indicative of a mixed fluid that had a molar composition of ~50:50 H_2O-CO_2 composition (Liu et al. 2005). Our experiments were performed assuming $P_{total}=P_{H2O}$. Such an assumption likely has very little effect on phase equilibria temperatures because CO_2 is a trace element (0.0005 wt.%) that would not affect major element activities or mineral stability (Gardner et al., 2014). Pressure constraints, however, could vary greatly (Liu et al. 2005). Assuming a 50:50 H_2O-CO_2 mixed fluid composition that was vapor saturated at depth, then the upper water pressure constraint of 75 MPa is consistent with a maximum total pressure of 165 MPa (Liu et al. 2005). Using a crustal density of 2,500 kg m^{-3}, that estimate corresponds to maximum storage depth of 7 km. Together, phase equilibria and geothermometry indicate the Central Plateau Member rhyolite magmas were relatively cool (750±25 °C), and were stored in the shallow crust (<7 km). Such depth estimates are consistent with recent high-resolution earthquake tomography that shows the modern crustal magma reservoir may be as shallow as 2 km (Smith et al. 2009, 2013).

Our phase equilibria results generate a phase assemblage similar to that predicted by Rhyolite-MELTS (Gualda et al. 2012), but our results do not compare favorably in many ways. First, Rhyolite-MELTS predicts quartz, sanidine, and plagioclase stabilize at temperatures ~50 °C hotter than those observed in experiments. Rhyolite-MELTS also predicts quartz, sanidine, and plagioclase form over a small temperature range. In our experiments, sanidine stabilizes at the highest temperatures. Quartz is the next felsic phase to stabilize, and forms at temperatures ~20 °C cooler than sanidine. Plagioclase is the last to join the assemblage, and forms at temperatures 25 to 75 °C cooler than quartz. A similar discrepancy between experimental results and Rhyolite-MELTS is described in Gardner et al. (2014).

Decompression rate

To quantify the decompression rate, and by extension, ascent rate, we compare natural microlite textures to those produced through continuous decompression. Microlites nucleate and grow in the melt in response to undercooling (ΔT) (Swanson et al. 1989; Geschwind and Rutherford 1995; Hammer et al. 1999; Hammer and Rutherford 2002). During eruptive ascent, volatile degassing from the melt induces undercooling, a process simulated by decompression experiments (e.g., Geschwind and Rutherford 1995; Hammer and Rutherford 2002; Brugger and Hammer 2010; Martel 2012). Although past studies have used decompression experiments to understand microlite crystallization and eruptive ascent rates in rhyolite melt during eruptive ascent, they relied on discontinuous decompressions. Discontinuous decompressions follow a step-wise progression, in which pressure drops are instantaneous and are followed by isobaric plateaus. Few previous studies have used continuous decompression pathways (e.g., Brugger and Hammer 2010; Martel 2012). When compared, discontinuous decompression experiments generate textures that correspond to textures formed at faster rates in continuous decompressions. This difference is attributed to the kinetic shock that step-wise decompression steps place on the system (Brugger and Hammer 2010). We recognize that magma ascent may be either pulsatory (discontinuous), continuous, or vary in space and time in the conduit. Importantly, our continuous decompression experiments explore one end member that has so far received relatively little attention.

Our experiments were designed to investigate microlite crystallization across the range of possible storage conditions. Accordingly, we performed decompressions at 720 °C, 750 °C, and 780 °C, using initial pressures to ensure small ΔT at the start. Experiments were generally quenched at 10 MPa, which corresponds to ΔT of 110 °C, 80 °C, and 50 °C, for isothermal decompressions at 720 °C, 750 °C, and 780 °C, respectively (Fig. 8). Although additional experiments are required to fully explore the relationship between phase stability and ΔT, our preliminary results demonstrate temperature plays an important role in addition to ΔT for microlite formation.

To estimate the natural decompression rate of Central Plateau Member lavas, we compare experimental microtextures to the natural microlite assemblage of Fe-Ti oxides, clinopyroxene, and alkali feldspar. Clinopyroxene and Fe-Ti oxide formation appears insensitive in decompression experiments, whereas alkali feldspar and quartz appear to form readily during experiments (e.g., Castro and Gardner 2008). First, quartz microlites are not found in natural samples, but formed in all decompressions at 720 °C. Hence, magmatic ascent mostly likely occurred at temperatures above 720 °C, which is in line with the pre-eruptive magmatic temperature estimates from QUILF and phase equilibria. Alkali feldspar never stabilized in decompressions at 780 °C, even at rates as slow as 0.75 MPa hr^{-1}. Experiments at such slow decompressions contained both Fe-Ti oxides and clinopyroxene, and are thus texturally similar to most natural samples. Because alkali feldspar was never observed, 0.75 MPa hr^{-1} provides a plausible estimate, but the melt may have decompressed at significantly slower rates. Alkali feldspar microlites only occur in rare Central Plateau Member samples. When they do occur their number densities are $10^{8.0\pm1.0}$ cm^{-3}. Number densities that range from zero to $10^{8.0\pm1.0}$ are consistent with textures generated by decompressions at 750 °C at rates of 0.9 and 2.7 MPa hr^{-1}. The lack of alkali feldspar in most samples indicates that most microlite formation in Central Plateau Member lavas occurred in response to degassing during eruptive ascent at ~2.7 MPa hr^{-1}. The rare samples that contain alkali feldspar most likely degassed during slower ascent rates, on the order of ~1 MPa hr^{-1}. These microtextural constraints imply spatially and/or temporally variable decompression histories during conduit ascent for the effusive Central Plateau Member rhyolites. This conclusion aligns with inferences that variable degassing occurred during other rhyolitic effusions elsewhere based on tuffisite veins and flow bands (Stasiuk et al. 1996; Gonnermann and Manga 2003; Tuffen and Dingwell 2005).

Assuming that a pre-eruptive temperature of ~750 °C is indeed appropriate, then the natural microlite assemblages in Central Plateau Member rhyolites were largely generated at decompression rates near 1 MPa hr^{-1}. That rate is equivalent to an ascent rate of 11 mm s^{-1} (~1 km d^{-1}), assuming a lithostatic gradient and a melt density of 2350 kg m^{-3} (Lange and Carmichael 1990). Our experimentally constrained rates are 1 to 2 orders of magnitude faster than those estimated using the empirical model of Toramaru et al. (2008), which links microlite number density to decompression rate. That model predicts

Central Plateau Member lavas experienced decompression rates of 0.02 to 0.14 MPa hr^{-1}, equivalent to slow ascent rates of 0.2 to 1.7 mm s^{-1} (Toramaru et al. 2008; Chapter 2). The disparity between experimental and model predictions may indicate that the magmatic temperature during ascent was hotter, such as 780 °C. If true, then our experimental results indicate that ascent mostly likely occurred at rates slower than 0.75 MPa hr^{-1}. Alternatively, the disparity may demonstrate that the model by Toramaru et al. (2008) is not appropriate to use with high silica rhyolites. Indeed, the model is calibrated for melts with compositions as silicic as dacite, but not rhyolite.

Granophyre implications

The Central Plateau Member rhyolites are monotonous with respect to phenocryst content and composition, indicating similar magmatic conditions. Granophyre had not been identified previously in Solfatara Plateau, or any other Central Plateau Member rhyolite, and its discovery presents a unique opportunity to gain new insights to the magmatic system and/or eruption dynamics. The composition of sanidine in granophyre is indistinguishable from phenocrystic sanidine, which most likely means that they formed under similar storage conditions. When present, granophyre occurs as overgrowths on phenocrysts or occurs as individual, rounded blebs. Granophyre-bearing samples also contain discontinuous bands defined by small quartz and alkali feldspar fragments, whereas non-granophyre samples do not show this feature. Indeed, some bands can be traced to granophyre and appear to be disaggregated granophyre. In places the transition from granophyre-bearing to granophyre-free portions corresponds with a sharp topographic break, with the granophyre-bearing portions at lower elevations on the flow (Fig. 5a,b). The topographic break is considered to be unrelated to post-emplacement erosion because it and other surface features appear directly related to emplacement. The spatial distribution of granophyre within Solfatara Plateau preserves a petrologic record of a previously unrecognized magmatic or volcanic process.

Granophyric intergrowths are thought to represent rapid crystallization of quartz and alkali feldspar in response to significant undercooling of the melt at low pressures (Barker 1970; Lipman et al. 1997; Lowenstern et al. 1997; Morgan and London 2012). If true, then granophyres may record sudden changes in the thermal conditions of magma in response to degassing or shallow magmatic emplacement. The distribution of granophyre solely in distal, early-extruded portions of Solfatara Plateau may record dissolution of granophyre-bearing crystal mush in response to thermal disequilibrium initiated by a magmatic heating event that preceded (and possibly triggered) the effusive eruption (e.g., Bachmann et al. 2002; Girard and Stix 2010; Morgan and London 2012). The rounded blebs and discontinuous bands of small quartz and alkali feldspar fragments possibly record dissolution and digestion of granophyre in response to elevated temperatures. Elevated temperatures in the magma chamber could cause complete dissolution of granophyre in late-erupted melt, whereas early-erupted portions of magma remained cool enough to partially preserve the granophyre. Thermal disequilibrium caused by temperature increases a few thousand years prior to eruption has been suggested for Upper Basin lavas at Yellowstone, as recorded by compositional zonation in sanidine and clinopyroxene crystals (Till et al. 2013). The timing of the heating event may have been much faster, because we find that sanidine and quartz melt and disappear after just a few weeks at temperatures above 800 °C in our experiments. If the Solfatara Plateau magma was subjected to a heating event, it must have been initiated by underplating of a hotter magma prior to eruption because phenocrysts in Solfatara Plateau are compositionally unzoned, and do not preserve evidence of pre-eruptive thermal disequilibrium, magma-mixing, or convective overturn.

The previous interpretation considers Solfatara Plateau as a single flow, with the granophyre-bearing lava representing early-erupted portions of the single magma batch. Because the distribution of granophyre switches near a change in topography, the granophyre-bearing lava may instead be the product of an earlier, temporally unrelated effusive event that was overridden by a younger, granophyre-free flow. Even if that were the case, the aforementioned magmatic process remains relevant to the occurrence of granophyre in the older flow. Furthermore, it indicates that Solfatara Plateau is a composite unit comprised of at least two flows. Other, large-volume Central Plateau Member lavas may also be composite flows. Indeed, we observe similar topographic discontinuities on West Yellowstone and Pitchstone Plateau, but we have observed no petrologic differences in samples from those domains.

CONCLUSIONS

The effusive eruptions that emplaced the Central Plateau Member rhyolites were sourced from crystal-poor melts that were at least temporarily stored as batches of magma with volumes up to 70 km^3. Comparisons of the natural phenocryst assemblage and high-temperature experiments indicate those melts were stored at relatively cool conditions (725-800 °C) in the shallow crust (<7 km). Such P-T conditions are largely consistent with pressure estimates from high-resolution seismic tomography (Smith et al. 2009, 2013), but are 50 to 150 °C cooler than previous temperature estimates for Yellowstone and Snake River Plain rhyolite volcanism (Honjo et al. 1992; Valley et al. 2003; Branney et al. 2008; Cathey and Nash 2009; Vazquez et al. 2009; Ellis et al. 2010; Wolff et al. 2011; Almeev et al. 2012). Comparisons between natural and experimental microlite textures indicate the effusive eruptions experienced eruptive decompression rates near 1 MPa hr^{-1}, which are equivalent to ascent rates ≤ 11 mm s^{-1}. Such ascent rates are consistent with other estimates for effusive eruptions in which degassing could occur (Eichelberger et al. 1986; Gonnermann and Manga 2003; Rutherford 2008).

The discovery of granophyre-bearing domains at Solfatara Plateau provides a unique petrologic clue about the storage and/or eruption of Central Plateau Member lavas. We favor the hypothesis that it is evidence for the systematic dissolution of granophyre in response to a heating event. Indeed, heating, via replenishment or underplating, has been cited as a possible cause for destabilization of Central Plateau Member reservoir(s) 100's to 1000's of years prior to eruption (Girard and Stix 2010; Till et al. 2013). The distribution of granophyre demonstrates that Solfatara Plateau is a complex flow, or possibly a composite unit generated by temporally unrelated eruptions. That observation implies the eruptive history of Yellowstone may yet contain unidentified, volumetrically-significant eruptive events, which is critical for hazard assessment at Yellowstone. The distribution of granophyre must also be considered when interpreting samples collected during past and future petrologic and isotopic studies of

Solfatara Plateau and other Central Plateau Member rhyolites (e.g., Girard and Stix 2010; Watts et al. 2012; Stelten et al. 2013).

Table 1.1

Ages and physical parameters of target Central Plateau Member lavas.

	Age (ka)	Volume (km^3)	Max length (km)	Thickness (m)
Pitchstone Plateau	79±11	70	16.5	200
Solfatara Plateau	103±8	7	15.30	57
West Yellowstone	114±1	41	21.70	105
Trischmann Knob	~115	0.014	0.25	17
Summit Lake	124±10	37	17.70	92

Data from Christiansen (2001) and Christiansen et al. (2007).

Table 1.2

Compositions of major phenocryst phases.

Mineral	Sample[a]	SiO_2	TiO_2	Al_2O_3	FeO[a]	MgO	MnO	CaO	K_2O	Na_2O	Total	n
Fayalite	Solfatara Plateau	30.09 (0.33)	0.04 (0.05)	0.01(0.01)	64.88 (0.91)	2.75 (0.10)	1.62 (0.08)	0.28 (0.01)	-	-	99.69 (1.14)	25
	West Yellowstone	30.48 (0.24)	0.02 (0.03)	0.01 (0.01)	64.65 (0.46)	3.06 (0.09)	2.24 (0.11)	0.26 (0.02)	-	-	100.70 (0.47)	32
	Summit Lake	30.31 (0.33)	0.02 (0.02)	0.01 (0.01)	64.34 (0.58)	3.11 (0.08)	2.23 (0.10)	0.27 (0.03)	-	-	100.57 (0.68)	31
	Pitchstone Plateau	30.09 (0.30)	0.02 (0.03)	0.01 (0.01)	65.84 (0.49)	2.03 (0.07)	2.33 (0.03)	0.28 (0.01)	-	-	100.80 (0.57)	38
	Trischmann Knob	30.38 (0.15)	0.02 (0.03)	0.01 (0.01)	64.90 (0.72)	2.94 (0.08)	2.25 (0.06)	0.27 (0.01)	-	-	100.74 (0.74)	7
Clinopyroxene	Solfatara Plateau	49.45 (0.76)	0.21 (0.08)	0.45 (0.15)	26.70 (0.61)	4.12 (0.39)	0.73 (0.05)	18.68 (0.24)	0	0.31 (0.03)	100.65 (0.89)	55
	West Yellowstone	49.26 (0.61)	0.21 (0.05)	0.49 (0.03)	26.00 (0.70)	4.33 (0.41)	1.07 (0.07)	18.82 (0.27)	0	0.32 (0.04)	100.49 (0.71)	24
	Summit Lake	49.25 (0.59)	0.23 (0.05)	0.52 (0.16)	26.21 (0.63)	4.21 (0.39)	1.07 (0.07)	18.79 (0.26)	0	0.32 (0.04)	100.60 (0.58)	33
	Pitchstone Plateau	48.97 (0.53)	0.22 (0.04)	0.54 (0.27)	27.48 (0.45)	3.03 (0.17)	1.07 (0.08)	18.97 (0.30)	0	0.33 (0.04)	100.60 (0.57)	39
	Trischmann Knob	49.41 (0.42)	0.22 (0.04)	0.48 (0.14)	26.09 (0.57)	4.28 (0.44)	1.03 (0.05)	18.65 (0.17)	0	0.31 (0.05)	100.49 (0.54)	35
Magnetite	Solfatara Plateau	0.09 (0.03)	18.53 (0.65)	0.85 (0.08)	76.39 (1.12)	0.18 (0.03)	0.87 (0.04)	0.01 (0.01)	-	-	96.86 (1.37)	78
	West Yellowstone	0.09 (0.03)	18.45 (0.56)	0.78 (0.09)	77.86 (1.41)	0.20 (0.03)	0.87 (0.06)	0.01 (0.01)	-	-	98.25 (1.45)	59
	Summit Lake	0.10 (0.02)	18.53 (0.43)	0.82 (0.05)	78.07 (1.05)	0.22 (0.03)	0.90 (0.06)	0.01 (0.01)	-	-	98.62 (1.11)	69
	Pitchstone Plateau	0.10 (0.02)	17.67 (0.33)	0.75 (0.07)	79.33 (0.70)	0.12 (0.04)	0.86 (0.06)	0.01 (0.01)	-	-	98.85 (0.84)	85
	Trischmann Knob	0.10 (0.03)	18.92 (0.42)	0.86 (0.05)	76.84 (1.02)	0.21 (0.04)	0.90 (0.05)	0.01 (0.01)	-	-	97.85 (1.14)	35
Sanidine	Solfatara Plateau	66.42 (0.59)	-	18.94 (0.22)	0.09 (0.07)	-	-	0.39 (0.18)	8.28 (0.61)	5.57 (0.49)	100.07 (0.92)	136
	West Yellowstone	66.60 (0.36)	-	18.97 (0.19)	0.13 (0.03)	-	-	0.51 (0.04)	8.58 (0.17)	5.09 (0.13)	99.87 (0.59)	17
	Summit Lake	66.14 (0.67)	-	18.76 (0.26)	0.14 (0.03)	-	-	0.52 (0.05)	8.49 (0.12)	5.14 (0.09)	99.18 (0.97)	28
	Pitchstone Plateau	66.18 (1.25)	-	18.81 (0.36)	0.15 (0.03)	-	-	0.46 (0.04)	8.63 (0.11)	4.97 (0.07)	99.19 (1.72)	10
	Trischmann Knob	65.65 (0.94)	-	18.74 (0.17)	0.15 (0.02)	-	-	0.56 (0.05)	8.26 (0.10)	5.13 (0.10)	98.50 (1.15)	5

Analyses by electron microprobe. Major oxides reported in weight percent, and are averages of n samples. Values in parentheses represent standard deviation

"-" oxide was not analyzed

[a] Total iron reported as FeO

Table 1.3

Phase equilibria experimental conditions and products.

EXP	Starting material	Duration (hours)	P (MPa)	T (°C)	O_2 fugacity	Stable Phases
1	Y82	167	25	700	NNO+1	qtz, pyx, ox, san ($Or_{48\pm1}$)
2	Y82	167	25	850	NNO+1	ox
3	Y82	168	50	850	NNO+1	ox
4	Y82	168	50	775	NNO+1	ox, san ($Or_{51\pm3}$)
6	Y82	168	50	700	NNO+1	qtz, pyx, ox, san ($Or_{42\pm1}$)
7	Y82	168	50	750	NNO+1	qtz, pyx, ox, san ($Or_{54\pm5}$)
9	Y82	168	25	750	NNO+1	qtz, pyx, ox, san ($Or_{52\pm3}$)
11	Y82	170	125	700	NNO+1	qtz, pyx, ox, san ($Or_{66\pm4}$)
12	Y82	170	125	725	NNO+1	pyx, ox, san (na)
13	7 (melt)	169	100	750	NNO+1	ox
14	9 (melt)	168	25	800	NNO+1	pyx, ox, san ($Or_{40\pm8}$)
15	2 (crys)	168	25	800	NNO+1	pyx, ox, san ($Or_{44\pm4}$)
16	2 (crys)	167	75	750	NNO+1	pyx, ox, san (na)
17	Y82	167	75	800	NNO+1	ox
18	Y82	160	100	700	NNO+1	qtz, pyx, ox, san (na)
19	17 (crys)	160	75	725	NNO+1	qtz, pyx, ox, san ($Or_{62\pm6}$)
25	9 (melt)	168	25	850	NNO+1	ox
29	17 (crys)	168	75	750	NNO+1	pyx, ox, san ($Or_{60\pm3}$)
30	Y82	336	75	675	NNO+1	qtz, pyx, ox, san (na)
32	7 (melt)	168	50	825	NNO+1	ox
33	Y82	168	200	650	NNO+1	qtz, pyx, ox, san (na), plag (na)
36	3 (crys)	168	50	775	NNO+1	pyx, ox, san ($Or_{52\pm6}$)
41	4 (melt)	168	50	850	NNO+1	ox
42	17 (crys)	168	20	850	NNO+1	ox
46	18 (melt)	168	75	800	NNO+1	ox
47	Y82	168	75	825	NNO+1	ox
50	Y82	126	50	780	NNO+1	pyx, ox, san (na)
53	Y82	122	50	780	NNO+1	pyx, ox, san (na)
57	Y82	120	130	720	NNO+1	pyx, ox, san ($Or_{63\pm4}$)
58	Y82	120	90	780	NNO+1	ox

Table 1.3 (cont.)

61	47 (crys)	336	25	725	NNO+1	qtz, pyx, ox, san (Or$_{52\pm3}$)
62	47 (crys)	336	25	750	NNO+1	qtz, pyx, ox, san (Or$_{52\pm3}$)
63	47 (crys)	336	50	750	NNO+1	qtz, pyx, ox, san (Or$_{57\pm3}$)
64	50 (crys)	336	100	700	NNO+1	qtz, pyx, ox, san (Or$_{50\pm3}$)
67	50 (crys)	336	75	675	NNO+1	qtz, pyx, ox, san (Or$_{51\pm5}$)
68	50 (crys)	336	200	650	NNO+1	qtz, pyx, ox, san (Or$_{47\pm2}$), plag (Ab$_{80}$)
71	Y82	120	50	700	NNO+1	qtz, pyx, ox, san (Or$_{44\pm6}$)
72	Y82	120	100	800	NNO+1	ox
75	72 (crys)	167	100	750	NNO+1	ox
76	72 (crys)	167	125	725	NNO+1	pyx, ox, san (Or$_{64\pm4}$)
77	72 (crys)	167	125	700	NNO+1	pyx, ox, san (Or$_{63\pm5}$)
80	72 (crys)	147	100	675	NNO+1	qtz, pyx, ox, san (Or$_{58\pm5}$)
81	72 (crys)	333	150	675	NNO+1	qtz, pyx, ox, san (Or$_{66\pm5}$), plag (Ab$_{81\pm2}$)
85	58 (crys)	169	150	725	NNO+1	pyx, ox, san (Or$_{63\pm9}$)
88	57 (crys)	120	75	750	QFM	qtz, pyx, fay, ox, san (Or$_{52\pm2}$)
96	Y82	116	100	750	QFM	pyx, fay, ox, san (Or$_{51\pm1}$)
97	96 (crys)	120	50	825	QFM	ox
98	96 (crys)	120	50	750	QFM	qtz, pyx, fay, ox, san (Or$_{50}$)
99	96 (crys)	120	100	700	QFM	qtz, pyx, fay, ox, san (Or$_{58}$)
100	96 (melt)	120	100	800	QFM	ox
101	96 (melt)	120	50	825	QFM	ox
102	96 (crys)	120	150	725	QFM	pyx, fay, ox, san (Or$_{59\pm10}$)
103	96 (crys)	120	50	700	QFM	qtz, pyx, fay, ox, san (Or$_{56\pm3}$)

Table 1.4

Decompression experimental conditions and products

Experiment	Starting material	Duration (hours)	P_i (Mpa)	P_f (Mpa)	dP/dt (Mpa hour^{-1})	T (°C)	New Phases
73	57	6	130	10	20	720	acicular sanidine, rare quartz
74	57	4.5	130	108	5	720	acicular sanidine, rare quartz
79	57	24	130	10	5	720	coarsening and more sanidine, quartz
107	96	72	130	10	1.7	720	coarsening and more sanidine, quartz
86	23	72	75	10	0.9	750	sanidine (2x starting material)
87	23	50	75	30	0.9	750	sanidine (2x starting material)
93	23	24	75	10	2.7	750	none
94	23	16.6	75	30	2.7	750	none
95	51	24	75	10	2.7	750	none
55	53	60	50	5	0.8	780	none
56	53	30	50	5	1.5	780	none
60	58	3.24	53	10	13.3	780	none
69	58	12.9	53	10	3.3	780	none
70	58	24.3	53	10	1.8	780	none
105	96	15.8	53	10	2.7	780	none
108	106	25.9	53	10	1.7	780	none

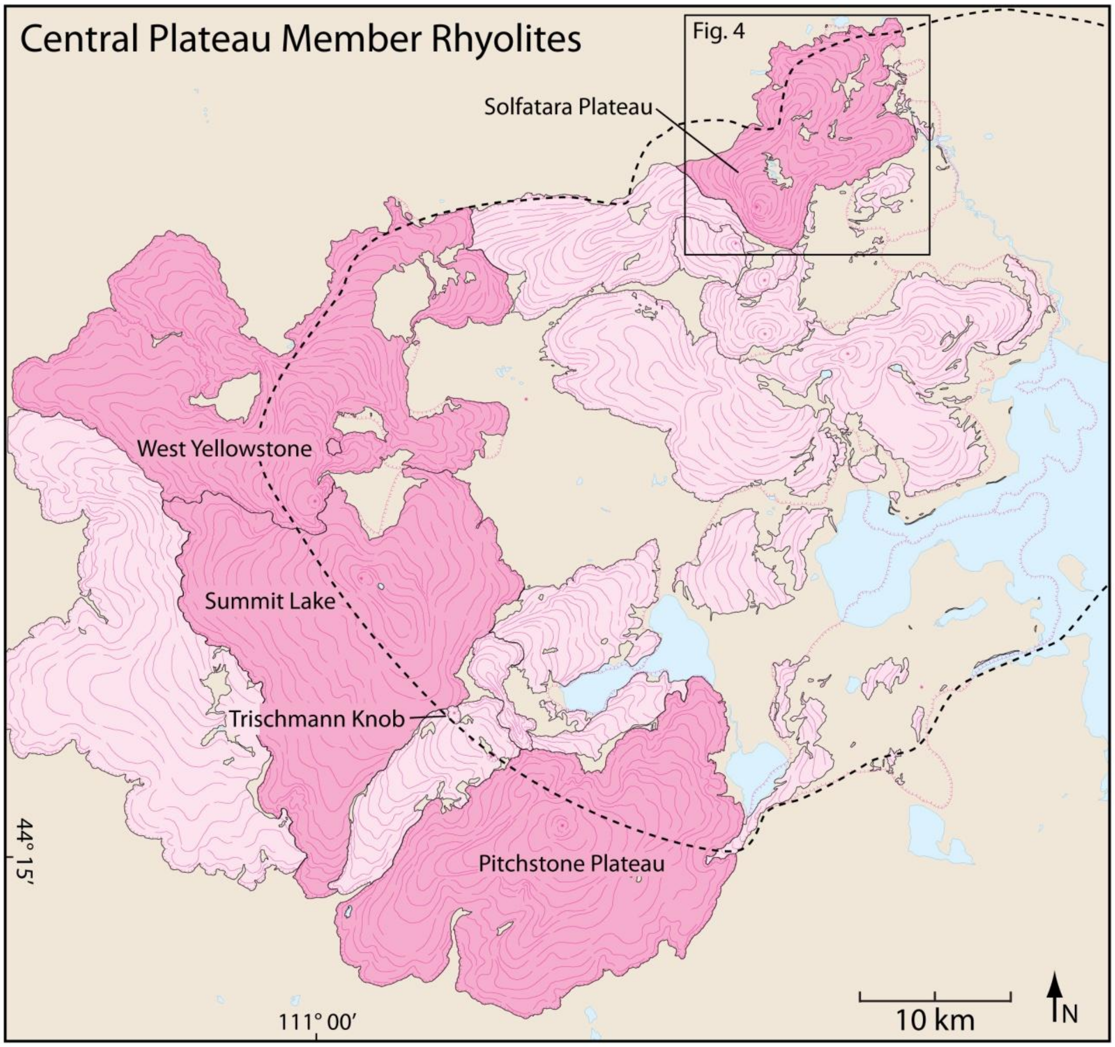

Fig. 1.1

Simplified geologic map of Central Plateau Member rhyolites in the Yellowstone volcanic field with target flows identified, modified after Christiansen (2001). Lava flows are shown in pink, with dark pink lines on Central Plateau Member lavas representing pressure ridges. The extent of Yellowstone caldera is shown by the dashed black line. Pink stars indicate vent locations.

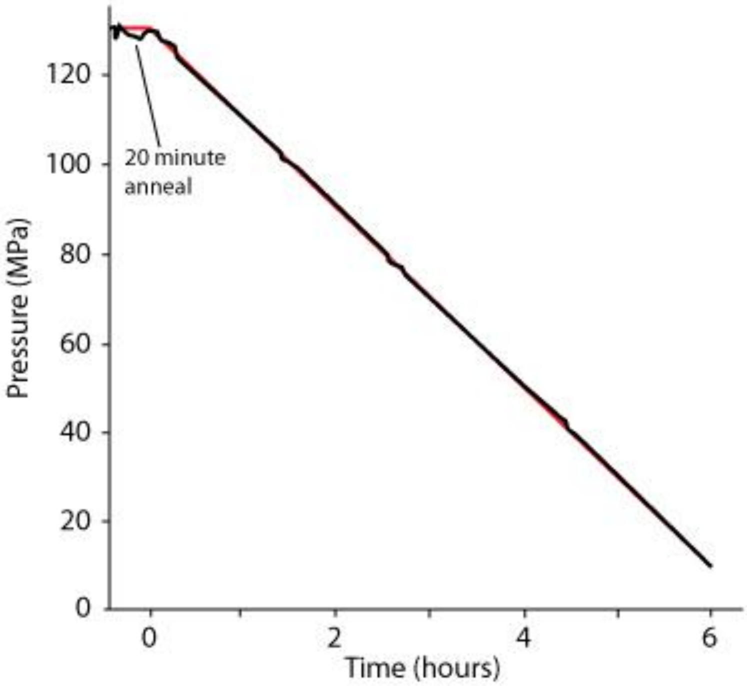

Fig. 1.2

Example of pressure-time pathway during a 6 hour decompression experiment (EX73).

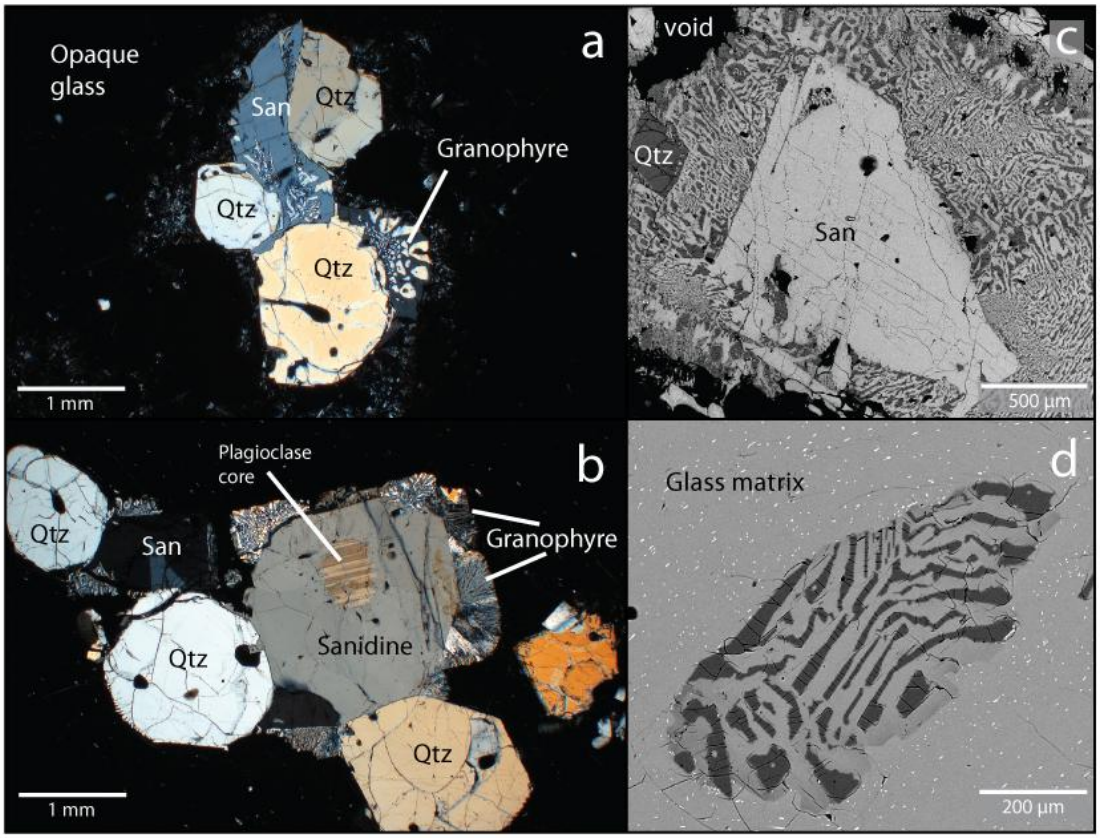

Fig. 1.3

a,b Photomicrographs and **c,d** backscattered images of quartz, sanidine, and granophyre in Solfatara Plateau. Granophyre occurs in association with glomerocrysts of sanidine and quartz, as overgrowths on sanidine and quartz, or as individual clasts.

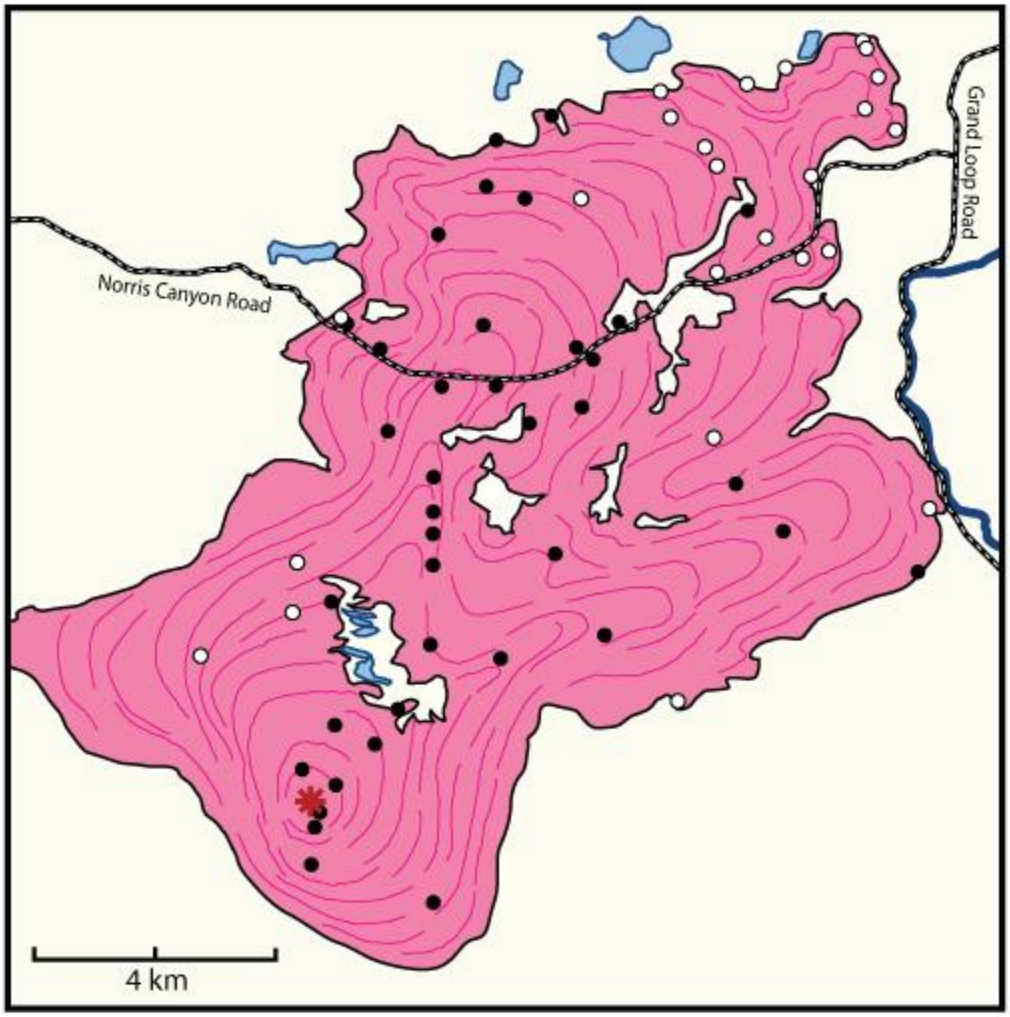

Fig. 1.4

Simplified geologic map of Solfatara Plateau, modified after Christiansen (2001). Sample locations are shown by circles. White circles indicate sample contained granophyre, whereas black circles represent samples without granophyre. Pink star indicates vent location.

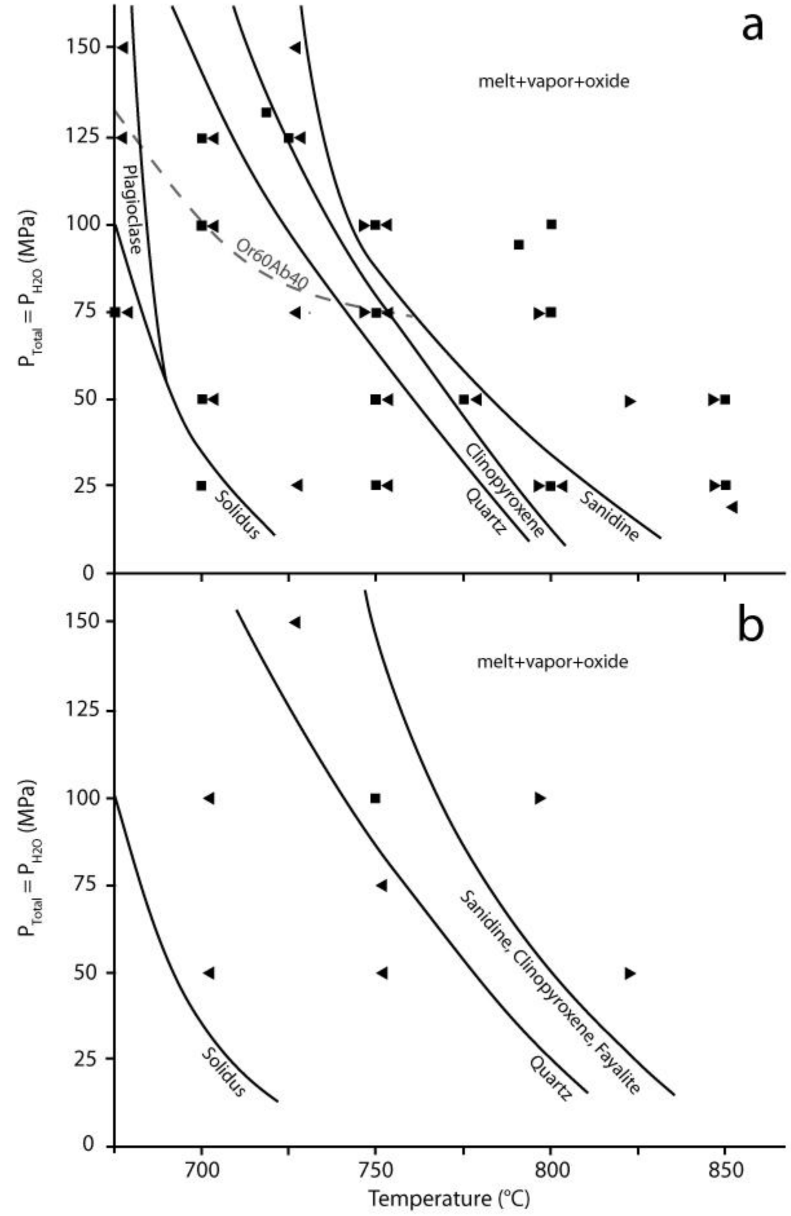

Fig. 1.5

Phase equilibria diagrams for Central Plateau Member rhyolite magma, assuming P_{H2O} equals P_{total}. Squares are initial experiments using powder from sample Y82, whereas right and left pointing triangles represent melting and crystallization experiments, respectively, that used powders from initial experiments. **a** Phase equilibria diagram performed at NNO+1. The dashed gray line marks the $Or_{60}Ab_{40}$ contour for sanidine composition. **b** Phase equilibria diagram performed at QFM.

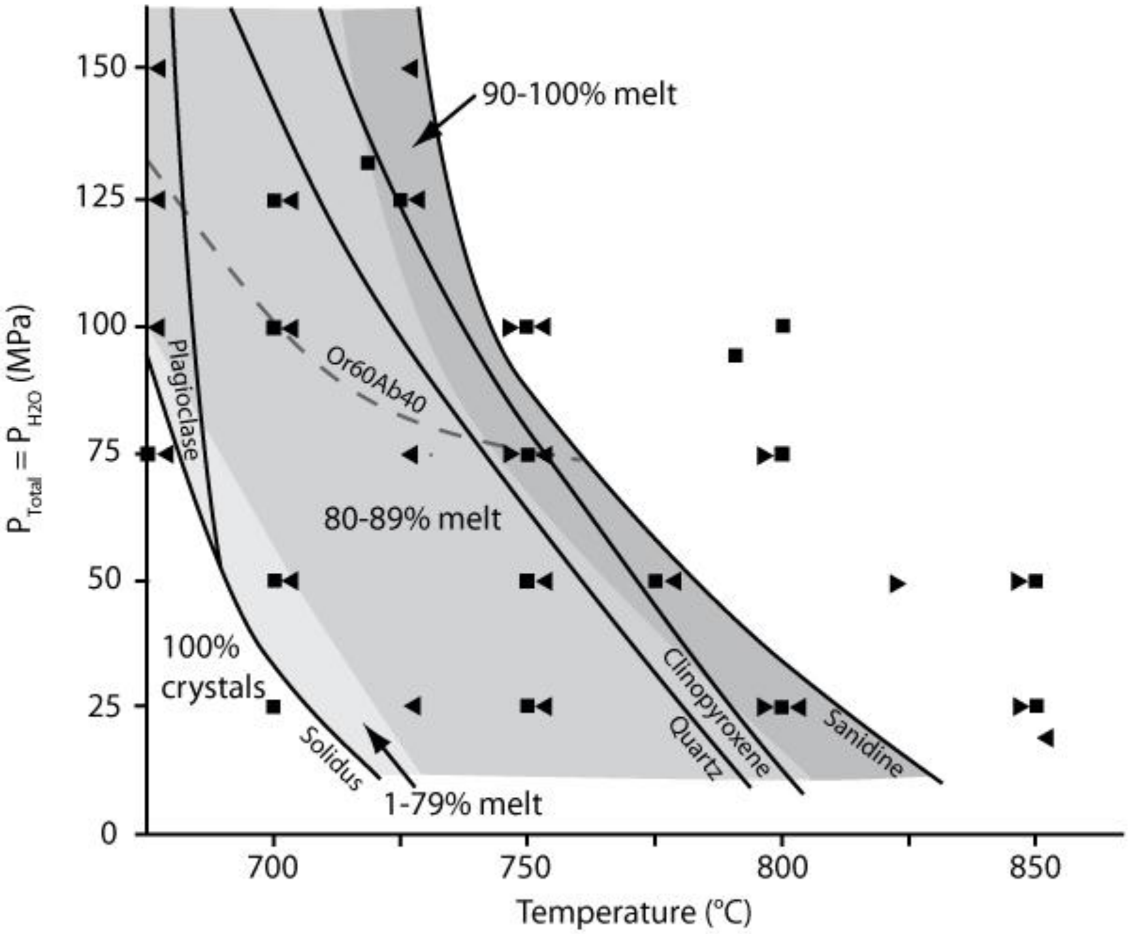

Fig. 1.6

Phase equilibria diagram (NNO+1) with estimates for percent melt remaining. Symbols are same as those in Fig. 5a. Shaded regions show amount of melt present. Most crystallization occurs at temperatures just above the solidus.

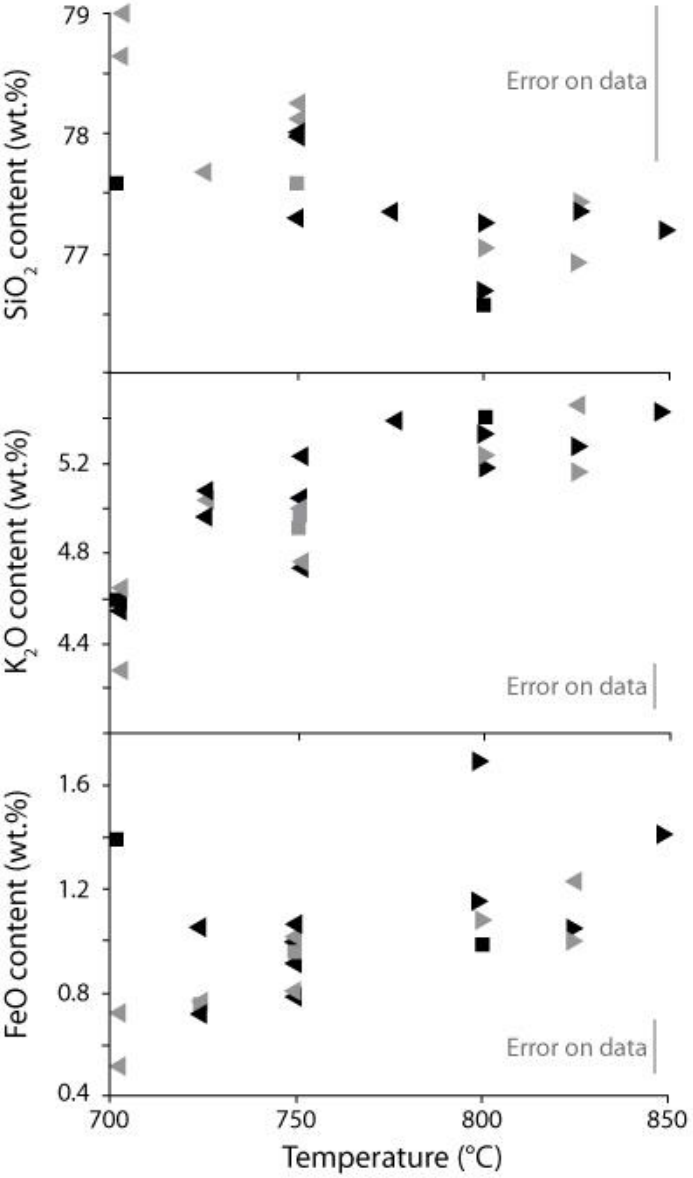

Fig. 1.7

Compositions of experimental glasses as a function of temperature. Black symbols are for NNO+1 experiments, whereas gray symbols are for QFM experiments. Triangles represent reversal experiments. Error bars for SiO_2, K_2O, and FeO analyses are shown by the gray bar on the right of the diagram.

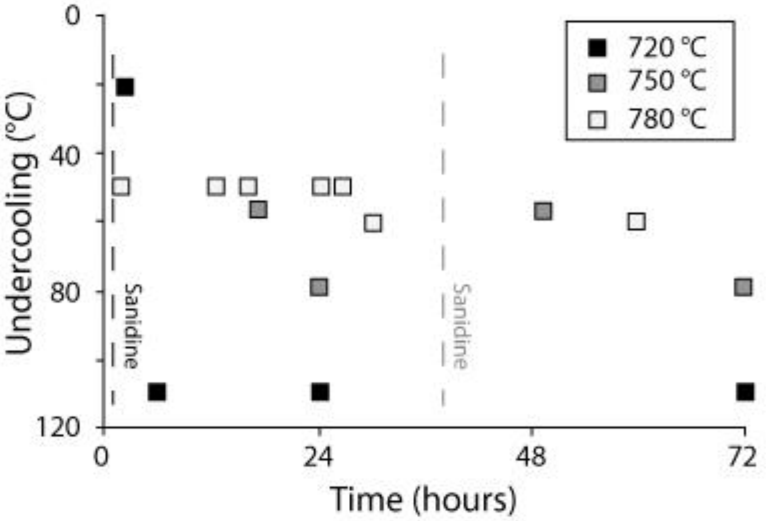

Fig. 1.8

Decompression experiments plotted as a function undercooling at quench and experiment duration. Black symbols are for decompressions at 720 °C, gray for decompressions at 750 °C, and white for experiments at 780 °C. Dashed black and gray lines distinguish the estimated sanidine stability field during decompressions. Note, experiment temperature controls the position of sanidine stability.

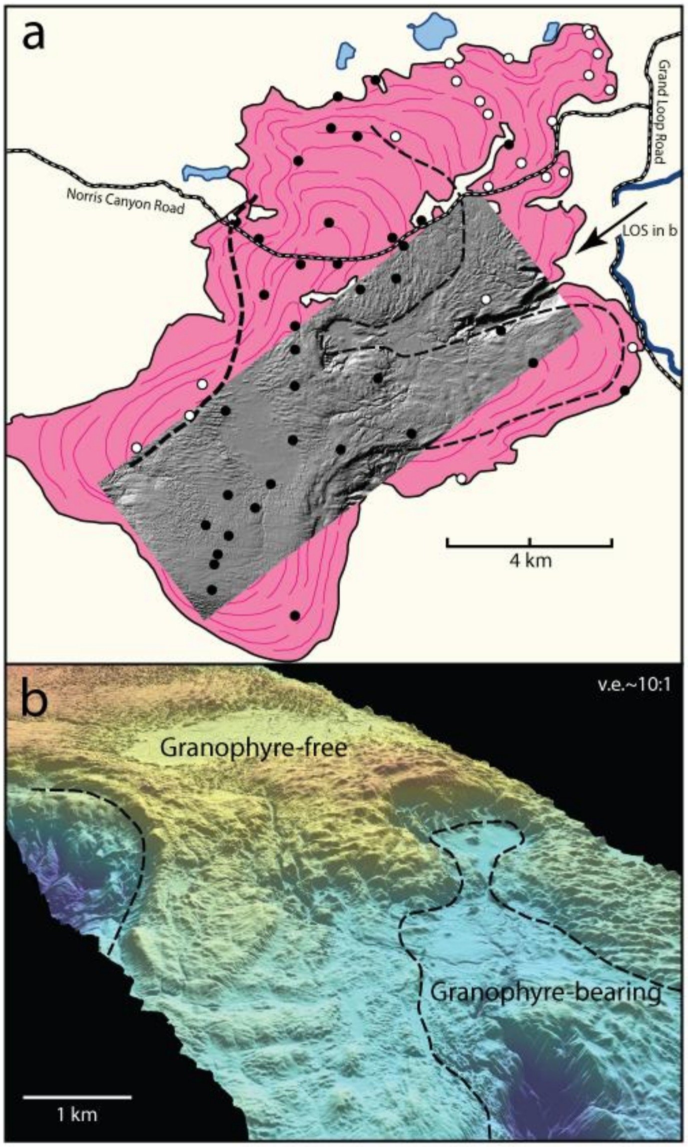

Fig. 1.9

a Distribution of granophyre-bearing and granophyre-free samples in Solfatara Plateau as in Fig. 3. The dashed black line separates Solfatara Plateau into granophyre-bearing and granophyre-free domains. The distribution of granophyre largely corresponds to a change in topography across the flow as highlighted using the DEM overlay from open source LIDAR data from *NSF OpenTopography*. **b** Aerial view of topographic change at Solfatara Plateau with the view looking to the southwest as shown by the line of sight (LOS) arrow shown in **a**. As before, the dashed black line separates granophyre-bearing and granophyre-free domains.

CHAPTER 2:

ASCENT AND EMPLACEMENT DYNAMICS OF RHYOLITIC OBSIDIAN LAVAS INFERRED FROM MICROLITE TEXTURES

Kenneth S. Befus[1], James E. Gardner[1], Matthew Williams[1], Michael Manga[2]

1. Department of Geological Sciences, The University of Texas at Austin, Austin, Texas, 78712, U.S.A.
2. Earth and Planetary Science, University of California, Berkeley, California, 94720, U.S.A.

INTRODUCTION

The recent effusive rhyolitic eruptions of two volcanoes in Chile—Chaitén in 2008-2009, and Cordón Caulle in 2011-2012—have led to renewed interest in conduit and emplacement processes during the eruption of rhyolitic lavas (Castro and Dingwell 2009; Alfano et al. 2011; Bernstein et al. 2013; Castro et al. 2013; Pallister et al. 2013; Tuffen et al. 2013). Those two eruptions provide new observational constraints on the emplacement of two isolated, small-volume eruptions (<1 km^3). Rhyolite effusions, however, can span eruptive volumes from 0.001 to 70 km^3 (Walker et al. 1973; Christiansen et al. 2007). Accordingly, most quantitative data about the emplacement of rhyolitic lavas largely comes from textural and structural field studies of Holocene flows (e.g., Fink 1980; 1983; Stevenson et al. 1994; Gregg et al. 1998; Iezzi and Ventura 2000; Castro et al. 2002; Smith 2002; Rust et al. 2003; Cañón-Tapia and Castro 2004), laboratory experiments using analog models (e.g., Griffiths and Fink 1992; Merle 1998;

Fink and Griffiths 1998), and numerical models (e.g., Huppert et al. 1982; Manley 1992; Stasiuk and Jaupart 1997; Melnik and Sparks 1999).

Once such approach for studying the behavior of effusive eruptions involves the use of microlite textures, which might record cooling and crystallization during eruption; this approach was used to infer the emplacement dynamics of Obsidian Dome from Mono-Inyo Craters, USA (Castro et al. 2002), and Douglas Knob from Yellowstone volcanic field, USA (Befus et al. 2014). Microlites are small (<100 µm) crystals that nucleate and grow in response to undercooling. Thus, the number and size of microlites indicate how they nucleated and grew as they ascended the conduit and/or were emplaced subaerially (Swanson et al. 1989; Geschwind and Rutherford 1995; Hammer et al. 1999; Hammer and Rutherford 2002). Elongate microlites act as rigid flow indicators, hence the orientation of microlites can preserve a record of how lava flows and deforms (Manga 1998; Castro et al. 2002; Befus et al. 2014). Populations of microlites in all samples from Obsidian Dome and Douglas Knob are aligned, and generally trend in the flow direction inferred from topography and surface features. At Obsidian Dome, microlite orientation distributions were found become progressively better aligned with position in the flow, which was interpreted to mean that the lava accumulated strain during flow (Castro et al. 2002). This interpretation was based on comparisons between flow front samples and a single sample from the vent, which may, or may not, have been representative. In contrast, microlite orientation distributions in Douglas Knob do not improve with distance from the vent, which was inferred to mean that they preserved strain as lava ascended the conduit, largely unmodified by flow at the surface (Befus et al. 2014).

Microtextures in Obsidian Dome and Douglas Knob were interpreted to have been generated by fluid deformation caused by flow at the surface or in the conduit, respectively. Clearly, there is potential to gain significant physical insights into how rhyolite lavas erupt using microlites, but detailed microtextural studies have only been performed on two small-volume end members Obsidian Dome (0.17 km^3) and Douglas Knob (0.011 km^3) (Miller 1985; Castro et al. 2002; Befus et al. 2014). The difference in how the microlites are systematically oriented in those flows may indicate that their sensitivity to flow dynamics may vary with the scale of subaerial emplacement. Because rhyolitic lava flows and domes can be morphologically diverse, from small domes to voluminous flood rhyolites (Walker et al. 1973). Thus, an opportunity exists to analyze microtextures in volumetrically diverse rhyolitic flows and domes to better understand how conduit ascent and emplacement dynamics vary with eruption volume.

Here, we present an extensive microtextural study of rhyolitic lavas that range in eruptive volume from 0.001 km^3 to 70 km^3. Our goal is to investigate how microlite number densities and orientations vary with distance from the vent and eruptive volume. Together, we use those microtextural datasets to infer rheological conditions during conduit ascent and subaerial emplacement in volumetrically diverse lava flows and domes. We find that microlite textures are similar across the range of erupted volume (5 orders of magnitude!). Importantly, their textures do not progressively change with their distance from the vent in individual flows. We suggest that microlite number density and orientation thus preserves an opportunity to quantitatively assess conduit dynamics.

LAVA FLOWS AND SAMPLES

Microlite textures were quantified in samples collected from high silica rhyolitic lavas from the Central Plateau Member rhyolites from Yellowstone caldera and from Mono Craters, CA (Table 1). Each lava is similarly composed of high silica rhyolite that contains less than 10% phenocrysts by volume, yet whose matrix contains abundant acicular microlites. We targeted obsidian samples from those lavas because the transparent glass allows microlite textures to be readily observed and measured petrographically. Lavas were selected to encompass a range of flow thicknesses (17 to 200 m) and eruptive volumes (0.001 to 70 km^3) (Table 1).

The Central Plateau Member rhyolites consist of ~30 high silica rhyolitic obsidian lava flows and domes that erupted within Yellowstone caldera during an era of predominantly effusive activity from 79 to 166 ka (Christiansen et al. 2007). All of the rhyolites are composed of high silica rhyolite glass with phenocrysts of quartz, sanidine, clinopyroxene, and magnetite (Christiansen 2001; Vazquez et al. 2009; Girard and Stix 2010).

We collected 1-2 kg samples of dense obsidian from outcrops from Pitchstone Plateau, Grants Pass, Solfatara Plateau, West Yellowstone, Trischmann Knob, Bechler River, Summit Lake, Buffalo Lake, and Dry Creek lava flows (Fig. 1). Pitchstone Plateau and Summit Lake flows represent large-volume flood rhyolites (70 and 37 km^3, respectively) that extruded symmetrically about their central fissure vents. Samples from those huge flows were collected at multiple locations along extensive transects that extended from vent to flow front. Similarly, we collected samples across the length of Solfatara Plateau, an elongate 7 km^3 lava that travelled to the NE and extends up to 16 km from its vent. We also sampled the West Yellowstone lava flow, which is also a large-volume flood rhyolite. We focused on its northwestern lobe that formed when the lava broke through a breach in the caldera wall or glaciated ridgeline, and was subsequently emplaced through that restriction ("chute") and over a relatively flat plain. The chute is located 9 km from the vent (Christiansen 2001). Today, the western lobe of West Yellowstone is preserved as a lobate body that extends ~11 km from the chute. Thus, this lobe presents an ideal example to test how microtextures vary when emplacement happens independent of conduit forcing. We collected samples systematically across the length and breadth of the western lobe, as well as in the ponded domain up to 3 km upstream from the chute. Finally, we present microtextural data from more samples collected from Grants Pass, Trischmann Knob, Bechler River, Buffalo Lake, and Dry Creek lavas.

We collected 1-2 kg samples from two lavas from Northwest Coulee and the South Dome of Panum Crater at Mono Craters, CA (Fig. 1). Mono Craters is a volcanic chain comprised of 27 rhyolitic domes, flows, and associated pyroclastic deposits that erupted ~660 to 20,000 years ago along a gentle arcuate trend between Mono Lake and Long Valley Caldera (Wood 1983; Sieh and Bursik 1986; Hildreth 2004). Northwest Coulee is a ~0.3 km^3 lava that erupted 1500±300 years ago from a central fissure (Wood 1983). Panum Dome is a composite of four separate rhyolitic domes that were emplaced 660±20 years ago within the Panum Crater tephra ring (Sieh and Bursik 1986). We sampled surface outcrops of dense obsidian only from the 0.001 km^3 South Dome at Panum Crater, an obsidian lava emplaced via exogenous growth symmetrically about a central fissure (Sieh and Bursik 1986). Importantly, South Dome presents a volumetric end member in which lava experienced negligible transport away from the conduit (<100 m).

METHODS

Dense obsidian was collected from the targeted lava domes and flows from in situ outcrops. Orientations of the samples were recorded in the field by measuring the strike and dip of one surface of the sample. Polished thin sections were prepared from those samples, with the field orientation of the thin section recorded on each thin section.

Microlite number density (MND) was measured by counting microlites in rectangular prismatic sub-volumes of thin sections while continuously focusing through the transparent glass using a petrographic microscope. Rectangular volumes were generally 80 μm wide, 80 μm long, and 30 μm deep. Depth was measured using a petrographic microscope equipped with a linear encoder attached to the focusing drive. To ensure that a statistically significant number of microlites were counted in each analyzed thin section (>400 microlites), microlites were counted at multiple positions across the sample. Number density counts include Fe-Ti oxide, clinopyroxene, and alkali feldspar microlites. Each of those microlite phases occur as euhedral crystals in the glassy groundmass. Overall, the MND dataset is based upon individually characterizing and logging 35,800 microlites. Microlites define flow bands in some samples. In samples with flow bands, MND was measured in high and low density domains. Trichites and globulites, microlites with delicate and unusual curved morphologies, comprised of Fe-Ti oxide and clinopyroxene were rarely observed in samples. Because such fragile crystals are unlikely to be preserved in an actively deforming fluid, they most likely represent late-stage crystallization unrelated to ascent and emplacement (Harker 1897; Davis and McPhie 1996). We did not include them in the number density counts.

Microlite orientations were also measured using the petrographic microscope, following the methodology described in Befus et al. (2014). Only acicular microlites with aspect ratios that range from 6:1 to 14:1 were measured, in order to compare similar populations. The trend (ϕ) of an acicular microlite was measured using the stage goniometer. The length and width of each microlite was measured using the eyepiece reticle. Next, the depth in the thin section to each microlite tip was measured by focusing through the transparent obsidian and recording the depth measured by the linear encoder. Together those measurements were used to calculate the true length and plunge (θ) of each microlite. Trend and plunge measurements are accurate to ±0.5°and ±2°, respectively. For each sample, the orientations of 140+ microlites were measured. Microlites orientations were then rotated to their true field orientation using *Stereonet* (Cardozo and Allmendinger 2013). In all, the orientation dataset is consists of 7458 measurements. The average ϕ and θ of each population was calculated, with the degree of alignment for each population measured by the standard deviation of ϕ and θ (σ_φ and σ_θ), with smaller standard deviations indicating better alignment.

We used Fourier-Transform Infrared (FTIR) spectroscopy to determine dissolved water contents in matrix glasses from Solfatara Plateau, Summit Lake, Trischmann Knob, Northwest Coulee, and South Dome. FTIR spectra consist of 60 scans at a resolution of 4 cm^{-1} collected using a 40x40 μm aperture in the mid-IR range using a KBr beamsplitter and globar IR source. Water concentrations were estimated from absorbance at 3500 cm^{-1} using the Beer-Lambert Law, and an absorption coefficient of 100 L cm^{-1} mol^{-1} (e.g., Chapter 4). Background absorbance at 3500 cm^{-1} was assumed to be linear. Sample thickness was measured using a pin micrometer that is accurate to 2 μm.

RESULTS

Samples were collected on the erosional surfaces of rhyolitic obsidian lava domes and flows. The upper pumiceous carapace of each of the Central Plateau Member rhyolites has been stripped off by Pinedale glaciations, but pressure ridges remain preserved on the surface of the flows (Christiansen 2001). Because water solubility in rhyolitic melt is largely a function of pressure, we use the dissolved water content in the obsidians to estimate the erosional depth for the flows (Liu et al. 2005). Matrix glasses in Central Plateau Member rhyolites and South Dome contain 0.12±0.03 wt.% H_2O, and Northwest Coulee glass contains 0.17±0.01 wt.% H_2O.Those water contents are equivalent to 0.10 to 0.24 MPa (Liu et al. 2005). Those pressures can be used to calculate the thickness of the overburden that has been removed by erosion assuming reasonable estimates for the density of that eroded material. The upper surfaces of obsidian lavas are typically composed of pumiceous carapace (Fink 1983; Eichelberger et al. 1986; Manley and Fink 1987; Swanson et al. 1989). Using a density of typical pumice (700 kg m^{-3}), up to 20 meters have been removed. Estimates for the density of pumiceous carapace are significantly more dense that typical pumice, and are on the order of 1700 kg m^{-3} (Fink 1983, Manley and Fink 1987). Using that value, our samples represent lava 0 to 4 meters below the original surface of South Dome and Central Plateau Member lavas, and ~8 meters below the surface of Northwest Coulee. Although such calculations provide only rough depth estimates, they indicate that our samples were collected from the upper portions the lavas because the lavas are generally many 10's of m thick (Table 1).

Groundmass textures are defined by microlites. Some samples appear texturally homogenous, whereas others contain discrete to diffuse flow bands resulting from different microlite assemblages and number densities. Fe-Ti oxides are generally the most abundant microlite phase, with lesser amounts of clinopyroxene and feldspar, except in Northwest Coulee and South Dome, in which clinopyroxene is the most abundant phase (Fig. 2) (Table 2). Fe-Ti oxides, which are commonly overgrown by clinopyroxene, occur as equidimensional crystals, 1 to 2 μm in size, or as acicular rods 1 to 2 μm wide and 3 to 30 μm long. Clinopyroxene is present in all flows, except Buffalo Lake (Table 2). Clinopyroxene occurs as either individual crystals or as overgrowths on Fe-Ti oxides. Both types occur as skeletal to euhedral prismatic crystals, 1 to 10 μm wide and 2 to 20 μm long. Overgrowths tend to be more abundant and larger than individual crystals. Feldspar occurs in both lavas from Mono Craters, and in 6 of the 10 Central Plateau Member rhyolites. Feldspar microlites occur as elongate laths, 1 to 5 μm wide and 2 to 20 μm long, and commonly have swallowtail terminations. Hopper and skeletal forms were not observed. No other microlite phases were seen in the Central Plateau Member rhyolites, but rare biotite and amphibole are found in Mono Crater lavas. Those phases were not included in our textural analysis.

Number density

Microlite number density (MND) was determined for Pitchstone Plateau, Grants Pass, Solfatara Plateau, West Yellowstone, Trischmann Knob, Bechler River, Summit Lake, Buffalo Lake, Dry Creek, Northwest Coulee and South Dome at Panum Crater (Table 2). The average total MND of individual flows varies from $10^{8.11\pm0.03}$ to $10^{9.45\pm0.15}$ cm^{-3}. Average Fe-Ti oxide MND range from $10^{7.92\pm0.56}$ to $10^{9.37\pm0.13}$ cm^{-3}. Average clinopyroxene MND ranges from $10^{6.25\pm3.62}$ to $10^{9.19\pm0.37}$ cm^{-3}, except in Buffalo Lake in which it is not present. When present, average feldspar MND is variable and ranges from $10^{0.99\pm2.43}$ to $10^{5.07\pm3.16}$ cm^{-3}.

Microlite orientation

Microlite orientations were measured in samples collected systematically across the lava flows and domes. Measurements were performed on samples collected along transects from vent to flow front at Pitchstone Plateau and Summit Lake, across the western lobe of West Yellowstone, around the flow front at Northwest Coulee, and across South Dome at Panum Crater (Fig. 3a-e) (Table 2). We also reproduce orientation data from Douglas Knob from Befus et al. (2014) for comparison.

We find that acicular microlites are preferentially aligned in samples from all flows. Across individual flows orientations vary. The degree of microlite orientation generally does not correlate with distance traveled; although in some flows σ_θ and σ_φ

increase with distance, whereas in others it decreases. Microlite orientations in near-vent samples from all flows display a range of σ_φ from 14° to 38° and a range of σ_θ from 12° to 31°. Orientations show no correlation with eruptive volume. Indeed, small- and large-volume flows show similar degrees of alignment. Microlite plunge distributions are consistently more aligned than trend (e.g., $\sigma_\theta < \sigma_\varphi$). Values of σ_φ and σ_θ are independent of one another. In addition, microlite orientations do not correlate with MND. Microlite orientations in samples from even distal portions of the extensive Summit Lake and Pitchstone Plateau lava flows are indistinguishable from those at South Dome and Douglas Knob lava domes. Microlite orientations from samples at South Dome at Panum Crater, the smallest targeted lava, trend with no preferred direction and have plunge measurements that are largely close to horizontal. Standard deviations of trend and plunge in those samples have σ_φ that range from 22° to 59° and have σ_θ that range from 16° to 30°.

DISCUSSION

Number density of microlites is a function of nucleation and growth during ascent and/or emplacement, whereas the orientation of microlites is controlled by fluid deformation and the associated accumulation of strain. Together, these microtextural datasets present new constraints on physical processes associated with the emplacement dynamics of rhyolitic lava domes and flows.

Microlite nucleation and growth during surface flow

Thicker and more volumetric flows have the highest MND (Fig. 4). No other parameter, such as age or travel distance, displays a correlation with MND. No correlation exists between microlite assemblages and eruptive volume, thickness, age, or travel distance. MND for any single phase, or all combined, does not display clear, systematic variations across the length of any of those flows (Fig. 5). Instead, microlite phase assemblages and number densities fluctuate with position across individual flows. Indeed, those MND variations may exceed two orders of magnitude. Oxides have the most consistent MND, and are present in every sample collected from every flow. Although present in all flows except Buffalo Lake, clinopyroxene microlites are absent from some flow bands within samples. Conversely, feldspar microlites are absent in most samples from Central Plateau Member lavas, but rarely occurred, confined to specific flow bands.

If microlites crystallize during subaerial emplacement, then a progressive increase in number with distance travelled away from the vent should develop. No such increase in MND is observed (Fig. 5). Therefore, we conclude that microlites were unable to nucleate appreciably during flow along the surface. We suggest that slow diffusion (correlated with elevated viscosity) within the melt presented a kinetic barrier that limited microlite nucleation. Indeed a high-silica rhyolite melt at the estimated emplacement conditions (720-780 °C and 0.10 wt.% dissolved H_2O) would have a viscosity of $10^{9\text{-}10}$ Pa s (Giordano et al. 2008; Befus et al 2014; Chapter 1).

Microlite orientation during surface flow

Microlites act as rigid particles in a deforming fluid (lava), so they can be used to understand the kinematics of emplacement (Jeffrey 1922; Manga 1998; Castro et al. 2002). First, their preserved 3D orientations can be used to track the flow direction, because their long axes may align in the direction of local extension imparted by flow. Second, the degree to which microlites align as a whole (e.g., σ_φ and σ_θ) should improve with increasing strain imparted progressively during emplacement (Manga 1998; Castro et al. 2002). To estimate the shear style and amount of strain that accumulates in lava as it ascends or is emplaced, we compare observed microlite σ_φ and σ_θ to the theoretical response of a population of rod-shaped particles to strain in simple and pure shear flows (Jeffery 1922; Gay 1968; Manga 1998; Befus et al. 2014). Simple shear, pure shear, or a combination of the two act to align populations of microlite (Fig. 6). In response to simple shear, a population of microlites should progressively align, but individual microlites continuously rotate so that the population as a whole never becomes perfectly aligned. In contrast, microlites are predicted to eventually become perfectly aligned with increasing strain during pure shear (see Chapter 3 for more details).

An important first step in understanding lava dynamics using microlite orientations is to examine microlite orientations near vents where little lateral spreading has occurred. Such an approach will establish whether microlites are oriented before or after exiting the conduit. To do this, we measured microlite orientations in samples collected across South Dome at Panum Crater. South Dome has a very small areal footprint, and must have experienced <100 m lateral spreading away from the fissure vent during emplacement. Although the samples were geographically separated from one another by no more than 200 m, overall microlite orientations in each of those samples range from strongly preferred to near random (Fig. 5a). In addition, microlites in the samples generally plunge near horizontal, with plunge distributions better aligned than trend (Fig. 7a). Similar microlite orientations were observed by Befus et al. (2014) in near-vent samples at Douglas Knob lava dome (Fig. 7b). Microlite orientations measurements in small domes that were unaffected by surface emplacement, thus demonstrate that preferred orientations can be remnants of conduit flow.

Next, it is important to evaluate how microlite orientations evolve in response to flow at the surface. Microlite orientations from flows with eruptive volumes spanning 0.001 to 70 km^3 all display similar orientation behaviors. We find that microlites are preferentially aligned in samples from all flows, but the direction and degree of alignment are unsystematic. In other words, no relationship exists between a sample's microlite trend and anticipated flow direction estimated from preserved pressure ridges or its position relative to the vent. In most samples, microlites tend to be oriented closer to horizontal than vertical, but those plunge measurements do not correlate with their position in the flow. The degree of microlite orientation, as measured by σ_θ and σ_φ, is also insensitive to the sample's relative position in each of those flows. Indeed, even distal samples are statistically indistinguishable from near-vent orientation measurements (Fig. 8). Microlite orientations from South Dome and Douglas Knob are indistinguishable from those measured in the larger flows.

The western flow lobe of West Yellowstone lava flow provides an exceptional case to investigate microlite orientation. We assume transport through the chute resets microlite orientations, thus the emplacement should be entirely unrelated to conduit processes. We measured microlite orientations in 17 samples downstream of the chute and in 5 samples in the ponded domain upstream of the chute. Microlite trend and orientations are scattered with respect to distance from the chute (Fig. 5c, 7d). Strain estimates based on σ_θ and σ_φ are likewise scattered relative to their position in the flow. The orientation measurements indicate the microlites did not respond to the bulk flow field during the emplacement of the western lobe of West Yellowstone lava flow.

Microlite orientations in samples from the larger Northwest Coulee, Summit Lake, and Pitchstone Plateau flows were also not significantly modified during subaerial transport, which requires that strains accumulated in sampled portion of the flow during emplacement were small. In fact, strains less than 2 should cause noticeable alignment. The general lack of progressive microlite alignment may appear paradoxical, but the expected strain distribution within the flow can explain this observation. The velocity field of an incompressible, steady state flow of a Newtonian fluid with a free surface and variable viscosity with depth is

$$\frac{du}{dy} = \rho g \, \sin\theta \left(\frac{y}{\mu(y)} - \frac{H}{\mu(H)} \right) \qquad \text{Equation 1}$$

where $u(y)$ is velocity at depth y (m s^{-1}), ρ is melt density (kg m^{-3}), μ is viscosity (Pa s), θ is slope (degrees), and H is total flow thickness (m) (e.g., eq. 3.83 Furbish 1997). The flows were largely emplaced upon flat lying terrain, hence we set slope to 1±1°. We used values for flow thickness that are representative of the target flows (Table 2). We calculate the melt density and viscosity profiles with depth in the flow, but recognize that both parameters depend on the temperature and dissolved water content of the melt. The dissolved water content at depth was set to equal the maximum solubility in rhyolitic glass with depth (Liu et al. 2005). We estimated the temperature profile of the lava by numerically solving the one-dimensional conductive cooling model

$$\frac{dT}{dt} = D\left(\frac{d^2T}{dx^2}\right) \qquad \text{Equation 2}$$

where T is temperature (K), t is time (s), x is depth (m), and D is the thermal diffusivity of rhyolitic obsidian (5.5×10^{-7} m^2 s^{-1}) (Romine et al. 2012). Using those temperatures and water contents, melt density is ~2300 kg m^{-3}, and varies by less than 1% with depth (Lange and Carmichael 1990). Temperature and dissolved water content strongly control melt viscosity (Giordano et al. 2008). We find that minimum lava viscosity always occurs near the base of the flow, where the dissolved water content of the melt is the greatest and the flow remains thermally insulated (Fig. 8). Although maximum velocities are predicted at the flow's surface, the majority of flow-induced strain is accommodated at the base of the flow. The upper third of the flow is predicted to have very small strain rates. Although our strain profile is approximate, it illustrates why microlite orientations near the surface can remain unchanged. The fluid dynamics calculations predict most strain accumulation occurs near the base of a lava flow, whereas the surface, where our samples were collected, rafts inertly on the actively deforming lower portions. Consequently, microlite orientations from surface samples preserve orientations present near the vent.

Conduit implications

Microlite assemblages, number densities, and orientations do not correlate with relative lateral position in the flow, which implies that microlites textures are not appreciably modified during subaerial emplacement. Instead, microlite textures may record orientations present when the lava left the conduit, and thus preserve information about conduit dynamics during effusive rhyolitic eruptions. If true, then the diversity of MND and σ_θ and σ_φ across flows reflects spatially and/or temporally variable conditions inherited from the conduit.

Previous experimental studies have demonstrated that MND can be controlled by water loss from the melt, the rate of which is equated to decompression rate during eruptive ascent (e.g., Geschwind and Rutherford 1995; Hammer and Rutherford 2002; Castro and Gardner 2008; Brugger and Hammer 2010; Martel 2012). To generate the observed microlite assemblage and MND (Table 2), comparisons with continuous decompression experiments indicate the rhyolitic magmas experienced decompression rates of ~1 MPa hour^{-1} (Chapter 1). That decompression rate is equivalent to a slow ascent rate of ~10 mm s^{-1}, assuming a lithostatic pressure gradient and a melt density of

2300 kg m^{-3} (Lange and Carmichael 1990). It is remarkable that such rhyolitic lavas with volumes that vary by orders of magnitude have such similar microlite textures, thus suggesting they rose at similar rates. Overall, the slow ascent most likely allowed gas loss from the ascending magma, thus permitting effusive eruptions (Eichelberger et al. 1986, Jaupart and Allègre 1991; Burgisser and Gardner 2004). Similar slow ascent rates have been estimated for other lavas and domes emplaced effusively (Rutherford and Gardner 2000; Rutherford 2008), and our estimate is similar to constraints placed on ascent during the recent effusions at Cordón Caulle and Chaitén (Castro et al. 2013; Pallister et al. 2013).

MND variations at both the thin section scale and across lava flows indicate that microlite nucleation was both temporally and spatially variable. Because microlite nucleation is controlled by degassing, the microtexture variability could be due to waxing and waning ascent rates during a pulsatory eruption. It could also have been generated by networks of cm- to m-scale degassing pathways that modify the large-scale degassing process (Gonnermann and Manga 2003; Tuffen et al. 2003; Tuffen et al. 2008). Interestingly, no systematic pattern to the MND variability exists. For example, MND do not appear to preserve a record of decreasing ascent rates during the waning stages of eruptions, as was observed at Mount Saint Helens (Rutherford 2008).

The striking resemblance of microlite number densities across volumetrically diverse lavas suggests conduit ascent rates are similar. Because the eruptive volumes of those flows are different, variations in volumetric flux may be the cause instead of ascent rate. If true, then the conduit dimensions and eruptive durations of the large-volume flows must be significantly larger than those feeding the small-volume lavas. If we assume that each of the target flows was sourced from a fissure vent based on past interpretations for the emplacement of Summit Lake, Grants Pass, Douglas Knob, Bechler River, and Northwest Coulee (Sieh and Bursik 1986; Christiansen et al. 2007; Befus et al. 2014), we can estimate fissure length using the orientation of pressure ridges when possible.

The mean ascent rate U (m s^{-1}) of an incompressible magma during steady, laminar flow between two parallel dike walls is

$$U = \frac{w^2}{12\mu} dP/dz \qquad \text{Equation 3}$$

where w (m) is distance between the walls, μ is melt viscosity (Pa s), and dP/dz is the density contrast between melt and crust, which we assume to be 200 kg m^{-3} (Turcotte and Schubert, 1982; Petford et al. 1993). If we assume we know ascent rate is 10 mm s^{-1}, based on microlite textures, then we rearrange Equation 3 to calculate the minimum dike width feeding the eruptions. We calculate a representative range for melt viscosity to be $10^{5.9\text{-}7.3}$ Pa s during ascent, assuming a high-silica rhyolite composition (76±1 wt.%) with 2.5±0.5 wt.% H_2O, 5 wt.% crystallinity, and temperature of 760±20°C (Spera 2000; Giordano et al. 2008). Ascent at 10 mm s^{-1} yields dike widths ranging from 7 to 35 m. The ratio of ascent rate to conduit width provides strain rates of $\sim10^{-3}$ to $\sim10^{-4}$ s^{-1}. At such low strain rates rhyolitic melts are expected to erupt effusively and flow as Newtonian fluids that could only generate insignificant viscous heating (Webb and Dingwell 1990; Gonnermann and Manga 2003).

Together, our estimates for ascent rate, dike width, and dike length suggest the eruptions that fed the small-volume flows had an eruptive fluxes of 10-200 $m^3 s^{-1}$. Such estimates for the small-volume lavas are similar to fluxes at Chaitén and Cordón Caulle, which were 20-60 $m^3 s^{-1}$ initially and gradually decreased to 1-10 $m^3 s^{-1}$ as the eruptions waned (Pallister et al. 2013; Schipper et al. 2013; Tuffen et al. 2013). Although our calculations have considerable uncertainties that are difficult to minimize, our estimates are consistent with ascent rate, conduit size, eruptive flux, and durations estimated and measured for other small-volume lavas (Swanson et al. 1987; Vogel et al. 1989; Nakada and Motomura 1995; Fink and Griffiths 1998; Sparks et al. 1998; Hammer et al. 2000; Rutherford and Gardner 2000; Tuffen et al. 2003; Rutherford 2008; Hautmann et al. 2009; Tuffen and Castro 2009; Pallister et al. 2013). Also, our calculations can provide first-order rates and timescales on large-volume effusive eruptions for which we have no observational constraints, but are documented in numerous rhyolitic systems (Walker et al. 1973; Bonnichsen and Kauffmann 1987; Manley 1996; Pankhurst et al. 2011). Our estimates suggest that the large-volume flows had an eruptive fluxes of 300-3000 $m^3 s^{-1}$, and the eruptions lasted for months to years.

Eruptive flux and decompression estimates define the rates at which melt moves through the conduit. The fluid dynamics and flow of melt during conduit flow may be able to be understood using microlite orientation distributions. Strain estimates based on to σ_φ and σ_θ must be interpreted to have been caused by simple shear, pure shear, or a linear combination of the two (Manga 1998; Castro et al. 2002; Befus et al. 2014). Values of σ_φ range from being well-aligned (13°) to randomly aligned (~50°) (Fig. 10). If we assume that trend alignment was induced solely by end-member pure shear, then σ_φ indicates that melts experienced strains less than 1.7. If instead the melts were deformed by simple shear, then σ_φ measurements preserve strains up to 5.8. Plunge distributions are generally better aligned than trend with σ_θ values ranging from 9° to 41°. Values of σ_θ indicate strains of 0.7 to 4.2 assuming pure shear, and strains of 1.2 to 'infinite' assuming simple shear. The 'infinite' estimate occurs in 30% of the samples, results from the impossibility that simple shear can generate such good alignment. The impossible 'infinite' strain estimates and better alignment of plunge than trend lead us to prefer pure shear as the dominant deformation mechanism recorded in microlite orientations.

To further eliminate simple shear as a viable mechanism, we calculate strain resulting from simple shear caused by Poiseuille flow in the conduit (Fig. 11a). We estimate strain as the ratio of ascent distance to the half-width of the conduit. If the conduits are assumed to be 7 to 35 m wide, then movement of the melt would cause the melt to generate strains up to 5.8 by ascending only 100 m. Depth estimates for the magma chamber sources are much greater (e.g., >1 km)(Chapter 1), which requires that the microlite-bearing melts traversed much longer distances than 100 m during ascent, even if microlite formation is kinetically delayed during ascent. Strain that is caused by simple shear cannot explain the bulk of the observed microlite orientations. If simple shear does occur in conduits during ascent, then it may be isolated to narrow domains along the conduit walls, with the majority of the melt ascending as a non-deforming plug.

Support for pure shear being the dominant deformation mechanism during Plug flow can be found in nearly all samples as microlite plunges are aligned closer to horizontal than vertical, such that $\sigma_\theta < \sigma_\varphi$ (Fig. 7). Microlite orientations in our samples may preserve evidence for gravitational collapse of permeable foam in the conduits as the melt ascends (Eichelberger et al. 1986). Foams form in the conduit during eruptive ascent as bubbles nucleate and grow in response to decompression-induced degassing. Foams are stable when bubble vapor pressure is greater than or equal to the lithostatic load. When the porosity of the foam reaches a critical threshold, the foam becomes permeable, causing vapor pressure in the bubbles to decrease, which in turn allows the stress from the lithostatic overburden to collapse the foam (Eichelberger et al. 1986). Such expansion and collapse of permeable foam would strain the host melt, which could impart specific orientations to the microlite populations. Specifically, the long axes of microlites should align in the direction of local extension. If microlites align in response to extension during a foaming event, we would anticipate microlite orientations in samples to align vertically as melt is stretched in response to bubbles expansion. Instead, microlite orientations in the vast majority of samples are aligned close to horizontal, which we consider evidence for flattening caused by foam collapse (Fig. 11b).

We can estimate bulk strain caused by collapse of permeable foam within conduits with fixed walls. Permeability, and subsequent collapse, is probably achieved when the foam reaches a critical porosity (Eichelberger et al. 1986). Vesicularity of pumice is commonly ~65-70% (Sparks 1978; Gardner et al. 1996). If those values approximates the critical porosity of a permeable foam, then a single collapse event of a foam with 70% vesicularity to dense obsidian would generate a strain of 2.4 in the melt. Such an estimate is similar to strain estimates from microlite orientations. But permeability can also be reached when porosity is as low as 30-40%, or lower if there is shear (Klug and Cashman 1996; Saar and Manga 1999; Burgisser and Gardner 2004; Takeuchi et al. 2005). Importantly, a foam with 40% vesicularity that collapses would result in a strain of 0.7. That value is the same as the lowest strain estimate from microlite orientations, assuming pure shear. Multiple episodes of foam and collapse would thus be required to generate the range of strains estimated by microlite orientations in the lavas. If true, then the observed orientation variability may indicate unsteady, spatially-restricted foam and collapse events in the conduit.

CONCLUSION

Together, MND and microlite orientations indicate that effusive rhyolitic eruptions ascend the conduit slowly and the melt accumulates strain by pure shear. Textures in and across widely disparate volumetric eruptions are indistinguishable, suggesting similar conduit dynamics operate during effusive eruptions. Those textures vary dramatically between samples. Such variability suggests conduit conditions can be pulsatory and likely fluctuated with depth and lateral position in the conduit.

Table 2.1

Ages and physical parameters of target lavas.

		Age (ka)	Volume (km^3)	Max length (km)	Thickness (m)
Central Plateau Member lavas	Pitchstone Plateau (16)	79±11	70	16.5	200
	Grants Pass (2)	72±3	0.5	2.4	37
	Solfatara Plateau (15)	103±8	7	15.30	57
	West Yellowstone (20)	114±1	41	21.70	105
	Trischmann Knob (2)	~115	0.014	0.25	17
	Douglas Knob (11)	~115	0.011	0.13	70
	Bechler River (2)	116±2	8	13.70	35
	Summit Lake (11)	124±10	37	17.70	92
	Buffalo Lake (1)	160±3	54	16	97
	Dry Creek (1)	166±9	9	10	53
Mono Craters lavas	South Dome (6)	0.66±0.02	0.001	0.08	30
	Northwest Coulee (10)	1.5±0.3	0.3	1	150

Data is compiled from Sieh and Bursik (1986), Wood (1983), Christiansen (2001), Christiansen et al. (2007) and Befus et al. (2014). Number of samples are shown in after flow name.

Table 2.2

Microlite number density and microlite orientations

	Sample	UTM Coordinates	Total (log # cm^{-3})	Oxide (log # cm^{-3})	Pyroxene (log # cm^{-3})	Feldspar (log # cm^{-3})	Aspect ratio^{b}	σ_{ϕ°	σ_{θ°
Pitchstone Plateau	Average		9.01±0.39	8.84±0.31	8.25±0.85	1.08±2.86	-	-	-
n=5420 (MND)	Yell 15	527747/4899455	9.26-9.45	8.89-9.02	9.02-9.25	0	-	-	-
n=1320 (Orient)	Yell 20	51/029/4902499	8.90-8.99	8.86-8.89	7.91-8.25	0	-	-	-
	Yell 21	518540/4902023	8.50-8.87	8.40-8.80	6.75-8.02	0	-	-	-
	Yell 22	519894/4900303	9.08-9.14	9.01-9.11	7.94-8.25	0	-	-	-
	Yell 23	521796/4899169	8.30-8.50	7.93-8.48	0-7.30	0-8.05	-	-	-
	Yell 25	514414/4889716	9.37-9.54	9.17-9.34	8.93-9.10	0	-	-	-
	Y112	515961/4904434	-		-	-	8.9 (1.5)	16	31
	Y113	516140/4903494	-	-	-	-	8.6 (1.8)	26	18
	Y114	515999/4904434	-	-	-	-	10.6 (2.9)	52	37
	Y149	528043/4899265	9.21-9.27	8.82-8.97	8.97-8.98	0	9.2 (1.4)	51	19
	Y150	525977/4895300	-	-	-	-	9.6 (1.9)	56	18
	Y185	517178/4897717	-	-	-	-	9.5 (1.7)	45	29
	Y186	515902/4895582	-	-	-	-	8.8 (1.6)	22	33
	Y187	515071/4891401	-	-	-	-	10.7 (3.8)	16	21
	Y188	514413/4889707	-	-	-	-	10.0 (2.0)	40	21
	Y193	523241/4901708	-	-	-	-	12.0 (3.5)	39	41
Solfatara Plateau	Average		8.94±0.40	8.82±0.45	6.25±3.62	0.99±2.43			
n=6009 (MND)	Y46	533836/4950365	9.28-9.33	9.22-9.23	8.29-8.61	0			
n=264 (Orient)	Y50	533139/4949057	8.26-8.68	8.24-8.66	0-6.99	0			
	Y60	536520/4953333	8.66-8.69	8.56-8.59	9.98	0			
	Y76	531805/4941733	9.20	9.13	8.37	0			
	Y77	531604/4945591	9.38	9.38	0.00	0			
	Y81	530296/4944052	9.19	9.06	8.60	0			
	Y84	529639/4942656	8.52	8.41	7.86	0			
	Y87	529880/4942010	9.26	9.26	7.30	0			
	Y129	533967/4942410	8.10-8.22	8.09-8.21	0.00	0			
	Y134	536407/4955119	8.47-8.64	7.94-8.21	8.32-8.44	0			
	Y138	536150/4953789	8.93-9.00	8.36-8.55	8.77-8.83	0-6.99			
	Y143	535794/4951685	9.16	9.15-9.16	0.00	0			
	Y144	531944/4950111	9.21-9.51	8.93-8.59	8.84-8.95	0-6.94			
	Y223	533447/4947138	-	-	-	-	9.5 (1.3)	27	27
	Y241	529759/4943340	-	-	-	-	9.8 (1.5)	59	29

Table 2.2 (cont.)

Summit Lake	Average		8.98±0.31	8.71±0.39	8.00±0.74	4.08±4.48	-	-	-
n=4992 (MND)	Yell 54	507391/4921840	8.59-9.47	8.29-9.21	8.27-9.11	0.00	-	-	-
n=660 (Orient)	Yell 56	508053/4923253	8.61-9.15	8.50-8.59	7.14-7.95	6.96-9.03	-	-	-
	Yell 57	509321/4924062	7.85-8.59	7.78-8.23	0-7.66	0-8.91	-	-	-
	Yell 58	509553/4924796	9.20	9.17-9.18	7.11-7.30	7.51-7.74	-	-	-
	Y71	506033/4918669	9.13-9.43	8.56-8.91	8.99-9.28	0.00	-	-	-
	Y72	505270/4917940	8.93-9.44	8.87-9.20	8.03-8.12	0.00	-	-	-
	Y195	492222/4915841	-	-	-	-	9.5 (2.0)	36	28
	Y198	501561/4917443	-	-	-	-	10.1 (2.3)	38	22
	Y199	505988/4918910	-	-	-	-	9.4 (1.6)	22	19
	Y201	507420/4921681	-	-	-	-	9.3 (1.6)	36	28
	Y202	508436/4923560	-	-	-	-	10.1 (1.9)	20	24
West Yellowstone	Average		9.45±0.15	9.37±0.13	8.68±0.24	4.70±4.08	-	-	-
n=3491 (MND)	Yell 6	510511/4925929	9.38-9.70	9.31-9.59	7.82-8.48	0-7.60	-	-	-
n=2244 (Orient)	Yell 16	510154/4925898	9.05-9.56	8.99-9.49	7.07-8.17	0-6.89	-	-	-
	Yell 17	508615/4926453	9.38-9.59	9.28-9.51	8.27-8.70	0	-	-	-
	Y161	492121/4935069	-	-	-	-	10.4 (2.3)	37	32
	Y162	496300/4933345	-	-	-	-	10.6 (3.0)	33	14
	Y165	490411/4934556	-	-	-	-	8.7 (1.2)	13	16
	Y166	489201/4935453	-	-	-	-	9.6 (1.5)	33	15
	Y167	488443/4935747	-	-	-	-	9.4 (1.8)	21	27
	Y169	488961/4936836	-	-	-	-	9.6 (1.7)	37	23
	Y171	494070/4933833	-	-	-	-	12.1 (3.4)	25	32
	Y172	493717/4934611	-	-	-	-	10.2 (2.7)	38	32
	Y175	491159/4937315	-	-	-	-	8.8 (1.1)	16	12
	Y176	490650/4935523	-	-	-	-	9.7 (2.3)	40	23
	Y183	491762/4940196	-	-	-	-	8.6 (1.4)	36	9
	Y184	491768/4940838	-	-	-	-	9.8 (1.4)	32	23
	Y190	487705/4938221	-	-	-	-	9.2 (1.4)	23	13
	Y191	488516/4938568	-	-	-	-	12.2 (6.9)	27	30
	Y205	492517/4937176	-	-	-	-	10.1 (2.3)	41	17
	Y207	492881/4938379	-	-	-	-	11.0 (3.0)	47	16
	Y209	492874/4934227	-	-	-	-	10.8 (2.4)	25	19

Table 2.2 (cont.)

Grants Pass	Average		8.79±0.72	8.71±0.39	8.02±0.69	0	-	-	-
n=784 (MND)	Y101	512762/4909368	9.00-9.43	8.85-9.39	8.39-8.62	0	-	-	-
	Y102	513081/4910457	8.21-8.39	8.14-8.29	7.39-7.72	0	-	-	-
Trischmann Knob	Average		8.11±0.03	8.00±0.17	7.01±0.93	0	-	-	-
n=864 (MND)	Y96	509861/4909406	7.61-8.36	7.45-8.13	7.12-7.96	0	-	-	-
	Y97	510036/4909483	7.95-8.21	7.91-8.21	0-6.84	0	-	-	-
Bechler River	Average		8.63±0.49	8.30±0.54	8.35±0.45	3.01±4.26	-	-	-
n=1079 (MND)	Y98	511802/4909501	8.26-8.32	7.87-7.94	7.96-8.13	5.97-6.27	-	-	-
	Y99	512034/4907275	8.94-9.01	8.64-8.77	8.63-8.71	0	-	-	-
Buffalo Lake									
n=1191 (MND)	Yell 65	487232/4905800	9.04	9.04	0	0	-	-	-
Dry Creek									
n=451 (MND)	Yell 40	534704/4922057	8.58	8.52	7.73	0	-	-	-
Douglas Knob*	Average		8.40±0.43	8.28±0.48	7.20±0.49	3.09±3.89	-	-	-
n=9564 (MND)	Y88	512231/4906940	7.59-8.21	7.53-8.18	0-7.35	0-7.13	9 (2.0)	38	9
n=1682 (Orient)	Y89	512265/4906785	8.70-9.60	8.70-9.58	0-8.29	0	-	-	-
	Y90	512265/4906688	7.57-8.39	7.57-8.34	0-7.73	0	12 (1.9)	14	24
	Y92	512078/4906606	8.27-8.72	7.70-8.52	0-8.11	7.97-8.52	10 (2.1)	17	20
	Y116	512648/4906531	8.29-8.91	8.29-8.86	0-7.90	0	12 (1.5)	36	17
	Y117	512170/4906575	7.57-8.83	7.52-8.83	0-6.89	0	10 (2.1)	30	31
	Y118	512004/4906729	7.37-8.63	7.25-8.41	0-8.14	0-7.77	11 (1.6)	32	23
	Y119	512038/4906903	7.60-8.79	8.55-8.79	0-7.36	0	11 (2.0)	17	16
	Y120	412268/4906783	8.00-9.08	7.98-9.08	0-7.74	0	10 (1.4)	46	36
	Y121	512344/4906703	8.04-8.71	8.00-8.71	0-7.34	0-7.88	10 (1.9)	30	29
	Y122	512222/4906940	8.09-9.17	8.08-8.98	0-8.71	0	10 (2.9)	26	18

Northwest Coulee	Average		9.26±0.38	8.34±0.50	9.19±0.37	5.07±3.16	-	-	-
n=9128 (MND)	NWC-2	321241/4197301	8.92-9.37	7.65-8.19	8.90-9.35	0	10.8 (2.0)	58	25
n=2178 (Orient)	NWC-3a	321360/4197315	9.42-9.50	8.17-8.77	9.36-9.45	0	10.5 (1.9)	48	15
	NWC-3b	321360/4197316	-	-	-	-	9.9 (1.5)	36	28
	NWC-4	322570/4198386	9.01-9.66	7.22-8.85	8.92-9.59	0-7.41	10.7 (1.6)	27	27
	NWC-5	322437/4198490	8.36-9.47	7.57-8.54	8.25-9.42	0-7.76	10.4 (1.6)	18	24
	NWC-6	322417/4198540	9.94-10.20	9.22-9.63	9.85-10.07	0-7.41	9.6 (1.7)	27	19
	NWC-7	321445/4198672	8.74-9.52	7.57-8.74	8.70-9.44	0-7.25	10.0 (1.2)	55	40
	NWC-8	322013/4199084	7.56-10.10	7.02-9.25	7.37-10.03	0-7.33	9.8 (1.2)	23	17
	NWC-9a	321777/4198896	7.69-10.11	6.37-9.47	7.67-9.99	0-6.97	10.0 (1.3)	52	20
	NWC-21	320868/4197489	-	-	-	-	9.5 (1.2)	30	21
South Dome	Average		8.46±0.75	7.92±0.56	7.95±0.63	2.35±4.05	-	-	-
n=2428 (MND)	PCD-3	320230/4199804	7.11-8.97	6.86-8.26	6.39-8.87	0-6.69	12.4 (2.0)	59	25
n=792 (Orient)	PCD-6	320242/4199697	9.66-9.11	8.70-8.97	8.58-9.07	9.53-9.83	9.3 (1.5)	36	27
	PCD-7	320102/4199682	7.03-9.24	6.93-9.14	6.33-9.23	0	8.5 (1.4)	22	23
	PCD-8	320134/4199673	7.43-9.10	6.98-8.56	7.24-8.95	0	10.6 (1.8)	30	28
	PCD-10	320164/4199664	7.32-9.86	7.14-9.23	6.43-8.34	0-9.73	9.4 (2.4)	44	30
	PCD-12	320137/4199741	7.28-7.80	6.92-7.57	6.70-7.67	0	9.1 (1.1)	48	16

Dashed fields (-) microlite texture was not quantified.

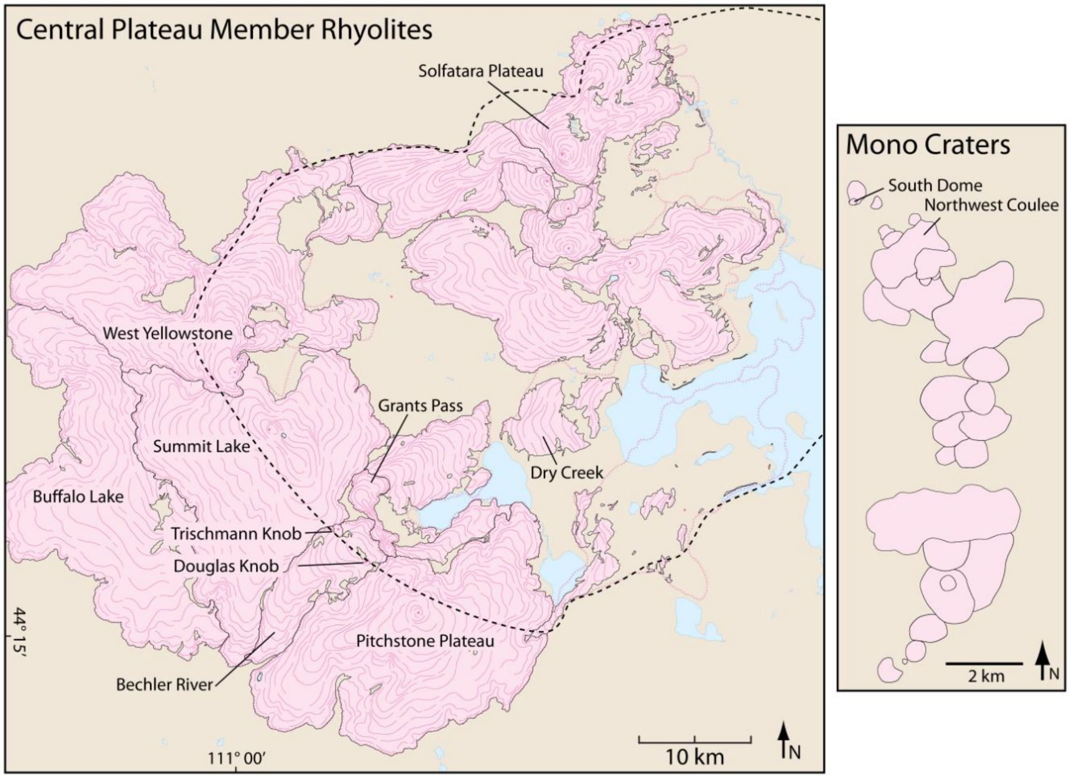

Fig. 2.1

Simplified geologic maps of Central Plateau Member rhyolites in the Yellowstone volcanic field and Mono Craters, CA modified after Christiansen (2001) and Sieh and Bursik (1986). Lava flows are shown in pink, with sampled lavas labeled an in a darker shade. Dark pink lines on Central Plateau Member lavas represent pressure ridges. Small pink stars show approximate vent locations. The extent of Yellowstone Caldera is shown by the dashed black line.

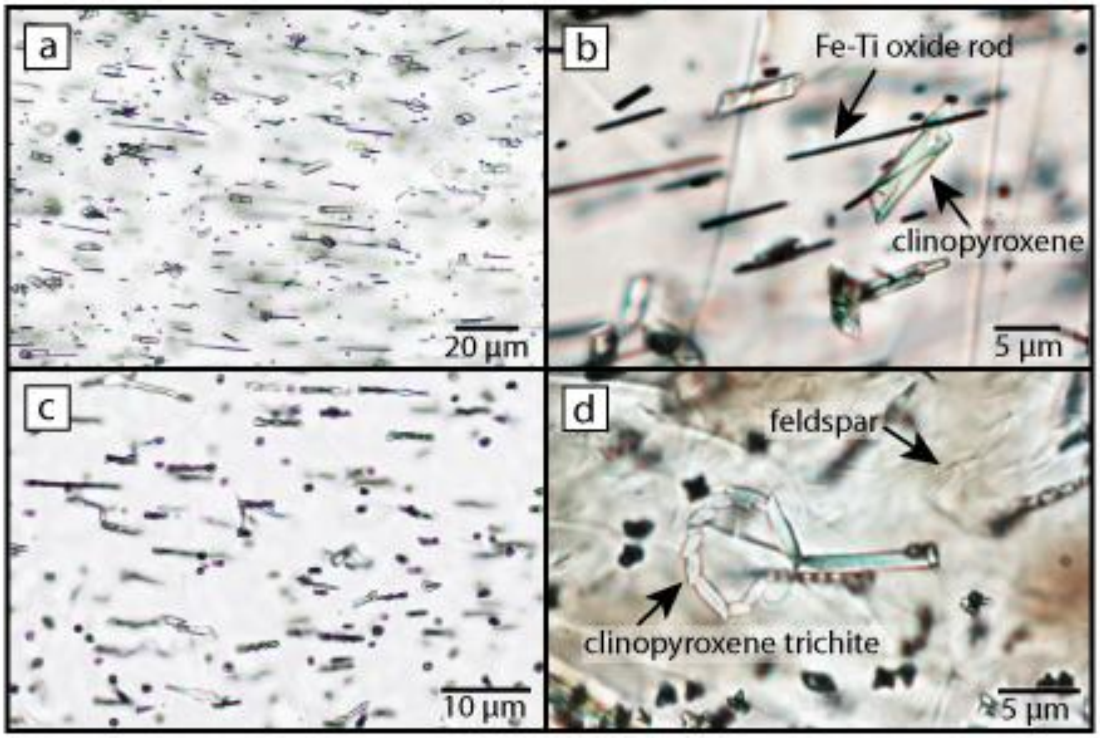

Fig. 2.2

Photomicrographs of microlite textures and phases. **a** Example of moderate MND groundmass with preferentially aligned Fe-Ti oxides (black acicular), some with clinopyroxene overgrowths (clear prisms). **b** Representative photo of Fe-Ti oxides and clinopyroxene crystals. **c** Preferentially aligned Fe-Ti oxide microlites encrusted with clinopyroxene overgrowths. **d** Example of a clinopyroxene trichite that cuts across primary fabric containing Fe-Ti oxides with clinopyroxene overgrowths and feldspar laths (similar index of refraction to glass makes them difficult to see).

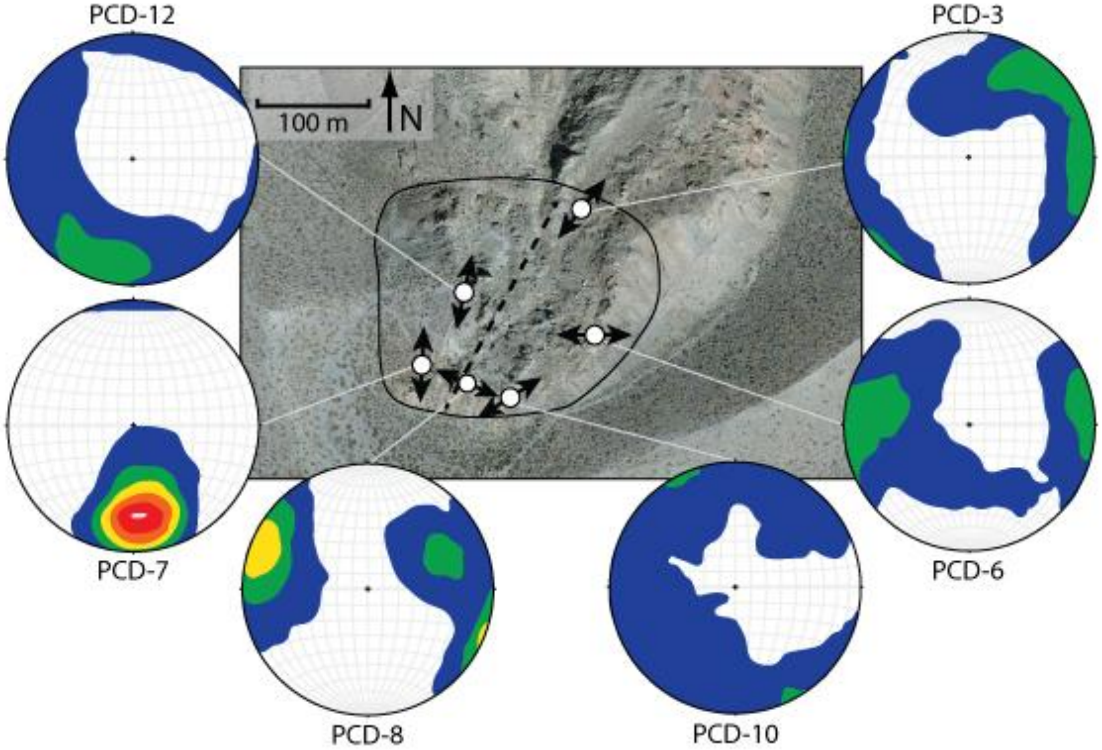

Fig. 2.3a – Panum Crater

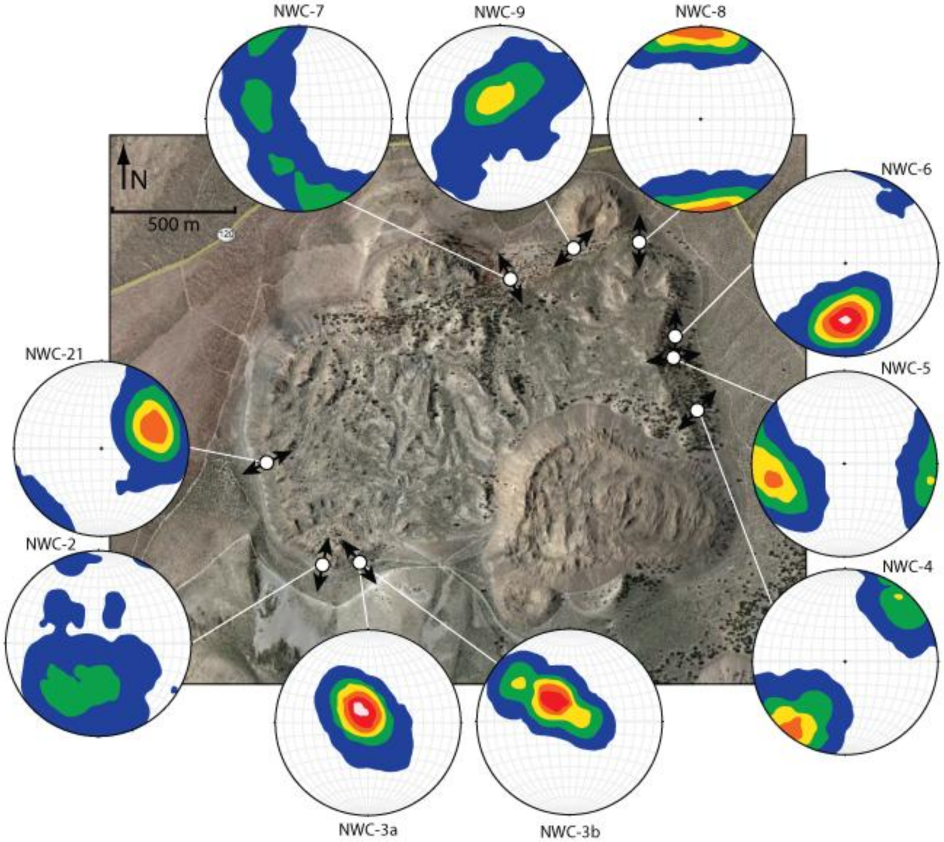

Fig. 2.3b Northwest Coulee

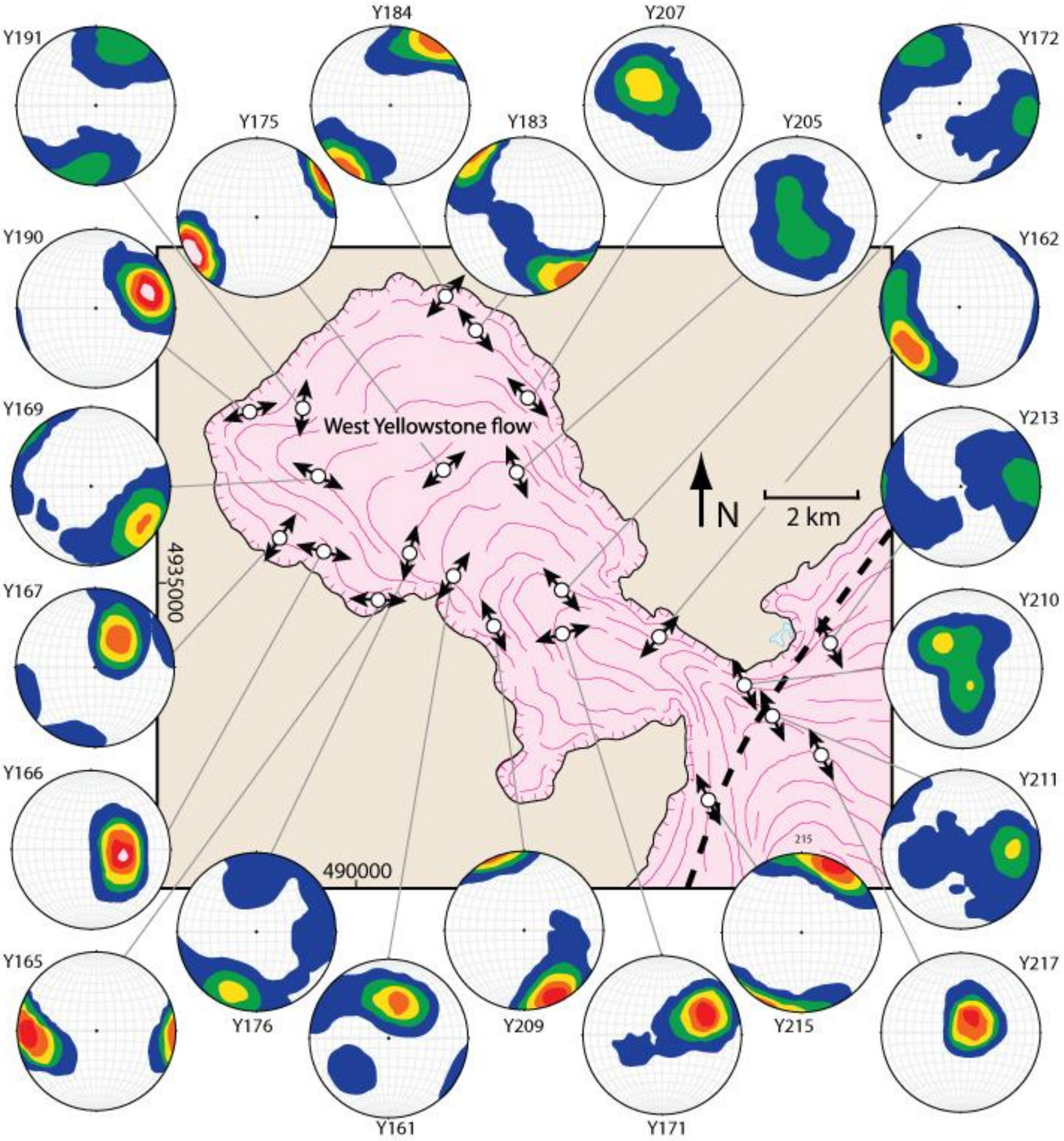

Fig. 2.3c Lobe of West Yellowstone

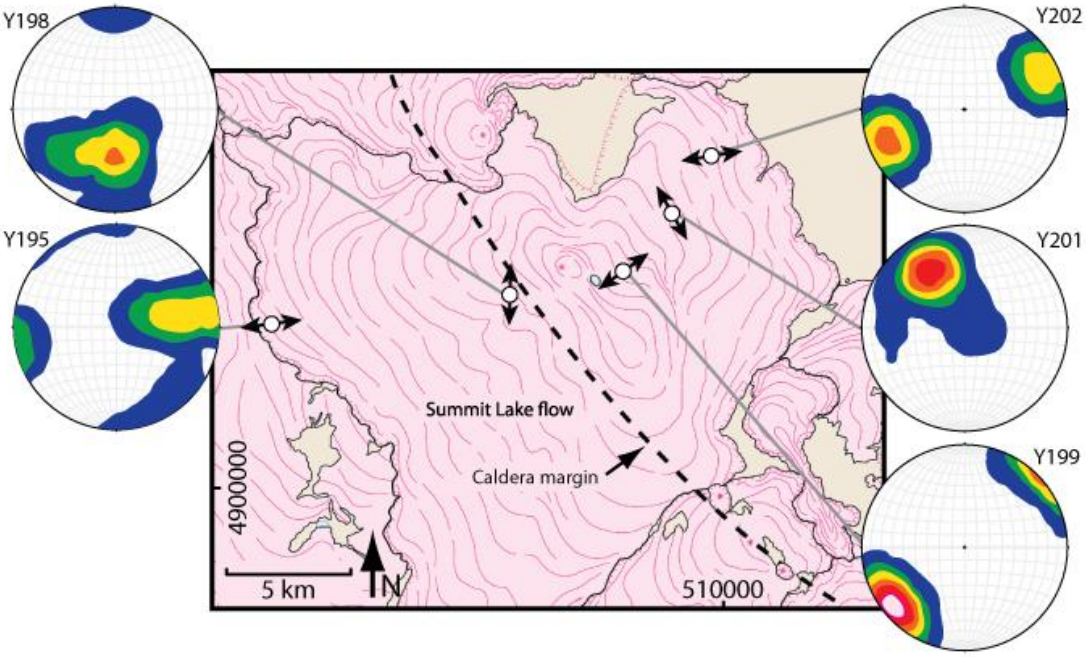

Fig. 2.3d Summit Lake

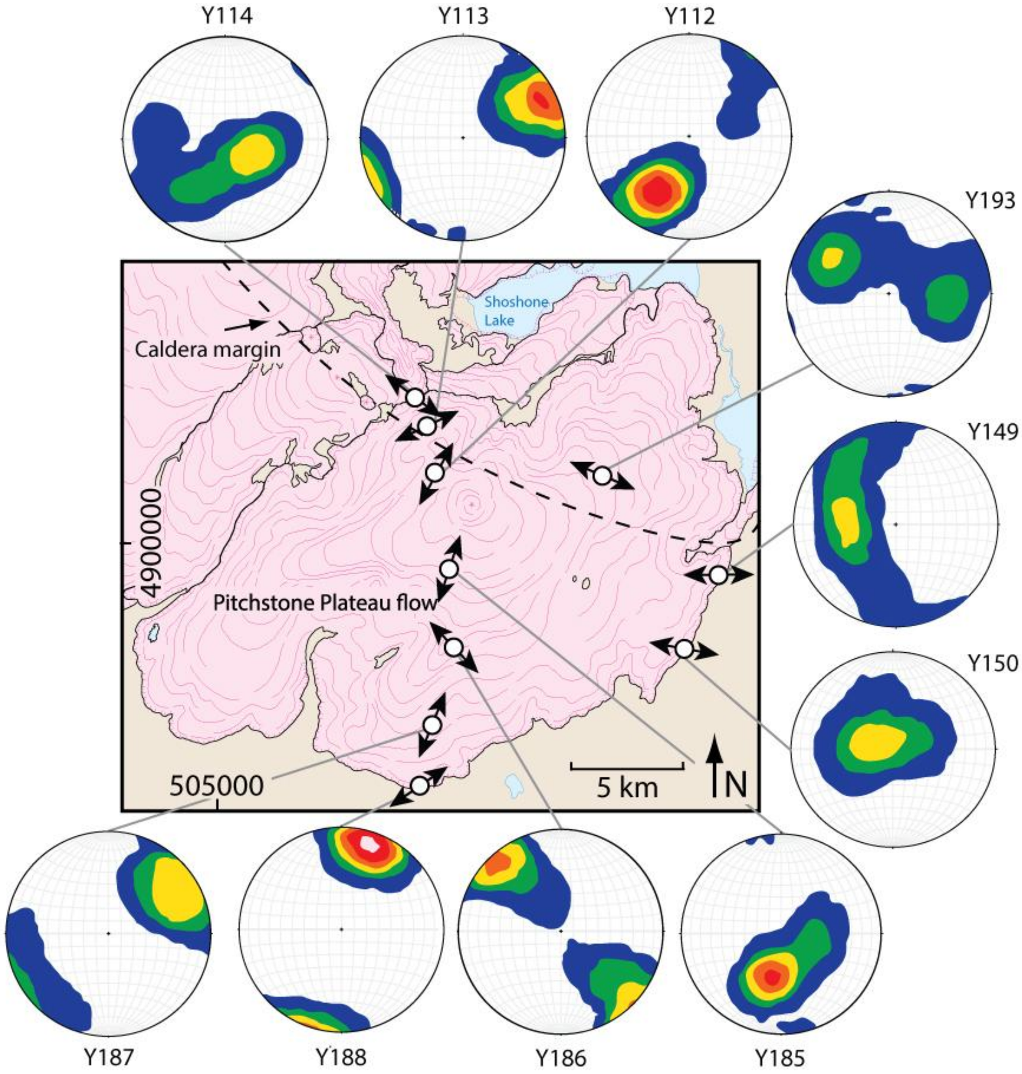

Fig. 2.3e Pitchstone Plateau

Fig. 2.3

Stereograms display the orientation distributions of acicular microlites samples (white circles) collected across the targeted lava flows and domes. The black arrows show the dominant microlite trend. The degree of microlite alignment is represented by stereograms with Kamb contours, with colors representing orientation frequency per unit area (where blue is 2%, green is 8%, yellow is 14%, orange is 20%, red is 26%, and pink is 32%). **a** Southwest dome at Panum Crater. The extent of the dome is marked by the black line. Trend of central fissure vent is marked by the dashed line. **b** Northwest Coulee **c** the western lobe of West Yellowstone **d** Summit Lake **e** Pitchstone Plateau. Air photos of Mono Craters are from Google Maps. Geologic maps of Central Plateau Member rhyolites (pink) are modified after Christiansen (2001). Dark pink lines on those flows represent pressure ridges.

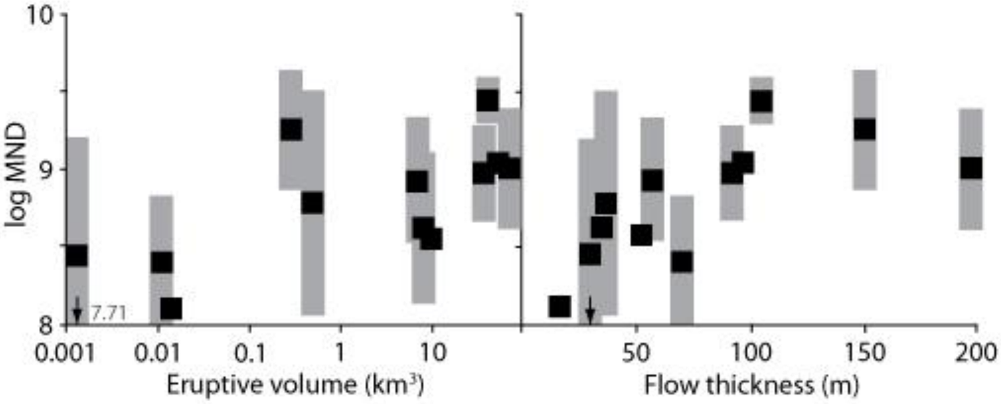

Fig. 2.4

Total MND as a function of eruptive volume and flow thickness. Black dots represent average MND. Gray bars encompass maximum and minimum values. The samples with downward pointing arrows indicate log MND in that sample extends to values as low as 7.71.

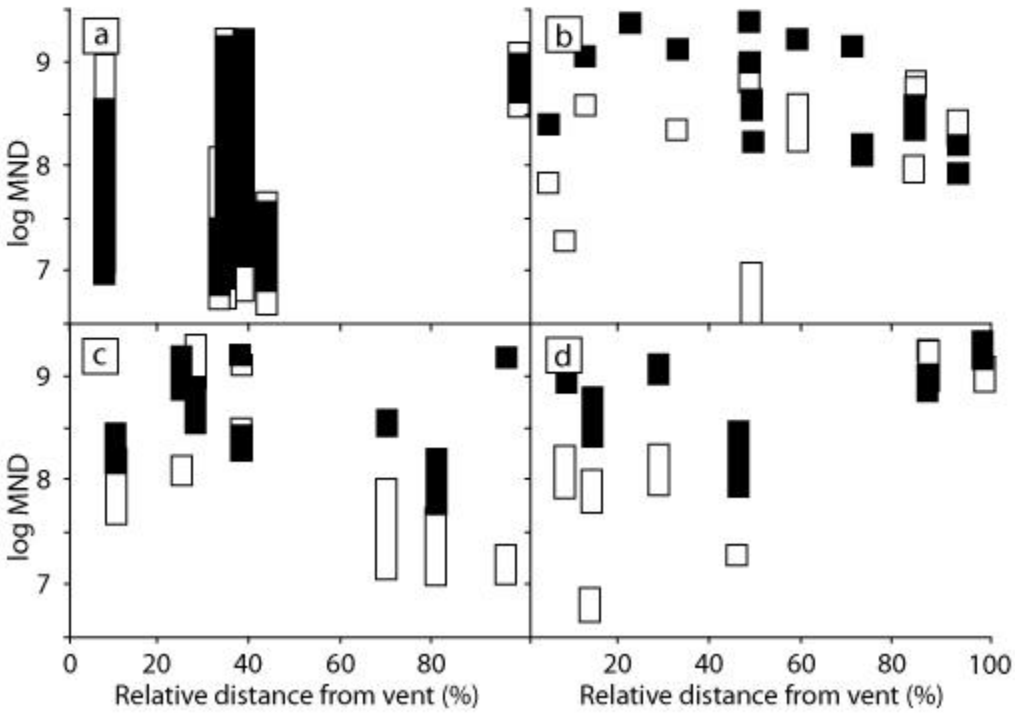

Fig. 2.5

MND as a function of position in **a** South Dome **b** Solfatara Plateau **c** Summit Lake and **d** Pitchstone Plateau lavas. Black and white symbols are for Fe-Ti oxides and clinopyroxene, respectively. The length of the symbol represents the range of values in a single sample.

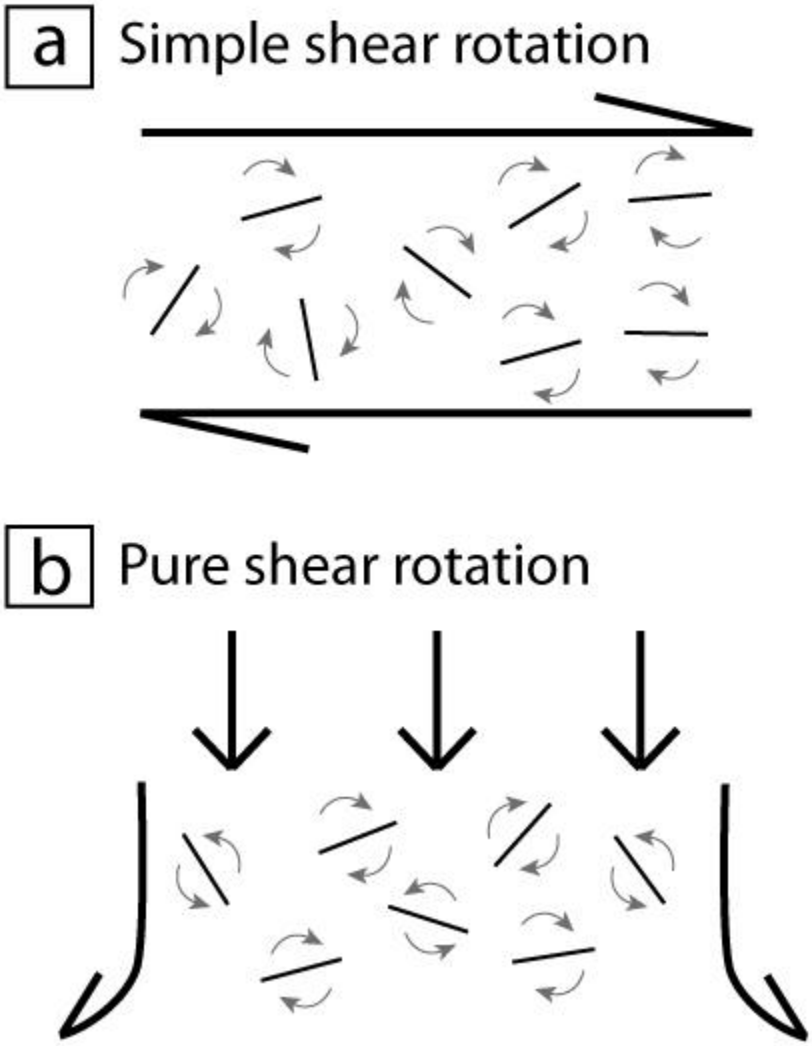

Fig. 2.6

Simplified schematic depicting the response of acicular microlites to simple and pure shear.

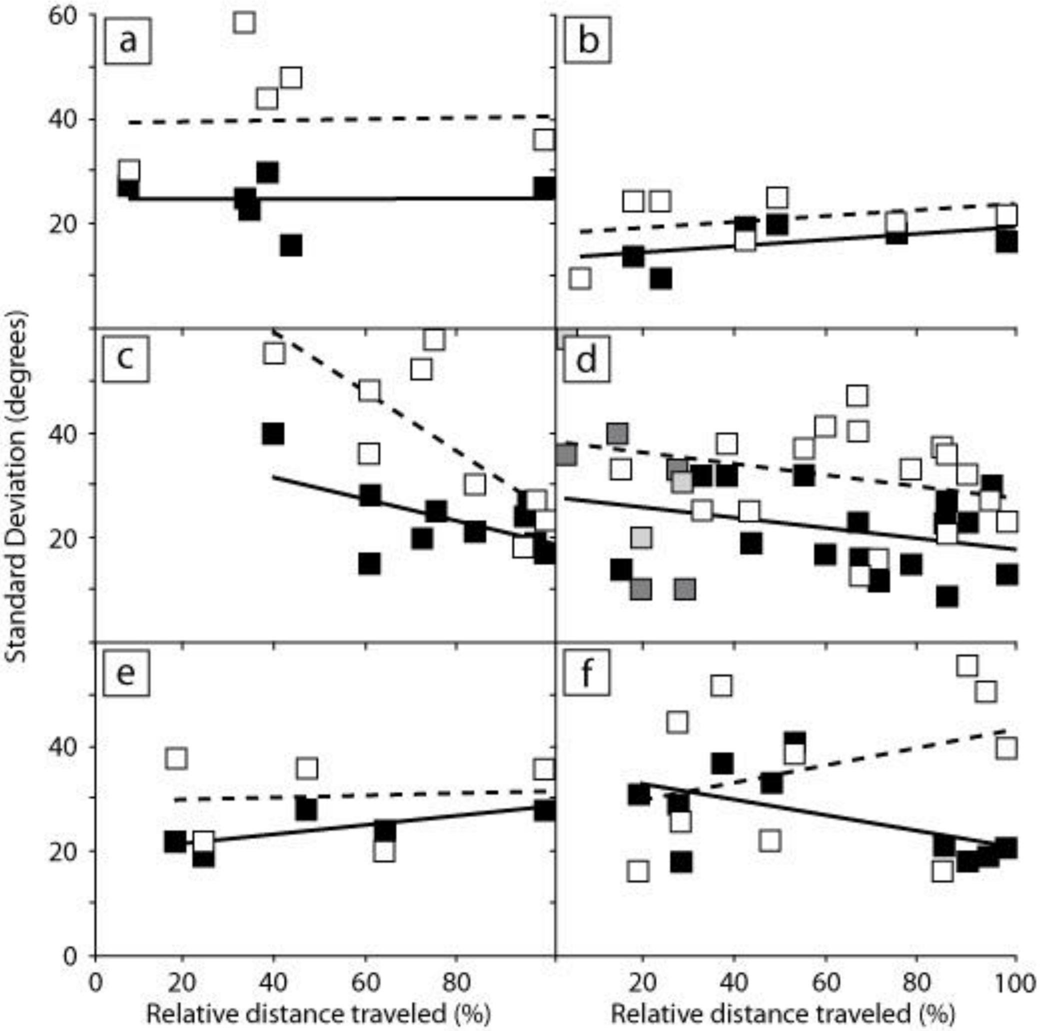

Fig. 2.7

Microlite orientation as a function of position in **a** Southwest dome at Panum Crater **b** Douglas Knob, reproduced from Befus et al (2014). **c** Northwest Coulee **d** the western lobe of West Yellowstone **e** Summit Lake **f** Pitchstone Plateau. White squares show standard deviation of trend, and black squares show standard deviation of plunge. Light and dark gray squares in **d** are standard deviation of trend and plunge, respectively, for samples collected upstream of the "chute." The dashed and solid black lines are linear regressions through the trend and plunge data, respectively. Relative distance travelled measurements are percentages of flow distance relative to total flow distance.

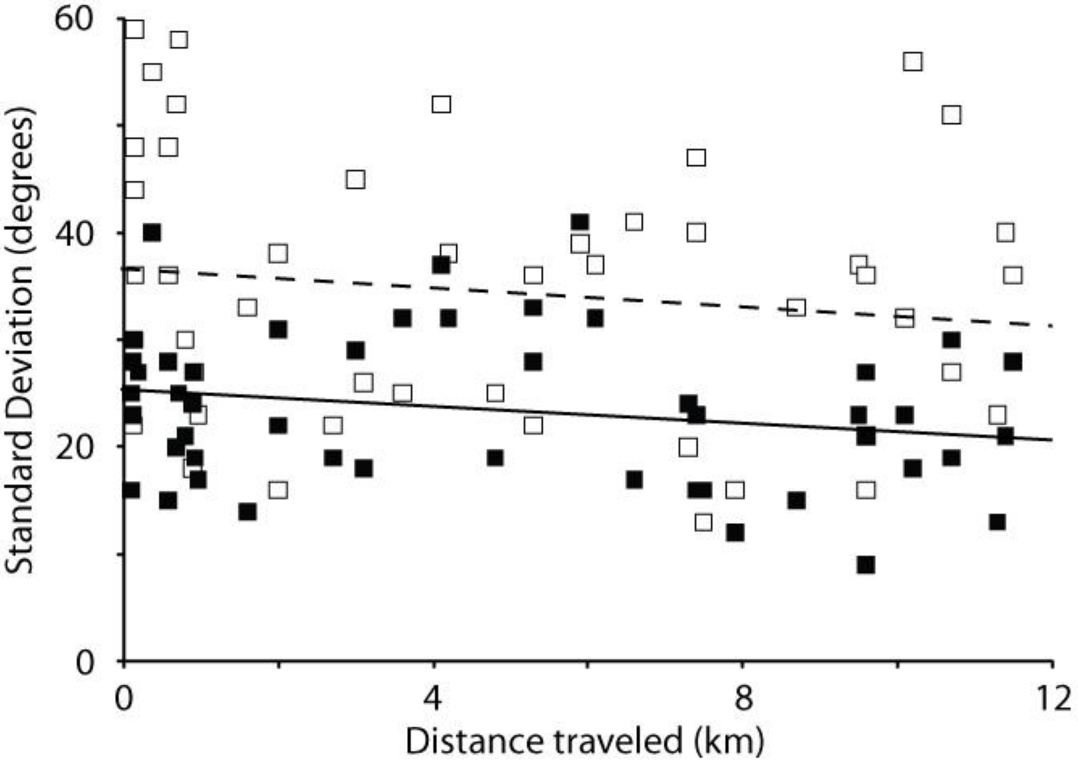

Fig. 2.8

Compilation for all of the flows of microlite orientations as a function distance travelled. White squares show standard deviation of trend, and black squares show standard deviation of plunge. The dashed and solid black lines are linear regressions through the trend and plunge data, respectively.

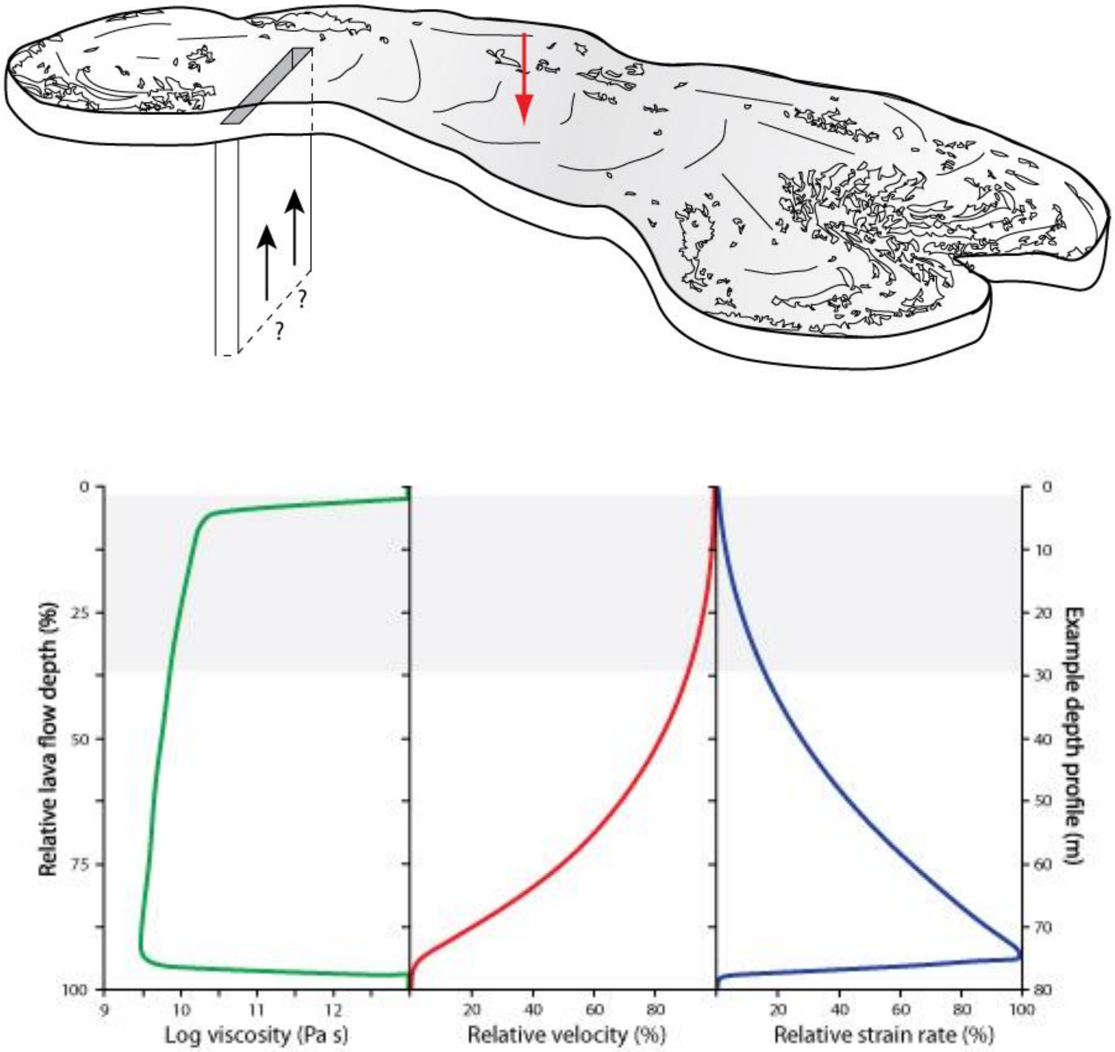

Fig. 2.9

Rheological estimates for a 1D slice through a lava. Red arrow on sketch of lava flow indicates possible position for model depth profiles and associated fluid dynamic properties shown below. This example represents a mature lava flow that has been allowed to conductively cool for 30 days from an eruptive temperature of 750 °C. The gray domain displays the estimated depth of samples from Yellowstone and Mono Craters that were used in this study.

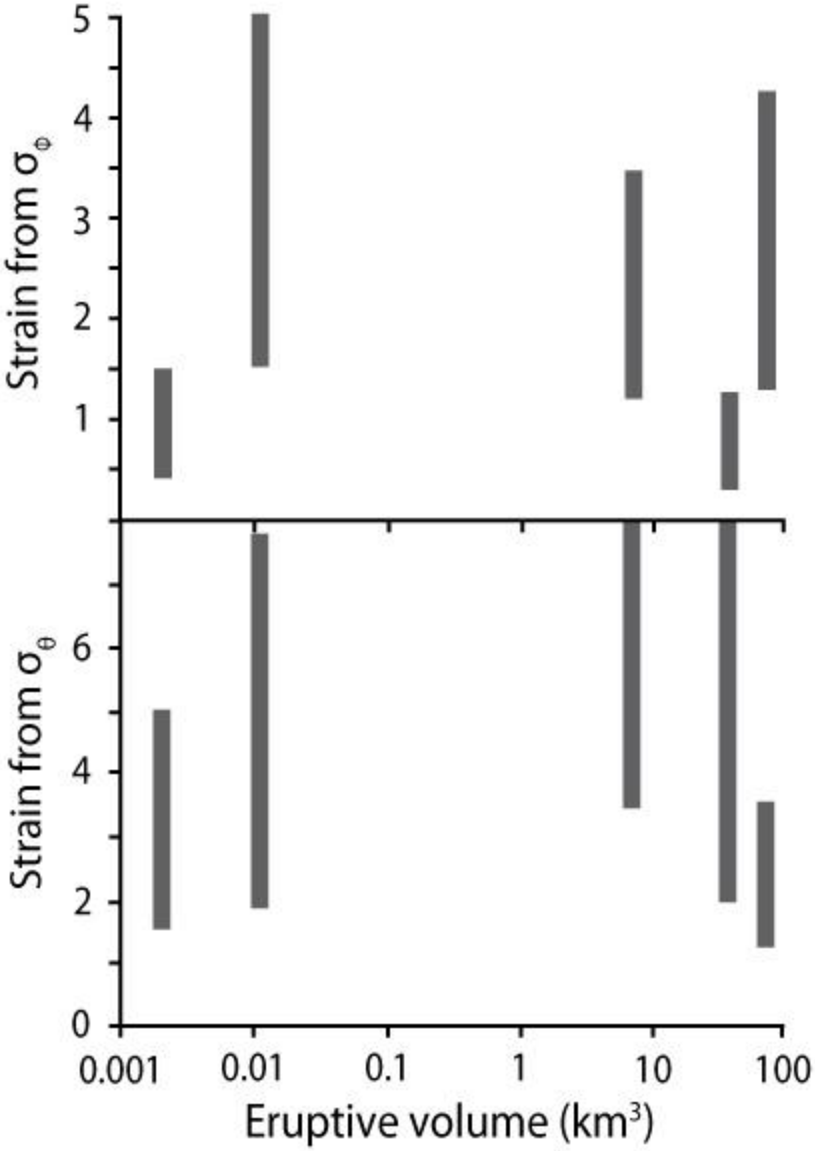

Fig. 2.10

Strain estimates based on microlite orientation distributions as a function of eruptive volume. Lower bound estimates represent strain induced solely by pure shear, and upper estimates assume strain induced only by simple shear. The range between those end members displays strain accumulated by combinations of simple and pure shear.

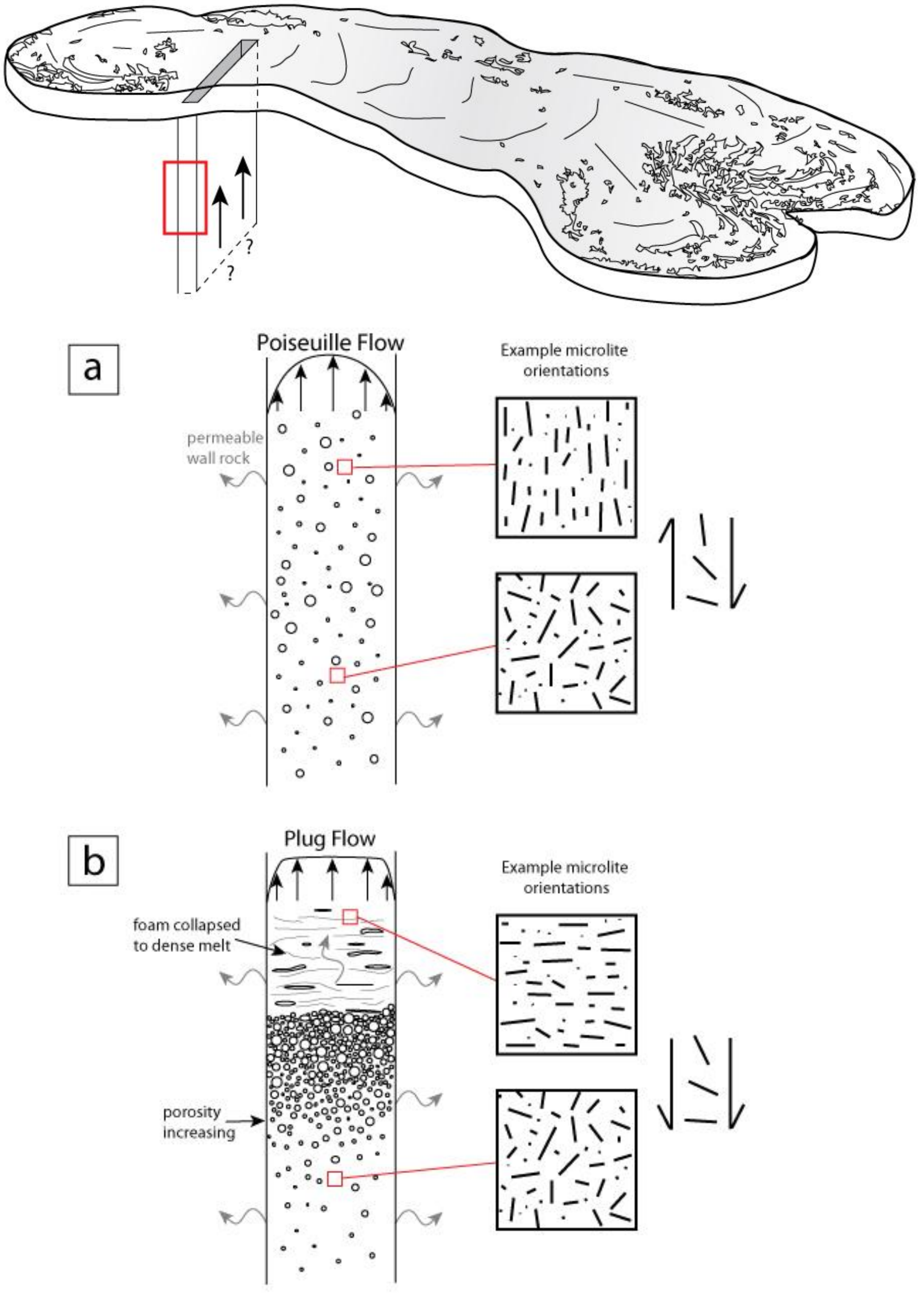

Fig. 2.11

Schematic illustration of fluid flow in conduit feeding an effusive rhyolite lava flow. Red box on sketch of lava flow conduit represents position of **a** and **b**. During **a** Poiseuille flow microlites progressively align in response to shear from conduit walls. Microlite alignment is envisioned as being caused by foam collapse during **b** Plug flow.

CHAPTER 3:

PRE-ERUPTIVE STORAGE CONDITIONS AND ERUPTION DYNAMICS OF A SMALL RHYOLITE DOME: DOUGLAS KNOB, YELLOWSTONE VOLCANIC FIELD, USA

ABSTRACT

The properties and processes that control the size, duration, and style of eruption of rhyolite magma are poorly constrained because of a paucity of direct observations. Here we investigate the small-volume, non-explosive end-member. In particular, we determine the pre-eruptive storage conditions and eruption dynamics of Douglas Knob, a 0.011 km^3, obsidian dome that erupted from a 500-meter-long fissure in the Yellowstone volcanic system. To determine pre-eruptive storage conditions, we analyzed compositions of phenocrysts, matrix glass, and quartz-hosted glass inclusions by electron microprobe and FTIR analyses. The pre-eruptive melt is high-silica rhyolite (~75 wt.% SiO_2), and was stored at 760±30 °C and 50±25 MPa prior to eruption, assuming vapor saturation at depth. To investigate emplacement dynamics and kinematics, we measured number densities and orientations of microlites at various locations across the lava dome. Microlites in samples closest to the inferred fissure vent are the most aligned. Alignment does not increase with distance travelled away from the vent, suggesting microlites record conduit processes. Strains of <5 accumulated in the conduit during ascent after microlite formation, imparted by a combination of pure and simple shear. Average microlite number density in samples vary from $10^{4.9}$ mm^{-3} to $10^{5.7}$ mm^{-3}. Using the magma ascent model of Toramaru et al (2008), microlite number densities imply decompression rates ranging from 0.03 to 0.11 MPa hr^{-1} (~0.4-1.3 mm s^{-1} ascent rates). Such slow ascent would allow time for passive degassing at depth in the conduit, thus resulting in an effusive eruption. Using calculated melt viscosity, we infer that the dike that fed the eruption was 4-8 m in width. Magma flux through this dike, assuming fissure dimensions at the surface represent its geometry at depth, implies an eruption duration of 17-210 days. That duration is also consistent with the shape of the dome if produced by gravitational spreading, as well as the ascent time of magma from its storage depth.

Keywords: lava dome, microlite, obsidian, rhyolite, ascent rate, strain

INTRODUCTION

Rhyolite domes and lavas have a wide range of sizes, from ≤0.01 km^3 to ≥70 km^3 (Walker et al. 1973; Christiansen et al. 2007). The effusion of rhyolite lava remained scientifically unmonitored until the eruptions of Chaitén and Cordón Caulle volcanoes in Chile during 2008-2009 and 2011-2012, respectively (Castro and Dingwell 2009; Alfano et al. 2011; Bernstein et al. 2013; Castro et al. 2013; Pallister et al. 2013; Tuffen et al. 2013). The rarity of such eruptions means that there is little quantitative data on the ascent dynamics and formation of rhyolite lavas, despite their prevalence in major silicic volcanic systems and in the Holocene volcanic eruption history of the western United States. There is an opportunity to assess the controls on eruption size and duration, and better constrain the hazards associated with the effusion of high silica lavas, by studying the hundreds of well-exposed, but still unstudied, rhyolitic lava domes and flows around the world. Although direct monitoring of those prehistoric eruptions is obviously not possible, petrologic and textural studies can provide quantitative constraints on the pre-eruptive magmatic storage conditions, the magma ascent rate, and eruption duration.

Much has been learned from the eruptions of Chaitén and Cordón Caulle volcanoes. Each eruption was preceded by relatively brief, small volume, sub-Plinian to Plinian eruption (Castro and Dingwell 2009; Alfano et al. 2011; Castro et al. 2013; Schipper et al. 2013; Tuffen et al. 2013). They were sourced from magmas stored at 50-200 MPa and 800±100 °C (Vogel et al. 1989; Gibson and Naney 1992; Castro and Gardner 2008; Castro and Dingwell 2009; Alfano et al. 2011; Castro et al. 2013). In addition, photogrammetry and LIDAR datasets have shown that the effusive eruption of Chaitén constructed a 0.8 km^3 dome over 2 years by exogenous and endogenous growth. The average effusion rate feeding the eruption during the first four months was ~45 $m^3 s^{-1}$, and gradually waned until the eruption ceased (Pallister et al. 2013). A similar sequence of eruptive activity was observed at Cordón Caulle. Initially the effusive eruptive flux was estimated to be 20-60 $m^3 s^{-1}$, which decreased to 1-10 $m^3 s^{-1}$ as the eruption progressed (Schipper et al. 2013; Tuffen et al. 2013) The magmatic ascent rate was estimated to have been <10 mm s^{-1} (Castro et al. 2013).

Much has also been learned from drilling Obsidian Dome in eastern California. The prehistoric eruption of the 0.17 km^3 Obsidian Dome lava dome is inferred to have been fed by pulsatory ascent through a conduit ~7 m in diameter over ~250 days. Emplacement took place by radial spreading away from an elliptical vent with near-vent and distal portions of the flow flattening via pure shear, and the base of the flow deforming by simple shear (Miller 1985; Swanson et al. 1989; Fink and Griffiths 1998; Castro et al. 2002; Castro and Mercer 2004).

Here, we investigate the textural and petrographic features of Douglas Knob, a small-volume, high-silica rhyolite dome erupted at ~120 ka from the western portion of Yellowstone Caldera (Fig. 1) (Christiansen et al. 2007). Douglas Knob forms an ellipsoidal lava dome approximately 700 m long and 500 m wide, which rises ~70 m above the surrounding terrain. Exposure is poor (~5%), with much of the dome covered by vegetation and thin soil. Outcrops up to 20 m^2 are composed of dense obsidian glass with rare small zones of vesicular obsidian. Devitrified rhyolite occurs rarely. Surface features common to well-exposed silicic domes such as crease structures and pressure ridges are not observed. The dome experienced little erosion during Pinedale glaciations, as evidenced by sparse remaining veneers of flow breccia and pumiceous carapace. Assuming much of the original form of the dome remains preserved, the dimensions indicate a subaerial eruptive volume of 0.011 ± 0.002 km^3. Douglas Knob is the smallest documented Central Plateau Member obsidian lava from Yellowstone. We use phenocryst compositions and volatile contents in glass inclusions to constrain magma storage depth and temperature. We use microlite number densities to assess ascent rates, and microlite orientations to identify when and where strain accumulated in the erupted rhyolite. Those measurements, when combined, allow us to infer ascent rate, dimensions of the pathway through which the magma rose, and the duration of the eruption.

METHODS

Samples

Samples of obsidian were collected at 10 locations across the dome (Fig. 1a). Each was collected at approximately the same height on the edifice, 50±20 m above its base. Six of the samples were oriented prior to collecting by recording the up-direction and the strike and dip of a planar surface from an outcrop of lava thought to be in place (i.e., not rotated by autobrecciation or erosion). Polished thin sections were prepared from all samples, with special care taken to record the orientation of the thin section relative to the field-oriented sample. Mineral separates of quartz, sanidine, magnetite, fayalite, and clinopyroxene were hand-picked from 3 crushed obsidian samples.

Quartz crystals, 1-2 mm in size, were examined while submerged in mineral oil to identify glass inclusions that were isolated from the edge of the crystal and not intersected by cracks. All inclusions contain vapor bubbles and crystallites. A population of crystals that contained isolated polyhedral glass inclusions ≥40 μm in size were loaded into a $Ag_{80}Pd_{20}$ capsule and placed inside a TZM pressure vessel at 850 °C and 150 MPa for 24 hours in order to rehomogenize the inclusions to bubble- and crystallite-free glass (e.g., Skirius et al. 1990).

Geochemical analyses

Mineral and glass compositions were analyzed using the JEOL JXA-8200 electron microprobe at the University of Texas at Austin. Minerals were analyzed using a

10 nA beam current, 15 keV accelerating voltage, and a focused beam. Glasses were analyzed using a 10 nA beam current, 15 keV accelerating voltage, and a defocused beam (10 μm diameter) to minimize Na and volatile migration (Nielson and Sigurdsson 1981). During glass and feldspar analyses, Na migration was corrected using the Na-migration capability of *Probe for Windows*^{TM}. Working standards for each analyzed phase were analyzed repeatedly to monitor for analytical quality and instrument drift.

Dissolved water and carbon dioxide contents of 16 doubly exposed glass inclusions and matrix glass were determined by Fourier-Transform Infrared (FTIR) spectroscopy, using a ThermoElectron Nicolet 6700 spectrometer and Continuμm IR microscope. FTIR spectra consist of 60 scans at a resolution of 4 cm^{-1}. Spectra from all samples were collected using a 40x40 μm aperture in both the mid-IR range, using a KBr beamsplitter and globular IR source, and near-IR range, using a CaF_2 beamsplitter and white light. For glass inclusions, concentrations of dissolved molecular and hydroxyl water were determined from absorbances at ~5200 cm^{-1} and ~4500 cm^{-1}, respectively, using the model of Zhang et al (1997). Water contents (H_2O) are reported as the averaged sums of dissolved molecular water and hydroxyl contents. For matrix glasses water concentrations were estimated using the absorbance at ~3500 cm^{-1}, using the Beer-Lambert Law and an absorption coefficient of 71±2 (L cm^{-1} mol^{-1})(Befus et al. 2012). Dissolved molecular carbon dioxide (CO_2) contents were determined from absorbance at ~2350 cm^{-1}, using the Beer-Lambert Law and an absorption coefficient of 1214±16 (L cm^{-1} mol^{-1}) (Behrens et al. 2004). Linear backgrounds were assumed for absorbances at 2350, 3500, and 5200 cm^{-1}. Background for absorbances at the 4500 cm^{-1} peak was estimated using a flexicurve set tangential to the IR spectrum on either side of the peak. The thickness of each inclusion at the spot of the FTIR analysis was measured optically by focusing on the top and bottom of the sample using a petrographic microscope equipped with a Heidenhain focus drive linear encoder. The standard error on those measurements is ±0.6 μm, as determined by repeatedly focusing through a sample of known thickness.

Microlite measurements

The number density of microlite crystals (MND) was determined in each sample by counting the total number of microlites within set volumes of the thin section. Counts include Fe-Ti oxide, pyroxene, and rare feldspar microlites. Microlites were continuously counted at changing depths through the thin section by focusing through the transparent host obsidian glass using an optical microscope. The shape of volumes of glass used for the microlite counts were rectangular prisms, whose volumes were calculated from the dimensions of the selected surface area (i.e., 60x60 μm) and thickness of the thin section, as measured by the optical method described above.

Orientations of microlites were measured in all samples. Because the development of a preferred orientation of microlites depends on their aspect ratios (Manga, 1998), we measured orientations of acicular microlites with aspect ratios between 8 and 15, taking care to avoid microlites with mineral overgrowths. For all samples the average width of measured microlites was 1 μm. First, the trend (ϕ) of an acicular microlite was measured using the goniometer on the microscope stage (Fig. 2a).

Individual ϕ measurements are accurate to ±0.5°. Next, the width and apparent length of the microlite was measured using the reticle in the binocular eyepiece. The depth of each endpoint of the microlite was then measured by focusing through the transparent obsidian glass and recording the depth measured by the Heidenhain focus drive linear encoder (Fig. 2b). With those measurements, the true length and plunge (θ) of the microlite were then determined. Individual θ measurements are precise to ±2°, as determined by repeatedly measuring the orientation of a microlite. After orientations for more than 120 microlites were determined in each thin section, their orientations were rotated to reflect their true field orientation using *Stereonet* (Cardozo and Allmendinger 2012). For the four unoriented samples, each was re-oriented such that the mean trend of the microlites is north and the mean plunge is horizontal, to show their relative degree of microlite alignment.

RESULTS

Phenocryst and glass composition

Douglas Knob obsidian is comprised of phenocrysts of quartz, sanidine, magnetite, clinopyroxene, and fayalite, all set in a glassy matrix of high-silica rhyolite, which comprises ~95% of the rock by volume (Table 1). Matrix glass contains 0.14±0.05 wt. % H_2O. Quartz occurs as subhedral to anhedral crystals, 800-2000 μm in diameter, and is occasionally embayed with reentrants. Quartz-hosted glass inclusions contain 1.2 to 2.5 wt. % H_2O and 56 to 254 ppm CO_2 (Fig. 3). Euhedral to subhedral crystals and crystal fragments of sanidine can reach 6 mm in size, and are compositionally unzoned

($Or_{50\pm1}Ab_{50\pm1}$). Magnetite ($Mgt_{48\pm2}$ $Usp_{52\pm2}$) forms euhedral, equant crystals 50-400 μm across, and generally occurs as glomerocrysts associated with clinopyroxene and rare fayalite. Clinopyroxene occurs as euhedral, elongate crystals up to 1000 μm long. They are compositionally unzoned ferroaugite ($En_{13\pm1}Fs_{46\pm1}Wo_{41\pm1}$). Fayalite is compositionally unzoned ($Fa_{90\pm1}$), and euhedral.

Microlite number density (MND) and orientations

MND across Douglas Knob varies between $10^{4.6}$ and $10^{6.2}$ mm^{-3} (Table 2). Petrographically, individual samples appear texturally homogenous, occasionally with diffuse flow bands and patchy microlite domains that cause MND to vary within individual samples by 0.4 to 1.2 orders of magnitude (Fig. 4). Average MND varies within individual samples from $10^{4.9}$ to $10^{5.7}$ mm^{-3}. Microlites are preferentially oriented in all samples (Fig. 5). Standard deviations of ϕ and θ (σ_φ and σ_θ) in field-oriented samples range from 17° to 46° and 16° to 36°, respectively (Table 2). σ_φ and σ_θ in unoriented samples range from 14° to 36° and 9° to 24°, respectively (Table 2).

DISCUSSION

Douglas Knob is a small-volume, 0.011±0.002 km^3, high-silica rhyolite dome which was emplaced at ~120 ka near the western margin of Yellowstone Caldera (Christiansen et al. 2007). Christiansen (2001) mapped the vent of Douglas Knob as a point source at the topographic high near the center of the dome (Fig. 1a). We note, however, that Douglas Knob is an elongate, NW-SE-trending ridge and its morphology is symmetric about the trend of the topographic high. Nearby Central Plateau Member rhyolite lavas, such as Summit Lake, Grants Pass, and Bechler River, are all interpreted to have erupted through fissures (Christiansen et al. 2007). Vents for those flows are all aligned NW-SE, similar to the long axis of Douglas Knob, an orientation which parallels the southwestern margin of Yellowstone Caldera. We thus conclude that Douglas Knob actually extruded through a fissure instead of a central vent. Using the petrology, volatile contents, microlite number density and orientation, we now seek to constrain: 1) Storage conditions, 2) ascent dynamics, and 3) emplacement history.

Storage conditions

Compositions of coexisting, compositionally unzoned magnetite, fayalite, clinopyroxene, and quartz indicate the rhyolitic magma was stored at 760±30 °C at an oxygen fugacity 0.4 log units below the quartz-fayalite-magnetite buffer, using QUILF (Andersen et al. 1993). That temperature is similar to those of other rhyolitic obsidian domes (Manley and Bacon 2000; Castro and Gardner 2008). It is cooler than nearly all published temperatures for magmas in the Yellowstone/Snake River Plain system, but agrees with the general trend that younger and more easterly erupted lavas were emplaced at cooler temperatures (Vazquez et al. 2009; Watts et al. 2011; Almeev et al. 2012). Measured concentrations of H_2O and CO_2 in quartz-hosted glass inclusions are dispersed along a closed-system degassing trend for melt in equilibrium with a fluid composed of 50±10 mol.% CO_2 (Fig. 3)(Liu et al. 2005). Geochemical trends of the glass inclusions indicate the range of volatile contents do not result from crystallization of the quartz host. Volatile saturation pressures, assuming equilibrium conditions, indicate magmatic storage pressures of 50±25 MPa (Liu et al. 2005). That value corresponds to a storage depth of 2±1 km, assuming depth-averaged crustal density of ~2500 kg m^{-3}. Results from Rhyolite-MELTS simulations of the observed phenocryst assemblage are consistent with those magmatic storage conditions (Gualda et al. 2012).

Eruption ascent rate

Microlite number density varies by little more than an order of magnitude across Douglas Knob. If the lava crystallized during emplacement, then the number density of microlites would be expected to increase with increasing distance from the fissure. Instead, MND does not vary systematically with distance in the flow. Nor does MND vary systematically for Fe-Ti oxides, pyroxene, or feldspar when treated separately. The lack of systematic increase suggests that all microlites nucleated at depth rather than during emplacement. Furthermore, the variability displayed by MND suggests that eruptive degassing, water content, and temperature varied with time and position during the eruption, but did so unsystematically (Fig. 6).

Microlites nucleate and grow in response to degassing during decompression, because the liquidus temperature of the melt rises as volatiles exsolve (Swanson et al. 1989; Hammer 2008). Previous studies have related MND to decompression rate, with faster decompression resulting in higher MND (e.g., Couch et al. 2003; Castro and Gardner 2008; Martel 2012). Using experimental data and kinetic theory, Toramaru et al. (2008) developed a model that quantitatively links pyroxene and oxide MND to the decompression rates of silicic magmas. Using compositional data of the pre-eruptive

Douglas Knob melt and the range in average MND, decompression rates are estimated to have been 0.03 to 0.11 MPa hr^{-1}. Such rates are equivalent to ascent rates of 0.4 to 1.3 mm s^{-1}, assuming a lithostatic gradient and a calculated magma density of 2330 kg m^{-3} (Lange and Carmichael 1990). Similar ascent rates (~1 mm s^{-1}) have been documented for effusive, silicic, dome-forming eruptions at Unzen, Mount Saint Helens, Soufriére Hills, and Mount Shasta (Devine et al. 1998; McCanta et al. 2007; Nakada and Motomura 1995; Rutherford and Devine 2003; Rutherford 2008). Slow ascent rates allow time for open system degassing in the conduit, which is why the magma effused instead of erupting explosively (e.g., Jaupart and Allégre 1991; Rutherford and Gardner 2000).

The microlite assemblage of Fe-Ti oxides, pyroxene, and plagioclase at Obsidian Dome appears identical to that of Douglas Knob. MND are likewise similar, with those from Obsidian Dome ranging from $10^{5.1}$ mm^{-3} to $10^{5.7}$ mm^{-3} (Castro et al. 2002). Those MND yield decompression rates of 0.2 to 4.1 MPa hr^{-1}, which correspond to ascent rates of 3 to 50 mm s^{-1} (Toramaru et al. 2008). Although MND are similar at Douglas Knob and Obsidian Dome, the order of magnitude faster ascent rate for Obsidian Dome is caused by its lower SiO_2 and higher H_2O contents, which are both important variables in the model (70-74 wt. % and 4.1±1.2 wt. %, respectively; Hervig et al. 1989; Vogel et al. 1989). The ascent rate of the effusive eruption at Cordón Caulle (~70 wt. % SiO_2) is estimated to be 10 to 40 mm s^{-1} (Castro et al. 2013). Although ascent rate for the effusive eruption at Chaitén (~75 wt. % SiO_2) is not known, the effusion rate is well-constrained. If we assume a range of reasonable estimates for the diameter of its circular conduit (10-100 m), then magmas ascended at 6 to 600 mm s^{-1} during the first four months of the effusion of the Chaitén lava dome (Pallister et al. 2013). Ascent rates at Obsidian Dome, Cordón Caulle and Chaitén are thus one to three orders of magnitude faster than those estimated for Douglas Knob. The faster ascent rates may be a consequence of their lower melt viscosities.

The ascent rate of Douglas Knob can be used to constrain the geometry of the fissure feeding the eruption. The mean ascent rate U (m s^{-1}) during steady, laminar flow of an incompressible magma between two parallel walls separated by a distance w (m), and driven by a pressure gradient dP/dz (kg m^{-3}), is

$$U = \frac{w^2}{12\mu} dP/dz \qquad (1)$$

where μ is viscosity (Pa s)(Turcotte and Schubert, 1982). Except near a dike tip, the ascent of silicic magma is determined by a balance between local buoyancy forces and viscous resistance (e.g., Lister and Kerr 1991). We equate dP/dz to the product of gravitational acceleration and density difference between magma and crust, typically assumed to be 200 kg m^{-3} (e.g., Petford et al. 1993) The viscosity of magma with the composition and average water content of the glass inclusions (1.8 wt.% H_2O), 5 wt.% crystallinity, and temperature of 760°C is $10^{6.9}$ Pa s (Spera 2000; Giordano et al. 2008). A temperature uncertainty of 30°C translates into a viscosity uncertainty of a factor of 2. Ascent rates of 0.4 to 1.3 mm s^{-1} thus imply that w is in the range of 4 to 8 m with an additional uncertainty of 50% if we allow for the possible range of temperatures. If we take the 500 m length of the fissure at the surface as representative of that at depth, the volume flux would have been 0.6 to 7.5 m^3/s. To emplace a 0.011 km^3 dome thus took 17 to 210 days. Interestingly, this duration is similar to the 20 to 70 days that would have been required for magma to ascend from the chamber to the surface, assuming the average pre-eruptive storage pressure of 50 MPa and the estimated decompression rates of 0.03 to 0.11 MPa hr^{-1}. A volume flux of 0.6 to 7.5 m^3 s^{-1} is similar to those observed during dome-forming effusions at Merapi, Mount St. Helens, Unzen, and Soufriére Hills (Swanson et al. 1987; Nakada and Motomura 1995; Sparks et al. 1998; Hammer et al. 2000; Pallister et al. 2013), and estimated for the rhyolitic dike at Hrafntinnuhryggur (Tuffen and Castro 2009), but smaller than during the historical rhyolite dome forming eruptions at Chaitén and Cordón Calle (20-60 m^3 s^{-1}; Castro et al. 2013; Pallister et al. 2013; Tuffen et al. 2013). We recognize all those duration and ascent rate estimates have significant uncertainties (many of which are difficult to reduce), and neglect processes such as degassing on magma viscosity and the evolution of dike geometry in space and time. However, our calculations do provide first-order estimates of time and length scales for systems in which we previously had few quantitative constraints.

Emplacement of the lava dome

Microlite orientations provide insight into the deformation history of melt and hence understanding of ascent and dome emplacement. Long axes become aligned in the direction of local extension, which allows microlite orientations to be used to infer the dominant directions of fluid stretching and track flow lines in a lava (Manga 1998; Castro et al. 2002). Microlites are oriented during simple shear flow by progressively aligning in the direction of extension with increasing strain, typically thought to be perpendicular to the flow front. Microlite orientation induced by pure shear can be either perpendicular or parallel to the flow margin, but should have a limited vertical component in response to gravitational flattening of the dome (Manga 1998; Merle 1998; Castro et al. 2002). Analog experiments and sparse field studies show that emplacement of lava domes is primarily controlled by pure shear mechanisms, especially in the upper portions of lavas where we collected samples, but natural lavas may experience simple shear, pure shear, or a combination of both especially in different parts of the flow (Merle 1998; Buisson and Merle 2002; Ventura 2004; Schipper et al. 2013).

Assuming Douglas Knob erupted from a 500 m long fissure that runs the length of the dome, two samples were collected where the rhyolite emerged at the surface (Fig. 1a). Microlites in those samples are strongly aligned, indicating significant strain (Fig. 5). Microlites in the field-oriented sample are preferentially oriented close to vertical, which suggests alignment was caused by deformation during vertical flow, as expected from ascent in the conduit.

Microlites in samples collected away from the fissure vent also have preferred orientations, roughly perpendicular to the flow front. We would expect some scatter in the preferred orientations, because some microlite orientations may record local flow fields, caused by flow folds or brittle deformation, which are relatively common in rhyolitic lavas (Merle 1998; Castro and Cashman 1999; Buisson and Merle 2002; Tuffen et al. 2003; Gonnermann and Manga 2005). It is unlikely, however, that strains induced from such local features could overprint dominant orientation trends. In each sample there is a significant vertical component to the preferred orientations of microlites, suggesting the importance of the inherited orientation from ascent in the conduit.

The degree of alignment of acicular microlites in Douglas Knob can be directly compared to theoretical results to estimate how much strain accumulated during emplacement following microlite formation (Appendix). Values of σ_φ indicate Douglas Knob accumulated strains of 0.2 and 5.0, assuming either end-member pure and simple shear, respectively. Values of σ_θ indicate Douglas Knob accumulated a minimum strain of 0.8 strain, but the upper limit is unconstrained because the σ_θ in those samples are too low (i.e., well-aligned) to be generated solely by simple shear, implying pure shear as a partial mechanism during deformation.

Strain estimates are scattered with respect to increasing distance from vent (Fig. 7). Microlites in vent samples are as well-aligned, or better, than those in samples farther from the vent. Importantly, the absence of increasing strain with increasing distance from vent indicates that the lava did not accumulate measurable strain (on the flow's upper surface) in the ≤240 m of subaerial flow during emplacement. Instead, strain estimates from σ_φ in distal samples are generally smaller than those at the vent. Thus, strain generated by emplacement was sufficient to rotate the preferred orientation of microlites from near vertical to roughly perpendicular to the flow front, but was unable to improve the microlite orientation distributions. It is plausible that the rotation of preferred orientations worsened the σ_φ in microlite orientation distributions. Alternatively, all of the variation in microlite orientation distributions record strain accumulated during conduit ascent. Thus, variations in strain reflect variations in conduit characteristics, such as diameter or ascent rate. If so, then the variations indicate that changes in conduit conditions were pulsatory to chaotic rather than systematic (e.g., Geschwind and Rutherford 1995).

Microlites indicate the sampled domains of Douglas Knob experienced negligible strain during subaerial emplacement, whereas strain was found to accumulate during emplacement of Obsidian Dome (Castro et al. 2002). We attribute this disparity to the vastly different sizes of the two flows. Obsidian Dome traveled hundreds to thousands of m more than did Douglas Knob. It is thus possible that the degree of microlite alignment in very small domes are vestiges of conduit flow, and thus preserve a record of conduit processes. In larger domes and flows, however, significant strain may accumulate during emplacement that erases and overprints microlite textures derived in the conduit (Castro et al. 2002).

Finally, the morphology of the dome also provides a constraint on eruption duration. The distance R (m) that magma spreads away from the vent depends on eruption rate and magma viscosity following:

$$R = 0.7\left(\frac{\rho g V^3}{3\mu}\right)^{1/8} t^{1/8} \qquad (2)$$

where ρ is density (kg m^{-3}), μ is viscosity (Pa s), V is eruptive volume (m^3), g is 9.8 m s^{-2}, and t is time (s)(Huppert 1982). This model assumes a constant viscosity and neglects the possible feedbacks between strain localization and viscous dissipation. Because viscosity during emplacement is unknown, we adopt the approach of testing whether the eruption rate inferred in the previous section is consistent with a reasonable viscosity. Assuming an eruption duration of 17 to 210 days, radial spreading of 240 m, and density of 2330 kg

m^{-3}, the viscosity of the lava must have been 10^{11} to 10^{12} Pa s. Such viscosities are higher than those estimated at depth ($10^{6.9}$ Pa s) owing to the loss of water (from ~1.8 wt.% to 0.14 wt.% H_2O) and cooling. Using the composition of matrix glass those viscosities imply surface emplacement temperatures between 695 and 735°C, and thus cooling of 25 to 65°C. As water content decreases from 1.8% to 0.14%, temperature will decrease about 30°C mainly as a result of decompression of the vapor phase (Proussevitch and Sahagian 1998; Mastin and Ghiorso 2001; Gonnermann and Manga 2007). There should be additional cooling owing to thermal conduction to the surrounding country rocks. The time scale for thermal diffusion (τ) is w^2/κ, where $\kappa=5x10^{-7}$ m^2 s^{-1} is the thermal diffusivity and w is fissure width (m)(Bagdassarov and Dingwell 1994). Using w equal to 4 to 8 m, as estimated previously from our ascent rate calculation, τ is about 0.5 to 2 years, long enough that the magma can reach the surface without solidifying (given the inferred ascent times), yet short enough that some cooling will occur. In sum, the eruption duration implied by the dome shape is consistent with that based on ascent rates and conduit dimensions.

The eruption duration also allows flow front advance rates to be estimated. Viscous flow is assumed to have been viable during the duration of the eruptive event, and likely continued for up to a few years following the end of the eruption (e.g., Tuffen et al. 2013). Assuming that, the flow front of Douglas Knob lava dome advanced at tens of cm to a few m per day. Those values are on par with velocity estimates from Cordón Caulle lava (1.5-3 m d^{-1}) (Tuffen et al. 2013). Such estimates provide first order constraints important for hazard assessment associated with the effusive eruptions from the Yellowstone volcanic system.

SUMMARY

The eruption of Douglas Knob tapped a high-silica rhyolitic magma that was shallowly stored at 50±25 MPa and 760±30 °C. Microlite number densities indicate ascent rates of 0.4 to 1.3 mm s^{-1}. Using the measured glass composition and volatile contents, the required fissure width is 4 to 8 m, similar to rhyolite dikes elsewhere (e.g., Tuffen and Castro, 2009). Such slow ascents are reasonable when compared to other silicic effusive, dome-forming eruptions, and slow enough to allow degassing to occur (e.g., Eichelberger et al. 1986; Gonnermann and Manga 2005; Castro and Gardner 2008; Rutherford 2008; Castro and Dingwell 2009). The emplacement time based on those ascent rates, as well as the morphology of the dome, is 17-210 days, equivalent to eruption rates of 0.6 to 7.5 m^3 s^{-1}. Microlites in all samples from Douglas Knob are well-aligned, especially in near-vent locations, and do not become better aligned with distance. Microlite alignment also demonstrates the lava accumulated strains <5, which were imparted by components of both simple and pure shear in the conduit following microlite nucleation during ascent.

APPENDIX A: MODELING MICROLITE ORIENTATION

The degree of alignment of a microlite population, irrespective of preferred orientation, can be used to understand how lavas are emplaced. Microlite alignment is measured by the standard deviation of ϕ and θ (σ_φ and σ_θ), with smaller standard deviations indicating better alignment. Those deviations can be compared to theoretical σ_φ and σ_θ of a population of 100,000 microlites that experience variable degrees of strain in either simple and pure shear flows. We use a discrete, finite-difference model with an explicit timestep to numerically integrate the differential equations that predict the motion of rod-shaped particles in either simple-shear flow and pure-shear flow (Jeffery 1922; Gay 1968; Manga 1998). Following Manga (1998), equations governing particle motion in simple shear flow are:

$$\frac{d\phi}{dt} = \frac{\mathrm{G}}{R^2+1}\left(R^2\cos^2\phi + \sin^2\phi\right) \tag{3}$$

$$\frac{d\theta}{dt} = \mathrm{G}\frac{R^2-1}{R^2+1}\sin\theta\cos\theta\sin\phi\cos\phi \tag{4}$$

and the equations governing particle motion in pure shear flow are:

$$\frac{d\phi}{dt} = \mathrm{G}\frac{R^2-1}{R^2+1}\sin(2\phi) \tag{5}$$

$$\frac{d\theta}{dt} = -\frac{1}{2}\mathrm{G}\frac{R^2-1}{R^2+1}\cos(2\phi)\sin(2\theta) \tag{6}$$

where G is strain rate (s^{-1}), R is microlite aspect ratio (dimensionless), and t is time (s). During flow the lava is assumed to deform solely with plane strain and the melt is assumed to be a Newtonian fluid. Microlite concentrations are assumed to be sufficiently dilute so that the microlites do not interact with one another. Original orientations are assumed to be random. Microlite concentration is considered dilute when MND*R^2*d is less than 1, where d is microlite diameter (Manga 1998). All samples from Douglas Knob meet that criterion for being a dilute suspension.

The model predicts that in simple shear flow initially randomly oriented microlites progressively align in the direction of extension with increasing strain, but that they continuously rotate, thus never becoming perfectly aligned. Conversely, microlites in pure shear flow are expected to eventually become perfectly aligned in the direction of extension with increasing strain (i.e., σ_φ and σ_θ go to zero). The degree of microlite alignment in natural lavas can thus be used to constrain the type of shear and the amount of strain imposed on microlites during flow (Fig. 8). Samples with small variances in trend or plunge cannot be explained solely by simple shear. Because equations of motion for pure and simple shear can be added linearly, we modeled how combinations of simple and pure shear affect microlite orientation distributions to quantify the relative proportions of pure shear and simple shear during emplacement (Fig. 9). The relative amounts of simple and pure shear create wide domains of θ with variations in strain (Fig. 9a). Vastly different styles of shear and accumulations of strain can thus adequately explain the observed alignments of θ. Conversely, simple shear and pure shear act similarly to align ϕ, forming narrow domains of ϕ with variations in strain (Fig. 9b). The style of deformation inferred from the degree of microlite alignment can be interpreted with a wide range of possible combinations of simple and pure shear.

Table 3.1

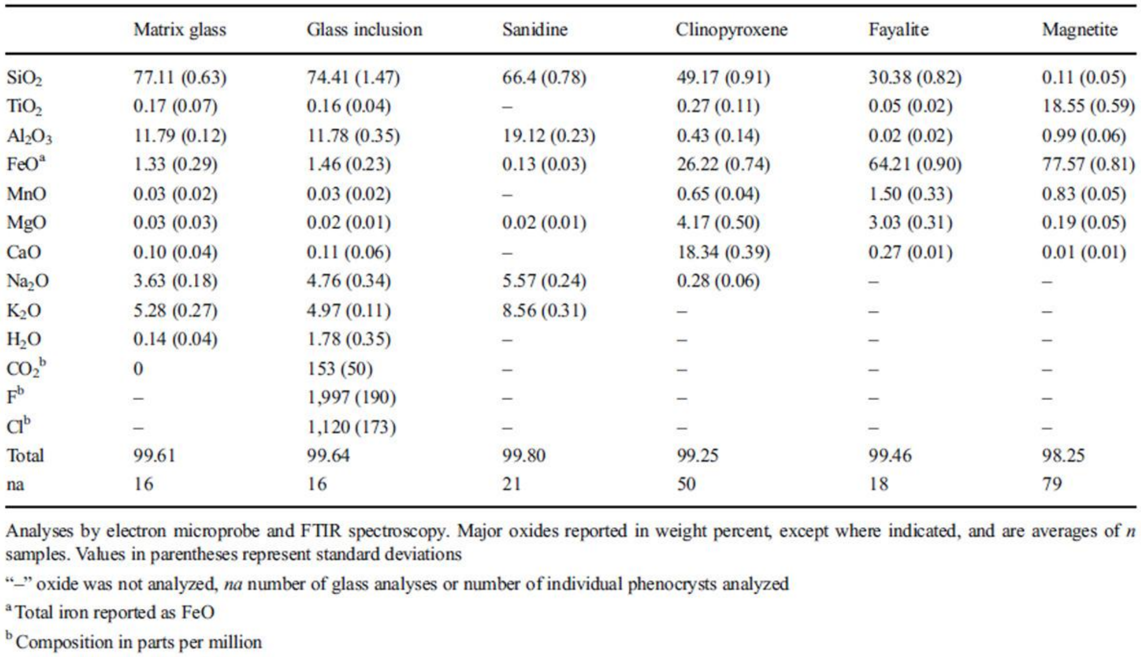

	Matrix glass	Glass inclusion	Sanidine	Clinopyroxene	Fayalite	Magnetite
SiO_2	77.11 (0.63)	74.41 (1.47)	66.4 (0.78)	49.17 (0.91)	30.38 (0.82)	0.11 (0.05)
TiO_2	0.17 (0.07)	0.16 (0.04)	–	0.27 (0.11)	0.05 (0.02)	18.55 (0.59)
Al_2O_3	11.79 (0.12)	11.78 (0.35)	19.12 (0.23)	0.43 (0.14)	0.02 (0.02)	0.99 (0.06)
FeO^a	1.33 (0.29)	1.46 (0.23)	0.13 (0.03)	26.22 (0.74)	64.21 (0.90)	77.57 (0.81)
MnO	0.03 (0.02)	0.03 (0.02)	–	0.65 (0.04)	1.50 (0.33)	0.83 (0.05)
MgO	0.03 (0.03)	0.02 (0.01)	0.02 (0.01)	4.17 (0.50)	3.03 (0.31)	0.19 (0.05)
CaO	0.10 (0.04)	0.11 (0.06)	–	18.34 (0.39)	0.27 (0.01)	0.01 (0.01)
Na_2O	3.63 (0.18)	4.76 (0.34)	5.57 (0.24)	0.28 (0.06)	–	–
K_2O	5.28 (0.27)	4.97 (0.11)	8.56 (0.31)	–	–	–
H_2O	0.14 (0.04)	1.78 (0.35)	–	–	–	–
CO_2^b	0	153 (50)	–	–	–	–
F^b	–	1,997 (190)	–	–	–	–
Cl^b	–	1,120 (173)	–	–	–	–
Total	99.61	99.64	99.80	99.25	99.46	98.25
na	16	16	21	50	18	79

Analyses by electron microprobe and FTIR spectroscopy. Major oxides reported in weight percent, except where indicated, and are averages of *n* samples. Values in parentheses represent standard deviations

"–" oxide was not analyzed, *na* number of glass analyses or number of individual phenocrysts analyzed

[a] Total iron reported as FeO

[b] Composition in parts per million

Table 3.2

Microlite number density (MND), aspect ratio, and standard deviations of trend (φ) and plunge (θ)

Sample[a]	MND (mm^{-3})	Aspect ratio[b]	σ_{ϕ°	σ_{θ°
Y88	$10^{4.6}$ - $10^{5.2}$	9 (2.0)	38	9
Y90	$10^{4.6}$ - $10^{5.4}$	12 (1.9)	14	24
Y92	$10^{5.3}$ - $10^{5.7}$	10 (2.1)	17	20
Y116	$10^{5.3}$ - $10^{5.9}$	12 (1.5)	36	17
Y117	$10^{4.6}$ - $10^{5.8}$	10 (2.1)	30	31
Y118	$10^{4.4}$ - $10^{5.6}$	11 (1.6)	32	23
Y119	$10^{4.6}$ - $10^{5.3}$	11 (2.0)	17	16
Y120	$10^{5.0}$ - $10^{6.1}$	10 (1.4)	46	36
Y121	$10^{5.0}$- $10^{5.7}$	10 (1.9)	30	29
Y122	$10^{5.1}$ - $10^{6.2}$	10 (2.9)	26	18

[a] Sample locations are shown in Figure 1A.

[b] Aspect ratio equals microlite length divided by width, values in parentheses represent 1σ error.

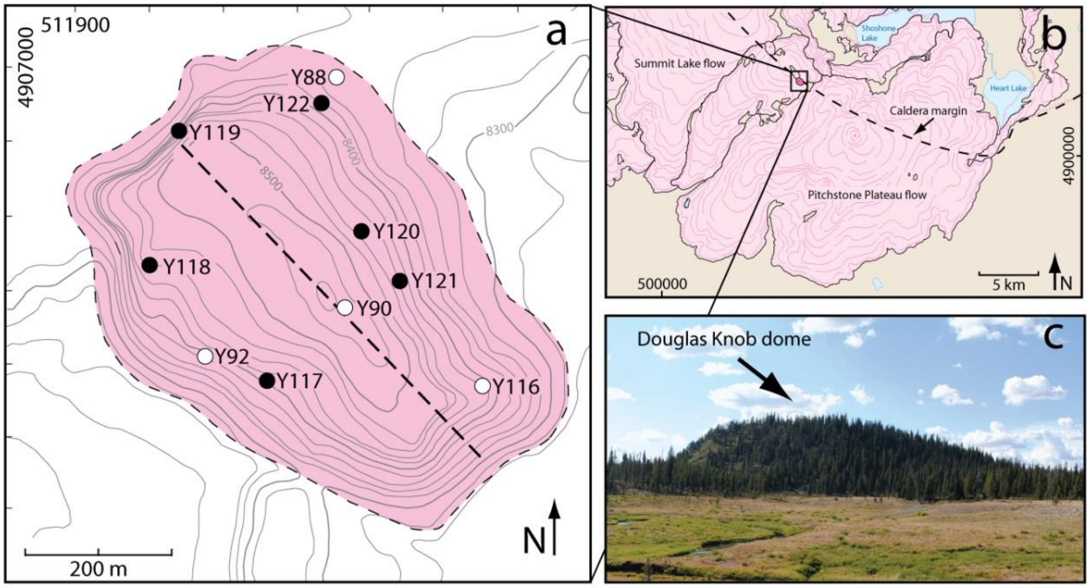

Figure 1

Fig. 3.1

Location and form of Douglas Knob lava dome. **a** Geologic map of Douglas Knob. Locations of oriented and unoriented samples are shown by black and white circles, respectively. Trend of proposed fissure vent marked by black dashed line. Topographic contours are shown in gray (20 ft interval). **b** Simplified geologic map of the southern portion of the Yellowstone volcanic field surrounding Douglas Knob. Central Plateau Member Rhyolites are shown in pink, the margin of Yellowstone caldera is shown by dashed black line. **c** Panoramic field photograph of Douglas Knob, view looking southwest.

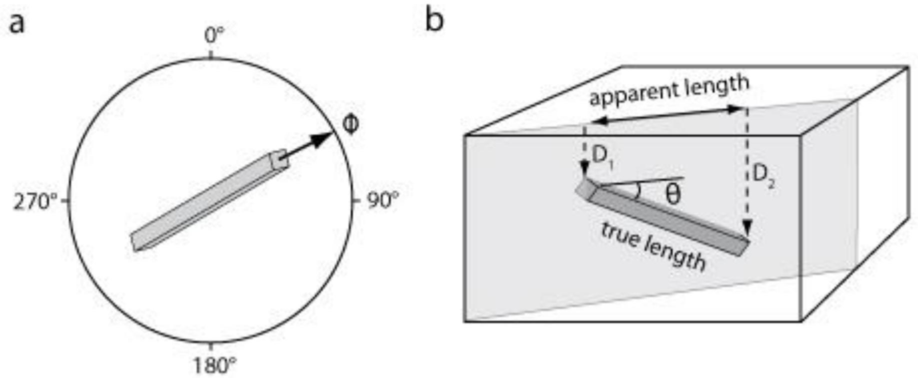

Fig. 3.2

Schematic diagram showing how the trend (φ) and plunge (θ) of microlites are measured in obsidian glass relative to the plane of the thin section. **a** φ is measured using the microscope stage goniometer. **b** Microlite length and θ are calculated geometrically using the apparent length and difference in depths (D_2-D_1) to the tips of each end of the microlite. Modified after Castro et al. (2002).

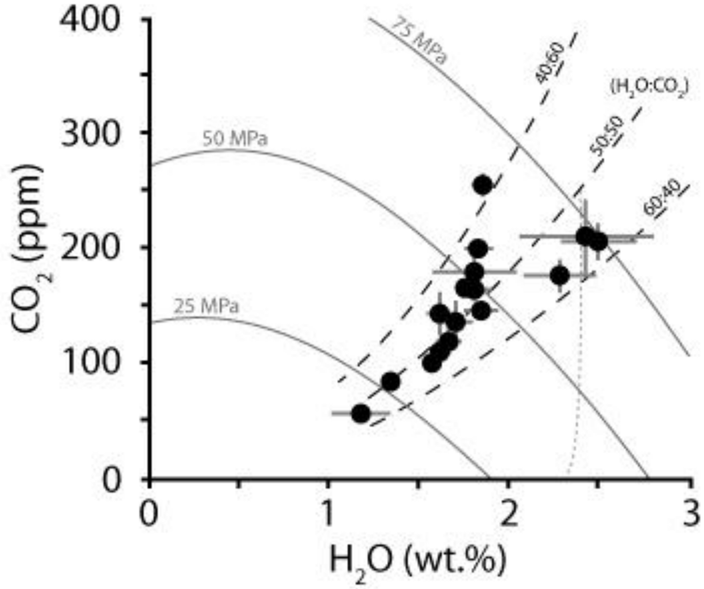

Fig. 3.3

Volatile contents dissolved in 16 quartz-hosted glass inclusions. Error bars (1σ) are shown in gray when larger than the symbol size and are from uncertainties in thickness measurements. Equilibrium solubilities at 25, 50, and 75 MPa and 760 °C are shown in gray (Liu et al., 2005). Dashed black lines are fluid compositions for closed system degassing pathways for rhyolite in equilibrium with a mixed H_2O-CO_2 fluid (Liu et al., 2005). Dotted light gray line represents the open system fluid degassing pathway for rhyolite in equilibrium with the highest H_2O-CO_2 concentrations found at Douglas Knob (Newman and Lowenstern, 2002).

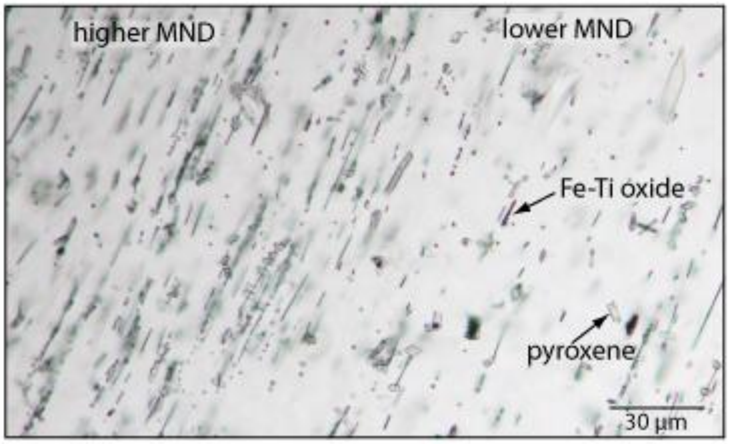

Fig. 3.4

Photomicrograph of obsidian displaying MND variations in a sample with strong microlite alignment. MND is higher on the left half of the image. Black acicular microlites are Fe-Ti oxides. Clear prismatic microlites are pyroxene.

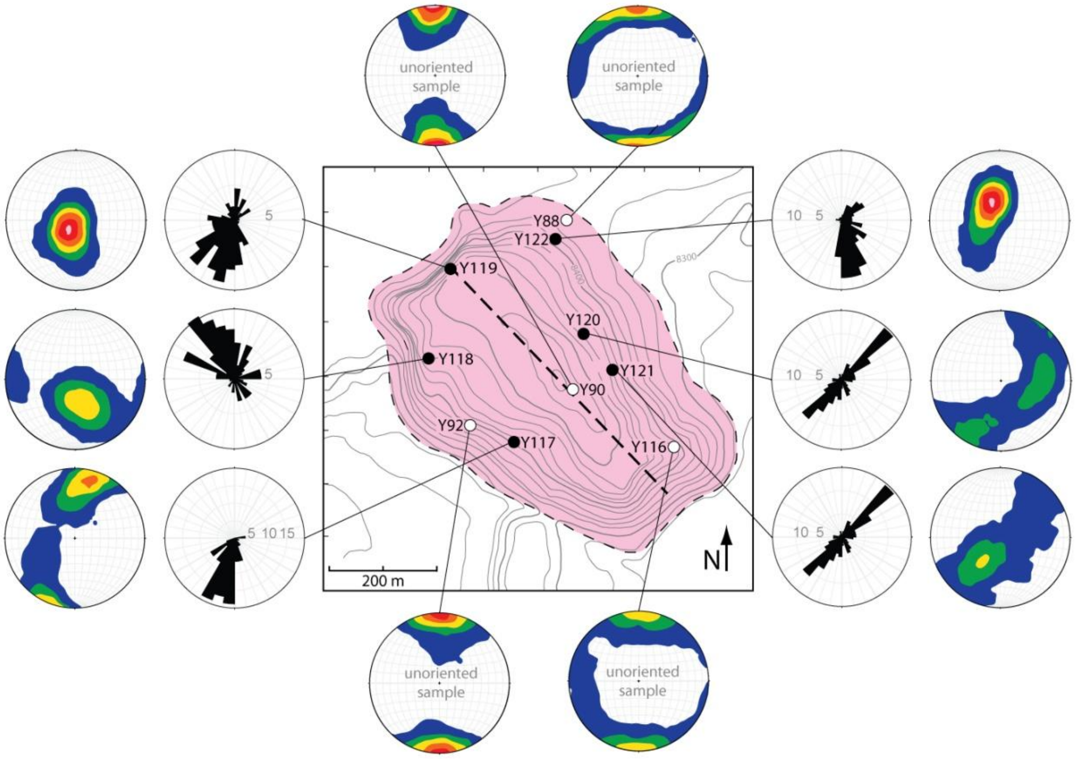

Fig. 3.5

Stereograms and rose diagrams show the orientations of acicular microlites of field-oriented samples (black circles) and unoriented samples (white circles). Rose diagrams display the orientation of acicular microlites. The degree of microlite alignment is represented by Kamb contours, with colors representing orientation frequency per unit area (where blue is 2%, green is 8%, yellow is 14%, orange is 20%, red is 26%, and pink is 32%). Trend of fissure vent marked by black dashed line.

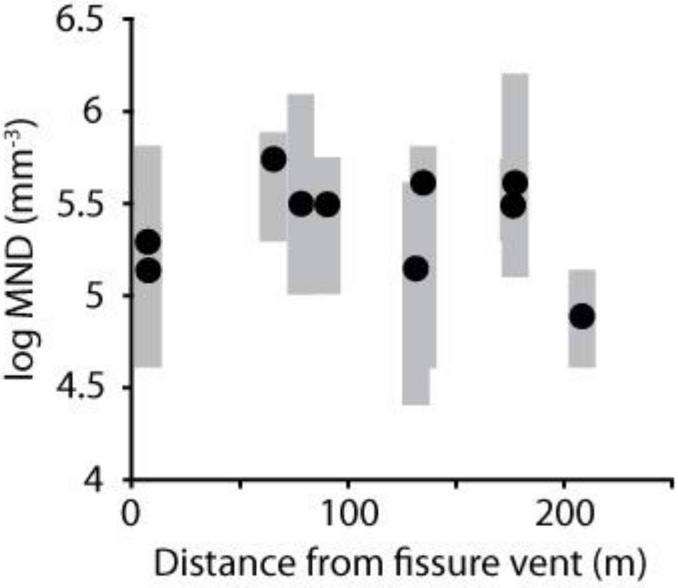

Fig. 3.6

Relationship between microlite number density (MND) and distance from fissure vent. Black dots represent average MND. Gray bars encompass maximum and minimum values within sample.

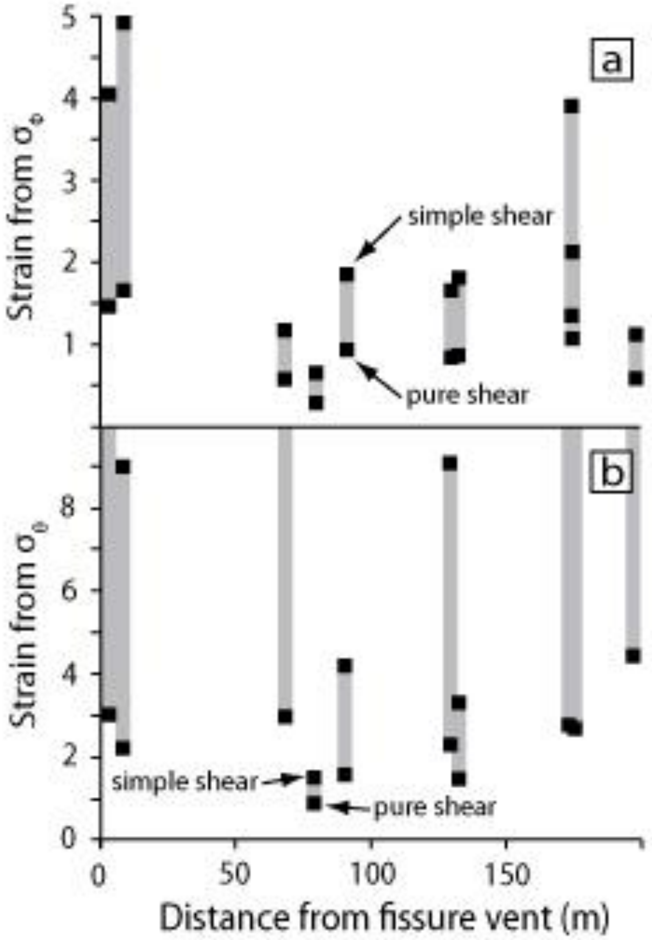

Fig. 3.7

Strain estimates recorded by the standard deviation of φ **a** and θ **b** of microlites plotted against distance from fissure vent. The lower bound estimates represent strain induced solely by pure shear, whereas upper strain estimates assume strain induced by only simple shear. The range between those end members displays strain accumulated by combinations of simple and pure shear. Microlites are so well-aligned with respect to θ in some samples that they leave the upper bound for those strain estimates extending to infinity.

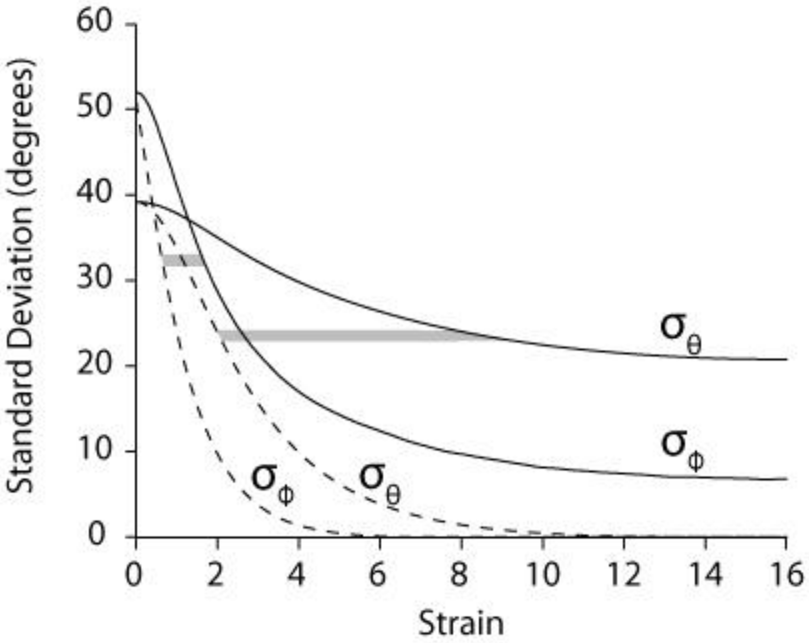

Fig. 3.8

Model standard deviations of the φ and θ of a population of rod-shaped microlites with an aspect ratio of 10 plotted as a function of strain accumulated during simple (solid curves) and pure shear (dashed curves). Standard deviations for sample Y118 are plotted in gray domains as an example for obtaining strain estimates from the degree of microlite alignment.

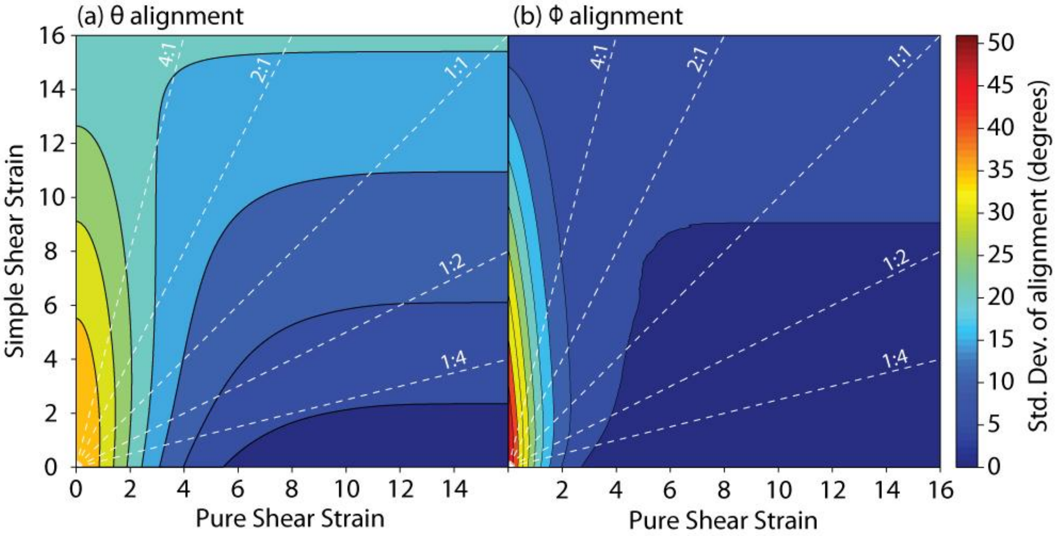

Fig. 3.9

Modeled effects of combining relative proportions of strain induced by end member simple shear and pure shear on the alignment of microlite θ **a** and φ **b**. Proportions of simple shear to pure shear are shown by white dashed lines. Any degree of microlite alignment can be explained by variable proportions of simple shear and pure shear.

CHAPTER 4:

RHYOLITIC OBSIDIAN COOLING AND EMPLACEMENT RATES INFERRED FROM SPHERULITE GROWTH

INTRODUCTION

Direct observations of the rhyolitic effusions at Chaitén and Cordón Caulle volcanoes in Chile in 2008-2009 and 2011-2012, respectively, have provided unprecedented insights to the emplacement of effusive rhyolitic eruptions (Castro and Dingwell 2009; Alfano et al. 2011; Bernstein et al. 2013; Castro et al. 2013; Pallister et al. 2013; Tuffen et al. 2013). Before these eruptions, effusive rhyolitic eruptions had been largely absent from the historic record, requiring that much of our understanding of their eruptive behavior and transport come from studying past events (e.g., Fink 1983; Griffiths and Fink, 1993; Stevenson et al. 1994; Anderson et al. 1998; Manga 1998; Castro and Cashman, 1999; Castro et al., 2002; Rust et al. 2003; Befus et al., 2014).

To understand how rhyolite lavas are emplaced, it is critical to know how long rhyolitic eruptions remain mobile. Mobility is directly controlled by how fast lavas cool, which in turn is largely determined by how efficiently the upper crust and basal breccia can insulate the interior of the flow from heat loss (Walker et al. 1973; Malin 1980; Fink 1983; Stevenson et al. 1993; Manley 1996; Griffiths 2000; Harris and Rowland, 2009; Tuffen et al. 2013). Because cooling exerts such a strong control on flow behavior, techniques to derive cooling rates from ancient lavas of variable size are needed. Numerical models of heat conduction suggest rhyolite lavas that are tens of meters thick cool at rates as slow as 0.01 °C d^{-1}, and thus may take decades to cool to the glass transition temperature of 600 to 700 °C (Manley 1992). Using relaxation geospeedometry, a technique that uses differential scanning calorimetry to measure the cooling history at the glass transition, frontal flow ramps at the exterior of Rocche Rosse rhyolite flow of Lipari, Italy, are calculated to have cooled at 43 to 290 °C d^{-1} (Gottsmann and Dingwell 2001). Samples collected from the base of a 20-70 m thick pantellerite obsidian lava of Mayor Island, New Zealand suggest the insulated interior cooled at ~1 °C d^{-1} (Gottsmann and Dingwell 2002).

Estimates for the thermal history of obsidians using the aforementioned models and analytical techniques are similar and demonstrate the interiors of obsidian lavas cool more slowly than the exteriors. To build upon our understanding of physical processes of emplacement and to better quantify rhyolite cooling rates, additional methods to accurately measure the thermal history of obsidian lavas would be useful. In this contribution, we develop the use of compositional gradients surrounding spherulites as an in-situ technique to track the thermal history of host obsidian lava (Castro et al. 2009; Watkins et al. 2009; Gardner et al., 2012).

Spherulites are spherical to ellipsoidal bodies of radiating, intergrown crystals, typically feldspar and quartz, that form by rapid crystallization of lava in response to significant undercooling (Lofgren 1971a, b; Fenn, 1977; Swanson, 1977; Castro et al. 2009; Watkins et al. 2009; Gardner et al., 2012). As spherulites grow, incompatible constituents are expelled into the surrounding matrix, creating enrichments of those elements along the spherulite-matrix boundary (Fig. 1) (Castro et al., 2008; Watkins et al., 2009; Gardner et al., 2012). With time, the expelled constituents diffuse into the surrounding matrix at temperature-dependent rates. The combined effects of expulsion and diffusion of the incompatible elements generate concentration profiles, the shapes of which vary as a function of spherulite growth rate, element diffusivity, and the cooling rate of the lava (Gardner et al., 2012).

Because the gradients are controlled by spherulite growth behavior and lava cooling, previous investigations have been unable to provide a unique solution to lava cooling (e.g., Castro et al. 2008; Watkins et al. 2009; Gardner et al. 2012). To improve the technique it is critical to apply it to a system in which at least one of those parameters is known independently. Thus, we have used differential scanning calorimetry to determine the cooling rate for a spherulite-bearing obsidian sample collected from Pitchstone Plateau lava flow, Yellowstone Caldera. We then analyzed spherulites and their surrounding matrix glass in that sample. Together, the differential scanning calorimetry cooling rate and form of compositional gradients surrounding spherulites are used to uniquely determine spherulite growth form and rates. Knowing these things, we use the model to allow compositional gradients to be used as in-situ recorders of the thermal history of the host lavas.

SAMPLE

A hand sample of spherulite-bearing obsidian was collected from Pitchstone Plateau lava flow, a 70 km^3 high-silica rhyolite obsidian lava that erupted effusively

79±10 ka from Yellowstone caldera (Christiansen et al., 2007). The sample was collected as a single 2 kg block from an outcrop of dense obsidian where the flow is ~180 m thick (UTM zone 12 T, 0525548 m N and 4899434 m E) (Fig. 2). Although the upper pumiceous carapace of Pitchstone Plateau has been stripped by Pinedale glaciations (Christiansen 2001), the sample likely comes from the upper 10 m of the flow, as evidenced by the low dissolved water content in the glass.

Spherulites comprise a few percent of the obsidian sample by volume, and occur as near spherical ellipsoids, ranging from 1 to 10 mm in diameter. Individual spherulites are generally dispersed randomly throughout the sample, separated by tens of mm, with some clusters of 2 to 4 that impinge upon one another. All spherulites are composed of elongate crystals of alkali feldspar ($Or_{34\pm6}Ab_{64\pm6}$) and quartz that radiate outward from a nucleation center (Fig. 4). Minor phases include equidimensional Fe-Ti oxides and unoriented, irregularly-shaped voids. Quartz and alkali feldspar are both longer and wider near the center of the spherulites. The proportion of alkali feldspar relative to quartz increases gradually with distance from the spherulite core, from near equal proportions near the spherulite core to ~60% alkali feldspar approaching the spherulite margin. The outermost rims (~100 μm) of the spherulites are more porous, and are composed solely of radiating alkali feldspar and void space (Fig. 4C). Pockets of glass trapped within the spherulites were not observed.

The spherulites are hosted within a high-silica rhyolite glass that contains 5-10 vol.% phenocrysts of sanidine, quartz, magnetite, clinopyroxene, and fayalite. The glassy groundmass contains abundant acicular Fe-Ti oxide and clinopyroxene microlites, which define diffuse flow bands. Spherulites overprinted those earlier flow-induced textures, as evidenced by undeflected flow bands that can be traced from the matrix glass across many of the spherulites. Fe-Ti oxides in those bands are texturally distinct from Fe-Ti oxide microphenocrysts formed during spherulite growth.

The fist-sized obsidian sample was crushed gently to generate mm- to cm-sized chips. Pristine, crystal-free, glassy chips were separated from the gently crushed sample for calorimetry experiments. Next, chips that contained isolated spherulites encased in matrix glass were separated and immersed in epoxy. Those chips were mounted on glass slides and then ground until central sections of the spherulites were exposed. Once exposed, the samples were polished. Next, the sample was removed from the glass slide, flipped, and remounted to grind and polish the sample until the host obsidian glass was transparent. Each finished sample consisted of a doubly-polished wafer of glass, 150 to 350 μm thick, that contained a central section of a spherulite. In all, we analyzed 19 individual spherulites, taking care to select spherulites that span the range of spherulite sizes in the original hand sample.

TRACE ELEMENT AND WATER MEASUREMENTS

Trace-element concentrations were measured by LA-ICP-MS at the University of Texas at Austin in four separate analytical sessions, using a New Wave Research UP 193-FX fast excimer laser system (193 nm wavelength, 4-6 ns pulse width) laser system coupled to an Agilent 7500ce quadrupole ICP-MS. The laser system is equipped with a large format, two-volume laser cell, for direct sampling of the ablation plume with fast (< 1s) washout times to minimize spatial carryover. Laser-ablation parameters optimized from spherulite test ablations were 5 μm s^{-1} line traverses using a 10x100 μm rectangular slit aperture with long-axis normal to the scan direction, 70% power, 10 Hz repetition rate, and He cell flows of 200-300 mL min^{-1}. Laser energy densities (fluences) obtained for all sessions averaged 1106 J cm^{-2} with < 3% variation. The ICP-MS operated at an RF power of 1600 W and an average Ar carrier flow of 1.29 L min^{-1}. Oxide production rates as monitored by ThO/Th for NIST 612 were ≤ 0.21%. The quadrupole time-resolved method involved measurement of 13 masses (^{7}Li, ^{11}B, ^{23}Na, ^{25}Mg, ^{29}Si, ^{39}K, ^{45}Sc, ^{55}Mn, ^{85}Rb, ^{88}Sr, ^{133}Cs, ^{137}Ba, and ^{208}Pb) using integration times between 5 and 100 ms. The analytical sampling period of 0.75 s, equivalent to a reading every 3.7 μm, corresponds to 95.7% measurement time. Time-resolved intensities were converted to concentration (ppm) equivalents using Iolite software (Univ. Melbourne), with ^{29}Si as the internal standard. Baselines were determined from 60 s glass blank intervals measured while the laser was off and all masses were scanned by the quadrupole. NIST 612 was used as the primary reference standard for all analytes. Recoveries (relative 1σ deviations versus GeoREM preferred values) among analytes for a secondary standard (NIST 610), run as an unknown against the primary standard, were typically better than 2%. Based on those observations, we conservatively assign 5% relative uncertainties. Laser traverses on sample wafers were oriented along radial projections from spherulite centers, typically beginning within the spherulite and continuing across the spherulite-matrix boundary far into (>1000 μm) the host matrix glass. Element concentrations were calculated assuming a concentration of 77 wt.% SiO_2 in the matrix glass and spherulite. Such a value is equivalent to the overall SiO_2 concentration within spherulites based on the relative proportions of quartz (100 wt.% SiO_2) and alkali feldspar (66 wt.% SiO_2) observed in the spherulites. An SiO_2 concentration of 66 wt.% SiO_2 was used to calculate element concentrations in the porous spherulite rims, which are comprised of alkali feldspar.

Dissolved water contents of the host obsidian were measured by Fourier-Transform Infrared (FTIR) spectroscopy along linear traverses near the LA-ICP-MS laser tracks. The majority of the FTIR analyses were performed by synchrotron-source light at the Advanced Light Source at Lawrence Berkeley National Laboratory using a Nicolet 760 FTIR spectrometer and a Spectra-Tech Nic-Plan IR microscope. Spectra were collected in <5 μm areas every 10 to 20 μm along the linear transects in the mid-IR range using a KBr beamsplitter and consist of 60 scans collected at a resolution of 8 cm^{-1}. A set of FTIR analyses were also collected using a Thermo Electron Nicolet 6700 spectrometer and Continuμm IR microscope at the University of Texas at Austin. For those, spectra were collected in mid-IR range using a KBr beamsplitter and a globar source. Spectra consisted of 60 scans collected at a resolution of 4 cm^{-1}. Analytical spots 10 μm wide by 40 μm long were collected every 10 μm along linear transects. Although the spatial resolution of the spectra collected using the synchrotron-source is superior, the FTIR spectra from either system are indistinguishable from one another.

Total H_2O contents for synchrotron and FTIR measurements were estimated using the absorbance at ~3500 cm^{-1} and a modified Beer-Lambert law. Background of the absorbance at ~3500 cm^{-1} was assumed to be linear. The molar absorptivity of H_2O at

~3500 cm^{-1} was assumed to be 100 L mol^{-1} cm^{-1}, an appropriate absorptivity for low water contents when the water speciation is predominantly hydroxyl (Newman et al. 1986). Glass density was assumed to be 2350 g L^{-1}, and was not adjusted for water content. The thickness of the sample at every analytical spot along each linear transect was measured optically using a petrographic microscope by focusing on the top and bottom of the sample and measuring the distance traveled by the microscope stage with a Heidenhain focus drive linear encoder.

To constrain the behavior of water speciation in the samples, we measured short transects in the near-IR range using a CaF_2 beamsplitter and white light. Absorbances of molecular water (H_2O_m) and hydroxyl (OH^-) were measured at ~5230 cm^{-1} and at ~4500 cm^{-1}, respectively. Background for the absorbances at ~5230 cm^{-1} and ~4500 cm^{-1} were treated as linear (Fig. 3) , and thickness was measured as described above. Concentrations of H_2O_m and OH^- were calculated using the model of Zhang et al. (1997).

DIFFERENTIAL SCANNING CALORIMETRY

The thermal history of the obsidian sample was estimated by differential scanning calorimetry (DSC) using a Netzsch ® DSC 404C Pegasus calorimeter at the Ludwig-Maximilian University of Munich, Germany, under a constant flow of Argon 5.0 to avoid oxidation of the samples during the heat-flux measurements. The pristine, crystal-free obsidian chips were cleaned and stored in a desiccator for 24 hours. A 28 mg sample of the glassy material was loaded into a circular Pt crucible and then closed with a Pt lid.

The sample was reheated at 10 °C min^{-1} until it reached its supercooled liquid field and was further heated for at least ~50 °C above the glass transition to assure complete enthalpic relaxation of the glass. The sample was then cooled and reheated repeatedly at matching rates (25, 20, 15 and 10 °C min^{-1}) to produce 4 calibration curves. A baseline was subtracted from the obtained heat-flux traces and the heat capacity (Cp) of the sample was calculated using the heat capacity of a single sapphire crystal.

The glass transition represents a temperature interval in which the structure of the glass relaxes and re-equilibrates during heating from the glassy state to the liquid state. Peak glass-transition temperatures (Tg peak), which are influenced by the previous cooling rate and actual heating rate, correspond to crests when plotting heat capacity against temperature. Each calibrated Cp curve was modeled following the phenomenological Tool-Narayanaswamy-Moynihan (TNM) approach (Tool 1946; Narayanaswamy 1971; Moynihan et al. 1976b), and using the rewritten equations from DeBolt et al. (1976) and the procedure outlined in Wilding et al. (1995). Activation enthalpy ΔH and pre-exponential factor A were calculated respectively from the slope and intercept of the fitted line formed by plotting –ln(cooling rate) against 1/Tg peak. Parameters x and β were estimated for each calibration curve and averaged. Lastly, the natural cooling rate of the obsidian was estimated with the TNM approach by modeling the Cp curve obtained with the first reheating of the sample, and using the 4 previously determined parameters. The resulting cooling rate corresponded to the curve fit with the least sum of squared residuals.

RESULTS

Compositional profiles

In the glass far from the contact between spherulite and matrix the concentrations of all analyzed elements are uniform. Across the spherulite-matrix boundary distinguishable profiles were observed. Li and K are depleted in the spherulite relative to the glass, and have uniform concentrations in the glass. Rb and H_2O are also depleted in the spherulite relative to the glass, but have variable concentrations in the surrounding glass. Na is enriched in the spherulite relative to matrix glass yet is constant in concentration in the glass. B, Cs, Mn, Mg, Pb, Sr, Ba and Sc are all uniform in concentrations across the spherulite-matrix contact.

Overall, three groups of elements are recognized, following Gardner et al. (2012). One group seem to follow "Type 1" behavior, in which concentrations are constant in the glass up to the spherulite rim. At the spherulite-matrix boundary there is a step-wise change in concentration, with elements being depleted inside the spherulite. Such profiles reflect elements that rapidly diffuse away from the boundary after being expelled from the growing spherulite (Gardner et al. 2012). Elements with Type 1 profiles diffuse rapidly enough that enrichments are not preserved at the spherulite boundary. The other group follow "Type 2" behavior, which is similar to Type 1 profiles in that they are depleted inside the spherulite relative to far field background concentrations. But Type 2 profiles are enriched in the matrix glass outside the spherulite rim. Such enrichments are consistent with diffusive behavior, indicating that spherulite growth and elemental diffusion occurred on similar time- and length-scales (Gardner et al. 2012). Another group of incompatible elements follow “Type 3” behavior, in which profile concentrations are unchanged across the spherulite-glass transition. Type 3 profiles form for elements that diffuse too slowly to be fractionated by spherulite growth (Gardner et al. 2012).

Li and K concentrations form Type 1 profiles (Fig. 5). Li is strongly depleted inside the spherulites relative to the steady glass concentrations (~10 ppm and ~60 ppm, respectively). Importantly, Li is the fastest diffusing element among those analyzed (Jambon and Semet 1978). K is also depleted inside the spherulites, and occurs in constant concentrations throughout the exterior. K concentrations inside the spherulites are ~ 50,000 ppm, whereas they are 80,000 ppm in the matrix glass.

B, Cs, Mn, Mg, Pb, Ba, Sr, and Sc occur in Type 3 profiles marked by constant concentrations, with no differences between the inside and outside of the spherulite (Fig. 5). Ba, Sr, and Pb could have been compatible given the spherulite mineralogy, whereas B, Cs, Mn, and Mg were likely incompatible. Despite the range in compatibility, none of the elements were expelled from the spherulite during growth. The diffusivity of B, Cs, Mn, Mg, Pb, Ba, Sr, and Sc are all orders of magnitude slower than the diffusivities of Li and K (Zhang et al. 2010).

Rb behaves as a Type 2 element (Fig. 6). Rb is incompatible in quartz and sanidine, thus it is excluded from the spherulite during growth. Indeed, background Rb concentrations far from the spherulites are ~200 ppm, whereas they are 60 to 120 ppm within the spherulite. Enriched concentrations of Rb are observed outside each spherulite analyzed. The Rb profiles have a simple concave form, in which the slope continually increases with proximity to the rim. Peak concentrations at the spherulite rim range from 549 to 851 ppm, and those enrichments extend 100 to 200 μm away from the rim into the matrix.

H_2O concentrations also form Type 2 profiles (Fig. 6). Although H_2O was not measured within the spherulites, it is expected to be depleted in the spherulites because they are composed exclusively of anhydrous phases (e.g., Castro et al. 2008; Watkins et al. 2009). H_2O concentrations in the glass far from the spherulites are ~0.1 wt.%. Approaching the spherulite rim, H_2O concentrations increase from background values to concentrations as great as 0.4 wt.%. Concentrations statistically above background extend 340 to 1500 μm from the spherulite rim. H_2O abruptly increases in concentration within 50-100 μm of the rim in many samples (Fig. 6).

Watkins et al. (2009) attributed similar steep enrichments at spherulite rims to hydration processes unrelated to spherulite growth. To test for late-stage hydration, we analyzed H_2O speciation along traverses in the enrichment profiles and background matrix far from spherulites (Fig. 7). In the background and gradually sloping concentration profiles, the majority of the H_2O occurs as hydroxyl (OH^-), as would be expected for H_2O speciation at high temperatures (Newman et al. 1986). In the steep portions, near the spherulite rims, the majority of the H_2O occurs as molecular water (H_2O_m). Analytical traverses that cross cracks in the glass are also marked by steep concentration gradients that range up to 0.40 wt.% H_2O, and are largely comprised of H_2O_m (Figure 7b). In addition, the steep enrichments extend ~50 μm from both spherulite rims and cracks in the matrix glass. Together, the speciation and enrichment distances suggest that the sharp increases result from late stage hydration, and are thus not included in our investigation. If the abrupt increase is not included, H_2O concentrations at the rim range from 0.12 to 0.18 wt.%.

Differential scanning calorimetry

For a heating rate of 25 °C min^{-1} during the first heating treatment, the peak glass transition temperature is 736±1 °C, and for a cooling and heating rate of 10 °C min^{-1}, 733 ±1 °C (Fig. 8a). Those temperatures are significantly higher than estimates of 600-670 °C calculated or measured for a rhyolitic melt (Hess and Dingwell, 1996; Dingwell 1998; Giordano et al. 2008). The TNM modeling approach produced a cooling rate estimate for the Yell-24 obsidian sample of $10^{-5.3}$ °C s^{-1} with an uncertainty of +0.2 log units and -0.5 log unit, equivalent to 0.47±0.30 °C d^{-1}(Fig. 8b). The high overshoot observed in the C_p curve is characteristic of slowly cooled glasses. The fit of the model curve to the natural C_p curve is very good. The four parameter values used to model the natural C_p curve are $\Delta H = 2.91e\text{-}05$ J mol^{-1}, $A = 6.4e\text{-}14$ s, $x = 0.91$ and $\beta = 0.71$. The calibration C_p curves were very noisy, which rendered the determination of peak and supercooled liquid temperatures rather difficult, but we were consistent in selecting the temperatures and are confident that they are realistic.

DISCUSSION

Enthalpy-relaxation geospeedometry indicates that the lava cooled at a rate of $10^{-5.3}$ °C s^{-1} (0.47±0.30 °C d^{-1}) across the glass transition interval where the sample was collected. Although only representative of the cooling rate across the glass transition interval the value should closely approximate the slope of the thermal history of a conductively cooled lava over the majority of its cooling (Manley 1992). To test if the DSC cooling rate offers a valid estimation, we assume overall spherulite growth is similar and consistent with spherulite growth described and modeled in Gardner et al. (2012). When compared with those results, the form of our compositional gradients indicate spherulite growth occurred as the lava cooled at $10^{-4.5}$ to $10^{-5.5}$ °C s^{-1} (0.3 to 3 to °C d^{-1}), which agrees well with the cooling rate estimate from DSC.

It appears that 10^{-5} °C s^{-1} is a reasonable approximation for cooling rate, and thus we assume that value to evaluate spherulite growth. To fully evaluate growth we must first determine the temperature window of spherulite growth and define the style of radial growth. After those factors are established, specific growth rates and nucleation temperatures for spherulites of different size can be determined. To constrain each of those aspects we compare the forms of the observed element gradients to predictions from numerical advection-diffusion models of spherulite growth (Supplemental Information).

First, we address the temperature range over which spherulites grow. To find the upper and lower temperature limits of spherulite growth we compare the presence (or lack thereof) of gradients for elements of diverse diffusivity. The upper temperature limit for spherulite growth is constrained by Type 3 gradients, because elements that form those gradients diffuse too slowly to be fractionated by spherulite growth. Instead they remain trapped within the spherulite. If growth were to occur at higher temperatures then diffusivity would increase, allowing that element to form a Type 2 gradient. In a similar fashion, rapidly diffusing elements with Type 1 gradients define the lower limit of spherulite growth. If growth occurred at progressively lower temperatures then element diffusivity would decrease, causing that element to form a Type 2 gradient.

The elements forming Type 1, Type 2, and Type 3 gradients establish the temperature range of spherulite growth. For example, Mn forms Type 3 gradients, which indicates Mn diffusivity was so slow during spherulite growth that Mn was effectively immobile. Mn has the highest diffusivity of all the elements that form Type 3 gradients, thus Mn establishes the upper bound on spherulite growth. By iteratively running the model, we predict Mn should form Type 3 gradients only if spherulite growth occurred at temperatures less than 730 °C. Similarly, other elements that form Type 3 gradients such as B, Cs, Pb, etc. indicate spherulite growth did not occur at temperatures greater than ~730 °C. Rapidly diffusing Li is predicted to form Type 1 gradients only when spherulite growth occurs at temperatures greater than 300 °C. Li would be expected to generate Type 2 profiles if the spherulites grew below 300 °C, temperatures where Li diffusion is sufficiently slow for profiles to be preserved. Rb concentration gradients show no evidence for post-growth diffusion indicating spherulite growth must have continued until 400 °C, cold enough for Rb diffusion to become sluggish (e.g., Watkins et al. 2009). When considered together, those diffusion profiles indicate spherulites began to grow at temperatures below 750 °C and ceased growing near 400 °C (Fig. 9). Interestingly, this suggests spherulite growth began when the melt was near the glass transition temperature, which is estimated to be 600 to 720 °C (Hess and Dingwell, 1996; Dingwell 1998; Giordano et al. 2008). T_g peak was experimentally determined to be 733±1 °C for a cooling/heating rate of 10 °C min^{-1}, which means that T_g peak was most likely even lower for a much slower cooling rate of ~10^{-5} °C s^{-1}.

Now that we have constrained the temperature of spherulite growth, we use the relationship between spherulite size and the form of the Type 2 gradients (Rb and H_2O) to establish growth style. To quantify the form of each profile we describe their shape using three parameters: enrichment, *e*-fold distance, and propagation distance (Table 1). Enrichment (ε) is defined as the ratio of concentration of an element in the glass at the spherulite rim relative to its concentration far from the spherulite. Spherulite growth rates strongly control ε with faster growth leading to greater ε. Uncertainty estimates for ε are calculated using the standard deviation of the concentrations within 20 μm of the spherulite rim and matrix concentrations far from the spherulite. The *e*-fold distance (e_Δ) parameter is sensitive to element diffusivity and time. It is defined as the distance from the spherulite boundary where the concentration has decreased from its peak value by a factor of *e* (e.g., ε/e). Propagation distance (P_Δ) is defined as the distance between the spherulite rim and the position where the elemental concentration is more than 2 standard deviations above concentrations in the glass matrix far from the spherulite boundary. It thus measures how far a gradient extends away from the spherulite, which is controlled by a combination of diffusivity, thermal history, and spherulite growth rate. Slower cooling, growth at higher temperatures, and/or faster growth can all cause P_Δ to extend.

We compare the behavior of ε, e_Δ, and P_Δ to spherulite size to better understand how the form of the concentration gradients relate to spherulite growth and the thermal history of the host lava. We find that larger spherulites have greater ε for both Rb and

H_2O, and P_Δ also increases with spherulite radius (Fig. 10). No correlation exists between e_Δ and spherulite size. Instead, e_Δ values for Rb and H_2O vary about a constant value, with e_Δ values for H_2O being approximately one order of magnitude greater than Rb (Fig. 11).

We compare the form of the Rb and H_2O profiles with model results using constant, linearly decreasing, and exponentially decreasing radial growth styles. Such model results help distinguish how natural spherulites grow in cooling rhyolitic lavas (Gardner et al. 2012). Spherulites did not grow by constant radial growth because that growth style always generates profiles with ε much greater than those observed. Linearly decreasing and exponentially decreasing radial growth models generate positive correlations between ε, P_Δ, and spherulite size for both Rb and H_2O, similar to observations (Fig.10). Linearly decreasing growth, however, always generates ε that are greater than those of the observed profiles for a given P_Δ or spherulite size. That divergence in ε indicates linearly decreasing growth rates do not capture the growth style, and instead are too fast during the latter stages of growth. We conclude that exponentially decreasing radial growth best explains the observed gradients. In addition, that growth style is consistent with observed crystal size distributions in spherulites, which decrease from core to rim (Lofgren, 1971a; Gardner et al. 2012).

By comparing model results to the analyzed e_Δ values, which are largely constant for both Rb and H_2O, we can constrain another aspect of spherulite growth. Diffusivity and time control e_Δ, with time being a function of the lava cooling rate and temperature window of spherulite growth. Thus, e_Δ can be used to solve for a unique solution for any one of those variables if the other two can be determined independently. If we use the lava cooling rate of $10^{-5.3}$ °C s^{-1}, established by enthalpy relaxation geospeedometry, the published diffusivities for Rb and H_2O and measured e_Δ values can only be matched by modeling when the temperature window of spherulite growth was 600 to 400 °C. That estimate falls within the aforementioned range determined using presence and absence of elemental profiles (<750 to 400 °C), yet is more precise. This technique may also be used in the future to solve for element diffusivity. Indeed, when we treated diffusivity as an unknown, we were able to closely predict previously published equations for the diffusivity for both Rb and H_2O.

To quantitatively constrain spherulite growth rates and nucleation temperature we iteratively modeled the behavior of Rb and H_2O during exponentially decreasing spherulite growth. In these models we consider lava cooling, growth rate, and nucleation temperature as unknowns, and allow them to vary from 10^{-3} to 10^{-7} °C s^{-1}, <0.1 to >100 µm hr^{-1}, and 800 to 400 °C, respectively. Growth rates were set to specific values at nucleation and allowed to decrease following exponentially decreasing radial growth from that temperature. The best fit to the Rb data indicates that spherulites grew at 1.2±0.6 µm hr^{-1} while the lava cooled at $10^{-5.1\pm0.2}$ °C s^{-1} (Fig. 11). The best fit to the H_2O data indicates that spherulites grew at 0.6±0.3 µm hr^{-1} while the lava cooled at $10^{-5.4\pm0.2}$ °C s^{-1}. The variation in of ε/d_Δ for both Rb and H_2O follow trends that are consistent with a 50-100 °C range in spherulite nucleation temperature, with larger spherulites nucleating from 600 to 650 °C and smaller spherulites nucleated at 550 to 600 °C.

To test the viability of the modeling of concentration gradients around spherulites, and to better understand lava cooling and crystallization kinetics, we compare our results with past experimental constraints on spherulite formation. Experimental studies by Fenn (1977) and Swanson (1977) examined how felsic minerals crystallize from melt in response to variable degrees of undercooling. Undercooling was found to exert a major control on crystal form and growth rate. At small undercoolings tabular forms crystallize preferentially. Increased undercooling caused crystals to become smaller, more closely packed, and skeletal to dendritic. Spherulites were the stable form in experiments that experienced the large undercoolings that ranged from of 100 to 400 °C. Experimental growth rates of quartz and alkali feldspar in rhyolitic melt at such degrees of undercooling were estimated to range from 0.1 to 4 μm hr^{-1}, which are largely consistent with our estimates (Swanson 1977). The liquidus temperature of the Pitchstone Plateau lava with 0.1 wt.% dissolved H_2O is estimated to have been ~1050 °C using Rhyolite-MELTS (Gualda et al. 2012). If true, then our estimated spherulite nucleation temperatures of 600 to 700 °C are equivalent to undercoolings up to 450 °C, values similar to those determined experimentally.

SUMMARY

The form of the measured concentration gradients indicate that spherulites grow according to a exponentially decreasing radial style over a temperature window from 700 °C to 400 °C. Larger spherulites nucleate at higher temperatures than smaller spherulites.

When compared to numerical modeling, the compositional profiles associated with the growth of spherulites suggest a time-integrated cooling rate of $10^{-5.2\pm0.3}$ °C s^{-1} (2σ) for the host lava. That estimate, based only on the temperature range and style of spherulite growth, precisely matches the cooling rate of $10^{-5.3}$ °C s^{-1} measured by enthalpy relaxation geospeedometry. Consequently, modeling the compositional gradients outside spherulites provides a new technique to explore both the cooling rates and crystallization of lava.

SUPPLEMENTAL INFORMATION: NUMERICAL MODEL

To model spherulite growth we assume spherulites grow by crystallization of rhyolitic melt or glass in response to undercooling (e.g. Keith and Padden 1963; Lofgren 1971a,1971b; Fenn, 1977; Swanson, 1977). We treat the spherulite as a homogenous, spherical phase. The host glass is assumed to be homogenous high-silica rhyolite. With each increment of growth spherulites expel incompatible elements to the external melt or glass (Keith and Padden 1964; Lofgren 1971b). Bulk fractionation factors used in the model are based on the analyzed element concentration differences between the spherulite interior and surrounding matrix (e.g., 50% and 70% for Rb and H_2O, respectively). Incompatible elements are concentrated in the surrounding matrix, and diffuse away from the spherulite-matrix boundary with time. Thus, the concentration of incompatible elements surrounding spherulites is controlled by spherulite growth rate and elemental diffusivity. To simulate this advection-diffusion process, we use finite-difference numerical modeling to solve the radial diffusion equation:

$$\left(\frac{\partial C}{\partial t}\right)_i = \frac{1}{r^2} * \frac{\partial}{\partial r} * (D_i * r^2 * \left(\frac{\partial C}{\partial r}\right)_i) \quad (1)$$

where $\left(\frac{\partial C}{\partial t}\right)_i$ is the concentration of the incompatible constituent *i* at time *t*, $\left(\frac{\partial C}{\partial r}\right)_i$ is the concentration of *i* at a radial distance from the spherulite boundary *r*, and D_i is diffusivity of *i*. D_i varies with temperature following

$$D_i = D_{O,i} exp\left(\frac{-E_{A,i}}{RT}\right) \quad (2)$$

where $D_{o,i}$ is a constant, $E_{A,i}$ is the activation energy, *R* is the gas constant, and *T* is temperature (°C). Values for $D_{o,i}$ and $E_{A,i}$ are from Ni and Zhang (2008) and Zhang et al. (2010). Advection is modeled by simulating the motion of the spherulite-matrix boundary with time, and is controlled by the radial growth rate of the spherulite. Following Gardner et al. (2012), we assume radial-controlled spherulite growth, where each increment of growth adds mass as a proportion of its radius. Our model can simulate a constant radial growth, or radial rates that linearly or exponentially with cooling, as follows

Constant $$\left(\frac{dR}{dt}\right) = \left(\frac{dR}{dt}\right)_O \quad (3)$$

Linearly decreasing $\left(\frac{dR}{dt}\right) = \left(\frac{dR}{dt}\right)_O - \left(\frac{dR}{dt}\right)_O * \frac{(T_f - T_o)}{(T - T_o)}$ (4)

Exponentially decreasing $\left(\frac{dR}{dt}\right) = \left(\frac{dR}{dt}\right)_O * exp\ (-a * (T - T_o))$

(5)

where $\left(\frac{dR}{dt}\right)$ is the radial growth rate at a specific timestep, $\left(\frac{dR}{dt}\right)_O$ is the initial radial growth rate, T is the temperature model at a specific time (°C), T_o is the initial temperature in the model (°C), T_f is the final temperature in the model (°C), and a is an exponential fit parameter.

Temperature exerts a fundamental control on constituent diffusivity and the growth laws in our model. During model simulations temperature decreases with time (t) from the eruption temperature (T_O) to a final temperature where spherulite growth ceases (T_f) following

$$T = T_O \exp\left(-(bt)^n\right) \tag{6}$$

where b and n are fit parameters. The numerical model is governed by two boundary conditions. First, mass conservation during diffusion and incremental growth is maintained through a Neumann condition (e.g., flux), which ensures that the diffusive fluxes on either side of each cell are the same (LeVeque, 2002). Second, the bulk element concentration is set to a fixed value far into the surrounding matrix.

Table 4.1

Spherulite sizes and parameters defining Type 2 Rb and H_2O gradients

		Rb						**H_2O**					
	Radius (µm)	Peak (ppm)	Background (ppm)	ε (%)	e_{Δ} (µm)	P_{Δ} (µm)	ε/P_{Δ} (%/µm)	Peak (ppm)	Background (ppm)	ε (%)	e_{Δ} (µm)	P_{Δ} (µm)	ε/P_{Δ} (%/µm)
Yell-24-1	2900	810	200	405(60)	125(30)	265(80)	1.53(0.51)	-	-	-	-	-	-
Yell-24-2	875	549	225	244(52)	175(100)	205(105)	1.19(0.66)	0.106	0.086	123(9.0)	960(260)	960(400)	0.13(0.07)
Yell-24-3	3200	907	207	439(69)	95(25)	206(66)	2.13(0.76)	-	-	-	-	-	-
Yell-24-4	995	574	204	281(67)	135(80)	206(100)	1.37(0.74)	-	-	-	-	-	-
Yell-24-5	1530	635	216	294(56)	130(70)	254(170)	1.16(0.80)	-	-	-	-	-	-
Yell-24-6	1265	782	253	309(70)	95(60)	161(80)	1.92(1.05)	-	-	-	-	-	-
Yell-24-7a	925	600	212	283(67)	122(80)	205(165)	1.38(1.16)	-	-	-	-	-	-
Yell-24-7b	925	585	210	279(82)	80(40)	108(95)	2.58(2.40)	-	-	-	-	-	-
Yell-24-8a	4400	781	207	377(52)	120(50)	218(60)	1.73(0.53)	0.169	0.092	183(8.5)	630(70)	1280(230)	0.14(0.03)
Yell-24-8b	-	-	-	-	-	-	-	0.166	0.092	180(3.3)	830(80)	1460(235)	0.12(0.02)
Yell-24-9	500	427	206	207(35)	85(60)	100(25)	2.07(0.62)	-	-	-	-	-	-
Yell-24-10a	2800	851	214	398(72)	60(40)	160(22)	2.49(0.56)	0.148	0.089	166(5.1)	830(120)	1500(330)	0.11(0.03)
Yell-24-10b	-	-	-	-	-	-	-	0.144	0.098	147(7.0)	780(100)	1190(210)	0.12(0.03)
Yell-24-10c	-	-	-	-	-	-	-	0.150	0.096	157(5.0)	745(80)	1245(225)	0.13(0.03)
Yell-24-11	650	452	208	217(9)	160(20)	250(20)	0.87(0.08)	-	-	-	-	-	-
Yell-24-12	500	616	203	303(35)	124(35)	248(48)	1.22(0.28)	-	-	-	-	-	-
Yell-24-13	2050	661	207	319(15)	118(15)	280(40)	1.14(0.17)	0.147	0.094	156(12.1)	705(75)	825(225)	0.16(0.08)
Yell-24-14	885	477	245	195(10)	100(40)	135(30)	1.44(0.33)	0.126	0.109	116(5.0)	940(130)	930(480)	0.12(0.07)
Yell-24-15	1685	712	216	330(27)	113(30)	210(22)	1.57(0.21)	0.149	0.098	152(4.4)	770(110)	1400(200)	0.11(0.02)
Yell-24-16	2000	796	209	381(35)	109(20)	223(43)	1.71(0.36)	0.149	0.114	131(5.3)	1140(320)	1215(400)	0.11(0.04)
Yell-24-17	1250	617	218	283(13)	120(30)	280(59)	1.01(0.22)	0.179	0.111	161(3.1)	400(85)	990(190)	0.16(0.03)
Yell-24-18	2500	689	214	322(27)	78(25)	180(70)	1.79(0.71)	0.149	0.101	148(4.7)	645(70)	1005(270)	0.15(0.04)
Yell-24-19	3000	826	216	382(35)	100(20)	230(64)	1.66(0.49)	-	-	-	-	-	-

Values in parentheses represent uncertainties. Dashed fields (-) indicate no data.

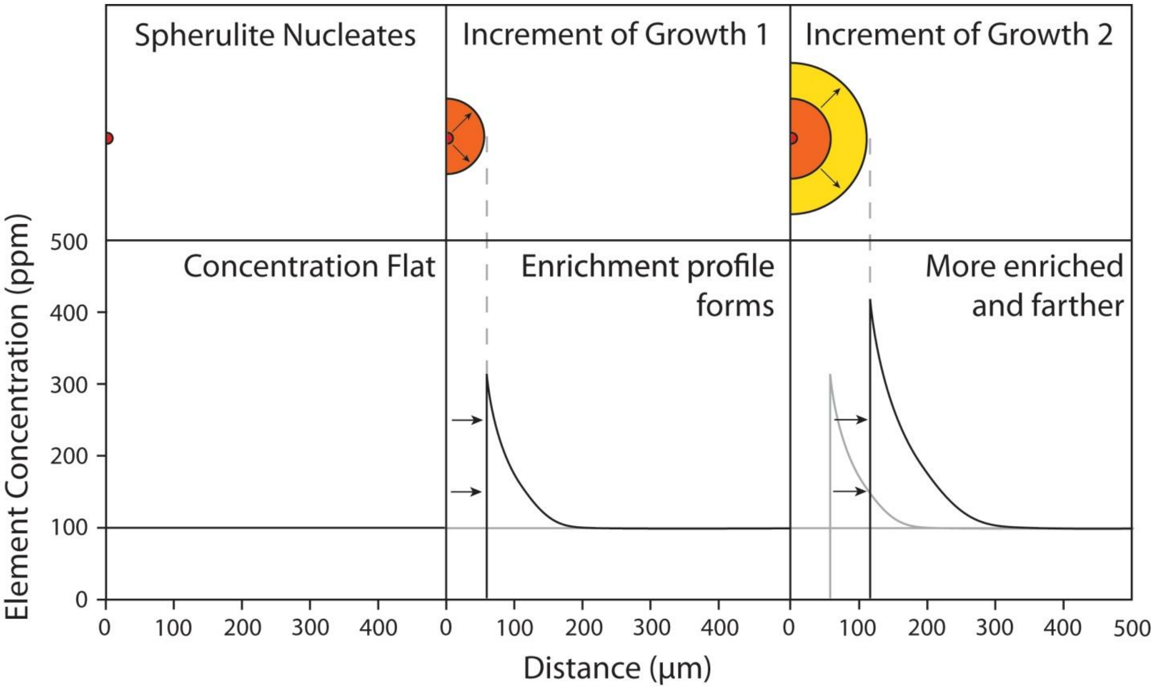

Fig. 4.1

Schematic diagram illustrating the process of spherulite growth (Top) and associated formation of enriched gradients surrounding spherulites (Bottom). Initially, the concentration of an incompatible element is homogenously distributed in the matrix glass at the point of spherulite nucleation. As the spherulite grows it expels the incompatible element. Diffusion acts to equilibrate the enrichment, thus generating an enrichment profile. Continued spherulite growth through time creates more enrichment along the spherulite boundary, and time allows the enrichment profile to extend farther into the glassy matrix via diffusion.

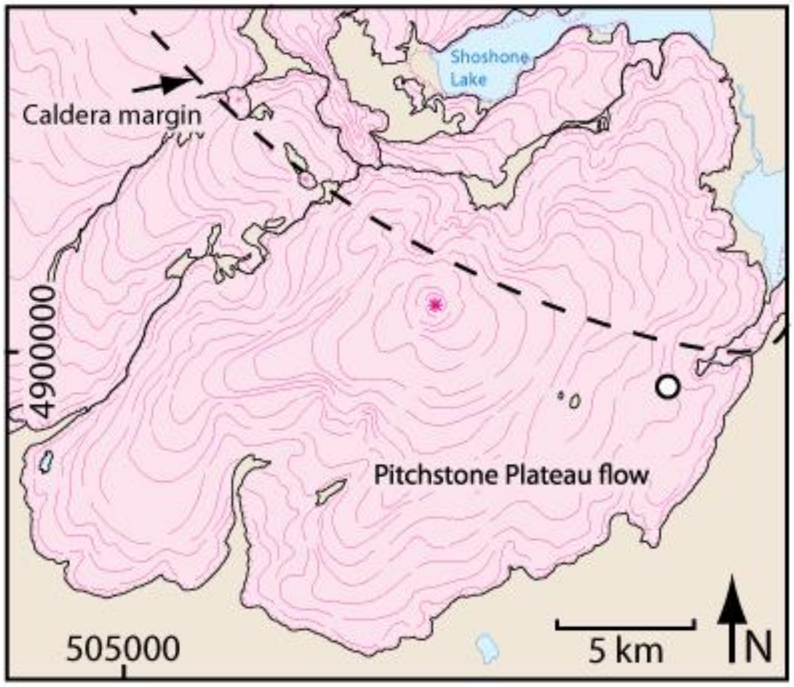

Fig. 4.2

Simplified geologic map of the southern portion of the Yellowstone volcanic field surrounding Pitchstone Plateau (modified from Christiansen 2001). The circle marks the sample location (Yell-24). Central Plateau Member Rhyolites are shown in light pink. Dark pink lines on individual flows demark lines of equal flow. The proposed vent location is shown by a small dark pink star. The margin of Yellowstone caldera is shown by a dashed black line.

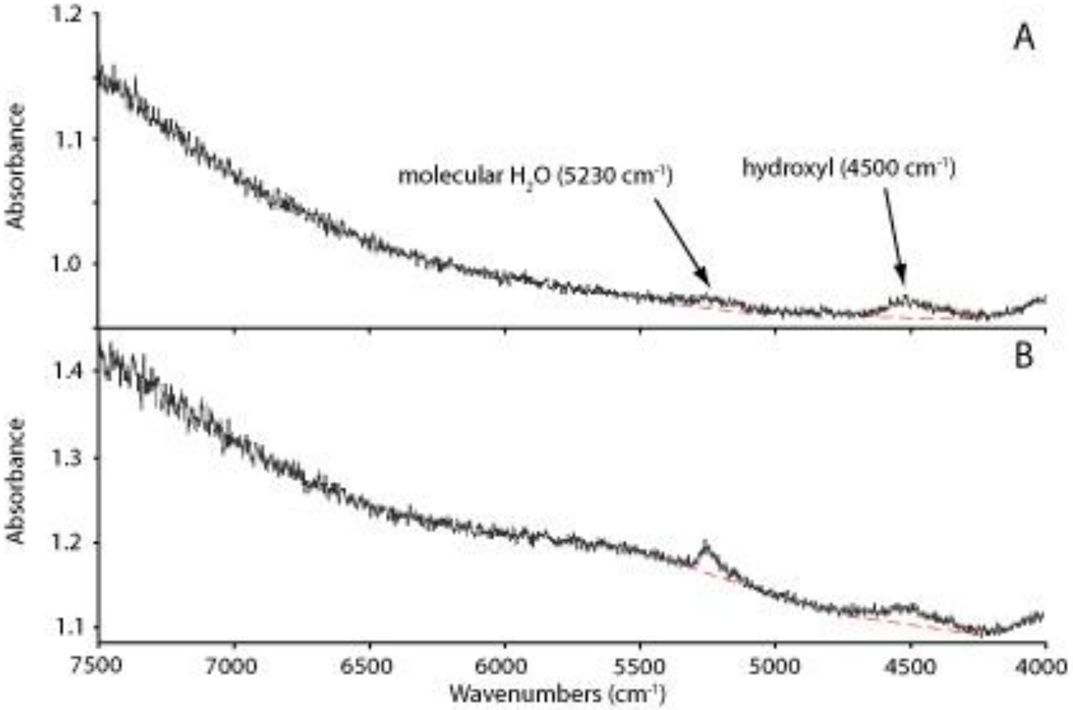

Fig. 4.3

Near-IR spectra for typical water concentrations **a** in background far from cracks and **b** within ~50 µm of cracks. Measured peaks are labeled. Linear background subtraction method is illustrated by the red dashed line.

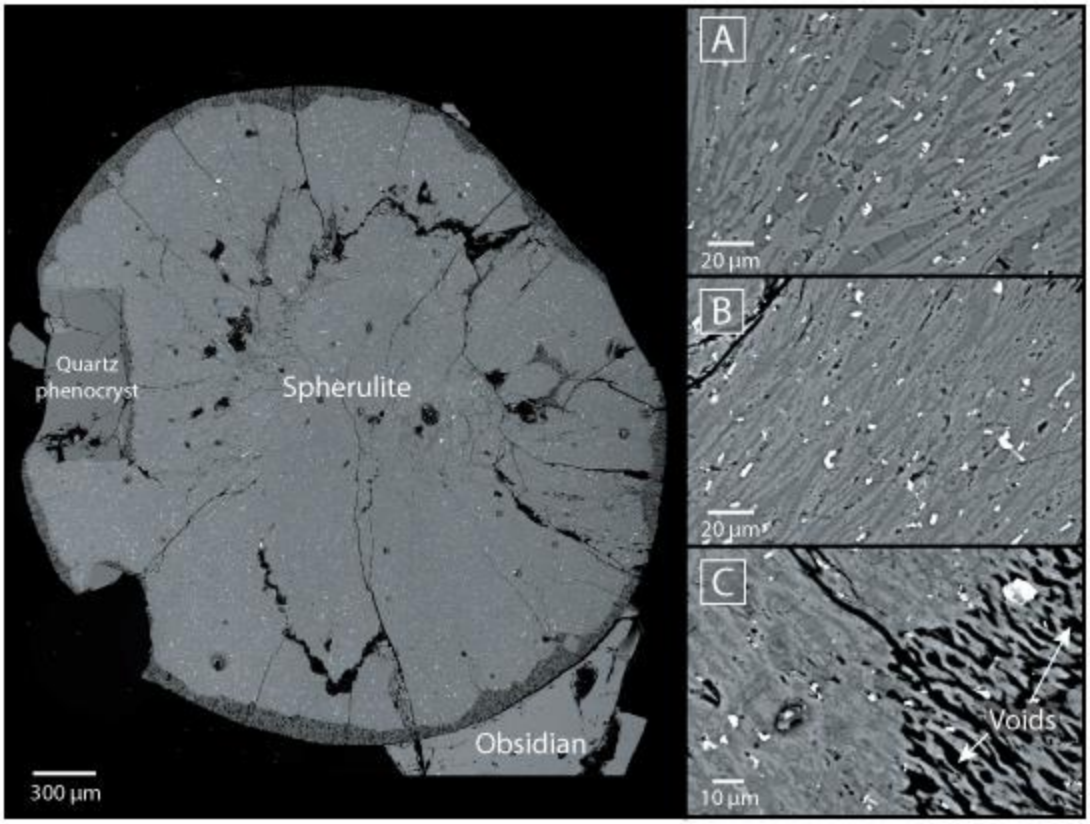

Fig. 4.4

Backscattered image of a central section through a spherulite. In the images quartz and sanidine crystals are dark and light gray, respectively. Oxides are white. Black areas are polishing imperfections and void space (vesicles). **a** Coarse radiating crystalline texture from near the core of the spherulite. **b** Fine-grained radiating texture from the spherulite rim. **c** Extreme close up of the textural transition from dense crystalline portions near the rim to the spongy rim comprised solely of sanidine and void space.

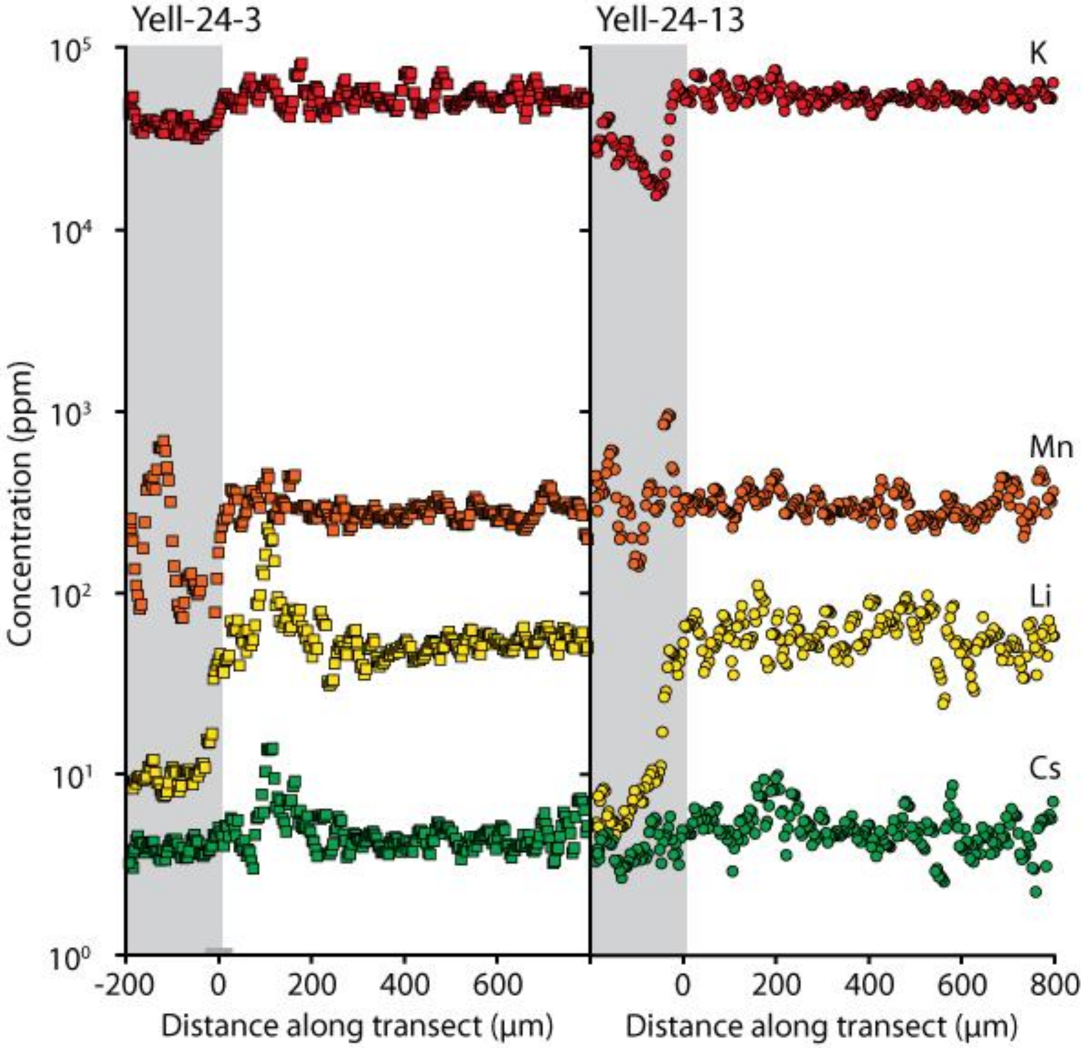

Fig. 4.5

Examples of Type 1 (K and Li) and Type 3 (Mn and Cs) profiles. The spherulite-matrix boundary occurs at 0 µm, with the spherulite portion shaded gray. Squares and circles represent concentrations for Yell-24-3 (3200 µm diameter) and Yell-24-13 (2050 µm diameter) spherulites, respectively. K concentrations are shown in red, Mn in orange, Li in yellow, and Cs in green.

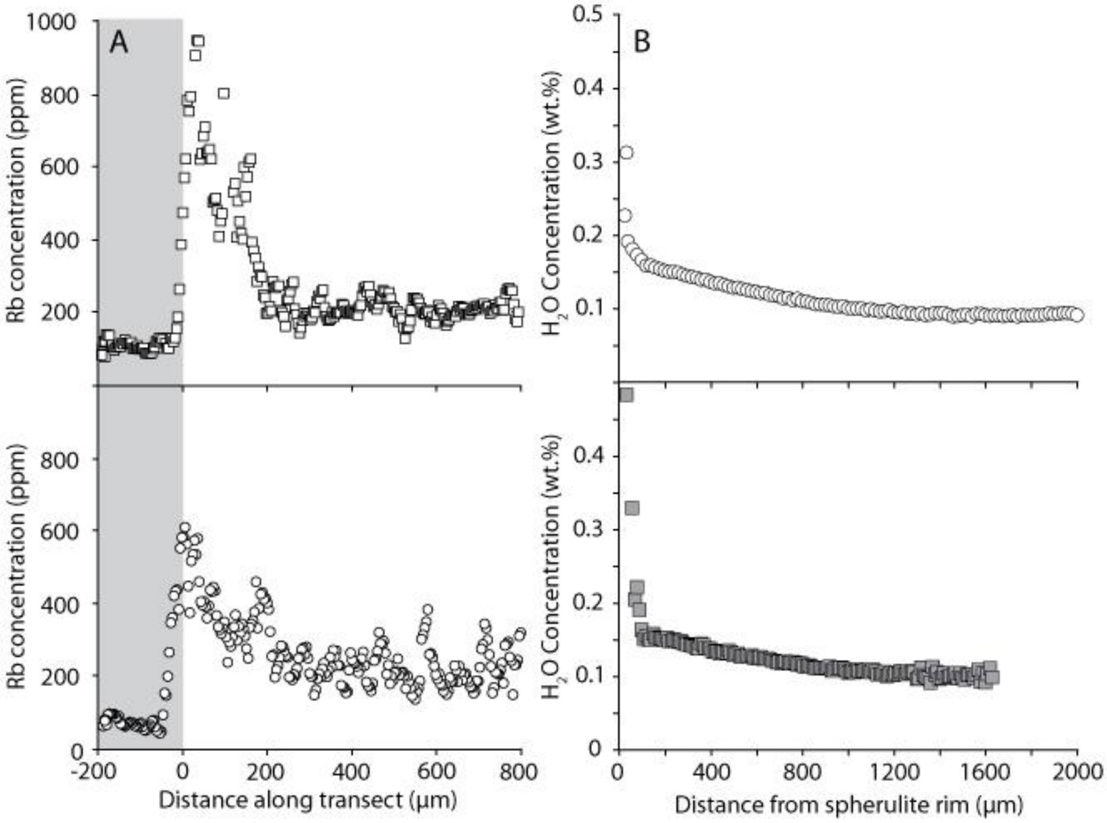

Fig. 4.6

a Rb concentration profiles for Yell-24-3 (3200 μm diameter) and Yell-24-13 (2050 μm diameter) spherulites marked by squares and circles, respectively. The spherulite-matrix boundary occurs at 0 μm, with the spherulite portion shaded gray. **b** H_2O concentration profiles Yell-24-8a (4400 μm diameter) and Yell-24-13 (2050 μm diameter) spherulites marked by white circles and gray squares, respectively. H_2O profiles display a long, gradual profile with a steep increase in concentration near the spherulite-matrix boundary.

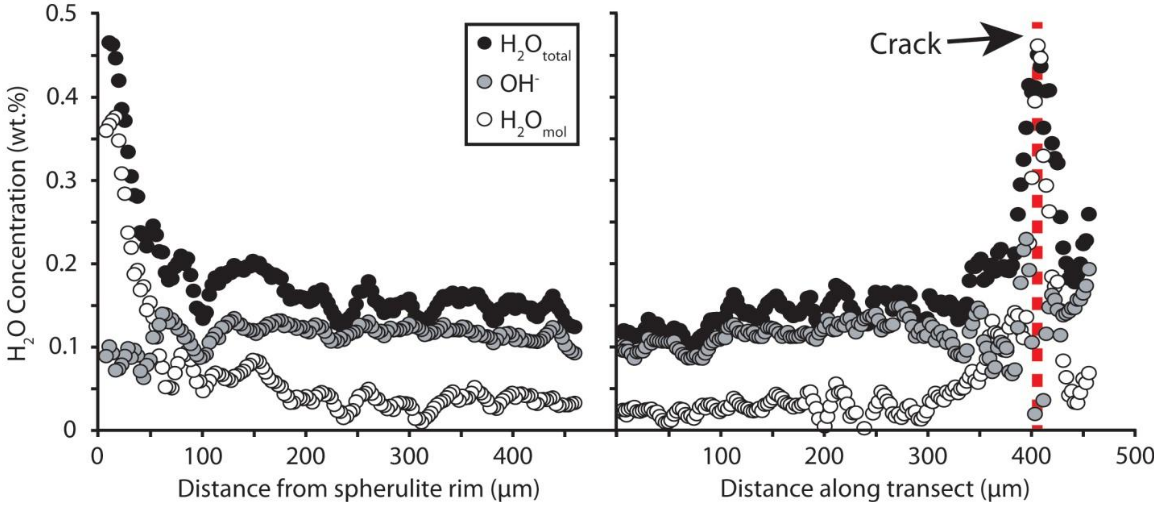

Fig. 4.7

The speciation of H_2O changes from dominantly hydroxyl (OH^-) in the shallowly sloped portion of the profile to largely H_2O_{mol} in the steep uptick near the rim. The same behavior occurs along transects at cracks (red dashed line), which indicates the steep concentration gradient is an artifact of low temperature hydration unrelated to primary spherulite growth.

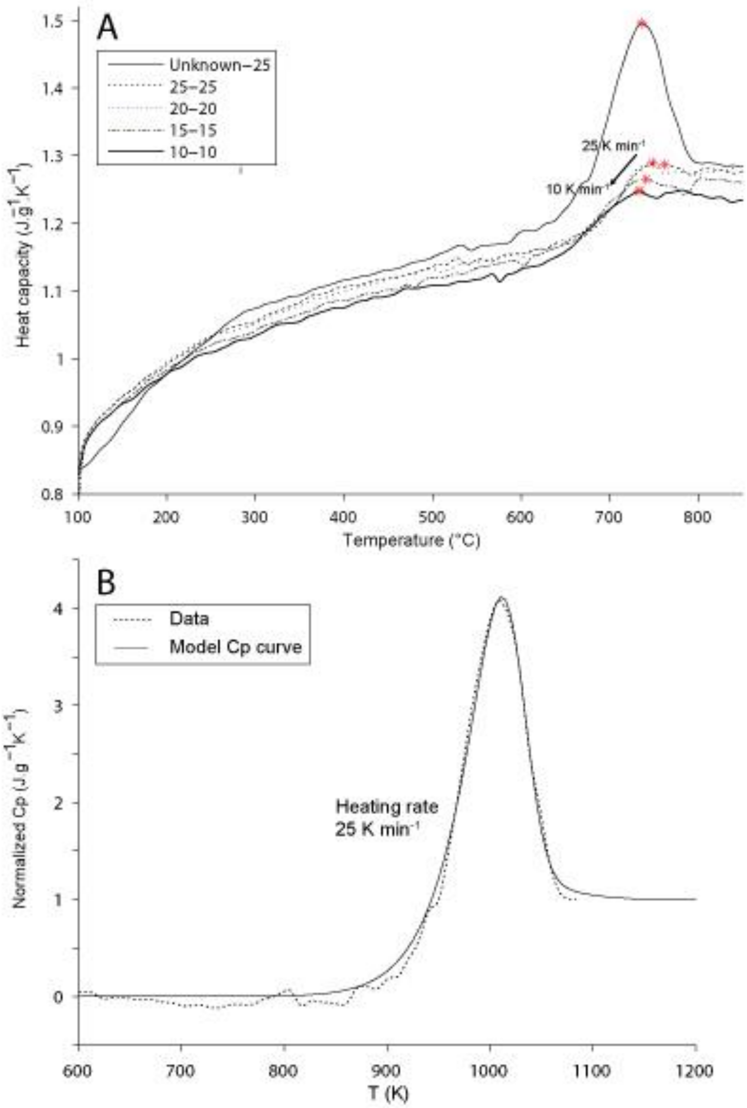

Fig. 4.8

Results from enthalpy-relaxation geospeedometry (A) Smoothed heat capacity (Cp) curves obtained from differential scanning calorimetry of obsidian sample Yell-24. The Cp curve with the high overshoot is the natural curve produced by the first reheating of the sample at 25 K min^{-1}. The previous cooling rate is thus unknown. The following cooling/heating treatments were performed with 25, 20, 15 and 10 K min^{-1}. Stars mark the peak glass transition temperatures (Tg peak) for each Cp curve. The arrow shows the decrease in Tg peak with cooling/heating rate. (B) Best fit to the normalized natural Cp curve. The natural cooling rate estimate is $10^{-5.3}$ °C s^{-1}.

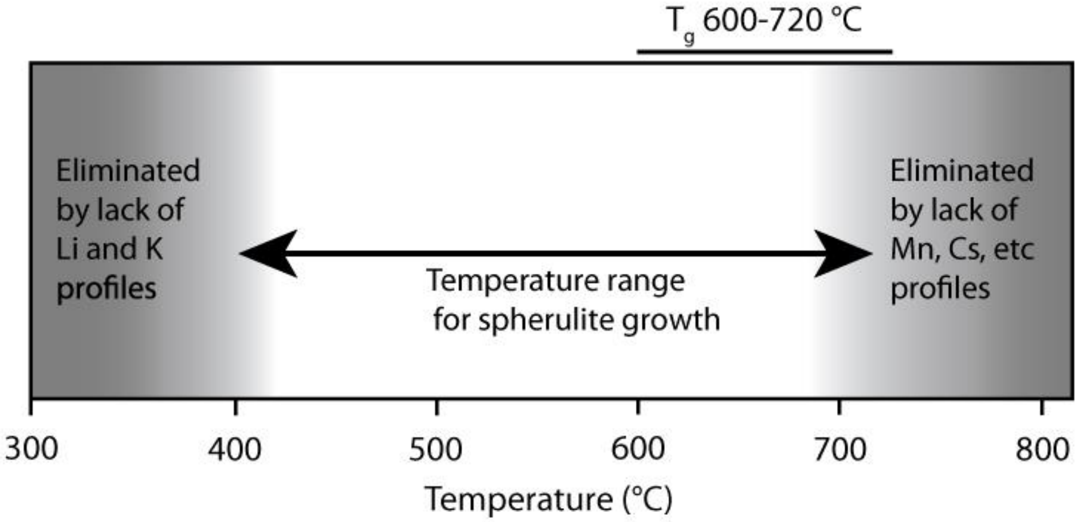

Fig. 4.9

Temperature window for spherulite growth as constrained by the presence and absence of enrichment profiles.

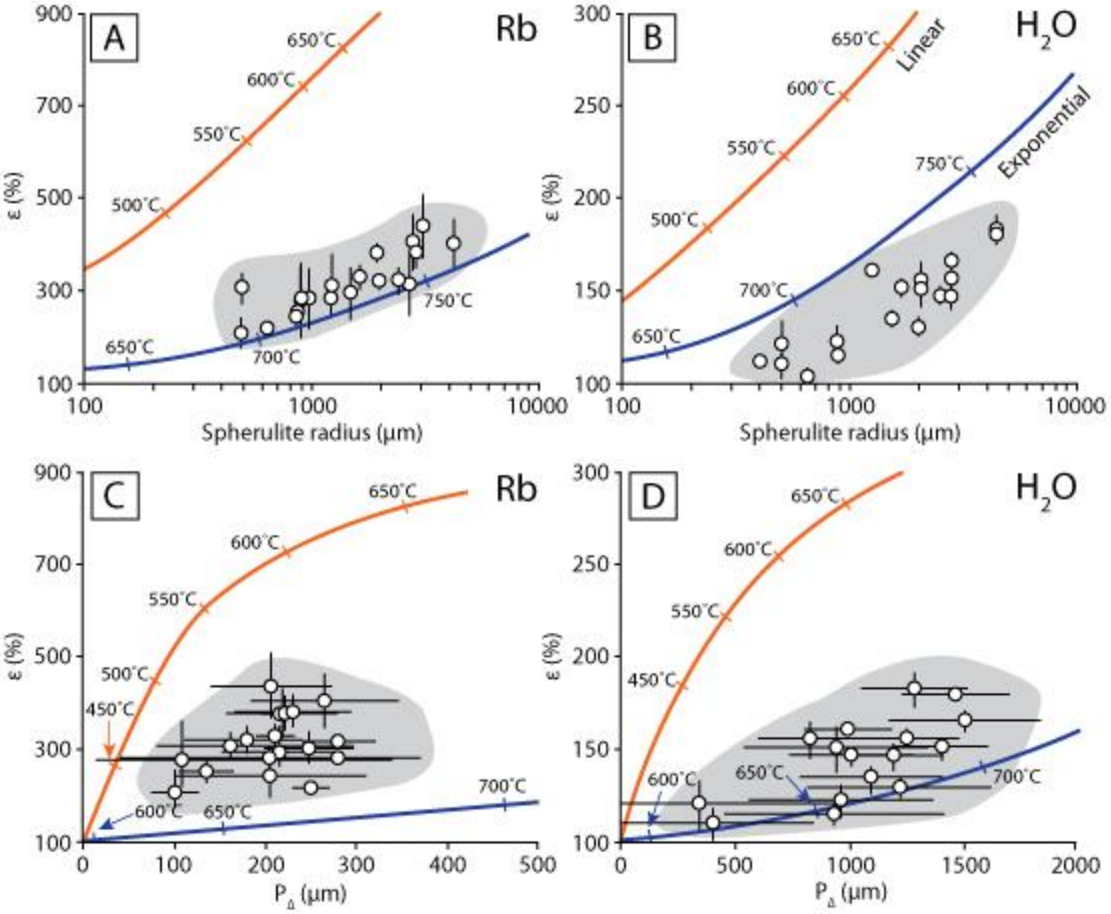

Fig. 4.10

Model variations of ε as a function of spherulite radius (A, B) and P_Δ (C, D) for linearly decreasing (Orange) and exponentially decreasing (Blue) radial growth. Results for Rb are shown in A and C. Results for H_2O are shown in B and D. The model results were generated assuming a cooling rate of 10^{-5} °C s^{-1} and a growth rate of 1 μm $hour^{-1}$ at 700 °C, which was then allowed to vary proportionally as a function of the chosen growth law and nucleation temperature (tick marks). Data are shown as white circles; black lines represent error bars unless smaller than symbol size. The range of ε and P_Δ of profiles around spherulites follow trends with positive slopes.

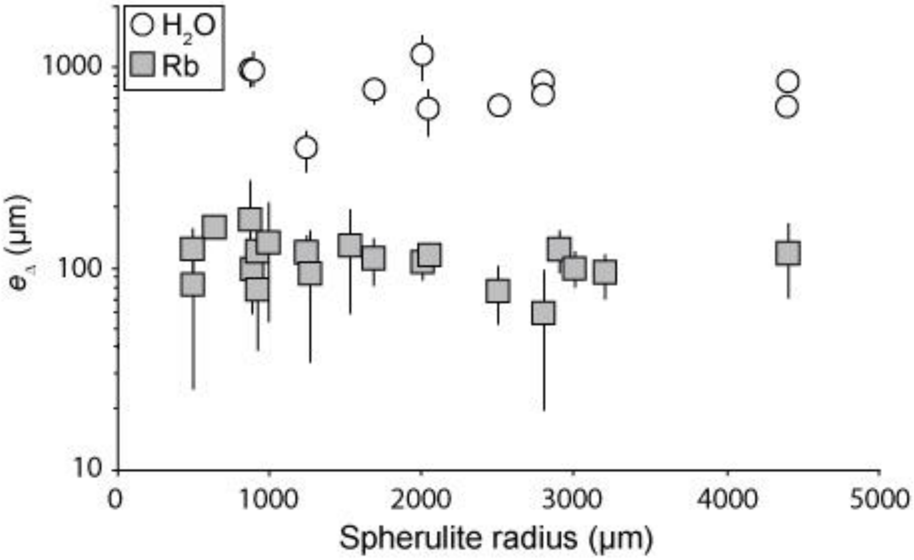

Fig. 4.11

Correlation between e_Δ and spherulite size for Rb and H_2O. Black bars represent measurement uncertainty.

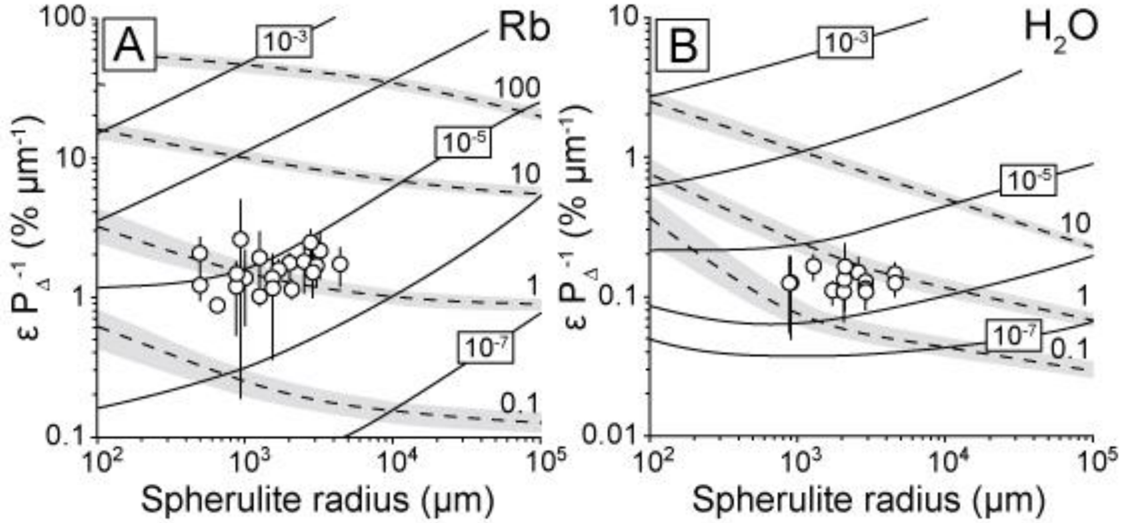

Fig. 4.12

The ratio of ε to P_Δ as a function of final spherulite size during exponentially decreasing growth for (A) Rb and (B) H_2O. Solid black lines show lava cooling rates in °C s^{-1}. Dashed black lines with gray fields are for spherulite growth rates in μm hour^{-1}. The gray fields represent model uncertainty. Data are shown as white circles with the black bars representing uncertainty, unless smaller than symbol size. Model results were generated assuming $T_{nucleation}$ of 600 °C at the specified growth and cooling rates.

CHAPTER 5:

ANALYZING WATER CONTENTS IN UNEXPOSED GLASS INCLUSIONS IN QUARTZ CRYSTALS

ABSTRACT

Fourier-Transform Infrared (FTIR) spectroscopy is commonly used to measure volatile contents dissolved in glass inclusions in minerals. The standard method is to doubly polish the crystal to fully expose the inclusion to allow infrared light to pass through the inclusion only. Glass inclusions are often a few tens of microns thick, which can limit the usefulness of FTIR because of how fragile samples become when thinned enough to doubly expose inclusions. Here, we test whether unexposed inclusions can be feasibly analyzed by measuring the dissolved volatile contents of a population of rehomogenized quartz-hosted glass inclusions at variable exposure levels. We analyzed 118 unexposed inclusions in 46 crystals. Of those, we analyzed the 74 inclusions in 38 crystals that survived being singly exposed. Of those, only 24 inclusions in 18 crystals remained to be analyzed when doubly exposed. Measuring the path length of light through the inclusion is critical to FTIR analyses. That length can be measured directly for doubly exposed inclusions. For those inclusions we find that water contents vary from 1.6 to 2.6 wt.%, averaging 2.2±0.3 wt.%. Path length is difficult to measure, however, in singly exposed or unexposed inclusions. Indeed, we find that path length is variably underestimated when measured using a well-calibrated optical method. Despite that difficulty, the

average water contents for the populations at each exposure level are statistically the same. But, on an inclusion-by-inclusion basis volatile contents at various exposure levels are highly discrepant because the typically underestimated thicknesses for non-doubly exposed inclusions result in anomalously high volatile contents. One way to measure path length in those inclusions is to reorient the host crystal in order to align the path length horizontally so it can be measured with the eyepiece reticle. Often, however, that technique proves impractical because small samples are difficult to handle. When path length cannot be measured directly, we find that using the average of the dimensions of the inclusion orthogonal to the path length can be used as a proxy for path length. That proxy allows volatile contents in unexposed inclusions to be analyzed accurately, which significantly reduces difficulties of sample preparation and can dramatically increase the number of potential target inclusions.

INTRODUCTION

Water dissolved in silicate melts has profound impacts on their crystallization, rheology and eruption (e.g., Ghiorso and Sack, 1995; Hammer and Rutherford, 2002; Giordano et al., 2008). Determining the amounts of water in silicate melts is thus paramount to both petrologists and volcanologists, but can be difficult because water can be lost during volcanic eruptions and magmatic crystallization. Dissolved water contents can be preserved in aliquots of melt trapped inside phenocrysts, which are quenched to glass during eruption. Many techniques have been developed to measure water contents in those glasses with one of the more accessible being Fourier-Transform Infrared (FTIR) spectroscopy, which measures the absorption of infrared light by water dissolved in glass (Ihinger et al., 1994; Devine et al., 1995; Lowenstern, 1995). FTIR is especially valuable because it allows different species of dissolved water (hydroxyl and molecular H_2O) to be measured simultaneously.

Despite the importance and relative ease of FTIR measurements, the technique is hindered by sample preparation (Devine et al., 1995). Because infrared light is transmitted through the inclusion, it can be absorbed not only by the inclusion but by everything else in its path. Crystals containing inclusions are thus usually doubly polished to expose the inclusion on both sides, so that light passes through only the inclusion. But, because inclusions are typically only 10's to 100's of microns in size, double exposure often results in very fragile samples that can easily disintegrate during polishing. Double exposure also often results in relatively thin samples whose thickness can be difficult to measure. Exposing small inclusions is thus difficult and painstaking (Lowenstern, 1995; Nichols and Wysoczanski, 2007). In fact, the error in thickness is often the largest uncertainty in an FTIR measurement.

One way to avoid losing precious samples during preparation and to decrease the error associated with thin samples would be to avoid doubly polishing the crystal and leaving the inclusion whole. To do that one would have to be certain that the crystal does not absorb infrared light, or if it does, the amount of absorbance needs to be taken into account (Bell et al., 1995; Rossman, 2006; Koch-Müller and Rhede, 2010). The thickness of the inclusion would also need to be measured accurately and precisely despite not being exposed, which would exclude most typical measuring techniques that use pin micrometers. Other studies have used the horizontal dimensions of unexposed inclusions as a proxy for thickness, but none have explicitly shown that those dimensions offer a reliable estimate (e.g., Signorelli et al., 1999; Atlas et al., 2006; Wysoczanski and Tani, 2006). Thickness can also been estimated using the interference fringes of reflection spectroscopy (Nishikida et al., 1995; Tamic et al., 2001). That technique can only be applied to unexposed inclusions if the refractive index of the sample is known and the relative proportions of inclusion and host crystal can be estimated (Nichols and Wysoczanski, 2007).

Here, we measure the path length of light through unexposed inclusions using a well-calibrated optical technique to test the accuracy and precision of measuring water contents in unexposed inclusions. We find that water content in an unexposed inclusion tends to be inaccurate when path length is determined using the optical technique. Water content can be analyzed accurately, however, if the dimensions of the inclusion orthogonal to the light pathway are used as a proxy for inclusion thickness. By measuring infrared absorbance in both the near and mid infrared regions, we also examine the ability to measure dissolved carbon dioxide contents.

METHODS

Samples and homogenization

Quartz crystals were extracted from pumice collected from the Tuff of Bluff Point, a 173±4 ka pyroclastic deposit erupted from the Yellowstone volcanic field

(Christiansen et al., 2007). We crushed pumice clasts and hand-picked quartz that were ~2-3 mm in diameter, and contained one or more large polyhedral glass inclusions that were 40 to 300 μm in size. Most inclusions contained one vapor bubble and trace amounts of crystallites. The crystals were thus rehomogenized by loading them in a $Ag_{80}Pd_{20}$ capsule, which was placed inside a TZM pressure vessel at 850 °C and 150 MPa for 24 hours, following the methods of Skirius et al. (1990). Those conditions were sufficient to rehomogenize most inclusions to clear glass, free of gas bubbles and crystallites (Fig. 1a). Each crystal was closely examined while submerged in mineral oil to identify and track the glass inclusions it held, as well as carefully noting inclusions to avoid (e.g., those with reentrants or with cracks which may have leaked).

Analytical techniques

Each quartz crystal was mounted in epoxy and adhered to glass slides using crystal bond. The first step was to grind and polish two sides of the crystal, so that it would lie flat and allow light to pass through unhindered (Fig. 1b). Once removed from the glass slide, the crystal was cleaned with acetone and ethanol. Next, a FTIR spectrum was collected from each unexposed inclusion and its thickness was measured (see below). Crystals were then remounted on glass slides and ground and polished to expose each inclusion on one side (Fig. 1c). The samples were removed from the glass slides and cleaned. Spectra were then collected from the singly exposed inclusions and their thicknesses were measured. Next, the crystals were remounted and ground and polished to expose inclusions on their opposite side (Fig. 1d). After being removed and cleaned, spectra from the doubly exposed inclusions were collected and thicknesses were measured. Special care was made during polishing in order to maintain the original orientations of crystals throughout. Many crystals contained more than one target inclusion, which required each one being remounted and polished multiple times. Because of that repeated polishing, the crystals accumulated more strain than typical (Fig. 1e). Accordingly, many samples disintegrated. Thus, 118 unexposed inclusions were measured, which decreased to 74 after the first exposure, and to 24 after the second exposure (Supplemental table).

We measured both the vertical and horizontal dimensions of each inclusion at every exposure level. The vertical dimension is the path length of light through the inclusion, and is equivalent to inclusion thickness. The horizontal dimensions are measurements of the plane orthogonal to the light pathway (e.g., the X-Y plane in Fig. 1a). Horizontal dimensions of each inclusion were measured using the reticle in the binocular eyepiece of the microscope, which is precise to 1 μm using the 50x objective. Vertical thickness was measured optically using a petrographic microscope by focusing on the top and bottom of an inclusion, and recording the distance with a Heidenhain focus drive linear encoder. Because light refracts within a sample, the focus drive movement does not equal thickness, and thus must be calibrated using glasses of known thickness. Although the amount of refraction varies as a function of refractive index, we have found that little error results from using a single calibration for glasses as different in composition as basalt and rhyolite. In this study, all samples are rhyolite glasses in quartz, and so there should be little difference in refractive indexes. The error on such thickness measurements depends on the ability to focus at specific levels, play in the focus drive, and the power of the objective lens used. For our system, the optimal average error using a 50x objective lens is ±0.6 μm, determined by repeatedly focusing through a sample of known thickness. Using that technique, we measured the thickness of each inclusion multiple times, and report the average and its standard deviation. Vertical thickness of each doubly exposed inclusion was also measured using a pin micrometer. The pin micrometer is mechanically precise to ~1 μm, but accuracy is effectively limited to ±10 μm because it measures the average thickness over a large area of the sample.

For a subset of the unexposed population we measured the thickness optically with the eyepiece reticle (Fig 1b). To do that we attached the crystal to the tip of the rotatable needle using crystal bond. Next, we submerged the crystal in the tank of mineral oil and rotated the needle to align the X, Y, and Z axes of the inclusion perpendicular to the field of view. We calibrated this technique by measuring a glass of known thickness. Because of the size of the mineral oil tank we could only use the 20x objective, which limited our precision to ±5 μm.

Dissolved water and carbon dioxide contents were measured using a Thermo Electron Nicolet 6700 spectrometer and Continuμm IR microscope at the University of Texas at Austin. Each spectrum consisted of 60 scans collected at a resolution of 4 cm^{-1} and was collected either in mid-IR range using a KBr beamsplitter and globular IR source, or in near-IR range using a CaF_2 beamsplitter and white light. Total water concentrations were estimated using the absorbance at ~3500 cm^{-1} (H_2O_{3500}), which results from a combination of vibrations associated with the symmetric stretching and bending of O-H bonds dissolved in aluminosilicate glass and thus considered to equal total water contents (McMillan, 1994). Absorbances were also measured from molecular water (H_2O_m) and bound hydroxyl (OH), which occur at 5230 cm^{-1} and at 4500 cm^{-1} and are attributed to either stretching or bending of O-H bonds, respectively (Ihinger et al., 1994). Concentrations of dissolved molecular carbon dioxide (CO_2) were determined from absorbance at 2350 cm^{-1}. We assumed linear backgrounds for absorbances at 5230 cm^{-1}, 3500 cm^{-1}, and 2350 cm^{-1} (Fig. 2). Background for absorbance at 4500 cm^{-1} was estimated using a flexicurve, which was set tangential to the IR spectrum on either side of the peak. When a spectrum consisted of absorbance of IR light by glass and quartz, then its background was the subtraction of the absorbance of IR light by quartz only, measured immediately adjacent to the inclusion (Fig. 2).

The concentrations of dissolved H_2O_{3500} and CO_2 were calculated using a modified Beer-Lambert law,

$$C = \frac{A*MW}{\rho*d*\varepsilon}*f \qquad (1)$$

where C is concentration of the volatile species (wt.% for H_2O_{3500} and ppm for CO_2), A is absorbance, MW is the molecular weight of water or CO_2, ρ is the glass density (g L^{-1}), d is sample thickness (cm), ε is the molar absorptivity (L cm^{-1} mol^{-1}), and f is a dimensionless conversion factor (10^2 for H_2O_{3500} and 10^6 for CO_2)(Stolper, 1982). For ε_{2350} we used a value of 1214±16 L cm^{-1} mol^{-1} (Behrens et al., 2004). Glass density was assumed to be 2355 g L^{-1}, and was not adjusted for water content. Concentrations of H_2O_m and OH were calculated from absorbances using the model of Zhang et al. (1997). The sum of concentrations of the two water species is termed H_2O_{total}.

Published values for the molar absorptivity of the broad H_2O_{3500} peak at 3500 cm^{-1} in rhyolitic glasses vary, and average 78±2 L cm^{-1} mol^{-1} (Ihinger et al., 1994; Behrens and Schmidt, 1998; Okumura et al., 2003; Leschik et al., 2004). We also used the molar absorptivities of Newman et al. (1986) and Dobson et al. (1989) in conjunction with the proportions of the species absorptions at 5200 cm^{-1} and 4500 cm^{-1} to calculate a total molar absorptivity of 71±2 L cm^{-1} mol^{-1} for the broad 3500 cm^{-1} peak. H_2O_{3500} contents estimated using either molar absorptivity show similar ranges and variations as those from H_2O_{total}.

RESULTS

Quartz absorbs infrared light significantly only at wavenumbers less than ~2100 cm^{-1} (Fig. 2c). Water species and molecular CO_2 absorb infrared light at higher wavenumbers, where quartz does not interfere. Absorbances at lower wavenumbers would be nearly impossible to discern, making it impossible to measure, for example, dissolved carbonate species (Dixon et al., 1995). Hence, careful consideration must be given to the impact of the host crystal on infrared light before unexposed inclusions are measured.

Volatile contents

A total of 118 unexposed inclusions in 46 quartz crystals were analyzed (supplemental data table). Of those, 74 inclusions in 38 quartz crystals survived being exposed on one side. Of those 74, only 24 in 18 crystals survived the second polishing to be analyzed (Table 1). Despite the changing exposure level, the mean concentrations for H_2O_{total} and CO_2 in the three populations are statistically indistinguishable. Unexposed inclusions yield the largest range and standard deviation in H_2O_{total} concentrations (Fig. 3a). Singly exposed inclusions define a narrower range in concentration and have a smaller standard deviation than do unexposed inclusions. Doubly exposed inclusions yield a much narrower range in concentration and have the smallest standard deviation. CO_2 concentrations behave similarly to H_2O_{total} contents, with unexposed and singly exposed inclusions having similar standard deviations, but the singly exposed inclusions define a narrower range in concentrations (Fig. 3b). Doubly exposed inclusions have the narrowest range in CO_2 concentrations and smallest standard deviation.

Thickness measurements

We obtained accurate thickness measurements of doubly exposed inclusions using both the optical focusing drive method and the pin micrometer. The accuracy of thicknesses measured using the pin micrometer is limited to ±10 μm because the technique only is able to provide average thickness over a relatively large area of the sample. The optically determined thicknesses for the majority of the doubly exposed inclusions fall within the range of those measured by the pin micrometer. In the remaining few the disagreement between the two methods was less than 25%.

It was difficult to measure the thickness of unexposed and singly exposed inclusions using the optical focusing drive technique because of optical complications associated with refraction of light through glass and quartz, and the similar refractive indexes of quartz and rhyolite. To demonstrate that difficulty, we compared the thickness of inclusions, as measured while submerged in mineral oil using the needle and reticle, with the thickness as measured using the optical focusing drive method (Fig. 4a). Each of the 19 inclusions was measured by the three authors separately. Overall, we found 22% error in thickness, with greater deviations for larger inclusions. As a comparison, the difference between the thickness, as measured using the needle and reticle, and that estimated from the horizontal dimensions using the X-Y proxy is 19%, but linear regression through the data demonstrates that the X-Y proxy better approximates thickness (Fig. 4).

DISCUSSION

Overall, measurements of water and CO_2 content are on average the same regardless of exposure (Table 1). To a first order, the degree of exposure has only a limited effect on FTIR-derived volatile measurements. Although some of the variation within the data may reflect variable entrapment conditions, the superior precision of the doubly exposed population is attributed to more precise thickness measurements, rather than an artifact of the smaller sample size. If only an approximation of the mean water and CO_2 contents for a population of inclusions is desired, unexposed inclusions appear to be the easier targets.

When volatile contents in specific inclusions are compared, those in unexposed and singly exposed inclusions do not match those in the same inclusions when doubly exposed (Fig. 5). Those differences may be attributed to changes in absorbance caused by optical effects, such as scattering, or to errors in thickness measurements.

Inaccurate volatile measurements can be caused by scattering of the IR beam. Typically, researchers mitigate the impact of scattering by doubly polishing sample surfaces and by analyzing clear samples, without microlites, bubbles, or cracks (Devine et al., 1995). Our samples are clear and polished, but scattering of the IR beam could be caused by refraction at the phase boundaries of the unexposed and singly exposed inclusions. Refraction at planar phase boundaries is controlled by the angle of incidence and refractive indices of the phases. Refraction at horizontal planar phase boundaries is negligible and the difference between refractive indices of quartz and rhyolitic glass is <0.1 (George, 1924; Nesse, 1991). Curved boundaries could cause scattering because an unexposed inclusion should act as a diverging lens. In this case we would expect smaller unexposed inclusions to scatter the IR beam more because they have more curvature relative to the light path. Our data shows, however, that volatile contents of the smaller unexposed inclusions better match their doubly exposed counterparts than do the larger inclusions. For those reasons, we conclude scattering has a negligible impact on absorbance.

Instead of scattering, we attribute the inaccurate volatile contents for unexposed inclusions to result from inaccurate thickness measurements. Accurate thickness measurements are critical for FTIR measurements because inclusions are typically thin, and so small errors in thickness translate to large errors in volatile contents. Pin micrometers are commonly used to measure thickness of doubly exposed inclusions, but they measure an average thickness over a relatively large area of the sample and easily damage fragile samples. Obviously, pin micrometers cannot be used to measure the thickness of an unexposed or singly exposed inclusion. Thickness measurements of doubly exposed inclusions using the optical focusing drive method match those made with the pin micrometer, therefore validating the optical method for doubly exposed inclusions. There are two advantages to measuring thickness optically. First, thickness measurements are simply made by focusing on the top and bottom surfaces of the sample. Second, the specific location where an FTIR spectrum was collected can be measured, even when the target is embedded in a crystal.

When thicknesses of unexposed and singly exposed inclusions measured by the various techniques are compared, there is a clear tendency to underestimate thickness when using the optical focusing drive method (Fig. 4a). For inclusions thinner than 50-100 μm, the differences are typically less than 15%, but are still significant enough to cause calculated volatile concentrations to be erroneously high. The tendency to underestimate thickness is more pronounced for inclusions larger than 150 μm, with differences exceeding 25%. Accordingly, the discrepancy in volatile contents between levels of exposure can be explained solely by thickness differences. The flaw is not in the calibration, but instead in the subjectivity of using the optical focusing drive of the microscope to measure inclusion thickness, which depends on the ability of the user to identify the top and/or bottom of pristine, clear glass inclusions in clear minerals of similar refractive index.

In order to quantify volatile contents in an unexposed inclusion, it is obviously best to directly measure its thickness. We believe the best way to measure unexposed inclusion thickness is by correctly orienting the crystal in mineral oil while viewed under the microscope, as described earlier. That technique is often not practical because the small sizes of the crystals make samples prohibitively difficult to handle. Therefore, it becomes important to find an objective method for estimating thickness. One such method is to approximate thickness from the horizontal dimensions of the inclusion (Fig. 4b). Using our so-called X-Y proxy, where thickness is equated to the average of the horizontal dimensions, estimates of volatile contents are the same for unexposed and doubly exposed inclusions (Fig. 5e, f).

Our X-Y proxy method assumes an inclusion has a regular polyhedral shape. An analogous method has been used previously in which inclusions were assumed to be ellipsoids, and inclusion thickness was assumed equal the horizontal length of the ellipse (e.g., Signorelli et al., 1999; Atlas et al., 2006). The X-Y proxy is similar to that method for equant inclusions, but may differ substantially as inclusions become more elongate. We thus consider either method appropriate to estimate thickness in roughly equant inclusions, but prefer the X-Y proxy for elongate inclusions.

The reflection spectroscopy technique of Nichols and Wysoczanski (2007) also provides a thickness approximation for unexposed inclusions. The X-Y proxy depends solely on optical methods, and is not reliant on precisely estimating the proportions of host crystal and inclusion in the sample. Thus, it provides an alternate approach for determining thicknesses, which may be important if interference with the host crystal or dissolved volatiles are concerns.

The use of the X-Y proxy method eliminates the need for glass inclusions to be doubly exposed, making sample preparation less time-intensive and less destructive. Moreover, it allows the user to analyze more than one inclusion per crystal, some of which could be lost while doubly-exposing others. Inclusions at different positions within a crystal can thus be analyzed, which allows the record of progressively changing compositional contents within the magmatic system to be measured. One drawback, however, is that unexposed, water-rich inclusions may be too thick to measure using absorbance at 3500 cm^{-1} (Ihinger et al., 1994). Consequently, measuring water contents in unexposed inclusions may require using absorbances in only near-IR.

Table 5.1

	*n**	Mean H_2O**	Range	Mean CO_2**	Range
Unexposed	118	2.5±1.0	0.7 - 6.9	494±194	102 - 1131
Singly exposed	74	2.5±0.8	0.5 - 5.0	471±179	50 - 896
Doubly exposed	24	2.2±0.3	1.6 - 2.6	479±98	114 - 585

*number of inclusions

**errors are 1σ

The mean and range of H_2O_{total} (wt.%) and CO_2 (ppm) content in the unexposed, singly exposed, and doubly exposed inclusions.

Table 5.1 (cont.)

Supplemental Data. Volatile contents of all analyzed glass inclusions.

Sample	H_2O (wt.%)*	CO_2 (ppm)*	Thickness (µm)$^{*,\#}$	H_2O (wt.%)**	CO_2 (ppm)**	Thickness (µm)$^{**,\#}$	H_2O (wt.%)***	CO_2 (ppm)***	Thickness (µm)$^{***,\#}$
1a	1.7±0.1	489±90	81	2.2±0.2	644±83	45	-	-	-
2a	1.6±0.3	391±90	101	-	-	-	-	-	-
2aa	1.3±0.1	350±13	102	-	-	-	-	-	-
2b	3.2±0.2	514±55	65	-	-	-	-	-	-
2c	1.9±0.1	516±31	112	1.2±0.1	429±55	38	-	-	-
2d	-	-	-	2.0±0.2	459±69	58	-	-	-
2e	-	-	-	1.6±0.1	391±39	71	-	-	-
2f	-	-	-	-	203±42	22	-	-	-
3a	1.0±0.1	180±20	58	-	-	-	-	-	-
4a	-	-	-	1.9±0.1	368±20	94	-	-	-
4aa	-	-	-	2.1±0.2	430±60	58	-	-	-
4b	2.2±0.3	424±114	112	0.5±0.1	113±2	231	-	-	-
5a	3.6±0.6	745±206	25	-	-	-	-	-	-
5b	2.8±0.1	592±45	147	-	-	-	-	-	-
6a	1.6±0.1	407±32	109	-	-	-	-	-	-
6b	1.6±0.1	284±24	144						
6bb	1.8±0.1	295±17	96	-	-	-	-	-	-
6c	1.7±0.1	231±23	64	1.4±0.1	278±33	39	-	-	-
6d	-	-	-	2.1±0.2	323±67	108	-	-	-
7a	3.4±0.2	412±40	68	-	-	-	-	-	-
7b	3.6±0.4	547±106	55	-	-	-	-	-	-
7c	1.9±0.3	498±106	50	-	-	-	-	-	-
7d	3.6±0.2	444±57	57	-	-	-	-	-	-
7e	1.6±0.1	402±42	59	-	-	-	-	-	-
7f	-	-	-	1.8±0.1	385±29	105	-	-	-
8a	3.6±0.5	703±175	42	-	-	-	-	-	-
8aa	2.0±0.2	399±49	74	-	-	-	-	-	-
8b	2.9±0.2	513±81	69	1.9±0.2	163±28	35	-	-	-
8c	2.4±0.1	500±22	129	-	-	-	-	-	-
8cc	2.0±0.1	389±26	161	-	-	-	-	-	-
8d	2.7±0.3	543±116	117	-	-	-	-	-	-
8dd	2.6±0.2	475±44	111	-	-	-	-	-	-
8e	1.9±0.2	411±68	37	-	-	-	-	-	-
8ee	1.2±0.1	239±27	58	-	-	-	-	-	-
8f	0.8±0.1	156±11	82	-	-	-	-	-	-
9a	1.7±0.1	389±31	78	-	-	-	-	-	-
9aa	2.2±0.1	453±42	68	-	-	-	-	-	-
10a	2.9±0.2	186±20	110	2.4±0.3	50±10	32	-	-	-
10b	-	-	-	1.7±.1	145±12	145	1.8±0.1	114±11	115
10bb	-	-	-	2.1±0.1	129±7	104	-	-	-
11a	2.0±0.1	362±35	71	-	-	-	-	-	-

Table 5.1 (cont.)

11b	2.0±0.1	359±26	58	-	-	-	-	-	-
12a	1.6±0.1	392±59	81	2.3±0.2	561±89	56	2.1±0.1	536±43	99
12aa	-	-	-	2.0±0.1	537±49	62	-	-	-
12c	2.2±0.1	513±41	123	2.3±0.1	550±27	114	2.0±0.1	513±65	91
12cc	1.9±0.1	451±35	144	-	-	-	-	-	-
12d	2.2±0.1	502±41	98	2.2±0.1	526±36	90	2.3±0.1	549±26	114
12dd	1.8±0.1	453±25	117	-	-	-	-	-	-
12e	1.7±0.1	434±30	121	2.3±0.1	563±52	93	1.9±0.1	514±51	81
12f	0.8±0.1	238±68	77	-	-	-	-	-	-
13a	2.0±0.1	414±30	99	2.0±0.2	435±51	58	-	-	-
13aa	1.8±0.1	392±22	108	-	-	-	-	-	-
13b	2.0±0.1	476±55	54	-	-	-	-	-	-
13bb	1.6±0.1	377±45	68	-	-	-	-	-	-
13c	2.5±0.2	443±67	66	1.6±0.4	362±368	70	-	-	-
13cc	-	-	-	2.5±0.2	463±65	60	-	-	-
14a	1.1±0.1	248±12	209	-	-	-	-	-	-
14b	0.7±0.1	102±5	175	-	-	-	-	-	-
15a	1.8±0.1	368±33	64	-	-	-	-	-	-
15b	2.1±0.1	406±42	36	-	-	-	-	-	-
16a	2.4±0.1	468±32	120	-	-	-	-	-	-
16b	2.1±0.1	364±33	130	-	-	-	-	-	-
16c	2.0±0.2	468±81	58	-	-	-	-	-	-
16d	2.9±0.3	427±66	83	-	-	-	-	-	-
16e	2.2±0.2	502±80	50	-	-	-	-	-	-
17a	2.4±0.1	458±44	70	-	-	-	-	-	-
18a	2.5±0.1	262±15	130	-	-	-	-	-	-
18b	2.1±0.2	673±98	69	-	-	-	-	-	-
19a	2.3±0.2	482±102	104	-	-	-	-	-	-
19b	1.7±0.1	279±45	96	-	-	-	-	-	-
20a	1.6±0.1	326±33	104	1.4±0.1	313±37	83	-	-	-
20aa	1.4±0.1	313±35	83	-	-	-	-	-	-
20b	1.6±0.1	292±40	63	-	-	-	-	-	-
20bb	1.6±0.1	298±39	57	-	-	-	-	-	-
20c	2.4±0.2	427±54	46	-	-	-	-	-	-
20d	2.0±0.3	384±88	59	-	-	-	-	-	-
20dd	1.8±0.2	374±53	46	-	-	-	-	-	-
21a	1.7±0.1	380±22	109	-	-	-	-	-	-
21b	1.8±0.1	370±34	74	-	-	-	-	-	-
21c	2.0±0.1	445±24	99	-	-	-	-	-	-
21d	1.8±0.1	377±42	79	-	-	-	-	-	-
21e	1.3±0.1	339±50	66	-	-	-	-	-	-
25a	-	-	-	3.0±0.3	610±106	138	2.3±0.1	492±36	127
25b	2.8±0.3	579±118	40	2.4±0.7	468±232	42	-	-	-
25c	2.4±0.2	473±68	114	3.4±0.4	630±113	46	-	-	-
26a	-	-	-	5.0±0.7	89±23	37	-	-	-
28a	2.4±0.1	509±33	146	3.2±0.3	540±91	62	2.0±0.1	523±37	89
28b	2.8±0.2	604±82	89	2.2±0.2	426±76	72	-	-	-

28c	2.7±0.3	498±98	49	1.7±0.1	322±43	72	-	-	-
29a	3.5±0.3	697±89	89	4.1±0.3	803±93	61	2.6±0.1	536±38	88
31a	-	-	-	1.3±0.1	399±60	44	-	-	-
33a	2.2±0.3	470±90	96	2.7±0.8	562±295	68	2.1±0.1	429±33	83
33b	2.7±0.3	436±74	66	2.1±0.3	454±104	26	-	-	-
33c	3.2±0.3	510±78	62	-	-	-	-	-	-
34a	4.9±0.5	1078±14	88	-	-	-	-	-	-
34b	3.2±0.2	498±71	100	-	-	-	-	-	-
34c	3.3±0.4	682±118	94	-	-	-	-	-	-
36a	3.5±0.3	675±114	81	3.0±0.4	557±127	83	2.4±0.1	469±40	78
36b	3.2±0.5	659±180	47	-	-	-	-	-	-
36bb	3.4±0.5	371±94	46						
37a	3.0±0.3	656±96	112	1.9±0.2	362±67	47	-	-	-
38a	3.4±0.3	678±82	71	2.2±0.2	462±66	106	-	-	-
38b	4.1±0.6	779±176	85	3.8±0.4	717±128	67	1.6±0.1	416±29	93
38c	-	-	-	2.2±0.2	427±71	39	-	-	-
38d	-	-	-	2.5±0.2	387±45	50	-	-	-
39a	2.9±0.3	576±104	91	3.0±0.3	652±105	77	-	-	-
39b	4.3±0.6	693±175	54	2.9±0.3	486±98	58	-	-	-
39c	4.6±0.4	717±85	51	3.6±0.4	527±81	50	-	-	-
39d	3.5±0.2	568±80	71	3.4±0.4	522±89	44	-	-	-
39e	-	-	-	3.9±0.4	644±102	52	-	-	-
40a	3.2±0.2	699±72	44	-	-	-	-	-	-
40b	-	-	-	1.8±0.2	387±71	53	-	-	-
41a	6.9±1.2	1131±29	70	3.5±0.4	576±115	91	2.3±0.1	458±27	108
42a	4.2±0.3	1072±13	87	2.6±0.2	784±130	92	2.0±0.1	555±28	128
43a	1.4±0.1	-	43	-	-	-	-	-	-
43b	-	-	-	2.3±0.1	634±37	98	-	-	-
44a	-	-	-	1.2±0.1	304±21	108	-	-	-
44b	3.1±0.4	763±150	96	-	-	-	2.2±0.1	572±30	96
45a	2.1±0.2	292±51	106	2.5±0.3	389±69	74	2.3±0.2	368±43	62
45b	3.3±0.2	471±54	89	3.1±0.2	459±70	76	2.4±0.1	386±42	58
45c	1.7±0.1	265±16	106	2.5±0.3	382±66	79	-	-	-
46a	4.0±0.2	830±79	100	3.3±0.2	709±80	98	2.5±0.1	543±38	97
46aa	-	-	-	-	-	-	2.3±.2	511±49	65
46b	3.6±0.3	636±110	61	2.7±0.2	597±87	53	-	-	-
46c	5.3±0.4	959±117	65	3.3±0.5	658±168	31	2.1±0.2	429±49	52
47a	-	-	-	3.1±0.3	565±75	80	-	-	-
48a	-	-	-	3.0±0.4	415±79	53	-	-	-
49a	4.5±0.6	851±189	114	3.6±0.1	896±48	75	1.8±0.1	429±27	103
49aa	-	-	-	2.1±0.1	-	117	-	-	-
50a	2.2±0.1	535±65	77	3.0±0.4	649±141	42	-	-	-
50aa	-	-	-	2.0±0.1	433±55	79	-	-	-
50b	3.1±0.2	635±83	68	2.5±0.2	-	50	-	-	-
50c	2.8±0.2	-	55	-	-	-	-	-	-
50d	-	-	-	1.7±0.2	306±54	47	-	-	-
51a	3.5±0.2	739±65	123	2.9±0.2	770±106	108	2.2±0.1	572±29	127

Table 5.1 (cont.)

52a	2.4±0.1	868±76	105	2.5±0.3	445±75	35	-	-	-
53a	2.1±0.3	448±86	101	2.7±0.2	593±63	59	2.4±0.2	492±69	38
53b	3.1±0.2	607±86	85	-	-	-	-	-	-
54a	4.0±0.4	951±160	109	3.1±0.3	858±118	82	2.6±0.1	585±45	100
55a	2.4±0.2	476±66	87	-	-	-	-	-	-
55b	-	-	-	2.7±0.3	-	142	2.2±0.1	492±45	88
55c	3.4±0.3	-	63	-	-	-	-	-	-
55d	3.0±0.2	-	82	3.2±0.3	554±88	53	-	-	-
56a	3.1±0.3	668±100	91	2.3±.2	557±83	55	-	-	-
56b	1.7±0.2	285±55	56	-	-	-	-	-	-

* unexposed inclusions

** singly exposed inclusions

*** doubly exposed inclusions

[#] Thickness measurements are from the optical focusing drive method.

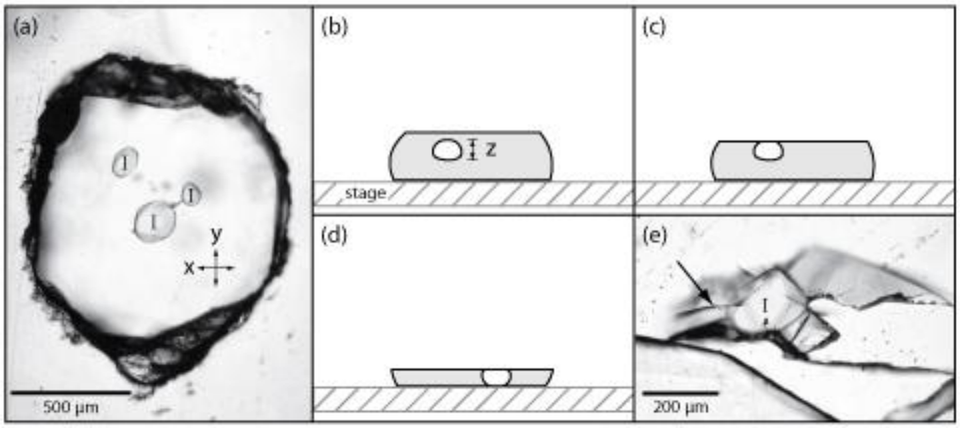

Fig. 5.1

(**a**) Photomicrograph of homogenized quartz-hosted glass inclusions (I). (**b-d**) Schematic diagrams of a target inclusion when it is (**b**) unexposed, (**c**) singly exposed, and (**d**) doubly exposed. (**e**) A doubly exposed inclusion (I) with cracks (example is arrowed) resulting from strain accumulated during polishing.

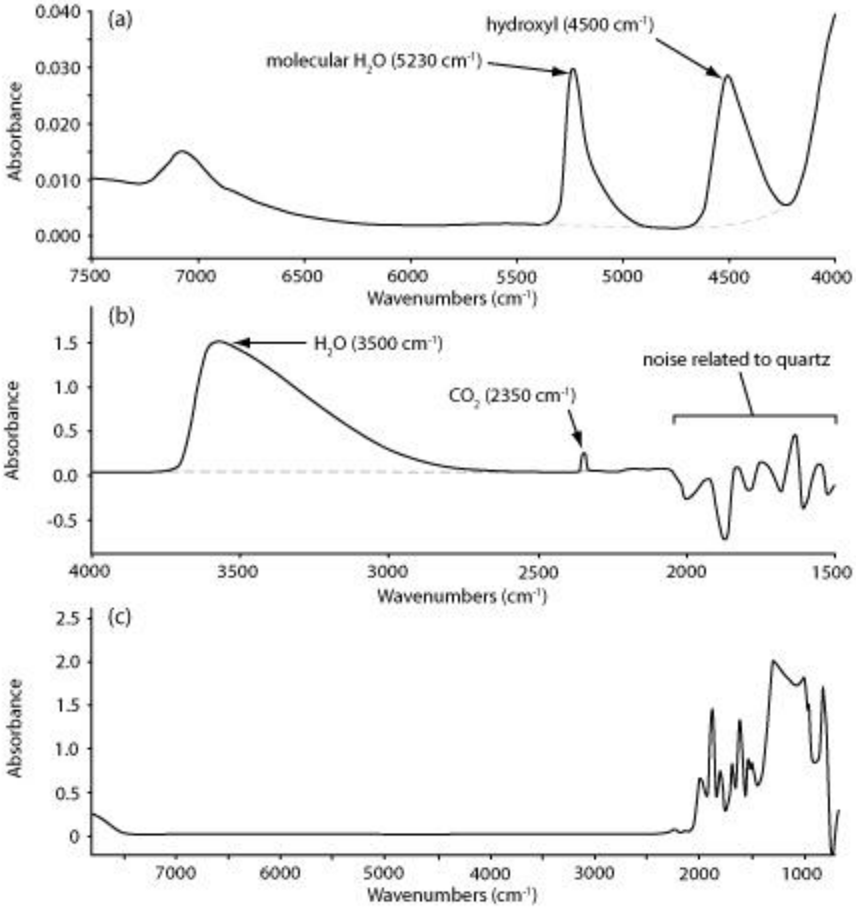

Fig. 5.2

Typical FTIR spectra of (**a, b**) unexposed glass inclusions and (**c**) quartz only. Quartz absorbs IR light at wavenumbers less than ~2100 cm^{-1}, which does not affect the absorbance of molecular H_2O, OH, or CO_2. Measured peaks are labeled. Background subtraction methods are illustrated by dashed gray lines. Note changes in range of wavenumbers in each panel.

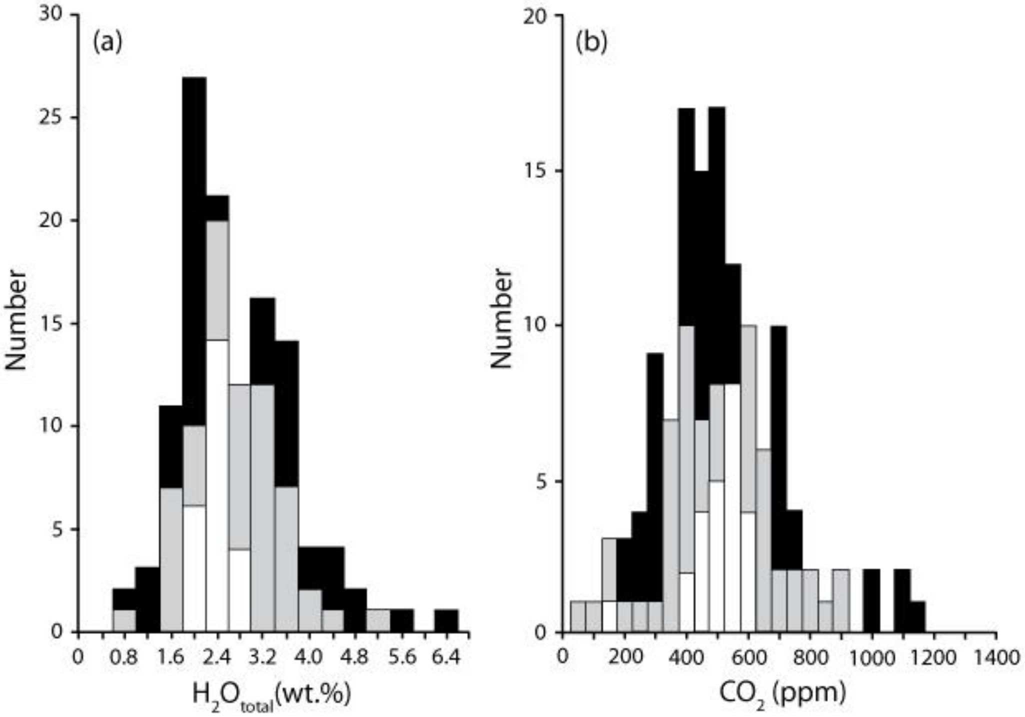

Fig. 5.3

Histograms of (**a**) H_2O_{total} and (**b**) CO_2 content. Unexposed data are black, singly exposed data are gray, and doubly exposed data are white. Wider ranges in the unexposed and singly exposed data are attributed to more imprecise thickness measurements.

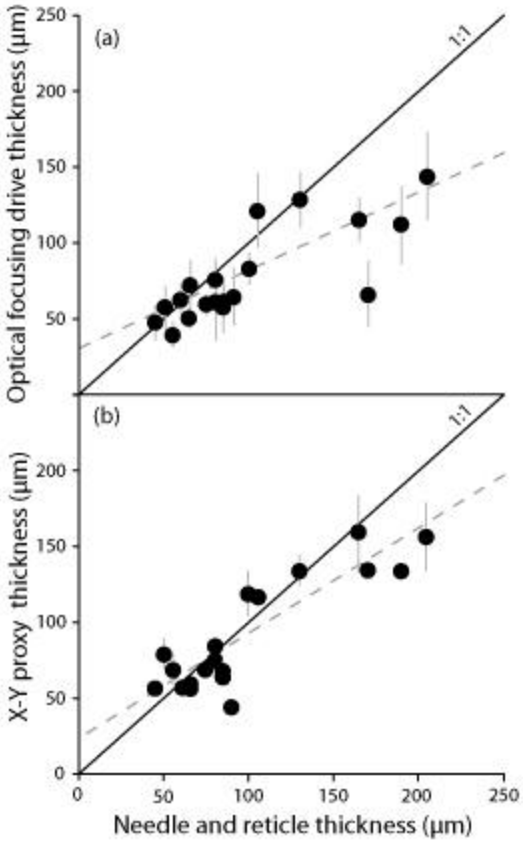

Fig. 5.4

Comparison of the unexposed inclusion thickness measured using the needle and reticle method with estimated thickness using (**a**) the optical focusing drive of the microscope method, and (**b**) the X-Y proxy method. Error bars (1σ) are shown in gray when larger than the symbol size. The dashed lines are linear regressions through the data. The linear regression of the X-Y proxy method has a slope closer to 1, demonstrating it better approximates thickness.

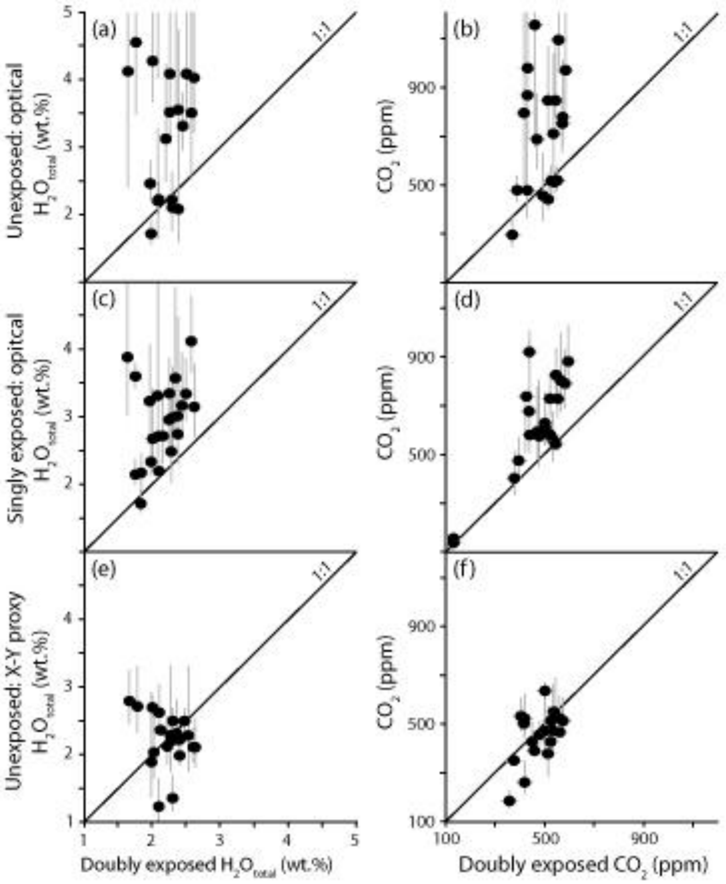

Fig. 5.5

Calculated volatile contents of the same population of inclusions at different levels of exposure. (**a, b**) Volatile contents in unexposed inclusions are highly enriched relative to those in doubly exposed inclusions when thicknesses were measured using the optical focusing drive. (**c, d**) Volatile contents in singly exposed inclusions are also enriched relative to those in doubly exposed inclusions when thicknesses were measured using the optical focusing drive. Error bars (1σ) are shown in gray when larger than the symbol size. (**e, f**) Volatile contents of unexposed and doubly exposed inclusions correspond well when the thicknesses of unexposed inclusions were estimated using the X-Y proxy method. Error bars represent the range of volatile contents possible if the maximum and minimum horizontal dimensions were used as a proxy for thickness.

CONCLUDING REMARKS

To conclude my dissertation, I would like to share my views on the broader significance of my research to the greater community. Overall, my most important contributions are found in the quantitative estimates I infer from the spherulite, microlite, and experimental datasets. Three questions guided my research over the course of my dissertation. The first question sought to unravel the pre-eruptive storage conditions of effusive rhyolitic eruptions. The second aimed at quantifying eruptive ascent rates. Lastly, the third question drove at understanding how rhyolite lavas cool and remain mobile.

The use of phenocryst compositions and high temperature phase equilibria techniques to understand magma chamber storage conditions has been used for decades. By applying this approach to effusive rhyolitic systems, which have often been overlooked, I found the magmas that fed effusive eruptions were stored at the same temperatures and depths as their explosive counterparts. Specifically, I found that no characteristics differentiate the pre-eruptive storage conditions of Central Plateau Member magmas that sourced effusive and explosive eruptions. Those rhyolitic melts from Yellowstone caldera were all stored at 750±25 °C in the shallow crust (<7 km). Indeed, even the dissolved volatile contents from the explosive Tuff of Bluff Point are indistinguishable from those in Douglas Knob lava dome. Storage conditions are also similar for effusions of vastly different eruptive volume. Thus, eruption style and volume are not controlled by magma temperature, storage depth, or volatile content.

Microlites were the key to understanding eruptive ascent. Microlite textures are not modified during subaerial emplacement, which allows them to be used to quantify conduit processes. Microlite number density in high silica rhyolite lavas with eruptive volumes ranging from 0.001 to70 km^3 indicate decompression rates of 0.02 to 0.14 MPa hr^{-1}, which are equivalent to ascent rates of 0.2 to 1.7 mm s^{-1}. Thicker, larger volume flows experienced the faster of those rates, but it is interesting that such volumetrically diverse lavas experienced such similar rates. Microtextural comparisons between natural and experimental samples are generally similar to those estimates, and indicate decompression rates < 1 MPa hr^{-1}, equivalent to <10 mm s^{-1}. Slow ascent led to gas loss from the ascending magma, which permitted effusive eruptions.

It is well established in the literature that effusive eruptions experience slower eruptive ascent rates, which permit the melt to degas passively. What is unclear, however, is why melts with the same pre-eruptive temperatures, depths, and volatile contents ascend at different rates, erupt with different behaviors, and/or generate such volumetrically-diverse effusions. Chamber overpressure is likely the “smoking gun” that controls overall eruptive behavior. I am not the first to come up with this idea. The concept is supported by analog and numerical models, and could be generated by tectonic stress or increasing the stored volume in the chamber. Certainly those processes could operate in some settings, but tectonism or magma recharge are not appropriate causes in the rhyolitic systems I studied. Instead, I believe overpressure was generated by volatile exsolution. This idea is a promising new avenue to explore.

The behavior of rhyolite lavas was another rewarding research avenue. I found that both microlite textures and spherulites provided quantitative constraints on lava emplacement. Compositional gradients outside of spherulites from a sample collected near the surface of Pitchstone Plateau indicate that portion of the lava cooled at $10^{-4.9\pm0.6}$ °C s^{-1} (~1 °C d^{-1}). Because few techniques can extract cooling rates from lava flows, the use of compositional gradients outside of spherulites presents a new opportunity to understand the timescales of lava emplacement because mobility is controlled by temperature. Microlite textures provide another measurement that can be used to understand emplacement. Microlite number density and microlite orientations do not evolve during emplacement in samples collected from the surfaces of the flow. The upper portions of the flows are too viscous, so they most likely raft inertly upon lower portions during emplacement. This aspect of the microlite research was initially a negative result. But, we realized it allowed us to use microtextures to investigate conduit processes such as ascent rate, as was summarized in the preceding discussion.

Lastly, the ascent rate and cooling rate estimates provide timescales that are critical for understanding conduit and emplacement processes. Rates allow a process to be visualized, and placed in context. Importantly, after a rate has been well-established, then rates of other associated processes can be bootstrapped to the initial estimate. For example, we know that rhyolite mobility ceases when the lava cools below the glass transition temperature. With the cooling rate and emplacement temperature established, the emplacement duration can be calculated. Knowing that duration allows us to calculate lava velocity because flow distance is also known. Using this bootstrapping technique, I was able to place first order constraints on dike width, eruptive flux, eruption duration, and flow velocity. Generally, those estimates align with recent observations of active rhyolite effusions at Cordón Caulle and Chaitén. Rates and timescales are important for understanding the behavior of volcanic systems, and are important for hazard assessment and mitigation.

Appendix 1

List of all samples collected during research trips to Yellowstone, Mono Craters, and Coso Volcanic field. Appendix 1 contains sample locations and field descriptions of samples.

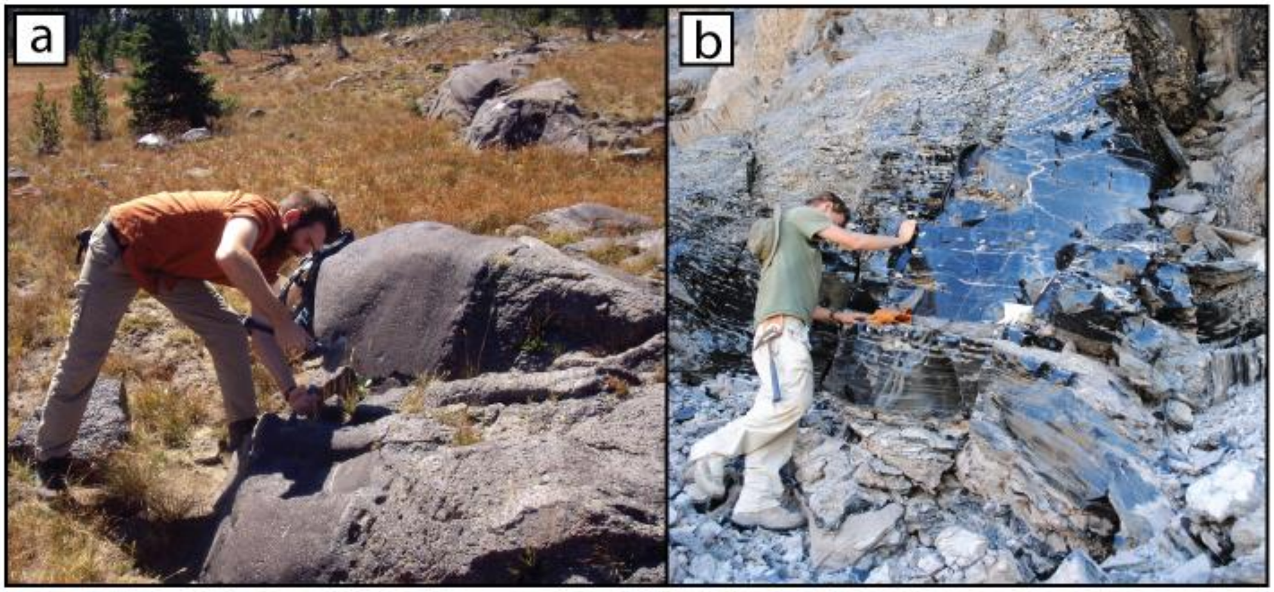

Fig.1

Typical obsidian outcrops at **a** Yellowstone and **b** Mono Craters. Undergraduate research assistants (Tim Prather and Robert Zinke) are demonstrating sample collection techniques.

Appendix 1. List of all samples and sample descriptions

Unit	Sample	Easting	Northing	Oriented	Field Orientation	Sample Description
Pitchstone Plateau	Y110	513647	4903186	Y	42/78e	dense obsidian, banding same as sample orientation
	Y111	514394	4902551	Y	315/28e	featureless obsidian
	Y112	515961	4902372	Y	44/73se	flow bands same as sample orientation, some unoriented spherulitic pieces
	Y113	516140	4903494	Y	58/60se	featureless obsidian
	Y114	515999	4904434	Y	82/65sse	flow bands same as sample orientation
	Y148	528516	4902077	Y	325/88ne	Flow front sample, west of Lewis falls
	Y149	528043	4899265	Y	46/43se	Heavily spherulitization, some large, many photos, some spheres broken by flow
	Y150	525977	4895300	Y	265/30n	flow front sample, good spherulites in dense obsidian
	Y185	517178	4897717	Y	245/52nw	Discordant domains of spherulitized obsidian, in situ, area to map km flow bands
	Y186	515902	4895582	Y	39/45e	dense obsidian
	Y187	515071	4891401	Y	307/43ne	mediocre quality outcrop, but best spot in miles
	Y188	514413	4889707	Y	65/36n	mediocre quality outcrop, but best spot in miles
	Y192	522869	4899034	Y	7/74e	dense obsidian, near Phantom fumarole
	Y193	523241	4901708	Y	70/87n	dense obsidian
Douglas Knob	Y88	512231	4906940	N	-	dense obsidian 20 feet upslope
	Y89	512265	4906785	N	-	in situ, fresh glass, featureless
	Y90	512265	4906688	N	-	in situ, sample parts are vesicular and others glassy, vague banding,
	Y91	512167	4906627	N	-	vesicular, aligned vesicles, pumice fragments as xenoliths(?)
	Y92	512078	4906606	N	-	vesicular obsidian, cut by flow bands defined by 2-3 mm spherulites
	Y93	512008	4906619	N	-	pumiceous carapace and dense obsidian, flow bands are folded in places
	Y115	512481	4906511	N	-	flow breccia with sample pumice collected
	Y116	512648	4906531	Y	9/25w	heavily spherulitized obsidian
	Y117	512111	4906595	Y	-	dense obsidian
	Y118	512004	4906729	Y	60/90	dense obsidian
	Y119	512038	4906903	Y	see notes	2 samples A (240/28se), B (202/87w) dense obsidian
	Y120	512268	4906783	Y	255/65n	dense obsidian
	Y121	512344	4906703	Y	222/60se	large spherulites in sample, broke in transport
	Y122	512222	4906940	Y	5/68e	dense obsidian

UTM coordinates are in NAD83.

Appendix 1. (cont) List of all samples and sample descriptions

	Sample	Easting	Northing	Oriented	Field Orientation	Sample Description
Solfatara Plateau	Yell 33	539231	4954272	N	-	Jim collected
	Yell 34	537798	4953107	N	-	Jim collected
	Yell 35	535791	4951773	N	-	Jim collected
	Yell 36	530323	4950602	N	-	Jim collected
	Yell 46	533836	4950365	N	-	Jim collected
	Yell 47	537401	4952151	N	-	Jim collected
	Yell 48	531600	4946885	N	-	Jim collected
	Yell 49	532016	4948152	N	-	Jim collected
	Yell 50	533139	4949057	N	-	Jim collected
	Yell 51	533605	4949782	N	-	Jim collected
	Yell 52	539802	4947630	N	-	Jim collected
	Yell 60	536520	4953333	N	-	Jim collected
	Y76	531805	4941733	N	-	dense obsidian
	Y77	531604	4945591	N	-	2 samples, dense obsidian and white vesicular "carapace" ~10% area
	Y78	531225	4944308	N	-	by Cygnet lakes, spherulitic or vesicular, altered obsidian
	Y79	530773	4943688	N	-	dense obsidian from small outcrop
	Y80	530295	4943220	N	-	dense obsidian from small outcrop
	Y81	530296	4944052	N	-	Obsidian, minor spherulites, no flow bands
	Y82	529801	4943578	N	-	small 2*3 foot outcrop, no features
	Y83	529703	4942815	N	-	collected 4 samples of devitrified, vesicular, near vent
	Y84	529639	4942656	N	-	devitrified, vesicular
	Y85	529719	4942594	N	-	Obsidian and major vitrified, vesicular portions, transitional
	Y86	529696	4942365	N	-	normal obsidian again, some % spherulites
	Y87	529880	4942010	N	-	dense obsidian from small outcrop
	Y123	537725	4952451	Y	356/88	road cut on north side of road, featureless obsidian
	Y124	537354	4952099	Y	248/87n	in valley south of road, in situ, good spherulites
	Y125	536369	4951735	Y	102/90	mediocre outcrop, hard to tell if in situ
	Y126	534798	4951042	Y	110/67s	high vesicularity to dense obsidian, spherulites
	Y127	534160	4950640	Y	60/63n	along telephone line trail, dense obsidian
	Y128	533633	4954229	Y	310/50ne	dense obsidian, flow bands orient 300/77ne
	Y129	533967	4953019	Y	310/80ne	in drainage, dense obsidian

UTM coordinates are in NAD83.

Appendix 1. (cont) List of all samples and sample descriptions

	Sample	Easting	Northing	Oriented	Field Orientation	Sample Description
Solfatara Plateau (cont.)	Y130	533292	4952943	Y	295/57n	dense obsidian
	Y131	532416	4953000	Y	165/87w	dense obsidian
	Y132	532449	4953547	Y	100/73s	dense obsidian, not sure if insitu
	Y133	531533	4952410	Y	135/15e	in situ, dense obsidian with flow bands oriented 330/60ne
	Y134	536407	4955119	Y	245/67n	flow bands same as sample orientation
	Y135	535232	4954789	Y	205/75e	probably in situ, dense obsidian
	Y136	535566	4954153	Y	17/40e	appears pitchy, perlitized(?), spherulites present
	Y138	536150	4953789	Y	35/68e	dense obsidian
	Y139	536572	4952793	Y	247/5nw	in situ, dense obsidian
	Y140	538657	4955163	Y	310/42ne	nice spherulites, probably in situ boulders, dense obsidian
	Y141	538851	4954765	Y	355/65e	probably in situ, dense obsidian
	Y142	538511	4954269	Y	95/90	on a pressure ridge, dense obsidian
	Y143	535794	4951685	N	-	dense obsidian, for granophyre mapping
	Y144	531944	4950111	N	-	dense obsidian from a 2 m block, not in situ
	Y145	530373	4950632	Y	225/55nw	definitely in situ, flow front sample of dense obsidian
	Y146	530999	4950285	N	-	dense obsidian
	Y147	533130	4950084	N	-	dense obsidian
	Y204	539431	4946848	Y	32/61se	outer rind of obsidian with devitrified core, high crystal content
	Y218	530272	4946249	Y	154/46w	dense obsidian, along prominent ridge, in situ
	Y219	529643	4946991	Y	136/31.5sw	in situ, on canyon wall, contains spherulites
	Y220	532469	4945284	Y	40/44e	very poor outcrop, didn't travel far but not in situ
	Y221	531934	4945117	Y	50/50se	excellent dense obsidian, in situ
	Y222	531632	4947564	Y	310/58ne	best outcrop in past 2 km, 50/50 if in situ
	Y223	533447	4947138	Y	180/61w	poor outcrop, hard to tell
	Y224	534576	4946120	Y	45/30se	poor out crop, in situ hard to tell
	Y225	535831	4945208	Y	67/65e	good outcrop, edge of flow
	Y230	537255	4947564	Y	310/58ne	best outcrop on thumb, 60% in situ
	Y231A	537034	4948755	Y	115/72sw	Mahogony obsidian on canyon wall
	Y231B	537034	4948755	Y	315/60NE,	bottom of same cliff, dense obsidian, flow bands and spherulites present
	Y232	536700	4949418	Y	121/50sw	excellent outcrop, flow bands trend 310/53sw
	Y233	531040	4949078	Y	172/26sw	excellent outcrop, south valley wall,

UTM coordinates are in NAD83.

Appendix 1. (cont) List of all samples and sample descriptions

	Sample	Easting	Northing	Oriented	Field Orientation	Sample Description
Solfatara Plateau (cont.)	Y240	529512	4946173	Y	20/48e	dense obsidian
	Y241	529759	4943340	Y	65/64se	totally crumbling
	Y242	528085	4945248	Y	20/63nw	dense obsidian
	Y243	531498	494177	Y	20/35	dense obsidian
	Y244	532767	4954104	N	-	dense obsidian, shakira
Summit Lake	Y70	506033	4918669	N	-	red to black obsidian define flow bands, spherulites up to 1 cm , ropy areas
	Y71	506033	4918669	N	-	flow banded obsidian, spherulitic zones nearby, sequence of photos
	Y72	505270	4917940	N	-	dense obsidian, east of lake
	Y73	503556	4917397	N	-	dense obsidian, closest to vent location
	Y74	503871	4917373	N	-	dense obsidian, in area with hydrothermal alteration, photos of Zinke
	Y195	492222	4915841	Y	43/48se	flow front sample, excellent outcrop
	Y196	494899	4917196	Y	66/59se	could be in situ blocks on little hill of obsidian, hard to tell
	Y197	497753	4916915	Y	154/40w	likely in situ, dense obsidian on little hill
	Y198	501561	4917443	Y	346/66sw	dense obsidian, not sure if in place
	Y199	505988	4918910	Y	129/65sw	not sure if in place
	Y200	506597	4919479	Y	53/81s	definitely in place, vertical flow bands
	Y201	507420	4921681	Y	265/79s	likely in situ, dense obsidian on little hill, near flow breccia location with photos
	Y202	508436	4923560	Y	256/85n	dense obsidian with spherulites up to 2 cm
	Y203	509716	4924235	Y	see notes	A (116/51s), B (164/83w overturned), flow front sample, excellent outcrop,
Bechler River	Y98	511802	4909501	N	-	flow banded obsidian, defined by spherulites, took photos
	Y99	512034	4907275	N	-	dense obsidian
Trischmann Knob	Y94	510093	4909467	N	-	flow banded obsidian
	Y95	509918	4909428	N	-	dense obsidian weathering out of decayed obsidian soil
	Y96	509861	4909406	N	-	dense obsidian weathering out of decayed obsidian soil
	Y97	510036	4909483	N	-	good exposure of dense obsidian, delicate flow banding 210/17s
Grants Pass	Y101	512762	4909368	N	-	dense obsidian
	Y102	513081	4910457	N	-	dense obsidian
	Y103	514057	4913809	N	-	dense obsidian
Cold Mountain	Y100	514755	4912803	N	-	densely welded tuff

UTM coordinates are in NAD83.

Appendix 1. (cont) List of all samples and sample descriptions

	Sample	Easting	Northing	Oriented	Field Orientation	Sample Description
West Yellowstone	Y160	490496	4941225	Y	217/85nw	Some spherulites in unoriented blocks
	Y161	492123	4935069	Y	142/65s	dense obsidian
	Y162	496300	4933345	Y	155/37sw	dense obsidian
	Y163	495825	4932710	Y	19/75sw	dense obsidian
	Y164	495155	4933568	Y	54/47s	dense obsidian
	Y165	490411	4934556	Y	55/68w	overturned orientation measurement
	Y166	489201	4935453	Y	153/68se	outcrop not very good
	Y167	488443	4935747	Y	146/60sw	dense obsidian
	Y168	488030	4937229	Y	192/71w	2 samples, nonoriented one with generations of spherulites,
	Y169	488961	4936836	Y	75/67	excellent spherulites in dense obsidian
	Y170	495207	4933788	Y	210/51w	dense obsidian
	Y171	494070	4933833	Y	70/60nw	collected of pressure ridge, much of outcrop is vesiculated
	Y172	493717	4934611	Y	200/61nw	dense obsidian
	Y175	491159	4937315	Y	300/41sw	dense obsidian
	Y176	490650	4935523	Y	150/64sw	dense obsidian
	Y177	489845	4936641	Y	245/60se	dense obsidian
	Y178	490037	4938061	Y	283/69sw	dense obsidian
	Y179	490808	4940072	Y	145/78sw	clasts of stony rhyolite in obsidian, flow bands wrap lithics
	Y180	489822	4940217	Y	260/40s	sample from recumbant fold, sketch in notes
	Y183	491762	4940196	Y	13/75w	Steep outcrop, over its height no systematic stratigraphy of bands or spheres
	Y184	491768	4940838	Y	322/78n	overturned measurement, flow front sample of dense obsidian
	Y190	487705	4938221	Y	338/21ne	dense obsidian
	Y191	488516	4938568	Y	162/67wsw	dense obsidian
	Y205	492517	4937176	Y	156/88sw	excellent outcrop on pressure ridge, flow fold nearby
	Y206	494002	4937389	Y	9/34e	no confidence of in situ, margin of upper flow
	Y207	492881	4938379	Y	304/86 ne	dense obsidian
	Y208	493608	4933227	Y	290/77s	dense obsidian
	Y209	492874	4934227	Y	187/40w	dense obsidian
	Y210	497431	4932832	Y	212/60e	dense obsidian
	Y211	498555	4932257	Y	64/61.5se	dense obsidian
	Y212	498913	4932199	Y	39/45e	dense obsidian

UTM coordinates are in NAD83.

Appendix 1. (cont) List of all samples and sample descriptions

	Sample	Easting	Northing	Oriented	Field Orientation	Sample Description
West Yellowstone (cont.)	Y213	500263	4932841	Y	186/53w	dense obsidian
	Y215	497664	4930953	Y	269/81n	located on levee ridge on flow front
	Y216	498714	4930244	Y	62/47nw	dense obsidian
	Y217	500000	4931296	Y	208/67nw	nice glass, flow bands along 20 ft portion of outcrop, part of pressure ridge
North Coulee	NC-1	324411	4197515	Y		
	NC-3	3229248	4196348	Y	305/61	Flow bands are sample as sample orientation
	NC-4	323444	4195889	Y	260/54	Obsidian
	NC-5	323754	4195937	N	-	flaggy on flow bands, most of surface of NC made of this
	NC-13	322932	4197160	Y	202/65nw	obsidian block
	NC-14	323254	4197261	Y	see notes	A (242/35), B (195/85e), C (70/205)
	NC-15	324043	4197688	Y	340/13e	flow bands are generally 260/8-30se, photo 116
	NC-16	324351	4197255	Y	326/88s	sample from jumbled flow breccia
	NC-17	324283	4197041	Y	267/49	some samples with spherulites and lithophysae
	NC-20	118 59.278'	37 53.903	Y	350/68w	dense obsidian
	NC-21	118 59.489'	37 53.761'	Y	210/21e	dense obsidian
	NC-22	118 59.520'	37 53.716'	Y	67/89w	dense obsidian
	NC-23	118 59.855'	37 53.584'	Y	20/45e	dense obsidian
	NC-24	119 00.130'	37 53.599'	Y	86/90	dense obsidian
	NC-30	118 59.336'	37 54.056'	Y	128/87n	dense obsidian
	NC-31	118 59.564'	37 54.059'	Y	149/88w	dense obsidian
	NC-32	118 59.712'	37 54.101'	Y	111/84s	dense obsidian
	NC-33	118 59.747'	37 54.088'	Y	32/78w	dense obsidian
	NC-34	118 59.913'	37 54.056'	Y	146/52w	dense obsidian
	NC-36	323252	4195316	Y	104/75s	flow bands orient 331/79e, best obsidian in area although vesiculated
	NC-37	322969	4195086	Y	264/7	flow bands orient 15/19nw
	NC-38	322863	4195076	Y	344/20w	flow bands same as sample orientation
	NC-39	322785	4195195	Y	209/69e	outcrop is intensely folded and brecciated, photo 130, spherulites in bands
South Coulee	SC-1	323850	4190380	Y	230/67e	sample contains spherulites and flow bands, amidst flow breccia

UTM coordinates are in NAD83.

Appendix 1. (cont) List of all samples and sample descriptions

	Sample	Easting	Northing	Oriented	Field Orientation	Sample Description
Panum Crater Dome	PCD-1	320131	missing	Y	110/22	flow banding and slightly devitrified, bands at 347/25w
	PCD-2	320187	4199814	Y	040/11nw	flow banded obsidian, vesicular in places. Ropy surface with tension gashes
	PCD-3	320230	4199804	Y	063/50s	flow bands 82/23
	PCD-4	320218	4199750	Y	198/76	flow bands strike 261/75
	PCD-5	320218	419726	Y	164/88	flow bands strike 60/89, ropy texture with tension gashes
	PCD-6	320242	4199697	Y	334/57	obsidian with ropy surface, "peeled back" texture, some silvery areas
	PCD-7	320102	4199682	Y	211/74nw	vitreous obsidian, flow bands at 274/48
	PCD-8	320134	4199673	Y	155/85	on a whale back feature, bands orient 333/47
	PCD-10	320164	4199664	Y	173/73	obsidian with spherulites nearby, bands orient 308/12
	PCD-11	320164	4199697	Y	257/64	Spherulite rich, bands orient 25/34
	PCD-12	320137	4199741	Y	294/65	flow banded obsidian, rich textural history, bands orient 73/26
Northwest Coulee	NWC-1	324411	4197515	Y	see notes	A (84/89N), B (189/41), C (270/44), blocks were in place, minor spherulites
	NWC-2	321241	4197301	Y	40/22	Flow banding on oriented in place obsidian, vitreous
	NWC-3A	321360	4197315	Y		
	NWC-4	322570	4198386	Y	254/11n	flow bands running parallel to slope, looks in place
	NWC-5	322437	4198490	Y	283/22	obsidian as bands and islands in stony rhyolite, bands 330/70w
	NWC-6	322417	4198540	Y	368/12w	mostly stony rhyolite
	NWC-7	321445	4198672	Y	275/45	intensely folded obsidian, spherulite zones and devitrified, flow breccia
	NWC-8	322013	4199084	Y	155/49n	spherulites and flow bands orient 83/67s
	NWC-9A,B	321777	4198896	Y	see notes	A (224/60), B (29/64e), flow bands orient 230/28
	NWC-10	321729	4198875	N	-	textures include alligator skin, ropes, oxidation spots, remelting(?) domains
	NWC-20	119 02.664'	37 54.474'	Y	104/84s	dense obsidian
	NWC-21	119 02.338'	37 54.511'	Y	69/64s	dense obsidian
	NWC-22	119 02.358'	37 54.708'	Y	31/41w	dense obsidian
	NWC-23	119 02.276'	37 54.813'	Y	71/66s	dense obsidian
Upper Dome	UpD-1	321954	4197564	Y	see notes	Collected A (160/37W) ,B (225/60E),C (not oriented)
	UpD-2	322033	4197552	Y	236/36	Boulder-sized chunks of obsidian float in gray devitrified rhyolite
	UpD-3	322599	4198200	Y	5/68ne	No flow bands, probably in situ

UTM coordinates are in NAD83.

Appendix 1. (cont) List of all samples and sample descriptions

	Sample	Easting	Northing	Oriented	Field Orientation	Sample Description
Sugar Loaf	SL-1	425969	3987895	Y	240/64nw	definitely in situ, somewhat vesiculated but glass portions
	SL-2	426212	3988391	Y	25/83SE	Beautiful outcrop 25 m long, in situ, litho and spheres
	SL-3	425250	3988649	Y	344/57w (LHR)	bands of dense obs in silver pumiciceous
	SL-4	425470	3989039	Y	296/76ne	excellent outcrop, in situ 100%, folded in portions, Travis photos
	SL-5A,B	500 m east of SL-4		Y	337/83ne, 97/52s	S/D is surface of flow bands, flaggy with laminar flow bands
	SL-6	425784	3986700	N	-	flow below sugarloaf, antiquity quarry, samples for spherulites
	SL-7	426725	3987156	Y	334/65ne	excellent outcrop, in situ 100%, flaggy 1-cm thick bands

UTM coordinates are in NAD83.

Appendix 2

Appendix 2 presents all of the microprobe analyses of natural samples and experiments. The results are presented in tables based on target phase, lava flow, and sample. I begin with natural sanidine, clinopyroxene, fayalite, and magnetite data. Then, I present compositions for experiment glasses, feldspars, and clinopyroxene/fayalite.

Feldspar

Appendix 2. (cont.) Compilation of all microprobe analyses of natural samples and experiments.

							Feldspar					
Sample		**Spot**	**SiO_2**	**Al_2O_3**	**FeO**	**MgO**	**CaO**	**Na_2O**	**K_2O**	**BaO**	**Total**	**Or#**
Solfatara Plateau												
Y52	**Cores**	6	66.78	19.13	0.00	0.52	0.16	5.61	8.58	0.12	100.90	49.8
		10	66.04	19.23	0.00	0.49	0.13	5.58	8.53	0.32	100.30	49.8
		11	66.83	19.18	0.00	0.48	0.17	5.34	8.62	0.16	100.77	51.1
		13	65.94	18.80	0.00	0.44	0.19	5.88	8.80	0.20	100.20	49.2
		14	66.43	18.80	0.00	0.51	0.12	5.83	8.62	0.15	100.44	49.0
		21	66.52	19.21	0.00	0.51	0.13	6.00	8.58	0.12	101.05	48.2
		23	66.51	19.06	0.00	0.49	0.19	5.55	8.61	0.12	100.50	50.1
		25	66.38	18.81	0.00	0.46	0.19	5.70	8.39	0.25	100.17	48.7
		26	66.27	18.93	0.00	0.46	0.14	5.40	8.60	0.23	100.03	50.8
	Rims	7	66.93	19.37	0.01	0.49	0.14	6.73	7.49	0.17	101.32	42.0
		8	66.21	18.97	0.00	0.46	0.16	5.55	8.66	0.20	100.22	50.3
		9	65.79	19.17	0.00	0.54	0.10	5.25	8.62	0.33	99.79	51.7
		12	65.81	18.99	0.00	0.53	0.15	5.52	8.55	0.24	99.79	50.1
		24	66.45	18.91	0.00	0.47	0.18	5.82	8.49	0.18	100.51	48.6
		27	67.20	19.27	0.00	0.49	0.12	5.85	8.67	0.13	101.71	49.1
		28	67.17	19.02	0.04	0.48	0.17	5.63	8.63	0.24	101.39	49.8
		29	66.62	18.88	0.00	0.47	0.11	5.44	8.69	0.19	100.39	51.0
	Granophyre	15	66.39	18.88	0.00	0.45	0.13	5.53	8.12	0.15	99.62	48.8
		16	66.90	18.75	0.00	0.44	0.17	5.57	8.89	0.00	100.71	50.8
		17	66.19	18.82	0.00	0.40	0.19	5.52	9.16	0.12	100.35	51.7
		18	66.27	18.56	0.00	0.29	0.13	5.28	9.07	0.08	99.68	52.8
		19	66.33	18.54	0.00	0.34	0.19	5.12	9.10	0.10	99.71	53.4
		20	66.56	18.79	0.00	0.38	0.19	5.74	8.66	0.04	100.36	49.4
Y36	**Cores**	34	65.91	19.24	0.01	0.85	0.21	6.23	6.84	0.72	100.00	41.5
		35	65.32	19.28	0.00	0.95	0.14	6.67	6.49	0.58	99.42	38.8
		37	65.97	19.18	0.02	0.68	0.17	5.85	7.33	0.52	99.71	44.8
		38	67.37	19.18	0.00	0.57	0.16	6.56	7.48	0.50	101.80	42.5
		48	66.42	19.27	0.00	0.72	0.19	6.09	7.43	0.63	100.76	44.1
		49	65.93	19.08	0.00	0.69	0.17	6.26	7.07	0.74	99.92	42.3
		51	66.46	19.43	0.02	0.74	0.20	6.30	7.14	0.77	101.07	42.3
		53	66.22	18.93	0.06	0.56	0.11	5.76	7.69	0.54	99.86	46.5

[a] Total iron reported as FeO, "-" indicates oxide not analyzed

							Feldspar					
Sample		**Spot**	**SiO_2**	**Al_2O_3**	**FeO**	**MgO**	**CaO**	**Na_2O**	**K_2O**	**BaO**	**Total**	**Or#**
Solfatara Plateau												
Y36	**Cores**	55	66.74	19.08	0.01	0.59	0.10	6.06	7.50	0.41	100.49	44.7
		56	67.41	19.07	0.00	0.52	0.15	6.55	7.81	0.35	101.86	43.6
		57	66.05	19.72	0.01	1.24	0.15	7.20	5.77	0.67	100.83	34.2
		58	66.46	19.04	0.00	0.67	0.14	6.21	7.40	0.30	100.21	43.6
	Rims	36	63.67	19.03	0.00	0.91	0.20	6.34	6.67	0.74	97.56	40.5
		39	66.70	19.22	0.01	0.63	0.15	6.48	7.27	0.58	101.03	42.1
		50	66.45	19.21	0.00	0.70	0.17	6.01	7.36	0.73	100.60	44.3
		52	66.81	18.80	0.00	0.50	0.25	5.69	7.86	0.63	100.55	47.0
		54	66.09	19.09	0.00	0.58	0.15	6.19	7.36	0.41	99.85	43.6
		59	66.89	18.94	0.01	0.55	0.20	6.04	7.49	0.61	100.73	44.5
	Granophyre	40	66.75	19.23	0.00	0.52	0.14	5.83	7.80	0.74	101.00	46.5
		41	66.45	19.55	0.01	0.69	0.16	5.88	7.57	0.80	101.12	45.5
		42	65.86	18.83	0.00	0.66	0.14	5.75	7.54	0.75	99.53	46.0
		43	65.94	19.24	0.00	0.56	0.16	6.16	7.44	0.79	100.28	43.9
		44	66.08	19.08	0.01	0.54	0.15	6.08	7.74	0.67	100.36	45.2
		45	65.96	19.19	0.00	0.69	0.18	6.54	6.55	0.83	99.93	39.3
		46	67.72	18.28	0.04	0.59	0.21	6.75	6.03	0.72	100.34	36.6
		47	66.85	19.48	0.00	0.67	0.19	7.00	6.19	0.81	101.21	36.4
Y47	**Cores**	84	66.68	19.16	0.02	0.55	0.14	5.89	8.46	0.18	101.06	48.3
		93	65.94	19.17	0.00	0.52	0.13	5.57	8.60	0.20	100.10	50.1
		95	65.64	19.18	0.02	0.56	0.19	5.82	8.34	0.20	99.96	48.1
		96	66.19	18.94	0.01	0.42	0.20	5.82	8.85	0.20	100.62	49.5
		103	66.43	19.06	0.15	0.02	0.54	5.39	8.73	0.15	100.47	50.2
		104	66.89	18.82	0.12	0.00	0.44	5.23	9.24	0.15	100.89	52.6
	Rims	85	67.00	19.21	0.02	0.47	0.13	5.89	8.44	0.15	101.32	48.2
		92	66.37	19.24	0.00	0.47	0.11	5.73	8.24	0.13	100.27	48.3
		94	67.13	19.25	0.02	0.51	0.21	6.45	8.03	0.19	101.78	44.6
		97	66.41	19.11	0.08	0.01	0.51	5.73	8.85	0.12	100.81	49.2
		105	66.91	18.88	0.16	0.00	0.45	5.31	8.98	0.18	100.87	51.5

[a] Total iron reported as FeO, "-" indicates oxide not analyzed

Appendix 2. (cont.) Compilation of all microprobe analyses of natural samples and experiments.

							Feldspar					
Sample		**Spot**	**SiO_2**	**Al_2O_3**	**FeO**	**MgO**	**CaO**	**Na_2O**	**K_2O**	**BaO**	**Total**	**Or#**
	Granophyre	79	66.56	18.75	0.02	0.41	0.18	5.54	8.73	0.09	100.28	50.5
		80	65.97	18.91	0.02	0.47	0.23	5.78	8.16	0.12	99.65	47.6
		81	66.33	18.94	0.01	0.38	0.16	6.26	8.31	0.12	100.51	46.3
		82	65.72	18.60	0.00	0.42	0.14	5.77	8.57	0.01	99.23	49.1
		83	65.74	18.94	0.00	0.51	0.16	6.00	7.85	0.20	99.36	45.9
		86	66.58	18.92	0.00	0.42	0.20	6.00	8.82	0.13	101.06	48.7
		87	66.67	19.10	0.02	0.47	0.17	5.33	8.72	0.09	100.57	51.4
		88	66.51	19.19	0.02	0.63	0.19	5.88	8.28	0.07	100.77	47.6
		89	66.65	19.02	0.00	0.41	0.15	5.66	8.79	0.06	100.70	50.2
		90	66.39	19.01	0.00	0.47	0.09	5.99	8.56	0.09	100.57	48.3
		91	66.15	18.98	0.00	0.48	0.19	5.31	8.86	0.18	100.16	51.8
		98	67.01	19.16	0.00	0.43	0.14	5.38	8.74	0.12	100.99	51.3
		99	66.34	19.20	0.01	0.56	0.13	5.73	8.43	0.11	100.50	48.9
		100	66.74	19.12	0.02	0.40	0.18	5.18	9.12	0.13	100.89	53.2
		101	66.80	19.12	0.00	0.44	0.16	5.55	8.83	0.10	100.97	50.8
		87	65.97	18.97	0.13	0.00	0.40	5.31	8.97	0.19	99.94	51.6
		88	65.80	18.93	0.14	0.00	0.50	5.79	8.81	0.11	100.08	48.9
		93	66.67	18.65	0.17	0.01	0.39	5.36	8.89	0.13	100.27	51.2
		94	66.72	18.84	0.16	0.00	0.40	5.30	9.01	0.11	100.54	51.8
		95	67.02	18.86	0.15	0.03	0.38	5.23	9.14	0.09	100.90	52.5
		96	66.48	19.13	0.11	0.00	0.46	5.52	9.04	0.09	100.84	50.7
		98	66.55	18.64	0.16	0.00	0.40	5.48	8.95	0.15	100.33	50.8
		99	65.43	18.62	0.18	0.01	0.42	5.42	8.83	0.09	99.01	50.7
		100	66.43	19.06	0.14	0.00	0.52	5.80	8.47	0.10	100.52	47.8
		101	66.70	18.85	0.18	0.00	0.43	5.66	8.80	0.11	100.72	49.6
		102	66.91	18.79	0.13	0.02	0.45	5.58	8.99	0.14	101.01	50.4
		106	66.71	18.96	0.17	0.02	0.42	5.23	9.12	0.20	100.83	52.3
Y60	**Cores**	69	66.06	18.77	0.15	0.02	0.47	5.03	8.65	0.12	99.27	51.8
		71	66.80	19.14	0.14	0.00	0.48	5.55	8.68	0.38	101.17	49.6
		80	66.66	18.91	0.15	0.00	0.51	5.53	8.82	0.22	100.80	49.9
		83	66.92	18.66	0.12	0.00	0.43	5.36	8.89	0.21	100.59	51.1

[a] Total iron reported as FeO, "-" indicates oxide not analyzed

			Feldspar									
Sample		**Spot**	**SiO_2**	**Al_2O_3**	**FeO**	**MgO**	**CaO**	**Na_2O**	**K_2O**	**BaO**	**Total**	**Or#**
Y60	**Rims**	70	66.18	19.01	0.16	0.02	0.52	5.49	8.60	0.14	100.12	49.5
		72	67.01	18.80	0.17	0.02	0.41	5.70	8.90	0.10	101.10	49.7
		76	66.93	18.68	0.15	0.03	0.37	5.56	9.21	0.15	101.08	51.3
		81	66.60	18.73	0.17	0.00	0.39	5.66	8.45	0.22	100.23	48.6
		84	67.22	19.00	0.16	0.02	0.50	6.56	7.81	0.18	101.44	42.9
	Granophyre	73	66.82	18.77	0.15	0.00	0.30	4.95	9.05	0.12	100.15	53.8
		74	66.47	18.87	0.19	0.00	0.44	5.38	8.46	0.14	99.94	49.8
		75	67.32	18.80	0.12	0.00	0.39	5.79	8.82	0.14	101.39	49.1
		77	67.23	19.06	0.16	0.04	0.52	5.76	8.54	0.17	101.46	48.2
		78	66.92	18.87	0.18	0.02	0.46	5.71	8.61	0.16	100.92	48.7
		79	66.74	19.03	0.14	0.00	0.44	5.54	8.97	0.11	100.99	50.5
		82	66.74	18.72	0.19	0.00	0.48	5.73	8.76	0.09	100.70	49.0
		85	66.97	18.94	0.14	0.00	0.53	5.81	8.77	0.14	101.28	48.6
		86	66.82	19.11	0.12	0.00	0.57	6.01	8.69	0.20	101.53	47.5
Y33	**Cores**	6	66.56	18.95	0.17	0.01	0.47	5.53	8.81	0.21	100.71	50.0
		10	66.43	18.95	0.14	0.01	0.54	5.72	8.49	0.20	100.46	48.1
		17	65.96	18.99	0.12	0.02	0.50	5.48	8.52	0.17	99.76	49.4
		23	66.27	18.65	0.11	0.00	0.42	5.32	8.80	0.07	99.64	51.1
		28	65.84	18.70	0.11	0.00	0.56	5.48	8.49	0.09	99.28	49.1
		35	66.46	18.60	0.18	0.00	0.50	5.30	8.74	0.16	99.94	50.7
		39	66.16	19.11	0.12	0.02	0.56	5.54	8.44	0.57	100.52	48.7
		45	66.25	19.03	0.16	0.00	0.55	5.71	8.40	0.25	100.35	47.9
		49	66.07	18.83	0.14	0.00	0.44	5.46	8.94	0.26	100.15	50.7
		52	66.54	18.97	0.08	0.00	0.48	5.58	8.57	0.24	100.47	49.1
		53	65.49	18.91	0.12	0.00	0.52	5.23	8.72	0.17	99.16	51.0
		59	66.41	18.97	0.15	0.00	0.52	5.92	8.60	0.24	100.81	47.7
		60	66.40	19.01	0.16	0.00	0.46	5.39	8.89	0.20	100.51	50.9
		62	66.16	18.83	0.12	0.01	0.52	5.60	8.76	0.25	100.23	49.5
		63	67.05	18.75	0.13	0.01	0.56	6.55	7.33	0.14	100.52	41.3
		106	65.03	18.35	0.14	0.00	0.47	4.98	8.51	-	97.48	51.7
		108	66.59	18.80	0.13	0.00	0.57	5.24	8.42	-	99.75	50.0
		110	66.01	18.75	0.15	0.01	0.54	5.13	8.49	-	99.08	50.7
		112	67.12	18.82	0.14	0.00	0.52	5.21	8.54	-	100.35	50.5

[a] Total iron reported as FeO, "-" indicates oxide not analyzed

Appendix 2. (cont.) Compilation of all microprobe analyses of natural samples and experiments.

							Feldspar					
Sample		**Spot**	**SiO_2**	**Al_2O_3**	**FeO**	**MgO**	**CaO**	**Na_2O**	**K_2O**	**BaO**	**Total**	**Or#**
Y33	**Cores**	114	67.58	19.16	0.10	0.00	0.44	5.25	8.47	-	101.00	50.3
		116	66.75	18.70	0.12	0.01	0.53	5.22	8.59	-	99.92	50.6
		118	67.42	19.00	0.15	0.00	0.51	5.02	8.66	-	100.75	51.8
		120	66.63	18.83	0.14	0.01	0.59	5.28	8.39	-	99.87	49.6
		122	66.48	19.18	0.12	0.00	0.58	5.31	8.44	-	100.11	49.6
		124	67.37	19.26	0.18	0.00	0.54	5.25	8.35	-	100.95	49.7
	Rims	4	66.51	18.81	0.12	0.01	0.51	5.52	8.58	0.16	100.21	49.3
		7	66.63	18.96	0.19	0.02	0.56	6.48	7.14	0.17	100.15	40.9
		11	65.99	18.76	0.18	0.04	0.49	5.23	8.72	0.19	99.60	51.1
		20	66.34	18.76	0.14	0.01	0.46	5.50	8.70	0.21	100.12	49.9
		22	66.54	18.76	0.16	0.00	0.46	5.56	8.84	0.23	100.53	50.0
		24	66.01	18.68	0.17	0.00	0.48	5.06	8.65	0.13	99.18	51.7
		26	66.30	18.71	0.12	0.00	0.48	5.59	8.55	0.21	99.96	49.0
		29	66.58	18.98	0.20	0.01	0.69	7.32	6.15	0.16	100.09	34.4
		40	66.40	18.66	0.14	0.00	0.51	5.39	8.67	0.18	99.96	50.1
		51	66.37	18.91	0.17	0.01	0.45	5.80	8.74	0.14	100.60	48.7
		54	65.96	18.98	0.19	0.00	0.55	6.35	7.50	0.21	99.74	42.6
		57	66.54	18.59	0.18	0.01	0.39	5.77	8.39	0.13	100.00	48.0
		107	66.53	18.90	0.13	0.00	0.51	5.02	8.54	-	99.60	51.4
		109	66.20	18.89	0.15	0.00	0.55	5.16	8.31	-	99.25	50.0
		111	67.12	18.99	0.17	0.00	0.53	6.20	6.83	-	99.84	40.9
		113	66.84	19.17	0.14	0.00	0.55	5.29	8.41	-	100.40	49.7
		115	66.81	18.62	0.14	0.04	0.47	5.82	7.56	-	99.47	45.0
		117	67.26	18.91	0.12	0.00	0.58	6.29	6.83	-	99.99	40.5
		119	66.39	18.75	0.13	0.00	0.54	5.14	8.43	-	99.35	50.5
		121	66.28	18.88	0.11	0.01	0.56	5.10	8.34	-	99.29	50.4
		123	66.41	18.67	0.16	0.00	0.44	6.10	7.20	-	98.99	42.8
		126	67.95	19.28	0.16	0.00	0.53	5.49	8.08	-	101.49	47.9
		127	67.30	19.20	0.13	0.00	0.55	5.80	7.23	-	100.22	43.8
		128	66.33	19.01	0.11	0.00	0.55	5.09	8.40	-	99.48	50.6
		129	66.31	18.84	0.17	0.00	0.48	5.09	8.56	-	99.45	51.3
		130	66.48	19.21	0.15	0.00	0.49	5.00	8.66	-	100.00	52.0
		131	65.96	18.66	0.12	0.03	0.54	4.97	8.47	-	98.75	51.4
		132	67.08	19.01	0.16	0.00	0.55	5.17	8.49	-	100.47	50.5

[a] Total iron reported as FeO, "-" indicates oxide not analyzed

Sample		Spot	SiO_2	Al_2O_3	FeO	MgO	CaO	Na_2O	K_2O	BaO	Total	Or#
Y33	**ıranophyre**	5	66.99	18.93	0.15	0.00	0.54	6.69	7.70	0.14	101.15	42.0
		8	66.31	18.60	0.12	0.00	0.46	5.85	8.71	0.14	100.18	48.4
		9	66.71	18.86	0.13	0.01	0.48	5.89	7.65	0.11	99.84	45.0
		13	67.64	18.90	0.13	0.00	0.42	6.63	7.19	0.07	100.98	40.8
		14	66.37	18.76	0.15	0.00	0.42	5.39	8.67	0.18	99.95	50.4
		15	67.13	17.78	0.25	0.02	0.52	6.21	6.25	0.12	98.28	38.7
		16	67.30	18.96	0.14	0.00	0.68	7.07	6.05	0.11	100.30	34.8
		18	66.26	18.69	0.17	0.01	0.46	5.77	8.50	0.17	100.04	48.1
		19	66.21	18.63	0.15	0.00	0.47	6.14	7.88	0.13	99.60	44.7
		21	67.85	18.82	0.11	0.00	0.68	7.39	5.20	0.12	100.18	30.6
		25	66.41	18.86	0.15	0.00	0.49	6.24	8.12	0.09	100.37	45.1
		27	66.54	18.54	0.15	0.01	0.39	5.85	7.76	0.11	99.36	45.7
		30	65.84	18.75	0.17	0.03	0.42	5.65	8.39	0.08	99.31	48.4
		31	66.71	18.89	0.20	0.00	0.61	7.03	6.10	0.08	99.63	35.2
		36	67.01	19.06	0.20	0.00	0.68	7.29	5.93	0.16	100.33	33.7
		37	66.76	19.03	0.20	0.01	0.42	6.14	7.85	0.21	100.63	44.8
		38	66.57	19.01	0.20	0.00	0.53	6.85	6.75	0.12	100.03	38.4
		41	67.50	19.16	0.15	0.00	0.63	7.90	5.43	0.04	100.81	30.2
		42	67.21	18.98	0.14	0.03	0.42	6.59	7.63	0.11	101.11	42.4
		47	66.62	18.98	0.15	0.03	0.56	6.52	7.03	0.08	99.96	40.4
		48	66.34	19.09	0.15	0.01	0.43	6.06	7.86	0.08	100.02	45.1
		50	66.41	18.89	0.26	0.00	0.36	5.86	9.02	0.09	100.89	49.5
		55	67.21	19.32	0.22	0.00	0.50	7.02	7.11	0.18	101.56	39.1
		56	66.52	18.75	0.17	0.01	0.69	7.89	4.90	0.12	99.04	28.0
		58	66.28	18.66	0.16	0.02	0.41	5.51	8.92	0.14	100.10	50.6
		61	66.96	18.76	0.16	0.00	0.36	5.20	8.92	0.14	100.51	52.1
		134	66.85	18.91	0.17	0.01	0.48	5.78	7.78	-	99.99	45.9
		135	67.24	19.05	0.15	0.02	0.45	5.54	8.03	-	100.48	47.7
		136	67.92	18.99	0.11	0.01	0.39	5.35	8.16	-	100.93	49.1
Y49	**Cores**	137	66.10	18.76	0.13	0.01	0.54	5.02	8.44	-	99.01	51.1
		141	65.06	18.42	0.10	0.00	0.50	4.83	8.40	-	97.31	52.0
		145	65.15	18.51	0.11	0.02	0.46	5.02	8.49	-	97.77	51.5
		147	66.13	18.75	0.16	0.00	0.55	5.03	8.35	-	98.96	50.8
		149	67.06	18.89	0.14	0.00	0.49	5.08	8.54	-	100.21	51.3

[a] Total iron reported as FeO, "-" indicates oxide not analyzed

Appendix 2. (cont.) Compilation of all microprobe analyses of natural samples and experiments.

Feldspar

Sample		Spot	SiO_2	Al_2O_3	FeO	MgO	CaO	Na_2O	K_2O	BaO	Total	Or#
Y49	**Cores**	151	66.53	18.97	0.15	0.01	0.56	5.19	8.46	-	99.87	50.3
		153	66.48	18.75	0.13	0.02	0.51	4.99	8.54	-	99.42	51.6
		155	64.52	18.41	0.12	0.00	0.56	5.00	8.38	-	96.99	51.0
	Rims	138	66.63	19.02	0.10	0.00	0.52	5.23	8.46	-	99.96	50.2
		140	66.18	18.63	0.13	0.00	0.59	5.06	8.35	-	98.93	50.5
		142	65.22	18.57	0.11	0.00	0.52	4.98	8.56	-	97.92	51.7
		146	65.88	18.85	0.17	0.00	0.52	5.21	8.41	-	99.03	50.2
		148	66.21	18.76	0.11	0.01	0.52	5.04	8.31	-	98.96	50.6
		150	66.99	18.89	0.16	0.00	0.49	5.05	8.56	-	100.11	51.4
		154	67.31	19.12	0.10	0.02	0.50	5.52	8.09	-	100.66	47.8
		156	65.33	18.48	0.17	0.00	0.52	5.06	8.51	-	98.05	51.1
		157	65.80	18.48	0.13	0.00	0.52	5.06	8.48	-	98.46	51.1
		158	66.85	18.82	0.19	0.00	0.54	5.09	8.48	-	99.95	50.9
		159	66.83	18.93	0.17	0.00	0.58	5.11	8.44	-	100.05	50.6
		160	67.25	19.08	0.15	0.02	0.52	5.18	8.42	-	100.62	50.3
		161	66.34	19.02	0.11	0.01	0.57	5.04	8.45	-	99.54	50.9
		162	65.41	18.77	0.13	0.01	0.60	4.93	8.56	-	98.41	51.7
		163	66.70	18.97	0.12	0.00	0.54	5.15	8.44	-	99.94	50.5
		164	66.47	18.85	0.13	0.00	0.53	5.06	8.56	-	99.60	51.3
		165	66.62	18.70	0.16	0.00	0.54	5.16	8.58	-	99.75	50.8
		166	66.15	18.87	0.14	0.00	0.51	5.06	8.48	-	99.21	51.1
		168	65.42	18.55	0.15	0.03	0.59	5.00	8.31	-	98.04	50.7
West Yellowstone												
	Cores	217	66.84	19.14	0.18	0.00	0.51	5.28	8.59	-	100.56	50.4
		223	66.67	19.01	0.10	0.00	0.45	4.85	8.84	-	99.93	53.3
		229	66.80	19.05	0.13	0.00	0.47	4.98	8.65	-	100.08	52.1
		231	66.59	19.10	0.14	0.00	0.48	5.18	8.61	-	100.11	51.0
		233	66.72	19.04	0.16	0.00	0.51	4.98	8.51	-	99.91	51.6
	Rims	218	66.27	18.82	0.13	0.00	0.55	5.14	8.45	-	99.35	50.5
		228	66.85	18.91	0.14	0.00	0.50	5.07	8.63	-	100.09	51.5
		230	66.63	18.99	0.13	0.00	0.51	5.01	8.61	-	99.89	51.7
		232	67.33	19.03	0.13	0.00	0.51	5.09	8.74	-	100.82	51.7

[a] Total iron reported as FeO, "-" indicates oxide not analyzed

Appendix 2. (cont.) Compilation of all microprobe analyses of natural samples and experiments.

							Feldspar					
Sample		**Spot**	**SiO_2**	**Al_2O_3**	**FeO**	**MgO**	**CaO**	**Na_2O**	**K_2O**	**BaO**	**Total**	**Or#**
	Rims	235	66.93	18.90	0.09	0.00	0.50	5.38	8.12	-	99.92	48.6
		236	66.03	18.65	0.11	0.00	0.52	5.12	8.58	-	99.01	51.1
		237	67.11	19.44	0.13	0.00	0.54	5.15	8.68	-	101.05	51.2
		239	66.16	18.70	0.08	0.00	0.44	4.98	8.70	-	99.05	52.3
		240	66.45	19.03	0.12	0.00	0.56	5.21	8.44	-	99.80	50.2
		242	66.50	18.87	0.18	0.00	0.47	5.06	8.73	-	99.80	51.9
		243	66.15	18.77	0.12	0.00	0.56	4.99	8.38	-	98.98	51.0
		244	66.19	19.01	0.13	0.02	0.53	5.10	8.53	-	99.51	51.0
Summit Lake												
Y74	**Cores**	27	65.68	18.30	0.07	0.00	0.52	5.15	8.42	-	98.14	50.5
		29	67.03	18.84	0.15	0.02	0.54	5.25	8.56	-	100.39	50.4
		31	66.86	19.09	0.18	0.00	0.59	5.08	8.57	-	100.37	51.0
		33	66.52	19.11	0.15	0.00	0.49	5.07	8.59	-	99.92	51.4
	Rims	28	65.17	18.69	0.16	0.01	0.56	5.03	8.25	-	97.87	50.4
		30	66.43	19.06	0.13	0.00	0.52	5.21	8.45	-	99.80	50.3
		32	65.99	18.79	0.16	0.01	0.57	5.06	8.45	-	99.04	50.9
		34	66.60	18.97	0.12	0.00	0.49	5.09	8.56	-	99.84	51.2
		35	66.86	19.16	0.12	0.00	0.50	5.15	8.65	-	100.45	51.2
		36	66.07	18.94	0.16	0.00	0.55	5.12	8.60	-	99.44	51.0
		37	66.89	19.03	0.13	0.00	0.59	5.25	8.49	-	100.36	50.1
		39	66.42	18.61	0.13	0.00	0.51	4.92	8.66	-	99.23	52.3
		40	66.45	18.87	0.16	0.00	0.54	5.07	8.59	-	99.67	51.3
		41	66.58	18.72	0.13	0.00	0.49	4.95	8.55	-	99.40	51.8
		42	66.86	18.90	0.15	0.01	0.52	5.17	8.39	-	99.99	50.3
		43	66.63	19.06	0.19	0.00	0.55	5.27	8.47	-	100.14	50.0
		44	65.52	18.74	0.10	0.00	0.49	5.17	8.43	-	98.44	50.5
		45	65.07	18.48	0.09	0.00	0.50	5.13	8.38	-	97.65	50.5
		46	64.74	18.47	0.19	0.00	0.58	5.08	8.30	-	97.35	50.3
		47	65.48	18.54	0.17	0.00	0.62	5.33	8.13	-	98.27	48.6
		49	65.63	18.62	0.16	0.01	0.51	5.12	8.46	-	98.51	50.8
		50	65.70	18.81	0.18	0.04	0.50	5.17	8.35	-	98.76	50.2
		52	64.78	18.38	0.12	0.01	0.54	5.17	8.41	-	97.40	50.3
		53	65.17	18.40	0.10	0.00	0.52	5.08	8.51	-	97.77	51.1

[a] Total iron reported as FeO, "-" indicates oxide not analyzed

Appendix 2. (cont.) Compilation of all microprobe analyses of natural samples and experiments.

							Feldspar					
Sample		**Spot**	**SiO_2**	**Al_2O_3**	**FeO**	**MgO**	**CaO**	**Na_2O**	**K_2O**	**BaO**	**Total**	**Or#**
	Rims	54	66.08	18.77	0.13	0.01	0.52	5.23	8.60	-	99.34	50.6
		56	66.33	18.53	0.12	0.00	0.45	5.23	8.45	-	99.10	50.4
		57	66.37	18.69	0.13	0.00	0.45	5.21	8.48	-	99.34	50.6
		58	66.40	18.54	0.10	0.01	0.39	5.03	8.66	-	99.13	52.0
Pitchstone Plateau												
Y187	**Cores**	179	63.96	18.25	0.11	0.02	0.44	4.94	8.53	-	96.26	52.0
		199	66.64	18.92	0.11	0.02	0.46	4.93	8.73	-	99.81	52.6
		201	66.68	19.06	0.16	0.02	0.49	4.92	8.55	-	99.88	52.0
		203	67.01	18.83	0.12	0.01	0.45	4.95	8.74	-	100.11	52.5
	Rims	180	64.82	18.33	0.13	0.00	0.42	4.90	8.63	-	97.23	52.5
		182	65.17	18.52	0.12	0.00	0.50	4.97	8.46	-	97.72	51.5
		200	67.93	19.18	0.17	0.00	0.40	5.10	8.77	-	101.54	52.0
		202	66.54	18.90	0.18	0.00	0.52	5.06	8.55	-	99.74	51.3
		204	66.83	19.25	0.20	0.00	0.48	4.96	8.72	-	100.44	52.3
Trischmann Knob												
	Rims	59	66.24	18.78	0.17	0.00	0.52	5.22	8.39	-	99.32	50.1
		60	66.59	18.94	0.12	0.01	0.55	5.26	8.17	-	99.64	49.1
		61	65.56	18.82	0.16	0.00	0.62	5.05	8.16	-	98.36	49.9
		62	65.69	18.69	0.16	0.00	0.61	5.09	8.29	-	98.52	50.1
		74	64.15	18.48	0.15	0.04	0.52	5.03	8.30	-	96.67	50.7
Douglas Knob												
Y88	**Rims**	45	65.92	19.02	0.09	0.04	0.00	5.63	8.87	0.24	99.82	50.8
		46	65.69	19.05	0.10	0.02	0.00	5.81	8.81	0.25	99.73	49.9
		48	67.39	18.95	0.09	0.02	0.00	5.47	7.99	0.29	100.20	49.0
		49	67.41	19.12	0.15	0.00	0.03	5.62	8.46	0.26	101.05	49.8
		50	67.33	19.07	0.11	0.00	0.00	5.65	8.28	0.20	100.64	49.1
		51	66.90	19.06	0.10	0.00	0.00	5.41	8.29	0.26	100.02	50.2
		52	65.38	18.75	0.17	0.00	0.00	5.47	8.59	0.21	98.56	50.8

[a]Total iron reported as FeO, "-" indicates oxide not analyzed

Feldspar

Sample		Spot	SiO_2	Al_2O_3	FeO	MgO	CaO	Na_2O	K_2O	BaO	Total	Or#
Y89	**Rims**	53	65.65	19.31	0.16	0.00	0.07	5.81	8.24	0.21	99.45	48.3
		55	65.71	19.26	0.14	0.02	0.00	5.57	8.50	0.15	99.34	50.0
		56	66.64	19.35	0.15	0.00	0.03	5.96	8.56	0.27	100.96	48.6
		57	66.38	19.35	0.13	0.00	0.00	5.31	8.47	0.42	100.06	51.2
		58	66.94	19.32	0.17	0.00	0.00	5.97	8.89	0.27	101.55	49.5
		59	67.80	19.44	0.12	0.00	0.00	5.48	8.55	0.17	101.56	50.6
Y90	**Rims**	8	66.92	19.07	0.09	0.00	0.00	5.82	8.83	0.39	101.04	50.0
		18	66.50	19.07	0.13	0.02	0.00	5.32	8.70	0.25	99.96	51.8
		21	66.61	19.03	0.11	0.00	0.00	5.59	9.05	0.27	100.55	51.6
		22	65.60	19.20	0.13	0.04	0.00	5.39	9.03	0.38	99.64	52.3
		23	65.86	19.06	0.15	0.01	0.00	5.44	8.80	0.36	99.63	51.6
Y90	**Rims**	60	67.01	18.93	0.15	0.02	0.04	5.31	8.07	0.21	99.74	49.9
		61	65.63	19.51	0.14	0.01	0.00	5.79	8.56	0.61	100.25	49.3
		62	65.12	18.55	0.19	0.01	0.00	5.06	8.14	0.35	97.41	51.4

---

[a] Total iron reported as FeO, "-" indicates oxide not analyzed

Clinopyroxene

Appendix 2. Compilation of all microprobe analyses of natural samples and experiments.

			Clinopyroxene									
Sample		**Spot**	**SiO_2**	**TiO_2**	**Al_2O_3**	**FeO**	**MgO**	**MnO**	**CaO**	**K_2O**	**Na_2O**	**Total**
Solfatara Plateau												
Y60	**Cores**	232	49.57	0.15	0.53	27.01	4.10	0.78	18.66	-	0.32	101.11
		249	49.05	0.07	0.55	26.23	4.67	0.78	19.02	-	0.32	100.68
		256	49.96	0.24	0.55	24.91	5.63	0.79	18.13	-	0.26	100.48
	Rims	228	48.66	0.25	0.59	27.02	3.98	0.79	18.16	-	0.32	99.76
		230	49.30	0.07	0.55	27.06	4.11	0.78	18.85	-	0.26	100.98
		231	49.46	0.15	0.52	27.28	3.66	0.81	18.81	-	0.35	101.04
		233	49.20	0.17	0.58	27.27	3.73	0.82	18.27	-	0.30	100.35
		237	49.14	0.23	0.54	26.59	4.31	0.75	18.98	-	0.29	100.83
		240	49.29	0.22	0.60	28.09	3.76	0.87	17.69	-	0.30	100.82
		243	49.91	0.22	0.55	27.16	3.91	0.80	18.88	-	0.28	101.70
		244	49.51	0.19	0.54	26.26	4.40	0.79	18.86	-	0.31	100.85
		247	48.14	0.17	0.54	27.04	4.01	0.75	18.75	-	0.29	99.69
		250	49.71	0.14	0.52	26.82	3.87	0.81	18.77	-	0.32	100.97
		252	49.76	0.21	0.59	26.92	4.08	0.76	18.73	-	0.32	101.37
		253	49.38	0.08	0.53	26.75	4.29	0.77	19.00	-	0.30	101.11
		255	49.46	0.32	0.57	27.31	4.03	0.82	18.43	-	0.32	101.26
		257	50.11	0.18	0.49	25.83	5.31	0.75	18.44	-	0.27	101.40
		259	49.67	0.17	0.54	25.85	4.97	0.76	18.85	-	0.30	101.10
		260	49.18	0.12	0.51	26.50	4.32	0.76	18.90	-	0.35	100.63
		261	49.05	0.16	0.52	25.65	5.31	0.76	18.79	-	0.25	100.49
		265	49.52	0.07	0.53	27.13	3.86	0.81	18.90	-	0.27	101.09
		266	49.80	0.09	0.52	26.98	3.90	0.83	18.84	-	0.30	101.26
		267	49.28	0.20	0.54	27.32	4.10	0.77	18.76	-	0.32	101.30
		343	49.60	0.21	0.17	24.57	5.37	0.67	18.42	-	0.33	99.35
		345	49.73	0.14	0.19	26.44	4.07	0.75	18.95	-	0.26	100.52
		346	49.85	0.35	0.24	26.05	4.33	0.72	18.89	-	0.30	100.72
Y82	**Cores**	310	50.14	0.22	0.25	24.92	5.00	0.75	18.61	-	0.28	100.18
		327	49.61	0.20	0.19	26.63	4.02	0.71	18.96	-	0.25	100.58
		336	51.85	0.35	0.32	20.67	8.69	0.66	18.98	-	0.31	101.82

[a]Total iron reported as FeO, "-" indicates oxide not analyzed

Appendix 2. (cont.) Compilation of all microprobe analyses of natural samples and experiments.

						Clinopyroxene						
Sample		**Spot**	**SiO_2**	**TiO_2**	**Al_2O_3**	**FeO**	**MgO**	**MnO**	**CaO**	**K_2O**	**Na_2O**	**Total**
Solfatara Plateau												
Y82	**Rims**	296	49.32	0.13	0.23	25.85	4.26	0.68	18.95	-	0.27	99.70
		307	50.49	0.23	0.26	26.47	4.22	0.72	18.61	-	0.28	101.28
		308	49.81	0.31	0.26	26.33	4.10	0.68	18.97	-	0.30	100.76
		309	49.56	0.16	0.18	26.30	3.98	0.69	18.81	-	0.28	99.96
		312	50.38	0.24	0.22	26.57	4.31	0.73	18.75	-	0.30	101.49
		316	50.86	0.25	0.23	26.71	4.11	0.71	18.76	-	0.27	101.91
		317	51.65	0.27	0.27	26.76	4.31	0.67	18.74	-	0.30	102.98
		319	50.83	0.38	0.21	26.20	4.25	0.77	18.80	-	0.30	101.74
		326	49.68	0.26	0.24	26.51	4.15	0.68	18.82	-	0.32	100.64
		332	50.48	0.43	0.21	25.81	4.55	0.74	18.65	-	0.29	101.16
		334	46.17	0.15	0.30	26.44	4.06	0.73	18.23	-	0.26	96.34
		335	50.39	0.31	0.23	26.30	4.18	0.70	18.85	-	0.31	101.27
		342	49.97	0.24	0.25	26.09	4.16	0.68	18.60	-	0.29	100.28
Y47	**Cores**	395	49.69	0.19	0.50	26.09	4.63	0.68	18.81	-	0.31	100.90
		405	49.53	0.20	0.59	27.14	4.37	0.68	18.61	-	0.30	101.41
		409	48.94	0.18	0.51	27.19	4.17	0.67	18.82	-	0.30	100.78
		410	49.70	0.39	0.57	26.55	4.20	0.68	18.78	-	0.38	101.23
		412	48.98	0.17	0.52	26.85	3.83	0.70	18.76	-	0.32	100.14
		422	48.96	0.21	0.55	26.94	4.04	0.67	18.54	-	0.31	100.20
	Rims	386	49.11	0.20	0.54	27.43	3.52	0.68	18.59	-	0.30	100.36
		388	49.28	0.35	0.58	26.81	4.16	0.75	18.53	-	0.32	100.76
		389	49.43	0.17	0.54	26.91	3.79	0.70	18.65	-	0.32	100.49
		390	49.07	0.27	0.54	26.25	4.43	0.66	18.76	-	0.31	100.29
		393	49.17	0.29	0.58	26.62	3.88	0.68	18.54	-	0.31	100.07
		394	49.46	0.18	0.55	26.87	3.89	0.71	18.67	-	0.32	100.66
		399	48.75	0.19	0.59	26.68	3.66	0.69	18.63	-	0.29	99.47
		400	49.04	0.26	0.59	27.66	3.60	0.75	18.60	-	0.30	100.80
		401	48.79	0.29	0.51	27.37	3.88	0.71	18.51	-	0.35	100.39
		402	49.27	0.20	0.52	26.48	3.93	0.68	18.83	-	0.27	100.17
		406	49.06	0.17	0.57	27.85	3.72	0.70	18.31	-	0.36	100.73

[a]Total iron reported as FeO, "-" indicates oxide not analyzed

Sample		Spot	SiO_2	TiO_2	Al_2O_3	FeO	MgO	MnO	CaO	K_2O	Na_2O	Total
						Clinopyroxene						
Solfatara Plateau												
Y47	**Cores**	407	49.25	0.23	0.52	26.70	3.92	0.66	18.78	-	0.26	100.32
		408	48.68	0.11	0.56	27.39	3.91	0.71	18.45	-	0.39	100.19
		411	49.10	0.09	0.52	26.96	3.97	0.71	18.73	-	0.33	100.42
		414	49.46	0.21	0.57	27.36	4.14	0.72	18.71	-	0.30	101.47
		416	48.65	0.26	0.54	27.08	3.99	0.75	18.65	-	0.31	100.23
		417	49.22	0.28	0.56	26.42	4.04	0.68	18.58	-	0.43	100.21
		419	49.62	0.15	0.51	27.07	3.94	0.66	18.64	-	0.38	100.98
		420	48.88	0.20	0.53	26.34	3.94	0.63	18.70	-	0.27	99.50
West Yellowstone												
	Rims	65	49.1	0.3	0.5	25.6	4.6	1.1	18.7	0.0	0.3	100.4
		66	49.2	0.2	0.5	26.2	4.2	1.1	18.7	0.0	0.4	100.5
		67	49.1	0.2	0.5	26.2	3.9	1.1	19.0	0.0	0.4	100.5
		68	49.1	0.2	0.4	25.9	4.2	1.0	19.0	0.0	0.4	100.2
		70	48.9	0.2	0.5	26.5	4.1	1.0	18.4	0.0	0.3	99.9
		71	49.2	0.2	0.5	25.7	4.8	1.1	18.6	0.0	0.4	100.6
		72	48.8	0.2	0.5	26.4	4.2	1.0	19.0	0.0	0.3	100.3
		73	48.4	0.2	0.5	25.6	3.9	1.1	18.9	0.0	0.3	98.8
		74	48.0	0.2	0.5	26.3	4.0	1.0	18.8	0.0	0.3	99.0
		75	48.9	0.2	0.5	26.1	4.2	1.0	19.0	0.0	0.3	100.2
		77	48.0	0.2	0.5	27.1	3.9	1.2	18.4	0.0	0.3	99.6
		78	48.8	0.3	0.5	25.6	4.1	1.0	18.9	0.0	0.3	99.6
		6	49.6	0.2	0.6	26.9	3.9	1.1	18.5	0.0	0.4	101.2
		7	49.5	0.1	0.5	26.4	4.2	1.0	19.2	0.0	0.3	101.2
		8	49.8	0.2	0.5	26.2	4.1	1.1	19.1	0.0	0.3	101.3
		9	50.1	0.1	0.5	24.6	5.0	1.1	19.1	0.0	0.3	100.8
		11	49.9	0.3	0.5	24.9	5.0	1.2	18.7	0.0	0.3	100.8
		12	49.3	0.2	0.5	25.8	4.2	1.2	18.9	0.0	0.3	100.4
		13	50.2	0.2	0.5	25.4	4.9	1.1	18.7	0.0	0.3	101.3
		14	50.0	0.2	0.5	25.5	5.1	1.0	18.7	0.0	0.3	101.3
		15	49.3	0.2	0.5	26.7	4.0	1.1	19.1	0.0	0.3	101.2
		17	49.5	0.2	0.5	25.1	4.9	1.0	19.1	0.0	0.3	100.6
		18	49.4	0.3	0.5	27.5	4.0	1.0	18.2	0.0	0.3	101.3
		20	50.1	0.2	0.5	25.4	4.4	1.0	18.9	0.0	0.4	101.0

[a] Total iron reported as FeO, "-" indicates oxide not analyzed

		Clinopyroxene									
Sample	**Spot**	**SiO_2**	**TiO_2**	**Al_2O_3**	**FeO**	**MgO**	**MnO**	**CaO**	**K_2O**	**Na_2O**	**Total**
Summit Lake											
Rims	29	49.0	0.2	0.5	25.8	4.3	1.2	18.7	0.0	0.3	100.1
	30	49.1	0.2	0.5	26.1	4.0	1.0	19.1	0.0	0.4	100.4
	32	47.5	0.3	1.4	27.6	3.6	1.1	17.7	0.0	0.4	99.7
	33	49.7	0.1	0.5	26.1	4.2	1.0	18.8	0.0	0.3	100.7
	34	49.4	0.2	0.5	25.8	4.4	1.0	19.2	0.0	0.3	100.7
	35	49.6	0.3	0.4	26.3	4.0	1.0	19.0	0.0	0.2	100.8
	36	49.3	0.2	0.5	26.3	4.0	1.1	19.0	0.0	0.4	100.7
	37	49.1	0.3	0.5	26.2	4.0	1.0	18.6	0.0	0.3	100.0
	38	49.3	0.3	0.5	26.3	4.0	1.1	18.7	0.0	0.3	100.4
	39	48.9	0.2	0.5	25.5	4.4	1.0	18.9	0.0	0.3	99.5
	41	47.8	0.2	0.5	26.8	3.8	1.2	18.8	0.0	0.3	99.5
	44	49.4	0.2	0.5	25.6	4.9	1.0	18.9	0.0	0.4	100.9
	45	49.2	0.1	0.5	25.4	4.5	1.0	18.8	0.0	0.3	100.0
	46	49.6	0.2	0.5	26.4	4.0	1.1	19.0	0.0	0.3	101.1
	47	49.3	0.2	0.5	26.6	4.0	1.1	18.9	0.0	0.3	100.7
	48	49.3	0.3	0.5	26.8	4.2	1.1	18.7	0.0	0.3	101.1
	49	48.7	0.2	0.5	26.5	4.0	1.1	18.9	0.0	0.3	100.3
	50	49.4	0.2	0.5	27.1	4.0	1.0	18.7	0.0	0.4	101.3
	51	49.2	0.2	0.5	25.9	4.1	1.1	19.1	0.0	0.3	100.4
	52	49.0	0.2	0.5	25.7	4.4	1.0	19.0	0.0	0.3	100.0
	53	48.9	0.2	0.5	27.0	4.0	1.2	18.5	0.0	0.4	100.6
	54	49.4	0.3	0.5	25.4	5.0	1.2	18.5	0.0	0.3	100.5
	55	49.7	0.3	0.5	26.5	4.0	1.0	18.9	0.0	0.3	101.3
	56	49.7	0.2	0.5	26.5	4.2	1.0	18.7	0.0	0.2	101.2
	59	49.2	0.3	0.5	25.6	4.5	1.1	18.9	0.0	0.3	100.4
	60	49.9	0.3	0.5	26.5	4.1	1.1	18.7	0.0	0.3	101.5
	61	50.8	0.2	0.5	24.4	5.7	1.0	18.6	0.0	0.3	101.4
	62	50.0	0.2	0.4	25.7	4.2	1.0	19.0	0.0	0.4	100.9
	63	49.5	0.2	0.5	26.5	4.2	1.0	18.8	0.0	0.3	101.1
	65	49.2	0.2	0.4	26.3	4.2	1.1	18.9	0.0	0.3	100.7
	66	49.2	0.2	0.5	27.0	4.1	1.1	18.7	0.0	0.3	101.1
	67	48.3	0.2	0.5	26.2	3.9	1.1	18.9	0.0	0.3	99.5
	68	49.4	0.3	0.5	26.8	4.1	1.1	18.6	0.0	0.3	101.2

[a] Total iron reported as FeO, "-" indicates oxide not analyzed

Appendix 2. (cont.) Compilation of all microprobe analyses of natural samples and experiments.

					Clinopyroxene						
Sample	**Spot**	**SiO_2**	**TiO_2**	**Al_2O_3**	**FeO**	**MgO**	**MnO**	**CaO**	**K_2O**	**Na_2O**	**Total**
Pitchstone Plateau											
Rims	42	49.4	0.2	0.4	27.2	3.0	1.1	19.3	0.0	0.3	101.0
	43	49.3	0.3	0.8	26.8	3.1	1.1	19.0	0.0	0.3	100.7
	44	49.1	0.2	0.4	27.6	2.9	0.9	19.2	0.0	0.4	100.6
	45	48.9	0.2	0.5	27.8	3.1	0.9	19.2	0.0	0.4	100.9
	46	49.2	0.3	0.5	27.1	3.2	1.1	19.1	0.0	0.4	100.7
	48	49.4	0.2	0.5	27.3	3.3	1.1	18.8	0.0	0.4	101.0
	49	48.7	0.2	0.4	28.7	2.6	1.3	18.2	0.0	0.3	100.2
	50	48.2	0.2	0.5	28.3	2.9	1.1	18.7	0.0	0.4	100.4
	51	48.3	0.2	0.5	28.3	2.8	1.2	18.9	0.0	0.3	100.5
	52	48.3	0.2	0.4	27.6	2.7	1.1	19.1	0.0	0.4	99.9
	53	47.9	0.3	0.5	27.0	2.8	1.1	19.1	0.0	0.4	99.1
	55	49.0	0.2	0.5	27.9	3.0	1.0	19.1	0.0	0.3	100.9
	56	48.5	0.2	0.4	26.7	3.0	1.1	19.1	0.0	0.3	99.3
	57	48.1	0.2	0.5	27.9	3.2	1.1	19.0	0.0	0.3	100.2
	58	48.1	0.2	0.5	27.2	3.1	1.0	19.0	0.0	0.3	99.4
	59	48.9	0.2	0.5	27.5	3.2	1.2	19.1	0.0	0.3	100.9
	60	48.8	0.2	0.5	27.8	3.0	1.1	19.3	0.0	0.4	101.2
	61	48.6	0.3	0.4	27.4	3.0	1.0	19.3	0.0	0.4	100.4
	62	48.0	0.3	0.5	27.8	3.3	1.2	18.5	0.0	0.3	99.8
	21	49.2	0.2	0.5	27.1	3.2	1.2	18.9	0.0	0.4	100.6
	22	49.7	0.2	0.5	27.1	3.0	1.1	19.3	0.0	0.3	101.1
	23	49.4	0.2	0.5	27.7	3.0	1.1	18.9	0.0	0.3	101.0
	24	49.4	0.2	0.4	26.7	3.3	1.1	19.0	0.0	0.3	100.4
	25	49.2	0.2	0.5	28.0	3.0	1.1	18.6	0.0	0.3	100.7
	27	49.4	0.3	0.5	27.6	3.1	1.0	18.9	0.0	0.4	101.1
	28	49.4	0.3	0.4	27.2	3.0	1.0	19.2	0.0	0.4	100.8
	29	49.2	0.2	0.5	27.2	3.2	1.1	19.1	0.0	0.3	100.9
	30	49.1	0.2	0.5	28.0	2.9	1.0	19.1	0.0	0.3	101.3
	31	48.0	0.3	2.0	27.2	2.8	0.9	17.9	0.0	0.3	99.3
	32	49.9	0.2	0.5	27.2	3.2	1.0	18.8	0.0	0.3	101.1
	33	48.9	0.2	0.5	27.5	3.0	1.0	19.2	0.0	0.3	100.6
	34	48.8	0.3	1.2	27.7	2.9	1.0	18.7	0.0	0.2	100.7
	35	49.4	0.1	0.5	27.5	3.0	1.0	19.2	0.0	0.4	101.0
	36	49.4	0.1	0.4	27.5	3.2	1.1	19.2	0.0	0.3	101.2

[a] Total iron reported as FeO, "-" indicates oxide not analyzed

Appendix 2. (cont.) Compilation of all microprobe analyses of natural samples and experiments.

					Clinopyroxene						
Sample	**Spot**	**SiO_2**	**TiO_2**	**Al_2O_3**	**FeO**	**MgO**	**MnO**	**CaO**	**K_2O**	**Na_2O**	**Total**
Pitchstone Plateau											
Rims	37	49.2	0.2	0.5	27.9	3.1	1.0	18.8	0.0	0.3	101.1
	39	49.2	0.3	0.5	27.6	3.2	1.1	19.1	0.0	0.3	101.2
	41	49.4	0.2	0.4	27.1	3.0	1.2	19.2	0.0	0.3	100.9
	42	49.9	0.2	0.8	26.9	2.9	1.0	18.9	0.0	0.3	100.9
	43	49.2	0.2	0.4	27.4	3.1	0.9	19.1	0.0	0.4	100.7
Trischmann Knob											
Rims	6	49.4	0.3	0.5	25.8	4.0	1.1	18.7	0.0	0.2	100.0
	11	49.1	0.2	0.5	26.6	4.2	1.1	18.5	0.0	0.3	100.5
	12	49.4	0.3	0.5	26.5	4.0	0.9	18.8	0.0	0.3	100.6
	13	49.5	0.2	0.5	26.1	4.1	1.0	18.9	0.0	0.3	100.5
	14	49.7	0.2	0.5	24.9	5.4	1.1	18.7	0.0	0.4	100.8
	15	49.0	0.3	0.5	26.8	3.9	1.1	18.3	0.0	0.3	100.1
	16	49.2	0.3	0.5	26.2	4.1	1.0	18.6	0.0	0.3	100.2
	17	49.7	0.2	0.5	25.4	4.8	1.0	18.8	0.0	0.4	100.8
	18	48.9	0.2	0.5	25.9	4.1	1.0	18.7	0.0	0.3	99.7
	19	49.4	0.2	0.5	25.5	4.2	1.0	18.9	0.0	0.3	100.2
	20	49.2	0.2	0.5	26.3	4.1	1.1	18.7	0.0	0.3	100.4
	21	49.1	0.2	0.5	25.9	3.9	1.0	18.7	0.0	0.3	99.6
	22	48.9	0.2	0.5	25.8	4.1	1.1	18.8	0.0	0.3	99.6
	23	48.6	0.2	0.6	26.6	3.9	1.0	18.5	0.0	0.3	99.6
	24	48.9	0.3	0.5	26.0	4.1	1.1	18.9	0.0	0.3	100.0
	25	48.4	0.2	0.5	26.4	4.1	1.0	18.9	0.0	0.3	99.9
	26	49.2	0.2	0.5	26.5	4.0	1.1	18.7	0.0	0.4	100.5
	27	49.0	0.2	0.5	26.0	4.1	1.1	18.7	0.0	0.2	99.8
	72	49.5	0.2	0.5	25.9	4.7	1.0	18.5	0.0	0.3	100.5
	73	49.7	0.2	0.5	26.3	4.1	1.1	18.5	0.0	0.4	100.7
	74	49.9	0.2	0.4	25.6	4.4	1.0	18.7	0.0	0.3	100.6
	79	49.9	0.2	0.4	26.4	4.5	1.0	18.6	0.0	0.4	101.4
	80	49.9	0.2	0.5	26.9	4.1	1.0	18.5	0.0	0.2	101.4
	81	50.2	0.3	0.5	24.6	5.9	1.0	18.4	0.0	0.3	101.1
	82	49.7	0.1	0.5	25.5	4.8	1.1	18.6	0.0	0.3	100.6
	83	49.5	0.2	0.5	26.6	3.9	1.1	18.6	0.0	0.3	100.9
	84	49.6	0.3	0.5	26.5	4.1	1.1	18.6	0.0	0.4	101.1

[a] Total iron reported as FeO, "-" indicates oxide not analyzed

Appendix 2. (cont.) Compilation of all microprobe analyses of natural samples and experiments.

			Clinopyroxene									
Sample		**Spot**	**SiO_2**	**TiO_2**	**Al_2O_3**	**FeO**	**MgO**	**MnO**	**CaO**	**K_2O**	**Na_2O**	**Total**
Trischmann Knob												
	Rims	85	49.8	0.2	0.5	25.2	4.7	1.0	18.8	0.0	0.3	100.4
		86	49.9	0.2	0.4	26.7	4.1	1.0	18.8	0.0	0.3	101.5
		87	49.3	0.2	0.4	26.6	4.0	1.0	18.4	0.0	0.4	100.3
		88	49.5	0.2	0.5	26.4	4.0	1.1	18.2	0.0	0.3	100.3
		89	49.8	0.3	0.5	26.7	4.0	1.0	18.7	0.0	0.3	101.2
		90	49.8	0.2	0.5	25.8	4.8	1.0	18.7	0.0	0.3	101.0
Douglas Knob												
Y88	**Rims**	36	49.83	0.35	0.50	25.55	4.24	-	18.55	-	0.31	99.32
		37	49.37	0.23	0.51	24.64	5.18	-	18.25	-	0.27	98.46
		38	48.48	0.07	0.50	25.85	4.09	-	18.19	-	0.28	97.45
		39	48.90	0.23	0.52	26.01	4.10	-	18.23	-	0.24	98.23
		40	48.67	0.27	0.50	26.05	3.87	-	18.28	-	0.29	97.93
		43	48.39	0.21	0.49	26.00	4.01	-	18.56	-	0.29	97.95
		44	49.01	0.27	0.49	26.41	3.96	-	18.49	-	0.29	98.92
		45	48.12	0.25	0.56	27.07	3.63	-	17.32	-	0.36	97.32
		46	47.74	0.25	0.49	26.56	3.96	-	18.12	-	0.24	97.36
		47	47.79	0.24	0.47	25.53	3.90	-	18.30	-	0.22	96.46
		48	49.14	0.16	0.51	25.87	4.40	-	17.90	-	0.08	98.05
		49	48.66	0.13	0.49	25.92	3.93	-	18.37	-	0.27	97.79
		18	50.18	0.28	0.26	26.68	3.95	0.63	18.48	-	0.35	100.79
		20	51.77	1.06	2.57	12.73	15.99	0.17	16.82	-	0.25	101.37
		21	50.11	0.23	0.29	26.78	3.82	0.64	18.72	-	0.25	100.83
		22	48.93	0.45	0.50	27.65	2.89	0.69	16.65	-	0.32	98.07
		23	49.66	0.29	0.37	26.83	4.53	0.64	16.60	-	0.28	99.20
		24	48.79	0.24	0.42	34.64	5.13	0.93	8.57	-	0.10	98.83
		25	53.89	0.49	1.32	19.38	20.30	0.33	5.93	-	0.13	101.76
		27	49.58	0.61	0.70	26.17	4.16	0.69	17.59	-	0.28	99.78
		29	48.77	0.49	0.67	27.73	3.24	0.61	17.78	-	0.33	99.60
Y90	**Rims**	50	48.72	0.24	0.50	25.20	4.63	-	18.48	-	0.19	97.95
		51	49.90	0.19	0.55	20.78	8.13	-	18.65	-	0.18	98.38
		52	47.29	0.18	0.49	25.50	4.94	-	18.08	-	0.29	96.77
		53	47.74	0.18	0.49	25.87	4.94	-	17.49	-	0.22	96.92

[a] Total iron reported as FeO, "-" indicates oxide not analyzed

Appendix 2. (cont.) Compilation of all microprobe analyses of natural samples and experiments.

						Clinopyroxene					
Sample		**Spot**	**SiO_2**	**TiO_2**	**Al_2O_3**	**FeO**	**MgO**	**MnO**	**CaO**	**K_2O**	**Na_2O**	**Total**
Douglas Knob												
Y90	**Rims**	54	48.38	0.28	0.48	25.41	4.01	-	18.50	-	0.07	97.13
		55	48.53	0.26	0.52	26.97	3.79	-	18.17	-	0.38	98.62
		56	49.03	0.30	0.48	25.00	4.56	-	18.49	-	0.24	98.10
		57	47.32	0.26	0.50	25.50	4.82	-	17.97	-	0.27	96.65
		58	48.61	0.25	0.50	25.89	4.57	-	17.97	-	0.28	98.07
		59	48.76	0.15	0.49	24.97	4.29	-	18.44	-	0.26	97.37
		17	48.13	0.25	0.50	26.27	4.00	-	18.27	-	0.35	97.76
		6	49.94	0.35	0.25	27.02	3.79	0.64	18.26	-	0.35	100.60
		7	49.96	0.25	0.29	27.35	3.80	0.68	18.38	-	0.37	101.07
		8	49.55	0.53	0.33	26.67	3.69	0.61	18.13	-	0.35	99.84
		9	50.52	0.16	0.26	26.31	5.41	0.66	17.85	-	0.31	101.49
		10	50.53	0.30	0.24	26.84	4.04	0.60	18.68	-	0.29	101.54
		12	49.92	0.11	0.36	26.27	4.04	0.59	18.60	-	0.35	100.25
		13	50.00	0.12	0.29	27.52	3.95	0.65	18.40	-	0.37	101.30
		14	49.09	0.25	0.28	27.32	3.76	0.62	17.41	-	0.34	99.07
		15	50.46	0.40	0.25	26.42	4.87	0.61	18.36	-	0.26	101.63
		16	50.18	0.20	0.28	25.85	3.92	0.63	18.71	-	0.35	100.12
		13	48.73	0.00	0.16	26.74	3.91	0.66	18.43	-	0.22	98.85
		15	49.20	0.00	0.03	26.15	4.22	0.60	18.76	-	0.30	99.26
		17	49.56	0.00	0.05	25.08	4.98	0.73	18.52	-	0.18	99.10
		18	50.43	0.00	0.06	25.55	4.11	0.69	18.99	-	0.24	100.07
		19	49.60	0.02	0.15	26.58	3.78	0.68	18.75	-	0.30	99.86
		24	49.66	0.00	0.00	26.49	4.01	0.65	18.87	-	0.21	99.90
		25	50.06	0.02	0.00	25.68	4.46	0.70	18.82	-	0.22	99.96
		26	50.16	0.12	0.00	26.57	3.92	0.76	19.10	-	0.20	100.83

---

[a] Total iron reported as FeO, "-" indicates oxide not analyzed

Fayalite

Appendix 2. (cont.) Compilation of all microprobe analyses of natural samples and experiments.

						Fayalite						
Sample		**Spot**	**SiO_2**	**TiO_2**	**Al_2O_3**	**FeO**	**MgO**	**MnO**	**CaO**	**K_2O**	**Na_2O**	**Total**
Solfatara Plateau												
Y60	**Rims**	229	30.1	0.0	0.0	64.3	2.7	1.8	0.3	-	0.0	99.2
		248	30.5	0.1	0.0	66.0	2.8	1.8	0.3	-	0.0	101.4
		254	30.3	0.0	0.0	66.7	2.7	1.8	0.3	-	0.0	101.8
		264	30.0	0.0	0.0	63.8	2.7	1.7	0.3	-	0.5	99.1
		344	30.0	0.0	0.0	64.8	2.7	1.6	0.3	-	0.0	99.3
		347	29.5	0.0	0.0	65.1	2.7	1.6	0.3	-	0.0	99.2
Y82	**Cores**	313	30.3	0.1	0.0	65.3	2.9	1.6	0.3	-	0.0	100.6
		314	30.0	0.1	0.0	63.7	2.7	1.7	0.3	-	0.0	98.4
		328	30.0	0.0	0.0	65.3	2.9	1.6	0.3	-	0.1	100.2
		330	30.2	0.0	0.0	64.9	2.9	1.6	0.3	-	0.0	99.9
	Rims	298	29.7	0.0	0.0	63.1	2.9	1.6	0.3	-	0.0	97.5
		301	29.9	0.0	0.0	65.2	2.7	1.6	0.3	-	0.0	99.6
		303	30.4	0.1	0.0	65.9	2.9	1.6	0.3	-	0.0	101.1
		315	29.5	0.0	0.0	62.7	2.8	1.6	0.3	-	0.0	96.9
		318	30.1	0.2	0.0	64.8	2.7	1.6	0.3	-	0.0	99.6
		329	29.9	0.0	0.0	64.0	2.9	1.6	0.3	-	0.0	98.7
		331	30.5	0.0	0.0	65.4	3.0	1.6	0.3	-	0.0	100.7
		333	30.0	0.1	0.0	65.6	2.9	1.6	0.3	-	0.0	100.5
		337	30.1	0.1	0.0	64.0	2.8	1.5	0.3	-	0.0	98.8
Y47	**Cores**	384	30.0	0.0	0.0	66.2	2.8	1.7	0.3	-	0.0	100.9
		403	30.0	0.1	0.0	65.4	2.6	1.6	0.3	-	0.0	99.9
	Rims	385	30.8	0.0	0.0	65.9	2.7	1.6	0.3	-	0.0	101.2
		387	30.2	0.0	0.0	65.0	2.6	1.6	0.3	-	0.0	99.7
		391	29.7	0.0	0.0	64.9	2.7	1.6	0.3	-	0.0	99.1
		392	30.1	0.1	0.0	65.3	2.7	1.6	0.3	-	0.1	100.2
		396	30.2	0.1	0.0	65.1	2.8	1.6	0.3	-	0.0	100.0
		404	30.8	0.1	0.0	64.3	2.7	1.6	0.3	-	0.0	99.7
		413	29.9	0.0	0.0	65.3	2.7	1.6	0.3	-	0.0	99.9
		418	30.3	0.1	0.0	65.0	2.6	1.6	0.3	-	0.0	99.8
		421	29.9	0.0	0.0	65.0	2.6	1.6	0.3	-	0.0	99.5

[a] Total iron reported as FeO, "-" indicates oxide not analyzed

					Fayalite						
Sample	**Spot**	**SiO_2**	**TiO_2**	**Al_2O_3**	**FeO**	**MgO**	**MnO**	**CaO**	**K_2O**	**Na_2O**	**Total**
West Yellowstone											
Rims	42	30.4	0.0	0.0	64.8	3.1	2.4	0.3	0.0	0.0	101.0
	43	30.1	0.0	0.0	65.0	3.0	2.3	0.3	0.0	0.0	100.7
	44	30.5	0.0	0.0	64.9	3.0	2.2	0.3	0.0	0.0	100.8
	45	30.6	0.0	0.0	64.6	3.0	2.2	0.2	0.0	0.0	100.6
	46	30.6	0.0	0.0	64.9	3.1	2.3	0.2	0.0	0.0	101.1
	47	30.3	0.1	0.0	65.4	3.1	2.3	0.3	0.0	0.0	101.5
	48	30.4	0.0	0.0	63.8	3.0	2.2	0.2	0.0	0.0	99.6
	50	30.1	0.0	0.0	65.1	2.9	2.4	0.3	0.0	0.0	100.7
	51	30.1	0.1	0.0	64.9	3.1	2.4	0.3	0.0	0.0	100.7
	52	30.4	0.0	0.0	64.4	3.1	2.3	0.3	0.0	0.0	100.4
	53	30.4	0.0	0.0	64.8	3.2	2.2	0.3	0.0	0.0	100.7
	56	30.5	0.0	0.0	64.1	3.1	2.3	0.3	0.0	0.0	100.3
	57	30.1	0.1	0.0	64.5	3.0	2.2	0.3	0.0	0.0	100.0
	58	30.3	0.0	0.0	64.5	3.1	2.2	0.3	0.0	0.0	100.5
	64	30.4	0.0	0.0	64.8	3.1	2.5	0.3	0.0	0.0	101.1
	76	30.0	0.1	0.0	65.1	3.0	2.4	0.3	0.0	0.0	100.8
	36	30.7	0.1	0.0	63.5	3.1	2.1	0.3	0.0	0.0	99.7
	37	30.8	0.1	0.0	64.7	3.0	2.1	0.3	0.0	0.0	100.9
	38	31.0	0.0	0.0	64.3	3.1	2.2	0.3	0.0	0.0	100.9
	39	30.8	0.0	0.0	65.1	2.9	2.2	0.3	0.0	0.0	101.2
	40	30.7	0.1	0.0	64.4	3.2	2.2	0.2	0.0	0.0	100.7
	41	30.4	0.0	0.0	65.3	3.0	2.3	0.3	0.0	0.0	101.3
	42	30.5	0.0	0.0	65.2	3.3	2.3	0.3	0.0	0.0	101.5
	43	30.6	0.1	0.0	64.5	3.2	2.1	0.2	0.0	0.0	100.7
	44	30.7	0.0	0.0	64.6	3.0	2.3	0.3	0.0	0.0	100.9
	45	30.8	0.0	0.0	63.8	3.1	2.1	0.2	0.0	0.0	100.0
	47	30.4	0.0	0.0	65.5	3.0	2.2	0.2	0.0	0.0	101.4
	48	30.5	0.0	0.0	64.4	3.1	2.2	0.3	0.0	0.0	100.5
	50	30.5	0.0	0.0	64.3	3.0	2.3	0.3	0.0	0.0	100.3
	51	30.6	0.0	0.0	64.6	3.2	2.1	0.3	0.0	0.0	100.8
	52	30.6	0.0	0.0	64.3	3.1	2.1	0.3	0.0	0.0	100.4
	54	30.7	0.0	0.0	64.6	3.0	2.1	0.3	0.0	0.0	100.7

[a] Total iron reported as FeO, "-" indicates oxide not analyzed

Sample		Spot	SiO_2	TiO_2	Al_2O_3	FeO	MgO	MnO	CaO	K_2O	Na_2O	Total
						Fayalite						
Summit Lake												
	Rims	12	29.9	0.0	0.0	64.2	3.1	2.3	0.3	0.0	0.0	99.8
		18	30.3	0.0	0.0	65.3	3.0	2.3	0.3	0.0	0.0	101.2
		19	29.7	0.0	0.0	65.6	3.2	2.3	0.3	0.0	0.0	101.1
		21	30.3	0.0	0.0	63.4	3.0	2.3	0.3	0.0	0.0	99.3
		23	30.1	0.0	0.0	64.3	3.0	2.3	0.3	0.0	0.0	100.0
		28	30.8	0.0	0.0	64.7	3.0	2.5	0.3	0.0	0.0	101.3
		66	31.0	0.0	0.0	64.9	3.1	2.3	0.3	0.0	0.0	101.5
		67	30.7	0.0	0.0	64.4	3.1	2.2	0.3	0.0	0.0	100.7
		68	30.1	0.0	0.0	63.7	3.0	2.3	0.3	0.0	0.1	99.5
		69	30.6	0.0	0.0	63.9	3.2	2.2	0.3	0.0	0.0	100.2
		70	31.1	0.0	0.0	64.7	3.1	2.2	0.3	0.0	0.0	101.4
		71	30.8	0.0	0.0	63.6	3.2	2.3	0.3	0.0	0.0	100.3
		72	30.6	0.0	0.0	64.3	3.1	2.3	0.3	0.0	0.0	100.4
		73	30.7	0.0	0.0	64.4	3.3	2.2	0.3	0.0	0.0	100.9
		74	30.6	0.1	0.0	64.7	3.2	2.1	0.2	0.0	0.0	101.0
		75	30.7	0.0	0.0	64.5	3.2	2.2	0.3	0.0	0.0	100.8
		76	30.8	0.0	0.0	64.4	3.1	2.3	0.3	0.0	0.0	100.9
		77	30.8	0.0	0.0	64.7	3.1	2.1	0.3	0.0	0.0	100.9
		78	30.6	0.1	0.0	62.9	3.2	2.0	0.4	0.0	0.0	99.1
		79	30.9	0.0	0.0	64.2	3.1	2.2	0.3	0.0	0.0	100.6
		80	30.5	0.0	0.0	64.3	3.1	2.3	0.3	0.0	0.0	100.5
		81	30.6	0.0	0.0	65.1	3.1	2.3	0.3	0.0	0.0	101.4
		82	30.6	0.0	0.0	64.0	3.2	2.3	0.3	0.0	0.0	100.3
		83	30.0	0.0	0.0	63.7	3.2	2.2	0.2	0.0	0.0	99.3
		84	30.9	0.0	0.0	63.7	3.0	2.2	0.3	0.0	0.0	100.2
		85	30.6	0.0	0.0	64.8	3.0	2.3	0.3	0.0	0.0	101.1
		86	30.8	0.1	0.0	64.6	3.1	2.3	0.2	0.0	0.1	101.3
		87	30.9	0.1	0.0	64.4	3.1	2.2	0.3	0.0	0.0	100.8
		88	30.6	0.0	0.0	64.5	2.9	2.1	0.3	0.0	0.0	100.5
		90	30.8	0.0	0.0	64.9	3.3	2.2	0.3	0.0	0.0	101.4
		91	31.0	0.0	0.0	63.6	3.0	2.0	0.3	0.0	0.0	100.0

---

[a] Total iron reported as FeO, "-" indicates oxide not analyzed

					Fayalite						
Sample	**Spot**	**SiO_2**	**TiO_2**	**Al_2O_3**	**FeO**	**MgO**	**MnO**	**CaO**	**K_2O**	**Na_2O**	**Total**
Pitchstone Plateau											
Rims	28	30.2	0.0	0.0	66.2	2.1	2.4	0.3	0.0	0.1	101.3
	30	30.1	0.0	0.0	65.5	2.1	2.3	0.3	0.0	0.0	100.4
	31	30.4	0.1	0.0	66.3	2.1	2.5	0.3	0.0	0.0	101.5
	32	30.3	0.0	0.0	65.3	2.1	2.5	0.3	0.0	0.0	100.5
	33	30.1	0.1	0.0	66.1	2.0	2.4	0.3	0.0	0.0	101.0
	34	30.4	0.0	0.0	66.5	1.9	2.3	0.3	0.0	0.0	101.2
	35	30.4	0.0	0.0	65.9	2.0	2.4	0.3	0.0	0.0	100.9
	36	29.8	0.0	0.0	65.5	2.0	2.4	0.3	0.0	0.0	100.0
	37	30.2	0.0	0.0	65.9	2.0	2.4	0.3	0.0	0.0	100.8
	40	29.8	0.0	0.0	66.3	2.0	2.4	0.3	0.0	0.0	100.7
	41	29.7	0.1	0.0	66.3	2.0	2.4	0.3	0.0	0.1	100.9
	54	30.0	0.0	0.0	65.7	1.9	2.5	0.3	0.0	0.1	100.5
	6	29.6	0.0	0.0	64.7	1.9	2.2	0.3	0.0	0.0	98.6
	7	30.2	0.0	0.0	66.4	2.1	2.3	0.3	0.0	0.0	101.3
	8	29.9	0.0	0.0	65.7	2.1	2.3	0.3	0.0	0.0	100.4
	9	30.4	0.0	0.0	66.4	2.1	2.1	0.3	0.0	0.0	101.1
	11	30.5	0.0	0.0	65.8	2.0	2.3	0.3	0.0	0.0	100.9
	12	30.7	0.0	0.0	65.9	2.0	2.2	0.3	0.0	0.0	101.2
	14	30.4	0.0	0.0	66.0	2.1	2.3	0.3	0.0	0.0	101.0
	15	30.1	0.1	0.0	65.6	2.0	2.3	0.3	0.0	0.0	100.2
	16	31.0	0.0	0.0	65.2	2.1	2.2	0.3	0.0	0.0	100.8
	17	30.5	0.0	0.0	65.5	2.0	2.3	0.3	0.0	0.0	100.6
	18	30.3	0.0	0.0	66.3	2.0	2.3	0.3	0.0	0.1	101.2
	19	30.6	0.1	0.0	64.7	1.9	2.3	0.3	0.0	0.0	99.9
	20	30.6	0.0	0.0	65.9	2.1	2.3	0.3	0.0	0.0	101.2
	21	30.4	0.0	0.0	66.1	2.1	2.3	0.3	0.0	0.0	101.2
	22	30.4	0.0	0.0	66.1	2.0	2.3	0.3	0.0	0.0	101.2
	23	30.1	0.0	0.0	65.4	2.0	2.4	0.3	0.0	0.0	100.2
	24	30.5	0.0	0.0	64.9	2.0	2.3	0.3	0.0	0.0	100.0
	25	30.6	0.0	0.0	66.1	2.0	2.3	0.3	0.0	0.0	101.4
	26	30.4	0.0	0.0	66.2	2.1	2.4	0.3	0.0	0.0	101.3
	27	30.4	0.0	0.0	66.0	2.1	2.4	0.3	0.0	0.0	101.2
	28	30.6	0.0	0.0	66.3	1.9	2.3	0.3	0.0	0.0	101.4

[a] Total iron reported as FeO, "-" indicates oxide not analyzed

Appendix 2. (cont.) Compilation of all microprobe analyses of natural samples and experiments.

						Fayalite						
Sample		**Spot**	**SiO_2**	**TiO_2**	**Al_2O_3**	**FeO**	**MgO**	**MnO**	**CaO**	**K_2O**	**Na_2O**	**Total**
Pitchstone Plateau												
	Rims	30	30.7	0.1	0.2	65.5	2.0	2.3	0.3	0.0	0.0	100.9
		31	30.5	0.0	0.0	65.2	2.1	2.4	0.3	0.0	0.0	100.5
		32	30.7	0.0	0.0	65.7	2.0	2.3	0.3	0.0	0.0	101.0
		33	30.2	0.1	0.0	66.6	2.0	2.3	0.3	0.0	0.0	101.4
		34	30.2	0.0	0.0	65.9	2.1	2.3	0.3	0.0	0.0	100.7
Trischmann Knob												
	Rims	56	30.6	0.0	0.0	64.8	3.0	2.2	0.3	0.0	0.0	100.9
		57	30.5	0.0	0.0	64.1	2.9	2.3	0.3	0.0	0.0	99.9
		58	30.3	0.0	0.0	65.6	2.9	2.3	0.3	0.0	0.0	101.4
		59	30.2	0.0	0.0	65.7	2.9	2.3	0.3	0.0	0.0	101.3
		60	30.3	0.1	0.0	65.3	2.9	2.2	0.3	0.0	0.0	101.0
		61	30.2	0.0	0.0	63.8	2.9	2.3	0.3	0.0	0.0	99.5
		63	30.5	0.0	0.0	64.9	3.1	2.4	0.3	0.0	0.0	101.1
Douglas Knob												
Y90	**Rims**	6	29.9	0.0	0.0	64.0	3.0	1.5	0.3		0.0	98.7
		7	29.8	0.0	0.0	64.5	2.9	1.5	0.3		0.0	98.9
		8	29.9	0.0	0.0	65.9	3.1	1.5	0.3		0.0	100.7
		9	29.6	0.1	0.0	63.4	3.1	1.5	0.3		0.0	98.0
		10	29.4	0.0	0.0	61.1	2.0	1.5	0.3		0.0	94.4
		11	29.3	0.0	0.0	64.6	2.8	1.5	0.3		0.0	98.5
		12	30.0	0.0	0.0	63.6	2.8	1.5	0.3		0.0	98.0
		13	30.1	0.1	0.0	64.4	2.8	1.5	0.3		0.0	99.2
Y88	**Rims**	18	30.4	0.0	0.0	63.5	3.2	1.5	0.3		0.0	98.8
		19	32.7	0.0	0.0	62.7	3.5	1.5	0.3		0.0	100.7
		21	30.4	0.1	0.0	63.7	3.3	1.5	0.3		0.0	99.2
		22	30.6	0.0	0.0	64.6	3.1	1.5	0.2		0.0	100.0
		23	30.7	0.1	0.0	64.6	3.1	1.5	0.3		0.0	100.2
		24	31.2	0.0	0.0	62.6	3.1	1.5	0.3		0.0	98.6
		26	31.0	0.0	0.0	64.7	3.2	1.5	0.3		0.0	100.6
		27	30.0	0.1	0.0	65.6	3.2	1.5	0.3		0.0	100.7
		28	30.4	0.1	0.0	64.6	3.1	1.5	0.3		0.0	100.1
		29	31.3	0.1	0.0	64.9	3.2	1.5	0.3		0.0	101.3

[a]Total iron reported as FeO, "-" indicates oxide not analyzed

Magnetite

Appendix 2. (cont.) Compilation of all microprobe analyses of natural samples and experiments.

		Magnetite								
Sample	**Spot**	**SiO_2**	**TiO_2**	**Al_2O_3**	**FeO**	**MgO**	**MnO**	**CaO**	**Cr_2O_3**	**Total**
Solfatara Plateau										
Y60	25	-	17.73	0.85	76.16	0.19	0.90	-	-	95.83
	26	-	18.07	0.87	76.90	0.19	0.90	-	-	96.94
	27	-	18.22	0.89	76.66	0.17	0.87	-	-	96.81
	29	-	17.74	0.94	76.38	0.20	0.89	-	-	96.15
	31	-	17.50	0.87	77.10	0.13	0.90	-	-	96.50
	36	-	17.68	0.87	76.89	0.19	0.84	-	-	96.47
	38	-	17.69	0.92	75.93	0.18	0.89	-	-	95.61
	42	-	18.42	0.89	76.79	0.18	0.84	-	-	97.12
	43	-	18.68	0.86	76.23	0.19	0.82	-	-	96.78
	45	-	18.00	0.91	76.91	0.16	0.92	-	-	96.90
	46	-	20.10	0.88	73.02	0.16	0.97	-	-	95.12
	51	-	17.05	1.04	76.93	0.18	0.89	-	-	96.09
	52	-	17.31	0.88	76.76	0.17	0.87	-	-	96.00
Y82	57	-	18.96	0.84	75.72	0.20	0.91	-	-	96.62
	58	-	18.57	0.78	75.01	0.20	0.94	-	-	95.50
	61	-	18.84	0.88	75.05	0.18	0.89	-	-	95.84
	64	-	18.12	0.88	75.78	0.18	0.94	-	-	95.91
	68	-	18.98	1.23	74.98	0.19	0.90	-	-	96.29
	69	-	17.72	0.92	75.73	0.19	0.85	-	-	95.41
	70	-	18.23	0.89	75.26	0.22	0.86	-	-	95.46
	71	-	18.64	0.84	75.83	0.19	0.90	-	-	96.40
	72	-	18.17	0.85	75.29	0.21	0.88	-	-	95.40
	73	-	18.05	0.79	75.97	0.17	0.83	-	-	95.81
	75	-	18.62	0.90	75.06	0.18	0.90	-	-	95.65
	76	-	18.23	0.85	76.01	0.20	0.92	-	-	96.21
	77	-	18.05	0.88	75.10	0.17	0.89	-	-	95.09
	80	-	18.11	0.88	75.97	0.18	0.90	-	-	96.05
	81	-	18.48	0.86	75.30	0.18	0.84	-	-	95.66
	83	-	17.99	0.80	75.54	0.16	0.81	-	-	95.30
	84	-	19.10	0.85	75.61	0.17	0.83	-	-	96.56
	85	-	19.10	0.86	75.80	0.16	0.89	-	-	96.81
	86	-	18.68	0.88	75.48	0.21	0.85	-	-	96.09
	87	-	18.61	0.83	75.74	0.20	0.90	-	-	96.29

[a] Total iron reported as FeO, "-" indicates oxide not analyzed

		Magnetite								
Sample	**Spot**	**SiO_2**	**TiO_2**	**Al_2O_3**	**FeO**	**MgO**	**MnO**	**CaO**	**Cr_2O_3**	**Total**
Solfatara Plateau										
Y82	6	0.08	19.05	0.86	78.09	0.19	0.80	0.02	0.00	99.03
	7	0.11	18.85	0.81	78.11	0.17	0.85	0.01	0.04	98.95
	8	0.09	19.37	0.84	77.76	0.20	0.80	0.00	0.07	99.13
	9	0.11	19.23	0.77	78.00	0.17	0.81	0.00	0.12	99.20
	10	0.09	19.50	0.80	77.28	0.15	0.92	0.00	0.08	98.80
	11	0.10	19.11	0.73	78.27	0.21	0.85	0.01	0.00	99.20
	12	0.06	19.03	0.76	76.93	0.15	0.99	0.00	0.00	97.87
	13	0.11	19.00	0.81	76.65	0.18	0.86	0.01	0.00	97.62
	14	0.13	19.24	0.76	78.32	0.16	0.93	0.00	0.10	99.64
	15	0.07	19.25	0.82	77.07	0.21	0.89	0.01	0.08	98.40
	16	0.12	19.33	0.85	78.41	0.21	0.83	0.01	0.00	99.76
	17	0.09	19.34	0.78	77.45	0.23	0.87	0.00	0.04	98.79
	18	0.10	18.74	0.81	78.34	0.14	0.79	0.05	0.05	99.02
	19	0.11	19.37	0.78	77.73	0.19	0.85	0.00	0.04	99.06
	20	0.10	18.25	0.85	77.67	0.19	0.94	0.00	0.00	97.93
	21	0.11	18.83	0.81	78.05	0.20	0.83	0.00	0.00	98.77
	22	0.08	18.77	0.90	79.28	0.18	0.83	0.00	0.00	100.01
	23	0.15	17.95	0.80	77.30	0.16	0.86	0.01	0.01	97.24
	24	0.13	19.63	0.82	78.03	0.20	0.86	0.03	0.00	99.69
	25	0.12	19.38	0.74	77.81	0.23	0.84	0.02	0.04	99.17
	26	0.07	18.27	0.63	76.38	0.29	0.93	0.02	0.00	96.52
	27	0.08	18.99	0.72	74.64	0.17	0.89	0.00	0.01	95.48
	28	0.04	19.15	0.68	75.25	0.26	0.85	0.00	0.01	96.23
	29	0.11	19.28	0.73	75.56	0.20	0.87	0.00	0.00	96.68
	30	0.08	19.58	0.78	75.93	0.18	0.90	0.00	0.01	97.47
	39	0.04	19.32	0.77	74.71	0.16	0.84	0.00	0.00	95.77
	40	0.05	19.22	0.68	75.29	0.20	0.89	0.06	0.00	96.38
Y47	92	-	17.94	0.92	75.86	0.19	0.85	-	-	95.76
	93	-	18.24	0.82	76.05	0.15	0.88	-	-	96.14
	96	-	18.10	0.89	75.47	0.14	0.86	-	-	95.47
	102	-	18.39	0.87	76.47	0.18	0.85	-	-	96.76
	103	-	17.38	0.86	76.31	0.16	0.88	-	-	95.58
	107	-	17.87	0.93	75.83	0.15	0.92	-	-	95.71

[a] Total iron reported as FeO, "-" indicates oxide not analyzed

Appendix 2. (cont.) Compilation of all microprobe analyses of natural samples and experiments.

					Magnetite					
Sample	**Spot**	**SiO_2**	**TiO_2**	**Al_2O_3**	**FeO**	**MgO**	**MnO**	**CaO**	**Cr_2O_3**	**Total**
Solfatara Plateau										
Y47	108	-	18.71	0.88	76.13	0.17	0.87	-	-	96.76
	110	-	17.81	0.84	75.64	0.19	0.84	-	-	95.33
	111	-	17.97	0.90	75.77	0.19	0.88	-	-	95.70
	112	-	18.07	0.92	76.34	0.16	0.85	-	-	96.33
	113	-	18.35	0.88	76.28	0.17	0.86	-	-	96.54
	115	-	18.21	0.94	76.04	0.16	0.90	-	-	96.24
	116	-	18.35	0.87	76.82	0.18	0.87	-	-	97.09
	117	-	17.59	0.86	76.53	0.15	0.85	-	-	95.97
West Yellowstone										
Y216	41	0.12	18.79	0.83	79.32	0.20	0.90	0.00	0.01	100.17
	42	0.07	18.64	0.85	78.77	0.19	0.86	0.01	0.02	99.40
	43	0.06	18.87	0.85	79.45	0.25	0.95	0.00	0.04	100.47
	44	0.06	17.80	0.86	78.52	0.17	0.75	0.01	0.03	98.20
	45	0.12	18.55	0.80	79.50	0.21	0.95	0.01	0.00	100.15
	46	0.13	18.51	0.89	79.30	0.24	0.84	0.00	0.01	99.91
	47	0.11	18.22	0.84	77.94	0.22	0.77	0.01	0.00	98.03
	49	0.14	18.43	0.80	78.16	0.15	0.86	0.01	0.00	98.54
	50	0.11	18.51	0.70	75.97	0.18	0.81	0.02	0.00	96.22
	51	0.13	18.86	0.70	76.78	0.15	0.85	0.01	0.00	97.44
	52	0.08	18.91	0.70	76.84	0.21	0.82	0.03	0.00	97.54
	53	0.05	18.95	0.66	76.30	0.22	0.90	0.03	0.00	97.09
	54	0.07	18.98	0.62	75.44	0.20	0.87	0.01	0.01	96.20
	57	0.11	18.32	0.69	76.02	0.17	0.76	0.01	0.02	96.10
	58	0.03	18.37	0.65	75.30	0.18	0.90	0.01	0.05	95.48
	59	0.10	18.26	0.67	75.84	0.21	0.91	0.02	0.00	96.00
	60	0.10	18.87	0.77	77.83	0.21	0.91	0.02	0.00	98.69
	61	0.05	18.70	0.74	75.81	0.18	1.03	0.02	0.00	96.51
	62	0.07	18.62	0.76	76.94	0.22	0.90	0.01	0.02	97.55
	67	0.04	19.05	0.62	74.75	0.17	0.92	0.02	0.06	95.65
	68	0.08	18.77	0.67	75.29	0.15	0.85	0.03	0.00	95.76
	69	0.08	19.47	0.62	75.26	0.23	0.85	0.00	0.00	96.44
	70	0.08	17.93	0.68	76.16	0.19	0.81	0.00	0.00	95.77
	71	0.05	18.62	0.68	75.92	0.19	0.88	0.02	0.04	96.40

[a] Total iron reported as FeO, "-" indicates oxide not analyzed

					Magnetite					
Sample	**Spot**	**SiO_2**	**TiO_2**	**Al_2O_3**	**FeO**	**MgO**	**MnO**	**CaO**	**Cr_2O_3**	**Total**
West Yellowstone										
Y216	73	0.09	18.77	0.67	77.84	0.16	0.89	0.01	0.06	98.48
	74	0.08	18.62	0.66	76.01	0.20	0.85	-0.01	0.07	96.49
	75	0.07	18.30	0.56	75.56	0.17	0.77	0.00	0.00	95.40
	77	0.09	17.69	0.68	78.90	0.23	0.96	0.01	0.00	98.54
	78	0.09	15.89	0.67	78.65	0.20	0.96	0.01	0.00	96.44
	52	0.08	18.05	0.88	77.45	0.19	0.87	0.04	0.00	97.56
	53	0.12	18.46	0.88	78.01	0.24	0.81	0.00	0.00	98.49
	54	0.04	18.57	0.93	78.80	0.18	0.88	0.03	0.00	99.29
	57	0.12	18.72	0.88	78.21	0.16	0.80	0.01	0.04	98.95
	58	0.13	18.19	0.90	77.18	0.18	0.95	0.01	0.00	97.54
	59	0.12	18.23	0.85	78.45	0.18	0.87	0.02	0.00	98.70
	60	0.10	18.65	0.76	78.52	0.22	0.83	0.00	0.00	99.00
	61	0.13	18.78	0.80	78.74	0.20	0.86	0.00	0.00	99.50
	62	0.11	18.34	0.97	78.03	0.24	0.84	0.00	0.00	98.47
	63	0.10	18.31	0.89	78.27	0.16	0.93	0.00	0.00	98.57
	64	0.08	18.29	0.81	78.31	0.16	0.82	0.00	0.00	98.39
	65	0.11	17.30	0.81	79.04	0.10	0.90	0.01	0.03	98.29
	66	0.11	18.64	0.76	77.86	0.21	0.86	0.01	0.00	98.40
	67	0.09	18.77	0.80	78.88	0.25	0.80	0.03	0.03	99.64
	68	0.07	18.60	0.82	78.29	0.17	0.90	0.00	0.05	98.90
	69	0.13	18.78	0.90	79.43	0.16	0.80	0.00	0.04	100.22
	70	0.09	18.71	0.88	79.11	0.20	1.03	0.02	0.00	100.01
	71	0.07	18.55	0.84	78.62	0.16	0.86	0.00	0.00	99.07
	72	0.09	16.61	0.75	80.56	0.18	0.76	0.02	0.06	99.03
	73	0.08	18.69	0.85	78.78	0.22	0.87	0.01	0.00	99.48
	74	0.10	18.71	0.85	78.80	0.17	0.92	0.01	0.00	99.57
	75	0.11	18.75	0.82	78.72	0.26	0.87	0.00	0.01	99.53
	76	0.10	18.41	0.81	78.71	0.14	0.88	0.00	0.00	99.03
	77	0.12	17.96	0.79	79.96	0.23	0.88	0.02	0.00	99.97
	78	0.13	17.83	0.81	78.88	0.27	0.82	0.02	0.01	98.77
	79	0.08	18.85	0.80	79.09	0.20	0.97	0.00	0.01	100.00
	80	0.12	18.66	0.82	78.81	0.18	0.75	0.00	0.00	99.31
	81	0.12	18.56	0.88	78.87	0.22	0.90	0.00	0.01	99.55
	82	0.12	18.76	0.86	78.22	0.23	0.80	0.01	0.03	99.05
	83	0.11	18.34	0.87	79.08	0.20	0.90	0.01	0.00	99.47

[a] Total iron reported as FeO, "-" indicates oxide not analyzed

		Magnetite								
Sample	**Spot**	**SiO_2**	**TiO_2**	**Al_2O_3**	**FeO**	**MgO**	**MnO**	**CaO**	**Cr_2O_3**	**Total**
Summit Lake										
Y74	125	0.09	17.95	0.89	78.29	0.20	0.87	0.00	0.05	98.33
	126	0.09	18.20	0.87	80.01	0.17	0.94	0.01	0.00	100.26
	127	0.12	18.51	0.83	78.77	0.23	0.91	0.00	0.06	99.43
	128	0.13	18.54	0.89	78.01	0.18	0.81	0.01	0.00	98.51
	129	0.10	18.41	0.80	78.67	0.20	0.94	0.03	0.01	99.17
	130	0.12	18.88	0.84	79.36	0.20	0.85	0.02	0.00	100.19
	131	0.13	18.14	0.78	77.41	0.21	0.86	0.00	0.00	97.42
	132	0.14	18.18	0.86	77.94	0.20	0.98	0.02	0.09	98.41
	133	0.07	17.98	0.89	78.84	0.24	0.89	0.01	0.05	98.98
	134	0.10	18.88	0.82	78.72	0.27	0.89	0.01	0.06	99.74
	135	0.14	18.77	0.87	78.66	0.16	0.81	0.00	0.02	99.43
	136	0.08	18.12	0.80	78.83	0.20	0.89	0.00	0.00	98.84
	137	0.11	18.30	0.79	78.31	0.25	0.89	0.02	0.00	98.66
	138	0.11	17.89	0.79	77.91	0.25	0.80	0.01	0.08	97.83
	139	0.09	18.01	0.78	78.84	0.17	0.76	0.02	0.00	98.66
	140	0.08	18.69	0.85	77.00	0.21	0.84	0.00	0.00	97.66
	141	0.08	18.58	0.79	77.74	0.20	0.83	0.01	0.00	98.18
	142	0.10	18.87	0.82	76.09	0.26	0.87	0.00	0.00	97.00
	143	0.12	17.38	0.83	78.91	0.18	0.82	0.00	0.06	98.27
	144	0.11	18.40	0.82	77.33	0.23	0.87	0.01	0.00	97.76
	145	0.09	18.32	0.78	78.23	0.23	0.92	0.00	0.00	98.51
	146	0.08	18.74	0.88	79.49	0.20	0.92	0.00	0.00	100.29
	147	0.12	18.54	0.87	78.60	0.22	0.97	0.04	0.05	99.41
	148	0.11	18.18	0.77	78.09	0.28	0.96	0.00	0.06	98.43
	149	0.11	18.02	0.74	77.29	0.23	0.97	0.01	0.00	97.33
	150	0.11	18.32	0.85	77.77	0.24	0.79	0.01	0.00	98.09
	151	0.10	18.26	0.86	78.59	0.19	0.85	0.01	0.04	98.91
	152	0.07	18.72	0.88	77.38	0.20	0.96	0.01	0.00	98.20
	153	0.09	17.43	0.70	79.31	0.21	0.85	0.00	0.00	98.54
	154	0.06	18.66	0.75	78.06	0.22	0.87	0.02	0.00	98.56
	155	0.07	18.45	0.74	76.55	0.18	0.85	0.00	0.00	96.79
	156	0.08	18.50	0.82	78.14	0.18	0.81	0.00	0.00	98.50
	157	0.10	18.81	0.80	79.91	0.13	0.78	0.00	0.06	100.58
	158	0.10	18.14	0.81	79.41	0.28	0.91	0.02	0.00	99.55

[a] Total iron reported as FeO, "-" indicates oxide not analyzed

					Magnetite					
Sample	**Spot**	**SiO_2**	**TiO_2**	**Al_2O_3**	**FeO**	**MgO**	**MnO**	**CaO**	**Cr_2O_3**	**Total**
Summit Lake										
Y74	159	0.13	18.75	0.85	79.61	0.21	0.86	0.00	0.00	100.33
	160	0.11	18.93	0.83	78.71	0.22	0.87	0.01	0.03	99.72
	161	0.12	17.58	0.86	78.50	0.22	0.93	0.00	0.00	98.10
	163	0.11	18.85	0.85	77.89	0.13	0.79	0.02	0.00	98.61
	164	0.08	18.64	0.85	79.35	0.22	0.79	0.03	0.02	99.98
	60	0.11	18.49	0.86	74.78	0.24	0.89	0.13	0.00	95.45
	61	0.09	19.11	0.85	77.97	0.23	0.97	0.02	0.04	99.28
	62	0.13	17.94	0.86	76.98	0.17	0.94	0.00	0.04	97.06
	63	0.07	19.12	0.84	78.04	0.20	0.86	0.00	0.00	99.09
	64	0.12	18.77	0.88	78.17	0.21	0.92	0.00	0.00	99.06
	66	0.09	18.67	0.81	79.02	0.19	0.83	0.02	0.00	99.61
	67	0.11	18.76	0.79	77.89	0.22	0.90	0.00	0.00	98.60
	68	0.09	18.27	0.82	78.87	0.24	0.94	0.03	0.00	99.23
	69	0.11	19.25	0.80	78.40	0.23	0.89	0.00	0.00	99.64
	70	0.07	19.62	0.83	78.09	0.23	0.94	0.00	0.00	99.72
	71	0.13	19.07	0.80	78.36	0.27	0.89	0.00	0.02	99.54
	72	0.09	18.54	0.86	77.66	0.18	0.81	0.01	0.00	98.14
	73	0.07	18.84	0.81	78.94	0.21	0.95	0.00	0.01	99.83
	74	0.12	18.78	0.88	79.35	0.24	0.99	0.00	0.00	100.33
	75	0.09	17.96	0.76	77.85	0.29	0.98	0.01	0.00	97.91
	76	0.07	18.03	0.76	77.47	0.23	0.99	0.00	0.01	97.56
	78	0.08	19.01	0.73	78.00	0.21	0.99	0.00	0.00	98.98
	79	0.12	18.53	0.79	77.32	0.19	0.96	0.04	0.04	97.98
	80	0.04	18.75	0.83	77.94	0.22	0.93	0.00	0.00	98.69
	81	0.09	18.75	0.79	77.76	0.23	0.92	0.00	0.00	98.47
	82	0.10	18.34	0.71	76.13	0.31	0.90	0.00	0.05	96.53
	83	0.08	18.65	0.70	76.25	0.22	0.97	0.02	0.02	96.90
	84	0.10	18.46	0.75	75.88	0.20	0.92	0.00	0.00	96.27
	85	0.10	18.51	0.77	75.48	0.25	0.95	0.01	0.00	96.06
	86	0.08	18.94	0.75	76.19	0.24	0.91	0.01	0.03	97.15
	87	0.11	18.62	0.77	78.14	0.23	0.89	0.03	0.08	98.87
	88	0.11	19.00	0.82	77.62	0.22	0.89	0.01	0.00	98.63
	89	0.08	18.91	0.85	78.95	0.23	0.92	0.01	0.00	99.84
	90	0.05	19.09	0.81	78.74	0.20	0.92	0.00	0.04	99.85
	93	0.08	18.97	0.87	77.91	0.22	1.00	0.00	0.01	99.05

[a] Total iron reported as FeO, "-" indicates oxide not analyzed

Appendix 2. (cont.) Compilation of all microprobe analyses of natural samples and experiments.

		Magnetite								
Sample	**Spot**	**SiO_2**	**TiO_2**	**Al_2O_3**	**FeO**	**MgO**	**MnO**	**CaO**	**Cr_2O_3**	**Total**
Pitchstone Plateau										
Y187	84	0.12	17.33	0.65	79.87	0.13	0.90	0.01	0.02	99.03
	85	0.12	17.55	0.77	80.67	0.13	0.91	0.00	0.08	100.23
	86	0.08	17.55	0.63	78.63	0.07	0.82	0.01	0.05	97.84
	87	0.06	17.44	0.63	79.47	0.11	0.88	0.01	0.01	98.61
	88	0.05	17.86	0.66	79.94	0.12	0.84	0.00	0.00	99.47
	89	0.10	18.25	0.67	80.18	0.09	0.90	0.00	0.04	100.22
	90	0.11	17.99	0.68	80.22	0.08	0.92	0.02	0.07	100.09
	91	0.08	17.69	0.63	79.33	0.09	0.92	0.00	0.00	98.73
	92	0.09	17.33	0.66	78.12	0.10	0.88	0.02	0.04	97.24
	93	0.08	17.48	0.66	78.70	0.11	0.78	0.00	0.00	97.74
	94	0.10	17.85	0.72	80.12	0.08	0.77	0.01	0.04	99.68
	95	0.10	17.57	0.72	80.32	0.14	0.88	0.01	0.00	99.72
	96	0.12	18.01	0.71	79.46	0.18	0.87	0.01	0.00	99.30
	97	0.11	17.87	0.77	79.34	0.12	0.95	0.00	0.03	99.20
	99	0.10	18.35	0.71	80.42	0.15	0.94	0.00	0.00	100.56
	100	0.10	17.84	0.65	79.88	0.09	0.87	0.00	0.09	99.52
	101	0.10	17.87	0.76	79.39	0.08	0.82	0.02	0.00	99.00
	102	0.09	17.63	0.68	80.69	0.13	0.81	0.01	0.08	100.13
	103	0.11	17.42	0.69	79.50	0.09	0.80	0.00	0.04	98.66
	104	0.12	17.89	0.70	79.89	0.13	0.82	0.00	0.00	99.50
	105	0.06	17.83	0.67	79.19	0.14	0.88	0.01	0.00	98.75
	106	0.11	17.11	0.66	78.67	0.13	0.87	0.05	0.00	97.60
	107	0.14	17.48	0.67	78.93	0.12	0.88	0.02	0.01	98.23
	108	0.09	17.54	0.77	80.59	0.13	0.80	0.00	0.05	99.97
	109	0.08	17.60	0.70	79.76	0.10	0.81	0.00	0.00	99.02
	110	0.10	17.33	0.71	80.04	0.09	0.78	0.02	0.06	99.12
	111	0.10	17.28	0.71	79.72	0.08	0.83	0.00	0.00	98.66
	112	0.14	17.47	0.72	80.17	0.16	0.87	0.03	0.00	99.53
	113	0.13	17.79	0.74	78.74	0.14	0.80	0.01	0.04	98.38
	114	0.10	17.74	0.77	80.01	0.16	0.82	0.00	0.00	99.55
	115	0.05	17.76	0.74	78.95	0.15	0.81	0.01	0.00	98.43
	116	0.09	18.07	0.74	80.38	0.11	0.84	0.00	0.07	100.29
	117	0.09	17.74	0.73	79.74	0.13	0.90	0.02	0.01	99.37
	118	0.11	17.41	0.68	77.69	0.12	0.80	0.03	0.00	96.79

[a] Total iron reported as FeO, "-" indicates oxide not analyzed

		Magnetite								
Sample	**Spot**	**SiO_2**	**TiO_2**	**Al_2O_3**	**FeO**	**MgO**	**MnO**	**CaO**	**Cr_2O_3**	**Total**
Pitchstone Plateau										
Y187	34	0.10	18.22	0.73	79.70	0.12	0.93	0.00	0.03	99.82
	35	0.10	17.83	0.76	78.76	0.16	0.98	0.00	0.00	98.56
	36	0.09	17.84	0.76	79.82	0.15	0.88	0.00	0.10	99.64
	38	0.07	18.18	0.77	79.21	0.13	0.84	0.00	0.00	99.20
	39	0.12	18.09	0.78	78.42	0.14	0.88	0.01	0.00	98.43
	40	0.09	17.65	0.84	78.66	0.08	0.77	0.02	0.04	98.15
	41	0.12	18.10	0.81	79.04	0.17	0.86	0.02	0.00	99.01
	42	0.10	17.76	0.82	77.55	0.13	0.85	0.03	0.00	97.24
	43	0.06	17.85	0.85	80.05	0.12	0.83	0.00	0.04	99.79
	44	0.09	18.00	0.75	79.99	0.10	0.94	0.00	0.00	99.81
	45	0.10	17.67	0.81	78.83	0.11	0.94	0.00	0.04	98.50
	46	0.14	18.04	0.81	78.30	0.14	0.82	0.00	0.01	98.24
	47	0.11	18.02	0.74	80.08	0.13	0.78	0.02	0.00	99.82
	48	0.08	18.01	0.84	79.48	0.14	0.90	0.02	0.01	99.47
	49	0.11	17.44	0.77	79.93	0.14	0.88	0.00	0.01	99.30
	50	0.11	17.75	0.81	79.41	0.11	0.73	0.01	0.05	98.98
	51	0.11	17.98	0.78	78.38	0.09	0.90	0.00	0.05	98.30
Trischmann Knob										
	6	0.07	19.66	0.91	77.40	0.20	0.85	0.00	0.00	99.07
	7	0.14	19.35	0.88	77.32	0.20	0.84	0.01	0.00	98.68
	8	0.11	19.22	0.87	76.22	0.22	0.92	0.00	0.00	97.57
	9	0.10	19.25	0.89	75.99	0.17	0.78	0.01	0.06	97.24
	10	0.10	19.42	0.84	77.83	0.24	0.86	0.00	0.11	99.40
	11	0.10	18.84	0.91	75.36	0.20	0.99	0.00	0.00	96.39
	12	0.05	18.69	0.86	77.58	0.17	0.82	0.01	0.03	98.21
	13	0.12	18.87	0.88	76.15	0.20	0.92	0.04	0.00	97.18
	28	0.09	18.64	0.95	77.27	0.29	0.95	0.01	0.00	98.18
	29	0.09	19.05	0.86	77.14	0.23	0.96	0.01	0.00	98.33
	30	0.10	18.55	0.93	76.96	0.22	0.96	0.00	0.00	97.72
	31	0.18	18.15	0.90	76.18	0.26	0.98	0.00	0.03	96.69
	33	0.11	17.59	0.89	76.96	0.23	0.90	0.01	0.00	96.68
	34	0.11	19.00	0.88	77.30	0.21	0.82	0.00	0.03	98.36
	36	0.10	18.91	0.89	76.16	0.19	0.90	0.01	0.00	97.11

[a] Total iron reported as FeO, "-" indicates oxide not analyzed

Magnetite

Sample	Spot	SiO_2	TiO_2	Al_2O_3	FeO	MgO	MnO	CaO	Cr_2O_3	Total
Trischmann Knob										
	37	0.10	19.13	0.87	77.74	0.20	0.85	0.01	0.00	98.90
	38	0.09	18.99	0.84	77.58	0.20	0.90	0.00	0.02	98.62
	39	0.14	18.49	0.89	78.34	0.20	1.02	0.00	0.00	99.04
	40	0.09	19.48	0.83	77.28	0.14	0.96	0.00	0.01	98.78
	42	0.16	18.98	0.91	77.49	0.24	0.87	0.00	0.07	98.72
	43	0.11	19.00	0.93	77.63	0.20	0.84	0.01	0.01	98.73
	44	0.13	19.21	0.92	77.94	0.21	0.94	0.03	0.00	99.39
	45	0.07	18.99	0.80	77.38	0.24	0.92	0.00	0.00	98.39
	46	0.12	18.71	0.84	77.85	0.18	0.86	0.01	0.00	98.55
	47	0.11	19.48	0.88	77.16	0.17	0.91	0.00	0.00	98.70
	48	0.11	19.18	0.89	77.70	0.17	0.85	0.02	0.00	98.92
	49	0.12	19.44	0.82	76.39	0.27	0.90	0.00	0.05	97.96
	50	0.13	18.62	0.86	78.37	0.19	0.90	0.00	0.05	99.12
	51	0.13	18.32	0.84	76.63	0.22	0.90	0.01	0.00	96.97
	52	0.05	18.70	0.80	76.28	0.22	0.85	0.00	0.02	96.91
	53	0.08	18.71	0.83	76.77	0.24	0.88	0.00	0.00	97.46
	54	0.12	18.71	0.76	74.36	0.22	0.90	0.01	0.00	95.03
	55	0.05	19.22	0.72	74.59	0.19	0.87	0.00	0.08	95.71
	56	0.07	18.64	0.76	75.28	0.26	0.95	0.01	0.09	96.05
	57	0.09	19.14	0.75	74.97	0.30	0.84	0.00	0.04	96.11
Douglas Knob										
Y88	11	0.10	19.48	1.00	78.01	0.22	0.85	0.01	0.00	99.70
	12	0.10	18.32	1.03	76.01	0.17	0.82	0.00	0.01	96.36
	13	0.10	17.70	0.97	78.93	0.16	0.78	0.02	0.01	98.65
	14	0.12	18.63	0.96	76.75	0.18	0.90	0.02	0.00	97.72
	18	0.08	17.91	1.02	75.93	0.17	0.86	0.03	0.01	96.02
	19	0.10	17.22	0.93	77.81	0.25	0.84	0.01	0.00	97.16
	20	0.12	17.68	1.00	78.40	0.10	0.82	0.00	0.02	98.18
	21	0.08	18.17	1.03	76.96	0.23	0.78	0.02	0.02	97.32
	22	0.13	19.15	0.99	78.04	0.19	0.87	0.01	0.00	99.39
	23	0.10	19.23	0.98	76.97	0.14	0.81	0.01	0.00	98.27
	24	0.09	17.86	0.95	76.11	0.24	0.76	0.03	0.02	96.01
	26	0.09	18.75	1.08	77.83	0.17	0.84	0.01	0.00	98.73

[a] Total iron reported as FeO, "-" indicates oxide not analyzed

		Magnetite								
Sample	**Spot**	**SiO_2**	**TiO_2**	**Al_2O_3**	**FeO**	**MgO**	**MnO**	**CaO**	**Cr_2O_3**	**Total**
Douglas Knob										
Y88	27	0.12	18.88	1.06	77.88	0.19	0.81	0.01	0.02	99.05
	28	0.12	18.49	1.00	77.50	0.26	0.90	0.02	0.01	98.30
	29	0.12	17.89	0.99	78.04	0.17	0.90	0.00	0.00	98.16
	30	0.10	18.87	1.01	76.09	0.24	0.77	0.01	0.02	97.07
	31	0.15	18.10	0.94	77.72	0.24	0.84	0.01	0.00	97.95
	32	0.11	19.13	0.99	77.43	0.33	0.79	0.01	0.00	98.73
	33	0.10	18.61	0.99	77.46	0.46	0.77	0.03	0.00	98.35
	34	0.09	18.49	0.99	77.88	0.20	0.84	0.05	0.01	98.42
	40	0.09	16.90	0.83	79.94	0.08	0.93	0.00	0.06	98.82
	41	0.07	18.69	0.94	76.92	0.21	0.86	0.00	0.08	97.80
	42	0.07	18.65	1.00	77.76	0.17	0.97	0.00	0.02	98.59
	44	0.09	17.89	0.94	76.88	0.19	0.87	0.00	0.05	96.87
	45	0.14	17.86	1.05	76.87	0.27	0.81	0.07	0.00	97.06
	46	0.13	18.20	0.87	79.54	0.18	0.88	0.00	0.00	99.67
	48	0.13	18.83	0.91	77.89	0.20	0.81	0.01	0.00	98.73
	49	0.12	18.60	1.02	78.35	0.12	0.80	0.03	0.02	99.07
	50	0.10	17.55	0.92	78.03	0.19	0.86	0.01	0.00	97.60
	51	0.14	18.07	0.98	77.72	0.16	0.86	0.03	0.00	98.06
	54	0.10	18.96	1.02	77.44	0.19	0.81	0.01	0.00	98.52
	56	0.07	19.31	0.98	78.22	0.20	0.84	0.01	0.00	99.52
	58	0.11	18.64	1.03	77.85	0.19	0.87	0.00	0.04	98.70
Y90	70	0.15	18.66	1.07	77.41	0.19	0.79	0.00	0.00	98.09
	71	0.10	17.86	1.01	77.39	0.18	0.85	0.01	0.03	97.44
	73	0.13	17.86	0.96	78.55	0.15	0.86	0.00	0.00	98.43
	74	0.09	18.68	1.05	77.86	0.13	0.85	0.00	0.00	98.64
	75	0.13	18.30	1.02	76.62	0.18	0.79	0.01	0.00	97.07
	78	0.11	17.83	1.05	78.07	0.13	0.90	0.00	0.00	98.04
	79	0.08	18.83	0.94	77.20	0.13	0.77	0.00	0.02	98.04
	80	0.06	19.57	0.85	77.05	0.23	0.81	0.00	0.00	98.51
	81	0.09	18.91	0.99	78.39	0.19	0.85	0.00	0.00	99.40
	82	0.15	18.21	0.83	75.05	0.15	0.81	0.01	0.02	95.30
	83	0.11	18.64	0.99	76.66	0.17	0.79	0.05	0.06	97.45
	86	0.08	19.60	0.96	77.85	0.16	0.72	0.00	0.00	99.43

[a] Total iron reported as FeO, "-" indicates oxide not analyzed

					Magnetite					
Sample	**Spot**	**SiO_2**	**TiO_2**	**Al_2O_3**	**FeO**	**MgO**	**MnO**	**CaO**	**Cr_2O_3**	**Total**
Douglas Knob										
Y90	87	0.09	18.35	0.96	78.85	0.14	0.81	0.00	0.01	99.14
	89	0.07	19.73	1.14	78.13	0.20	0.79	0.00	0.00	99.99
	91	0.08	18.88	0.98	77.85	0.19	0.86	0.00	0.00	98.98
	92	0.10	18.26	1.11	76.35	0.16	0.76	0.01	0.00	96.70
	93	0.12	18.53	1.06	77.38	0.20	0.80	0.01	0.01	98.08
	94	0.07	18.72	1.04	77.28	0.22	0.85	0.00	0.00	98.06
	95	0.08	18.78	1.06	77.45	0.18	0.82	0.01	0.00	98.28
	96	0.12	18.09	1.07	78.31	0.21	0.78	0.02	0.00	98.53
	97	0.09	18.64	1.04	77.48	0.28	0.81	0.00	0.03	98.43
	98	0.04	18.00	0.97	76.93	0.12	0.90	0.00	0.00	97.02
	99	0.13	18.99	0.86	77.26	0.19	0.83	0.01	0.00	98.18
	100	0.07	19.73	0.97	78.02	0.24	0.87	0.00	0.01	99.96
	101	0.11	19.59	0.95	77.61	0.10	0.81	0.00	0.00	99.17
	102	0.09	18.75	1.07	77.75	0.16	0.83	0.00	0.00	98.57
	103	0.12	19.34	0.90	77.14	0.24	0.78	0.01	0.06	98.71
	104	0.10	19.17	0.97	77.33	0.21	0.91	0.00	0.00	98.70
	105	0.14	17.49	0.96	77.71	0.13	0.74	0.00	0.00	97.20
	106	0.13	18.21	0.93	77.15	0.23	0.75	0.00	0.00	97.38
	107	0.11	18.24	1.04	78.10	0.19	0.84	0.01	0.00	98.54
	111	0.08	18.75	0.95	77.47	0.16	0.80	0.00	0.00	98.28
	112	0.12	18.69	1.05	76.40	0.22	0.84	0.00	0.00	97.42
	113	0.13	18.07	0.93	76.59	0.14	0.81	0.00	0.00	96.73
	115	0.12	18.25	0.96	77.99	0.21	0.79	0.00	0.03	98.43
	116	0.09	19.53	0.99	77.39	0.22	0.84	0.01	0.00	99.07
	117	0.10	18.75	0.99	77.99	0.19	0.81	0.00	0.02	98.91
	118	0.10	19.59	0.97	77.75	0.26	0.83	0.03	0.05	99.64
	119	0.16	18.69	0.99	78.39	0.20	0.89	0.01	0.02	99.35
	120	0.15	18.71	1.09	76.93	0.17	0.81	0.04	0.01	97.87
	121	0.11	18.40	0.96	79.33	0.19	0.82	0.02	0.02	99.82
	122	0.13	18.63	0.94	78.33	0.15	0.86	0.03	0.00	99.04
	123	0.07	18.55	0.83	78.24	0.24	0.88	0.02	0.00	98.87
	124	0.09	18.76	1.05	77.31	0.19	0.77	0.00	0.00	98.14
	125	0.21	18.46	0.99	76.82	0.20	0.84	0.01	0.03	97.64
	126	0.46	18.73	1.11	77.84	0.15	0.83	0.01	0.02	99.20

[a] Total iron reported as FeO, "-" indicates oxide not analyzed

Experiment Glasses

Appendix 2. (cont.) Compilation of all microprobe analyses of natural samples and experiments.

		Experiment Glasses									
Experiment	**Spot**	**SiO_2**	**TiO_2**	**Al_2O_3**	**FeO**	**MgO**	**MnO**	**CaO**	**Na_2O**	**K_2O**	**Total**
14	31	73.55	0.10	11.45	1.24	0.02	0.05	0.42	3.84	5.13	95.79
	32	74.60	0.09	11.71	0.59	0.00	0.08	0.44	3.35	5.32	96.16
	33	73.29	0.09	11.56	1.20	0.04	0.00	0.44	3.65	5.23	95.46
	34	72.93	0.20	11.32	3.09	0.03	0.07	0.42	3.43	5.11	96.61
	35	73.40	0.13	11.32	2.04	0.03	0.02	0.42	3.56	4.79	95.71
25	7	74.28	0.11	11.49	1.73	0.02	0.00	0.44	3.76	5.19	97.00
	8	75.28	0.13	11.12	1.43	0.02	0.00	0.44	3.52	5.19	97.15
	9	76.08	0.04	10.98	0.86	0.02	0.07	0.40	3.11	5.39	96.96
	10	74.40	0.12	11.60	1.22	0.00	0.03	0.38	3.75	5.32	96.81
	11	74.89	0.19	11.77	1.63	0.00	0.03	0.47	3.49	5.30	97.73
29	7	70.14	0.12	11.28	0.89	0.01	0.00	0.45	3.44	4.38	90.69
	8	68.79	0.00	10.67	0.47	0.00	0.03	0.39	3.81	4.65	88.82
	9	71.28	0.06	11.13	0.58	0.00	0.08	0.41	3.91	4.43	91.88
	10	71.00	0.07	11.13	1.15	0.02	0.04	0.45	4.23	4.45	92.54
	11	73.06	0.07	11.16	0.74	0.01	0.02	0.40	3.74	4.28	93.47
	12	72.81	0.05	10.74	0.88	0.02	0.03	0.42	3.94	4.42	93.31
36	31	73.73	0.09	11.25	0.64	0.00	0.00	0.36	3.23	5.15	94.45
	32	73.65	0.10	11.25	0.62	0.05	0.00	0.38	3.71	5.05	94.79
	33	73.11	0.05	11.14	0.95	0.03	0.06	0.39	3.99	5.27	94.98
	34	75.16	0.07	11.21	0.87	0.03	0.06	0.43	3.72	5.05	96.59
	35	73.76	0.09	11.57	1.32	0.06	0.00	0.42	4.07	5.05	96.32
	36	72.05	0.07	11.52	0.60	0.02	0.03	0.42	3.70	5.19	93.61
46	32	74.99	0.05	11.32	1.36	0.02	0.07	0.54	3.96	5.17	97.48
	33	73.33	0.07	11.49	0.96	0.05	0.07	0.43	3.86	4.99	95.26
	34	76.66	0.15	11.56	1.06	0.02	0.04	0.44	4.03	5.19	99.15
	35	73.14	0.11	11.22	1.14	0.01	0.11	0.44	3.35	4.79	94.32
	36	74.30	0.03	11.38	1.01	0.08	0.03	0.45	3.74	4.86	95.88

[a] Total iron reported as FeO, "-" indicates oxide not analyzed

Appendix 2. (cont.) Compilation of all microprobe analyses of natural samples and experiments.

		Experiment Glasses									
Experiment	**Spot**	**SiO_2**	**TiO_2**	**Al_2O_3**	**FeO**	**MgO**	**MnO**	**CaO**	**Na_2O**	**K_2O**	**Total**
62	7	77.92	0.08	11.76	0.89	0.02	0.13	0.36	3.99	5.21	100.37
	8	77.39	0.05	11.54	0.92	0.00	0.00	0.40	4.31	5.34	99.94
	9	74.69	0.01	11.95	0.86	0.00	0.04	0.39	3.55	5.23	96.69
	10	76.44	0.03	11.83	0.66	0.01	0.07	0.36	4.02	5.16	98.59
	11	75.89	0.11	12.08	1.22	0.01	0.00	0.34	4.09	5.06	98.79
	12	73.23	0.11	11.69	0.82	0.00	0.01	0.36	3.89	4.85	94.94
63	19	76.30	0.08	11.51	0.90	0.00	0.00	0.39	3.89	4.84	97.90
	20	73.98	0.03	11.10	0.78	0.00	0.00	0.39	3.52	4.86	94.65
	21	75.61	0.06	11.46	0.66	0.00	0.05	0.45	4.12	4.80	97.20
	22	74.34	0.11	11.36	0.71	0.00	0.01	0.39	3.76	4.77	95.44
	23	75.76	0.02	11.01	0.54	0.00	0.04	0.38	3.30	4.89	95.93
	24	73.11	0.07	11.74	0.93	0.01	0.03	0.40	3.36	4.86	94.51
70	31	75.28	0.14	11.94	0.66	0.02	0.05	0.08	4.09	5.08	97.35
	32	75.06	0.13	11.64	0.57	0.03	0.11	0.10	4.26	4.96	96.85
	33	76.56	0.14	11.95	0.60	0.05	0.00	0.13	3.78	5.16	98.33
	34	76.56	0.05	11.96	0.85	0.02	0.04	0.07	3.88	5.21	98.63
	35	77.77	0.19	11.90	0.59	0.01	0.08	0.12	4.23	5.17	100.06
	36	76.27	0.16	12.09	0.91	0.01	0.02	0.10	4.35	5.13	99.04
71	20	72.54	0.04	11.19	1.20	0.00	0.06	0.04	4.63	4.53	94.21
	21	73.40	0.03	11.18	0.75	0.01	0.02	0.04	4.19	4.32	93.94
	22	73.30	0.09	11.14	1.86	0.03	0.11	0.01	4.29	4.44	95.29
	23	72.36	0.24	11.04	1.16	0.00	0.02	0.07	4.02	4.35	93.25
	24	72.89	0.02	11.27	1.53	0.03	0.04	0.06	4.00	4.29	94.13
	7	74.33	0.07	11.60	1.44	0.02	0.00	0.36	4.00	4.37	96.19
	8	73.88	0.14	11.34	1.03	0.00	0.08	0.35	3.72	4.43	94.96
	9	74.33	0.14	11.49	1.34	0.00	0.05	0.41	3.71	4.46	95.92
	10	73.83	0.13	11.03	1.56	0.00	0.00	0.33	3.97	4.25	95.03
	11	74.87	0.14	11.17	1.65	0.00	0.03	0.36	3.65	4.23	96.08
	12	74.59	0.06	10.98	0.97	0.03	0.03	0.35	4.08	4.26	95.36

[a] Total iron reported as FeO, "-" indicates oxide not analyzed

Appendix 2. (cont.) Compilation of all microprobe analyses of natural samples and experiments.

		Experiment Glasses									
Experiment	**Spot**	**SiO_2**	**TiO_2**	**Al_2O_3**	**FeO**	**MgO**	**MnO**	**CaO**	**Na_2O**	**K_2O**	**Total**
72	7	70.80	0.19	11.35	0.89	0.02	0.02	0.10	3.62	4.91	91.90
	8	70.34	0.08	11.34	1.10	0.02	0.08	0.14	3.42	4.75	91.28
	9	70.20	0.04	11.37	0.93	0.03	0.01	0.11	3.96	4.71	91.36
	10	68.86	0.21	11.30	1.04	0.05	0.07	0.13	4.04	4.93	90.63
	11	68.11	0.16	11.63	0.89	0.05	0.06	0.15	3.83	5.01	89.91
	12	67.98	0.06	11.03	0.47	0.06	0.05	0.14	3.74	5.01	88.54
75	7	73.64	0.05	11.47	0.66	0.01	0.03	0.46	4.43	4.94	95.69
	8	73.62	0.10	11.30	0.99	0.01	0.01	0.46	3.84	4.78	95.10
	9	73.72	0.09	11.41	1.19	0.05	0.00	0.48	3.75	4.85	95.51
	10	73.34	0.02	11.32	1.06	0.04	0.00	0.43	3.55	4.75	94.50
	11	72.60	0.09	11.27	1.05	0.07	0.08	0.42	3.23	4.54	93.35
	12	73.24	0.04	10.83	1.13	0.00	0.00	0.39	3.47	4.65	93.74
76	19	70.80	0.18	11.43	1.69	0.01	0.05	0.53	3.25	4.71	92.65
	20	72.04	0.04	11.49	0.79	0.03	0.02	0.47	3.44	4.70	93.01
	21	72.07	0.05	11.57	0.65	0.04	0.04	0.42	3.80	4.78	93.42
	22	71.11	0.16	11.48	1.36	0.02	0.00	0.45	3.71	4.58	92.86
	23	71.22	0.13	11.31	0.58	0.03	0.00	0.44	3.28	4.68	91.67
	24	72.75	0.06	11.65	0.85	0.06	0.02	0.45	3.15	4.81	93.80
77	31	71.38	0.07	11.13	0.72	0.04	0.10	0.46	3.52	4.28	91.69
	32	71.89	0.04	11.19	0.90	0.01	0.05	0.48	3.13	4.28	91.97
	33	71.32	0.03	11.47	0.58	0.00	0.07	0.46	3.80	4.20	91.92
	34	73.43	0.08	11.31	0.54	0.00	0.00	0.48	3.33	4.17	93.32
	35	73.08	0.01	11.23	0.50	0.04	0.08	0.50	3.63	4.15	93.23
	36	72.59	0.06	11.37	0.72	0.01	0.07	0.48	3.48	4.31	93.09
85	7	70.26	0.04	11.42	0.43	0.01	0.00	0.44	4.17	4.43	91.20
	8	71.63	0.13	11.43	0.77	0.01	0.06	0.42	3.46	4.57	92.48
	9	71.84	0.06	11.40	0.54	0.03	0.00	0.45	3.57	4.61	92.49
	10	71.18	0.01	11.26	0.58	0.04	0.03	0.44	3.32	4.58	91.43
	11	70.43	-0.01	11.27	0.76	0.00	0.00	0.44	3.45	4.58	90.90
	12	71.72	0.13	10.90	0.87	0.02	0.07	0.45	3.24	4.60	92.00

[a] Total iron reported as FeO, "-" indicates oxide not analyzed

Appendix 2. (cont.) Compilation of all microprobe analyses of natural samples and experiments.

						Experiment Glasses					
Experiment	**Spot**	**SiO_2**	**TiO_2**	**Al_2O_3**	**FeO**	**MgO**	**MnO**	**CaO**	**Na_2O**	**K_2O**	**Total**
88	19	74.74	0.13	11.17	0.75	0.03	0.05	0.28	4.05	4.65	95.87
	20	76.18	0.12	11.49	0.70	0.04	0.00	0.36	3.78	5.22	97.87
	21	75.22	0.07	11.55	0.67	0.02	0.01	0.29	3.84	4.81	96.49
	22	76.78	0.18	11.20	0.86	0.00	0.06	0.26	3.08	4.56	96.95
	23	75.07	0.17	11.30	1.06	0.00	0.03	0.33	3.50	4.91	96.36
	24	75.57	0.06	11.34	0.59	0.01	0.03	0.35	3.35	4.78	96.07
96	19	73.81	0.11	11.24	1.01	0.00	0.09	0.35	3.71	4.72	94.99
	20	73.57	0.10	11.49	0.90	0.04	0.09	0.38	3.47	4.77	94.82
	21	74.01	0.07	11.43	0.90	0.03	0.00	0.37	3.85	4.80	95.45
	22	73.49	0.11	11.32	0.93	0.01	0.02	0.35	3.53	4.81	94.56
	23	73.53	0.14	11.44	0.71	0.00	0.02	0.34	3.54	4.72	94.43
	24	74.20	0.16	11.58	1.10	0.06	0.01	0.39	4.03	4.56	96.08
97	32	75.24	0.13	11.79	1.60	0.00	0.02	0.46	3.84	5.30	98.35
	33	75.29	0.07	11.76	1.21	0.04	0.06	0.47	3.59	5.17	97.65
	34	75.16	0.08	11.62	1.31	0.02	0.02	0.46	4.08	5.57	98.33
	35	75.52	0.13	11.64	0.93	0.08	0.04	0.45	3.63	5.24	97.65
	36	75.51	0.05	11.67	1.05	0.01	0.04	0.42	3.56	5.42	97.72
98	7	75.47	0.06	11.24	0.82	0.00	0.03	0.38	4.08	4.68	96.72
	8	74.90	0.07	11.36	1.98	0.00	0.05	0.35	4.04	4.39	97.13
	10	77.54	0.12	11.20	0.96	0.02	0.02	0.32	4.12	4.68	98.98
	11	76.91	0.07	11.32	0.62	0.00	0.05	0.39	4.07	4.91	98.33
	12	76.76	0.09	11.27	0.63	0.03	0.00	0.35	3.62	4.60	97.35
99	31	74.42	0.04	10.94	0.67	0.00	0.02	0.34	3.76	4.13	94.30
	32	73.60	0.11	10.62	0.62	0.02	0.00	0.31	4.34	3.88	93.50
	33	73.80	0.09	10.87	0.58	0.02	0.00	0.34	3.79	4.04	93.53
	34	73.04	0.13	11.13	0.70	0.01	0.01	0.38	3.72	3.95	93.06
	35	73.11	0.04	11.10	0.54	0.00	0.00	0.37	3.85	4.13	93.13
	36	73.35	0.11	10.86	0.94	0.01	0.06	0.36	4.04	3.90	93.63

[a]Total iron reported as FeO, "-" indicates oxide not analyzed

Appendix 2. (cont.) Compilation of all microprobe analyses of natural samples and experiments.

		Experiment Glasses									
Experiment	**Spot**	**SiO_2**	**TiO_2**	**Al_2O_3**	**FeO**	**MgO**	**MnO**	**CaO**	**Na_2O**	**K_2O**	**Total**
100	20	72.90	0.10	11.34	0.62	0.02	0.05	0.49	3.64	5.06	94.22
	21	72.79	0.09	11.52	1.17	0.00	0.05	0.51	3.54	4.88	94.53
	22	75.74	0.15	11.75	0.98	0.07	0.02	0.50	3.65	5.09	97.95
	23	75.64	0.12	11.61	1.17	0.03	0.05	0.49	3.71	5.01	97.84
	24	72.22	0.07	11.78	1.26	0.00	0.02	0.51	3.84	5.01	94.70
101	19	77.38	0.08	11.99	0.96	0.00	0.05	0.43	3.73	5.07	99.70
	21	76.96	0.11	11.56	1.24	0.03	0.00	0.44	3.67	5.14	99.15
	22	75.59	0.22	11.13	0.79	0.00	0.06	0.45	3.95	4.93	97.09
	24	77.87	0.06	12.14	1.07	0.06	0.05	0.46	4.46	5.34	101.51
102	7	73.61	0.07	11.29	0.52	0.00	0.04	0.34	3.68	4.76	94.32
	8	73.67	0.00	11.42	0.77	0.00	0.00	0.39	3.81	4.84	94.85
	9	72.67	0.08	11.43	0.52	0.00	0.03	0.37	3.51	4.75	93.35
	10	73.79	0.08	11.42	0.87	0.00	0.00	0.33	3.80	4.62	94.88
	11	71.21	0.03	11.36	0.67	0.00	0.00	0.35	3.72	4.63	91.98
	12	72.23	0.13	11.41	0.89	0.02	0.02	0.36	3.70	4.71	93.46
103	31	75.76	0.13	10.92	0.55	0.00	0.02	0.26	3.54	4.43	95.59
	32	74.51	0.05	10.90	0.39	0.00	0.01	0.29	3.98	4.10	94.22
	33	76.23	0.05	11.33	0.57	0.00	0.07	0.30	3.53	4.50	96.58
	34	76.85	0.08	11.39	0.29	0.00	0.01	0.30	4.13	4.54	97.58
	35	74.40	0.07	10.45	0.69	0.04	0.02	0.19	3.60	4.67	94.14
105	31	77.97	0.00	12.09	0.86	0.01	0.04	0.46	3.64	4.86	99.93
	32	77.14	0.21	11.95	1.09	0.01	0.05	0.44	3.79	4.97	99.65
	33	77.25	0.08	12.04	1.02	0.02	0.00	0.43	3.74	5.29	99.87
	34	76.36	0.13	11.93	1.21	0.02	0.11	0.47	4.20	5.20	99.64
	35	76.32	0.03	12.25	1.01	0.01	0.07	0.42	3.99	5.05	99.15
	36	77.00	0.19	11.64	1.75	0.03	0.12	0.44	3.79	4.94	99.89

[a] Total iron reported as FeO, "-" indicates oxide not analyzed

Appendix 2. (cont.) Compilation of all microprobe analyses of natural samples and experiments.

						Experiment Glasses					
Experiment	**Spot**	**SiO_2**	**TiO_2**	**Al_2O_3**	**FeO**	**MgO**	**MnO**	**CaO**	**Na_2O**	**K_2O**	**Total**
106	19	73.73	0.12	11.38	0.87	0.02	0.06	0.46	3.69	5.01	95.34
	20	74.07	0.16	11.47	1.39	0.05	0.02	0.43	3.40	4.96	95.95
	21	76.04	0.17	11.71	0.71	0.00	0.10	0.42	3.29	4.51	96.96
	22	74.82	0.16	11.67	0.71	0.03	0.02	0.39	3.46	4.48	95.73
	23	74.86	0.04	11.64	0.83	0.02	0.01	0.39	3.95	4.74	96.48
	24	74.67	0.12	11.64	1.04	0.03	0.01	0.42	3.54	4.68	96.13

---

[a] Total iron reported as FeO, "-" indicates oxide not analyzed

Experiment feldspar

Appendix 2. (cont.) Compilation of all microprobe analyses of natural samples and experiments.

					Experiment Feldspar						
Experiment	**Spot**	**SiO_2**	**Al_2O_3**	**FeO**	**MgO**	**CaO**	**Na_2O**	**K_2O**	**BaO**	**Total**	**Or#**
1	27	65.45	18.69	0.17	0.03	0.53	5.80	8.49	-	99.16	47.8
	28	66.08	18.96	0.15	0.00	0.55	5.81	8.50	-	100.05	47.8
	29	68.60	17.04	0.58	0.06	0.67	5.36	7.93	-	100.24	47.7
4	27	66.84	18.85	0.34	0.00	0.53	5.64	8.66	-	100.85	49.0
	28	66.35	18.90	0.18	0.00	0.53	5.66	8.78	-	100.36	49.2
	29	66.71	18.87	0.29	0.01	0.51	5.46	9.16	-	101.01	51.2
	30	66.82	18.41	0.75	0.00	0.50	5.43	9.05	-	100.96	51.1
	31	66.06	19.08	0.19	0.00	0.52	5.46	8.96	-	100.27	50.6
	32	66.74	18.84	0.69	0.00	0.40	5.14	9.33	-	101.11	53.4
	33	66.15	18.50	0.61	0.01	0.40	5.18	9.29	-	100.14	53.1
	34	66.92	18.75	0.25	0.00	0.52	5.32	9.00	-	100.76	51.4
	4	66.64	18.03	0.52	0.01	0.33	4.46	9.30	0.14	99.43	56.9
	7	66.84	19.46	0.15	0.00	0.73	5.28	7.16	0.21	99.81	45.3
	8	67.69	18.81	0.40	0.02	0.77	5.18	7.82	0.00	100.67	47.9
	14	67.19	18.22	0.47	0.02	0.33	4.79	9.12	0.09	100.24	54.7
	15	66.06	18.76	0.59	0.02	0.67	5.09	8.80	0.17	100.17	51.5
	17	66.93	18.57	0.55	0.00	0.53	5.03	8.63	0.17	100.41	51.6
6	44	65.25	18.82	0.53	0.04	1.25	5.87	7.40	0.21	99.37	42.60
	46	67.17	17.23	0.35	0.00	1.83	5.85	7.77	0.03	100.21	42.70
7	37	66.91	19.36	0.55	0.00	0.70	6.17	7.57	0.25	101.51	43.20
	40	66.91	18.43	0.68	0.00	0.30	4.40	9.56	0.11	100.39	58.00
	24	64.20	17.68	0.60	0.01	0.80	5.95	7.92	-	97.16	44.9
	25	66.17	18.68	0.13	0.01	0.58	5.63	8.59	-	99.79	48.7
	27	65.48	18.21	0.19	0.02	0.41	5.55	8.65	-	98.51	49.6
	29	66.31	17.62	0.37	0.01	0.23	5.09	9.78	-	99.42	55.2
	31	65.59	18.34	0.18	0.01	0.50	5.52	8.59	-	98.73	49.4

[a] Total iron reported as FeO, "-" indicates oxide not analyzed

Appendix 2. (cont.) Compilation of all microprobe analyses of natural samples and experiments.

						Experiment Feldspar					
Experiment	**Spot**	**SiO_2**	**Al_2O_3**	**FeO**	**MgO**	**CaO**	**Na_2O**	**K_2O**	**BaO**	**Total**	**Or#**
9	3	68.22	16.14	1.75	0.00	0.29	4.05	8.59	0.00	98.92	57.3
	4	66.78	18.17	0.45	0.00	0.23	4.90	9.37	0.14	100.01	55.1
	5	68.43	17.41	1.18	0.03	0.40	5.14	8.04	0.00	100.48	49.7
	61	67.66	17.19	0.80	0.00	-	4.77	8.97	-	99.39	55.3
	62	69.33	16.98	0.96	0.02	-	5.13	7.56	0.07	100.05	49.2
	63	69.23	16.56	2.09	0.01	-	4.89	8.11	0.08	100.97	52.2
	67	69.34	17.19	0.79	0.03	0.10	5.31	7.25	0.05	100.05	47.0
	72	67.87	17.88	0.82	0.00	0.05	5.60	7.54	0.05	99.81	46.9
10	3	68.22	16.14	1.75	0.00	0.29	4.05	8.59	0.00	98.92	57.30
	4	66.78	18.17	0.45	0.00	0.23	4.90	9.37	0.14	100.01	55.10
	5	68.43	17.41	1.18	0.03	0.40	5.14	8.04	0.00	100.48	49.70
11	12	65.84	15.64	0.48	0.04	0.45	3.04	10.05	-	95.54	66.7
	14	65.82	18.01	0.35	0.03	0.17	3.68	11.56	-	99.63	66.8
	15	67.58	18.50	0.24	0.00	0.37	4.43	10.61	-	101.71	60.1
	16	68.09	18.00	0.32	0.01	0.19	3.79	11.32	-	101.72	65.7
	17	68.87	16.90	0.40	0.01	0.26	3.32	10.18	-	99.94	65.9
	19	66.24	18.39	0.19	0.00	0.48	4.81	9.99	-	100.10	56.4
	20	65.19	17.99	0.36	0.01	0.28	3.92	11.00	-	98.77	64.0
	20	68.46	17.17	0.27	0.00	0.19	2.87	10.13	0.36	99.45	69.10
	21	66.95	17.45	0.39	0.03	0.13	3.24	11.18	0.11	99.48	68.90
	22	66.71	18.48	0.25	0.00	0.07	3.19	12.31	0.17	101.16	71.50
	23	67.35	17.90	0.71	0.06	0.19	3.14	11.15	0.14	100.64	69.30
	25	67.29	18.26	0.49	0.00	0.04	3.07	12.05	0.33	101.54	71.90
	27	67.06	18.91	0.23	0.01	0.41	4.08	10.65	0.19	101.54	62.00
	29	67.24	18.14	0.26	0.00	0.09	3.31	11.76	0.22	101.03	69.70

[a]Total iron reported as FeO, "-" indicates oxide not analyzed

Appendix 2. (cont.) Compilation of all microprobe analyses of natural samples and experiments.

					Experiment Feldspar					
Experiment	**Spot**	**SiO_2**	**Al_2O_3**	**FeO**	**MgO**	**CaO**	**Na_2O**	**K_2O**	**BaO**	**Total**	**Or#**
14	29.00	66.64	18.75	0.83	0.00	1.07	7.35	4.63	0.01	99.29	27.73
	30.00	66.95	18.47	0.57	0.01	0.15	5.75	7.80	0.09	99.78	46.80
	32.00	66.58	18.45	0.58	0.00	-	5.51	8.43	0.13	99.69	50.19
	34.00	66.30	18.60	0.67	0.01	0.64	6.50	6.39	0.11	99.23	38.01
	35.00	67.91	18.32	0.70	0.04	0.96	7.05	5.19	0.06	100.23	31.04
	38.00	66.87	18.47	0.49	0.04	-	5.74	8.10	0.00	99.71	48.14
	39.00	66.29	19.53	0.66	0.05	1.16	6.73	5.45	0.11	99.97	32.71
	43.00	66.50	18.44	2.16	0.00	0.09	5.79	7.48	0.15	100.61	45.71
	44.00	66.94	18.93	0.58	0.01	0.34	6.01	7.12	0.00	99.94	43.06
	45.00	66.97	18.66	0.56	0.04	0.23	6.12	7.23	0.00	99.81	43.24
	46.00	67.05	19.65	0.60	0.00	1.27	7.24	4.92	0.05	100.78	28.98
	49.00	67.04	19.05	0.63	0.00	0.26	6.18	7.25	0.08	100.49	42.97
	51.00	67.70	18.78	0.71	0.01	0.61	6.77	6.26	-	100.84	36.70
15	9.00	66.84	19.21	0.24	0.00	0.14	6.54	7.57	0.23	100.76	42.97
	11.00	67.94	19.09	0.47	0.00	0.43	6.45	6.50	0.10	100.97	39.01
	12.00	69.10	18.30	0.39	0.00	0.34	6.22	6.28	0.21	100.84	39.19
	17.00	66.91	19.13	0.16	0.01	-	5.90	8.11	0.21	100.42	47.49
	18.00	67.41	18.86	0.53	0.01	0.01	5.98	7.79	0.16	100.74	46.10
	20.00	67.88	18.78	0.53	0.00	0.63	6.75	6.22	0.20	100.98	36.60
	21.00	68.53	18.24	0.43	0.01	0.31	6.31	6.49	0.19	100.52	39.71
	22.00	66.67	19.02	0.50	0.00	0.26	6.44	7.13	0.25	100.28	41.60
	24.00	66.08	19.14	0.23	0.00	0.04	6.15	8.10	0.25	99.99	46.37
	11.00	67.91	18.15	0.22	0.00	0.55	5.92	8.38	-	101.13	46.98
	12.00	68.00	18.34	0.31	0.00	0.54	6.10	7.97	-	101.26	45.04
	13.00	68.86	17.44	0.33	0.00	0.23	5.18	9.37	-	101.40	53.73
	15.00	68.43	18.27	0.25	0.01	0.61	6.28	7.42	-	101.27	42.43
	16.00	69.25	17.34	0.54	0.02	0.72	6.00	6.97	-	100.83	41.78
	17.00	67.97	18.40	0.23	0.00	0.57	5.65	8.14	-	100.94	47.32
	18.00	68.89	18.39	0.47	0.00	0.59	5.82	7.76	-	101.92	45.37
	19.00	68.00	19.01	0.20	0.03	0.69	6.57	7.39	-	101.89	41.15
	20.00	68.22	18.44	0.40	0.03	0.64	6.51	7.30	-	101.55	41.14

[a] Total iron reported as FeO, "-" indicates oxide not analyzed

						Experiment Feldspar					
Experiment	**Spot**	**SiO_2**	**Al_2O_3**	**FeO**	**MgO**	**CaO**	**Na_2O**	**K_2O**	**BaO**	**Total**	**Or#**
19	24	64.86	18.44	0.11	0.01	0.50	5.49	8.93	-	98.34	50.5
	25	64.56	18.36	0.15	0.01	0.46	4.46	10.22	-	98.22	58.8
	26	65.36	18.20	0.24	0.00	0.46	4.98	9.52	-	98.76	54.5
	27	65.11	18.34	0.22	0.00	0.45	5.56	9.32	-	98.99	51.4
	31	65.53	18.02	0.31	0.00	0.12	3.76	11.30	-	99.02	66.0
	32	64.58	18.40	0.31	0.02	0.39	4.80	10.14	-	98.63	57.1
	36	65.96	18.82	0.40	0.00	0.47	3.96	10.58	-	100.17	62.2
	37	67.07	18.58	0.48	0.00	0.17	3.55	11.33	-	101.15	67.2
	38	67.25	18.06	0.91	0.00	0.21	3.75	10.56	-	100.75	64.2
	39	67.12	18.09	0.57	0.00	0.19	3.50	11.13	-	100.56	67.1
	40	67.08	18.23	0.34	0.00	0.23	3.97	10.66	-	100.52	63.1
	42	67.79	18.18	0.32	0.00	0.41	3.88	10.13	-	100.71	61.9
	43	66.70	18.28	0.47	0.00	0.21	3.70	11.23	-	100.59	66.0
	45	67.34	18.09	0.47	0.00	0.19	3.48	10.76	-	100.32	66.4
	46	66.72	18.62	0.63	0.01	0.12	3.44	11.17	-	100.72	67.7
29	12	68.85	17.54	0.33	0.00	0.07	3.96	11.05	-	101.80	64.5
	14	67.68	18.87	0.22	0.02	0.42	4.92	9.82	-	101.96	55.6
	16	68.19	18.23	0.35	0.00	0.26	4.91	9.81	-	101.74	56.1
	17	67.21	18.09	0.37	0.00	0.16	4.47	10.35	-	100.65	59.9
	18	68.68	18.01	0.47	0.02	0.11	4.49	10.43	-	102.21	60.1
	20	68.76	17.96	0.26	0.00	0.09	4.41	10.65	-	102.12	61.1
36	16	68.16	18.07	0.38	0.01	0.21	4.38	9.65	-	100.86	58.5
	18	69.87	16.33	0.48	0.01	0.28	3.97	8.49	-	99.44	57.5
	19	63.21	15.55	9.76	0.06	0.28	3.89	7.68	-	100.44	55.6
	20	65.36	18.98	0.35	0.00	0.94	5.95	7.96	-	99.52	44.7
	22	67.98	17.61	0.48	0.01	0.41	4.95	8.54	-	99.97	52.1
	26	65.68	18.81	0.20	0.02	0.49	5.86	7.98	-	99.04	46.1
	21	62.77	22.65	0.32	0.01	4.29	8.67	1.76	-	100.46	9.5
	24	60.56	24.76	0.09	0.01	6.20	7.66	1.15	-	100.43	6.4

[a] Total iron reported as FeO, "-" indicates oxide not analyzed

Appendix 2. (cont.) Compilation of all microprobe analyses of natural samples and experiments.

					Experiment Feldspar						
Experiment	**Spot**	**SiO_2**	**Al_2O_3**	**FeO**	**MgO**	**CaO**	**Na_2O**	**K_2O**	**BaO**	**Total**	**Or#**
40	21	65.37	19.05	0.21	0.02	0.56	5.44	8.48	-	99.12	49.2
	22	66.27	19.02	0.18	0.02	0.49	5.50	8.50	-	99.97	49.2
	23	65.84	18.95	0.25	0.00	0.51	5.44	8.67	-	99.67	49.9
	25	65.01	18.46	0.28	0.00	0.49	5.18	8.78	-	98.21	51.5
	27	64.57	18.30	0.20	0.03	0.38	5.41	8.71	-	97.59	50.5
	28	67.36	16.35	0.25	0.00	0.06	4.53	8.89	-	97.43	56.2
	29	66.33	19.11	0.24	0.01	0.44	5.35	9.05	-	100.52	51.6
50	21	67.85	18.11	0.26	0.00	0.26	4.06	10.97	-	101.49	63.2
	22	69.00	17.89	0.27	0.01	0.41	4.82	9.42	-	101.82	55.1
	23	67.82	15.60	0.90	0.00	1.38	3.32	9.83	-	98.84	61.3
	25	67.85	18.94	0.20	0.00	0.63	6.69	7.11	-	101.41	39.9
	26	67.52	19.08	0.24	0.00	0.53	5.89	8.30	-	101.57	46.9
	27	69.55	17.13	0.35	0.00	0.29	3.70	10.51	-	101.52	64.2
	29	67.36	18.87	0.20	0.00	0.52	5.32	9.20	-	101.47	51.9
	30	67.41	18.03	0.38	0.00	0.28	3.88	10.83	-	100.82	63.8
55	11	65.20	18.44	0.27	0.00	0.43	5.63	8.24	-	98.21	48.0
	12	64.78	18.33	0.25	0.02	0.37	5.60	8.42	-	97.78	48.8
	13	65.37	18.61	0.16	0.00	0.52	5.40	8.51	-	98.56	49.6
	14	66.06	18.38	0.56	0.00	0.75	5.67	8.07	-	99.48	46.6
57	32	66.17	17.74	0.42	0.00	0.26	3.60	10.62	-	98.81	65.1
	33	64.06	18.32	0.14	0.01	0.48	4.59	9.88	-	97.47	57.3
	34	66.76	16.58	0.62	0.00	0.09	3.28	10.51	-	97.85	67.5
	35	66.28	17.47	0.41	0.01	0.06	3.70	11.10	-	99.03	66.2
	36	65.67	17.96	0.83	0.00	0.23	3.76	11.07	-	99.51	65.2
	37	65.27	17.93	0.66	0.00	0.18	3.69	11.28	-	99.00	66.2
	38	66.19	16.09	0.35	0.01	0.19	3.13	9.35	-	95.31	65.5
	39	64.39	16.99	0.60	0.00	0.13	3.44	10.90	-	96.45	67.1
	40	65.80	18.11	0.94	0.00	0.27	4.34	10.09	-	99.54	59.6
	41	66.95	18.86	0.27	0.00	0.37	4.44	9.86	-	100.75	58.3
	42	66.23	18.25	0.30	0.02	0.42	4.29	10.15	-	99.66	59.6
	43	66.37	17.64	0.29	0.00	0.31	4.04	10.25	-	98.88	61.5

[a] Total iron reported as FeO, "-" indicates oxide not analyzed

						Experiment Feldspar					
Experiment	**Spot**	**SiO_2**	**Al_2O_3**	**FeO**	**MgO**	**CaO**	**Na_2O**	**K_2O**	**BaO**	**Total**	**Or#**
61	13	67.41	18.85	0.33	0.00	0.54	5.73	8.52	-	101.39	48.2
	15	67.87	18.38	0.35	0.01	0.24	5.55	9.26	-	101.67	51.8
	19	67.50	18.07	1.17	0.00	0.41	5.37	8.66	-	101.18	50.5
	17	68.79	15.91	0.81	0.01	0.25	4.28	8.40	-	98.45	55.6
	24	68.27	17.95	0.42	0.00	0.12	4.87	9.51	-	101.13	55.9
62	24	67.81	18.34	0.24	0.01	0.14	5.10	9.52	-	101.16	54.8
	25	69.61	16.95	0.41	0.02	0.37	5.02	7.61	-	99.99	48.9
	26	68.01	17.76	0.41	0.00	0.14	4.94	9.44	-	100.69	55.3
	27	66.86	18.13	0.26	0.02	0.20	5.54	9.01	-	100.02	51.2
	28	65.76	17.84	2.43	0.02	0.38	5.34	8.41	-	100.18	49.9
63	31	66.50	19.00	0.23	0.00	0.50	5.05	9.52	-	100.80	54.0
	32	66.89	18.93	0.25	0.03	0.47	5.39	8.99	-	100.96	51.1
	33	67.81	18.31	0.30	0.00	0.10	4.47	10.36	-	101.34	60.1
	34	67.57	18.44	0.32	0.01	0.29	5.10	9.61	-	101.33	54.6
	35	67.21	18.52	0.36	0.02	0.17	4.84	10.15	-	101.27	57.5
	36	67.84	18.27	0.35	0.00	0.08	4.65	10.46	-	101.65	59.5
	37	68.57	17.24	0.44	0.00	0.20	4.64	9.50	-	100.57	56.8
	38	65.86	18.58	0.36	0.00	0.56	4.94	9.55	-	99.84	54.5
	39	68.94	16.00	0.79	0.00	0.19	3.72	8.45	-	98.08	59.2
	40	67.15	17.71	0.46	0.00	0.34	4.51	9.66	-	99.82	57.5
64	11	65.88	18.33	0.26	0.00	0.26	5.69	8.42	-	98.82	48.7
	12	64.94	17.96	0.52	0.00	0.36	4.70	9.45	-	97.94	55.9
	13	65.16	18.68	0.17	0.00	0.49	5.50	8.41	-	98.40	48.9
	14	65.46	18.60	0.19	0.01	0.49	5.57	8.33	-	98.65	48.4
	15	64.92	18.95	0.19	0.01	0.46	5.42	8.73	-	98.68	50.3
	16	66.13	18.85	0.27	0.01	0.54	5.53	8.48	-	99.81	48.9
	17	65.63	18.53	0.22	0.00	0.44	5.61	8.34	-	98.77	48.4
	18	65.49	18.63	0.21	0.00	0.42	5.85	8.07	-	98.65	46.6
	19	66.33	17.52	0.35	0.02	0.17	5.24	8.70	-	98.32	51.8
	20	63.75	17.63	0.53	0.00	0.21	5.87	7.99	-	95.96	46.8

[a] Total iron reported as FeO, "-" indicates oxide not analyzed

Appendix 2. (cont.) Compilation of all microprobe analyses of natural samples and experiments.

						Experiment Feldspar					
Experiment	**Spot**	**SiO_2**	**Al_2O_3**	**FeO**	**MgO**	**CaO**	**Na_2O**	**K_2O**	**BaO**	**Total**	**Or#**
67	55	68.10	18.24	0.16	0.01	0.30	5.75	7.71	-	100.27	46.2
	26	67.14	18.43	0.23	0.00	0.23	5.31	8.99	-	100.32	52.1
	28	68.40	17.43	0.21	0.00	0.15	5.06	8.23	-	99.46	51.3
	29	67.31	18.35	0.24	0.00	0.11	5.18	8.72	-	99.88	52.2
	30	69.35	18.31	0.20	0.00	0.21	6.08	7.09	-	101.23	42.9
	31	66.98	16.42	1.67	0.03	0.13	4.02	9.00	-	98.26	59.1
	33	67.37	17.89	0.76	0.00	0.27	4.66	9.29	-	100.23	56.0
	34	65.53	18.54	0.89	0.00	0.49	5.43	8.04	-	98.92	48.1
	35	66.54	18.81	0.17	0.00	0.46	5.52	8.18	-	99.69	48.2
68	39	63.72	13.30	12.62	0.04	0.85	6.79	1.88	-	99.21	14.6
	42	65.72	18.36	0.56	0.00	0.23	5.37	8.00	-	98.24	48.9
	45	65.95	18.62	0.15	0.00	0.33	6.01	7.81	-	98.87	45.3
71	21	67.55	18.40	0.32	0.01	0.73	6.73	7.03	-	100.76	39.3
	22	68.51	17.28	0.87	0.00	0.23	5.09	8.75	-	100.72	52.5
	24	67.39	19.15	0.20	0.02	0.49	5.99	8.42	-	101.66	46.9
	25	67.61	18.75	0.31	0.00	0.75	6.89	6.75	-	101.06	37.8
	26	68.54	17.99	0.88	0.01	0.40	6.40	7.37	-	101.59	42.3
76	21	67.46	18.33	0.37	0.00	0.23	4.01	11.14	-	101.53	63.9
	22	67.13	18.27	0.28	0.00	0.42	4.01	11.00	-	101.07	63.1
	23	66.54	19.11	0.27	0.00	0.55	4.74	9.86	-	101.06	56.2
	24	67.22	18.42	0.29	0.00	0.21	3.60	11.40	-	101.11	66.9
	11	65.02	18.32	0.30	0.00	-0.26	3.82	11.19	-	98.37	66.7
	12	65.48	17.74	0.23	0.00	-0.27	3.66	10.58	-	97.45	66.5
	13	65.08	18.11	0.33	0.00	-0.39	4.13	11.38	-	98.61	65.6
77	12	65.43	18.82	0.26	0.02	0.42	4.24	10.43	-	99.62	60.6
	14	66.82	18.55	0.31	0.00	0.46	4.34	10.20	-	100.68	59.3
	15	66.74	18.78	0.23	0.02	0.43	4.51	10.37	-	101.09	59.0
	16	66.54	18.78	0.28	0.00	0.52	4.96	9.68	-	100.75	54.8
	17	68.83	17.00	0.36	0.02	0.22	3.42	9.95	-	99.80	64.9
	18	66.13	18.46	0.27	0.02	0.07	3.44	11.97	-	100.37	69.4
	19	68.72	17.20	0.27	0.00	0.12	3.39	11.14	-	100.84	67.9
	20	67.04	17.97	0.53	0.02	0.15	3.44	11.08	-	100.22	67.4

[a]Total iron reported as FeO, "-" indicates oxide not analyzed

Appendix 2. (cont.) Compilation of all microprobe analyses of natural samples and experiments.

Experiment Feldspar

Experiment	Spot	SiO_2	Al_2O_3	FeO	MgO	CaO	Na_2O	K_2O	BaO	Total	Or#
79	26	69.90	17.27	0.69	0.00	0.09	4.13	10.00	-	102.06	61.1
	29	67.63	18.06	0.34	0.01	0.10	3.86	11.25	-	101.25	65.4
	30	68.21	17.96	0.77	0.05	0.63	4.69	8.85	-	101.14	53.6
	31	70.68	16.13	0.42	0.03	0.87	4.65	7.38	-	100.17	48.6
	32	67.73	17.67	0.52	0.01	0.16	4.44	9.76	-	100.29	58.7
	33	67.40	18.26	0.31	0.00	0.46	5.15	9.47	-	101.06	53.6
	34	66.77	18.96	0.25	0.00	0.56	5.82	8.27	-	100.63	47.0
80	6	67.13	17.87	0.33	0.00	0.05	4.15	10.33	-	99.86	61.9
	7	67.69	18.25	0.26	0.00	0.16	5.01	8.97	-	100.33	53.7
	8	68.86	17.21	0.28	0.00	0.28	4.84	7.61	-	99.06	50.1
	9	67.33	18.10	0.35	0.00	0.05	3.57	11.37	-	100.76	67.5
	10	68.12	17.73	0.34	0.00	0.12	4.34	9.47	-	100.10	58.6
	11	67.95	18.58	0.28	0.00	0.27	4.75	9.48	-	101.30	56.0
	12	67.83	18.38	0.29	0.00	0.10	4.34	10.00	-	100.94	59.9
	13	67.55	17.98	0.47	0.00	0.07	4.05	10.05	-	100.18	61.8
	15	68.03	18.41	0.24	0.00	0.11	5.08	9.23	-	101.09	54.1
	16	67.63	18.31	0.46	0.00	0.13	4.71	9.40	-	100.64	56.4
81	19	66.69	18.23	0.28	0.01	0.12	3.37	12.09	-	100.78	69.8
	20	66.62	18.02	0.23	0.05	0.06	3.13	11.95	-	100.07	71.3
	21	67.60	18.17	0.25	0.01	0.08	3.91	10.79	-	100.82	64.2
	22	66.15	18.63	0.18	0.00	0.26	4.28	10.46	-	99.96	60.8
	23	66.75	18.42	0.30	0.00	0.12	3.52	11.47	-	100.56	67.8
	24	66.63	18.01	0.27	0.00	0.08	3.70	11.06	-	99.76	66.0
	26	66.82	17.91	0.23	0.01	0.15	3.40	11.36	-	99.88	68.2
	28	67.05	18.46	0.29	0.00	0.13	4.41	10.45	-	100.78	60.6
	30	67.96	17.51	0.26	0.00	0.04	3.49	10.76	-	100.03	66.9
	31	65.91	18.34	0.32	0.00	0.12	3.04	12.13	-	99.85	72.0
	32	66.34	18.38	0.27	0.00	0.08	3.11	12.07	-	100.23	71.6
	33	67.21	18.81	0.20	0.02	0.36	4.61	9.68	-	100.89	57.0
	34	67.00	18.66	0.29	0.01	0.19	4.09	10.77	-	101.01	62.8
	35	66.77	18.53	0.19	0.01	0.14	4.10	10.68	-	100.42	62.7

[a] Total iron reported as FeO, "-" indicates oxide not analyzed

						Experiment Feldspar					
Experiment	**Spot**	**SiO_2**	**Al_2O_3**	**FeO**	**MgO**	**CaO**	**Na_2O**	**K_2O**	**BaO**	**Total**	**Or#**
82	17	66.47	19.13	0.23	0.00	0.49	4.62	9.73	-	100.66	56.7
	18	66.20	18.70	0.23	0.01	0.59	4.80	9.10	-	99.63	53.9
83	14	63.46	18.37	0.21	0.00	0.48	4.28	9.15	-	95.96	57.0
	15	65.05	18.42	0.19	0.00	0.50	4.78	8.65	-	97.58	52.9
	16	69.55	16.40	0.70	0.01	0.26	4.00	8.78	-	99.70	58.2
84	12	67.59	17.01	0.32	0.00	0.30	3.70	9.77	-	98.68	62.4
	13	66.48	16.25	0.37	0.00	0.51	3.56	8.95	-	96.11	60.5
85	245	66.63	19.05	0.21	0.00	0.48	4.07	10.18	-	100.63	60.7
	247	66.48	18.43	0.20	0.00	0.29	3.00	11.73	-	100.10	71.0
	248	67.16	19.07	0.22	0.02	0.48	4.78	9.13	-	100.85	54.4
	249	66.61	19.14	0.18	0.00	0.50	4.64	9.03	-	100.10	54.7
	250	66.70	18.46	0.22	0.00	0.11	2.78	12.33	-	100.58	74.1
	252	66.45	18.71	0.22	0.00	0.44	3.65	10.95	-	100.43	64.9
	253	66.26	18.46	0.36	0.00	0.25	3.02	11.96	-	100.30	71.4
	255	67.06	19.26	0.22	0.02	0.54	5.30	8.59	-	100.98	50.2
88	10	66.26	17.59	0.44	0.00	0.20	5.74	8.83	-	99.06	49.8
	15	68.19	15.54	0.80	0.02	0.19	4.91	8.57	-	98.21	52.9
	16	69.41	16.22	0.09	0.01	0.13	5.02	8.91	-	99.80	53.5
90	9	65.60	17.89	0.19	0.00	0.47	5.41	8.73	-	98.29	50.3
	10	66.12	18.03	0.27	0.01	0.15	4.11	10.93	-	99.62	63.2
91	14	66.61	16.30	0.51	0.00	0.30	5.20	8.34	-	97.26	50.6
	15	65.04	18.31	0.20	0.00	0.48	5.07	9.12	-	98.20	53.0
	20	65.72	17.28	0.27	0.00	0.26	4.35	10.06	-	97.92	59.6
	21	65.68	18.85	0.25	0.01	0.54	5.63	8.41	-	99.37	48.3
93	8	65.71	17.96	0.26	0.01	0.45	4.97	9.35	-	98.71	54.1
94	26	63.76	17.35	0.64	0.00	0.44	5.11	9.29	-	96.58	53.3

[a] Total iron reported as FeO, "-" indicates oxide not analyzed

Appendix 2. (cont.) Compilation of all microprobe analyses of natural samples and experiments.

Experiment Feldspar

Experiment	Spot	SiO_2	Al_2O_3	FeO	MgO	CaO	Na_2O	K_2O	BaO	Total	Or#
95	28	65.96	18.31	0.21	0.02	0.41	5.30	8.84	-	99.04	51.3
	29	66.54	18.97	0.22	0.00	0.45	5.16	9.17	-	100.51	52.7
	31	66.28	19.17	0.17	0.01	0.48	5.22	9.14	-	100.47	52.3
96	42	63.02	18.32	0.21	0.00	0.49	5.13	8.86	-	96.03	51.9
	45	63.49	17.40	0.22	0.01	0.53	5.27	8.64	-	95.58	50.5
97	12	64.48	18.36	0.16	0.00	0.47	5.28	8.81	-	97.55	51.2
	16	64.57	18.71	0.19	0.00	0.49	5.47	8.42	-	97.83	49.1
	17	66.52	17.69	0.26	0.01	0.39	5.27	8.55	-	98.69	50.7
	18	64.90	18.47	0.19	0.01	0.56	5.42	8.33	-	97.89	48.9
	19	64.49	17.96	0.16	0.00	0.57	5.74	8.21	-	97.12	47.2
	20	64.89	18.25	0.18	0.01	0.57	5.21	8.39	-	97.50	50.0
98	21	63.00	18.89	0.19	0.00	0.55	5.06	8.10	-	95.78	49.8
99	40	66.51	18.02	0.22	0.02	0.16	4.57	9.84	-	99.34	58.2
102	21	66.50	18.84	0.30	0.00	0.45	4.67	9.73	-	100.49	56.5
	22	66.58	19.35	0.19	0.01	0.54	5.48	8.77	-	100.91	50.0
	24	66.88	19.67	0.21	0.00	0.14	3.46	11.99	-	102.34	69.1
103	11	66.33	18.94	0.24	0.00	0.51	5.07	9.02	-	100.11	52.6
	12	68.58	17.67	0.12	0.00	0.08	4.74	9.34	-	100.52	56.2
	13	66.29	19.70	0.22	0.01	0.50	5.08	8.87	-	100.67	52.2
	15	68.26	17.56	0.08	0.00	0.03	4.27	10.03	-	100.23	60.6
	16	67.57	19.00	0.07	0.00	0.13	4.79	9.57	-	101.12	56.4
	17	67.35	18.27	0.09	0.03	0.15	4.84	8.83	-	99.58	54.1
	18	66.26	18.28	0.20	0.00	0.40	4.61	9.62	-	99.37	56.7
	19	67.97	17.64	0.14	0.00	0.16	4.86	9.53	-	100.31	55.9
	20	68.38	19.78	0.13	0.00	1.20	9.27	2.43	-	101.18	13.9
107	9	67.98	18.22	0.22	0.02	0.47	4.82	9.77	-	101.50	55.9

[a]Total iron reported as FeO, "-" indicates oxide not analyzed

Experiment clinopyroxene and fayalite

Appendix 2. (cont) Compilation of all microprobe analyses of natural samples and experiments.

					Experiment Clinopyroxene and/or Fayalite					
Experiment	**Spot**	**SiO_2**	**TiO_2**	**Al_2O_3**	**FeO**	**MgO**	**MnO**	**CaO**	**K_2O**	**Na_2O**	**Total**
6	19	47.25	0.85	2.73	24.62	0.99	1.19	17.81	0.84	0.50	96.80
	20	50.22	0.64	4.27	25.49	0.54	1.24	16.58	1.54	0.93	101.45
11	21	48.59	0.19	0.81	26.16	3.87	1.13	17.95	0.45	0.25	99.39
	23	51.46	0.39	2.58	11.65	15.60	0.97	13.62	0.80	1.16	98.23
19	6	49.80	0.15	0.46	26.91	3.90	1.17	18.30	0.36	0.09	101.13
	7	48.22	0.25	0.53	27.48	3.71	1.17	18.74	0.32	0.10	100.51
	10	48.98	0.19	0.47	26.48	4.39	1.11	18.90	0.33	0.01	100.86
	11	51.43	0.15	1.54	16.43	7.24	1.83	21.11	0.82	0.13	100.67
29	13	49.66	0.40	2.18	18.26	5.83	1.52	19.92	0.72	0.31	98.78
	16	50.79	0.33	3.17	17.90	5.39	1.53	18.94	1.15	1.07	100.26
	19	50.13	0.39	2.46	17.57	5.91	1.28	19.80	1.01	0.60	99.15
61	9	49.71	0.60	0.90	25.04	1.88	1.81	20.91	0.67	0.16	101.67
	10	51.83	0.34	4.51	18.81	3.81	1.46	19.53	0.88	0.47	101.65
	13	48.82	0.87	2.99	19.44	5.07	1.38	21.55	0.82	0.11	101.06
	15	50.88	0.45	3.03	21.02	3.32	1.62	20.16	0.88	0.37	101.73
	16	55.87	0.44	4.87	17.82	3.74	1.28	18.26	1.27	0.79	104.35
	17	52.35	0.49	3.75	20.13	3.57	1.55	20.00	1.24	0.60	103.67
	18	46.79	0.81	3.02	20.03	3.75	1.46	20.65	0.85	0.25	97.61
63	9	49.77	0.39	1.85	18.12	5.73	1.36	21.00	0.83	0.26	99.30
77	17	51.01	0.24	2.93	17.81	4.91	1.48	18.19	0.65	1.87	99.09
	40	49.56	0.46	2.73	18.13	6.21	1.30	19.94	0.81	0.91	100.05
88	11	32.15	0.10	0.92	63.98	0.54	2.06	0.20	0.31	0.28	100.55

[a] Total iron reported as FeO, "-" indicates oxide not analyzed

Experiment Clinopyroxene and/or Fayalite

Experiment	Spot	SiO_2	TiO_2	Al_2O_3	FeO	MgO	MnO	CaO	K_2O	Na_2O	Total
96	12	33.84	0.01	0.73	63.21	1.36	1.84	0.20	0.33	0.31	101.83
	15	31.27	0.04	0.44	65.05	1.39	2.04	0.23	0.13	0.07	100.66
	19	34.34	0.12	2.06	61.01	1.13	1.85	0.21	0.45	0.48	101.64
	20	31.43	0.11	0.52	63.47	1.34	1.86	0.25	0.19	0.06	99.24
	23	29.96	0.05	0.14	65.27	1.30	2.04	0.21	0.09	0.03	99.10
	24	36.17	0.08	1.86	58.16	1.03	1.80	0.21	0.35	0.64	100.30
	25	33.37	0.06	1.13	61.27	1.25	1.88	0.22	0.37	0.41	99.96
	26	30.76	0.04	0.47	63.97	1.34	1.86	0.20	0.20	0.07	98.92
	27	30.55	0.10	0.21	64.23	1.24	2.01	0.20	0.13	0.08	98.74
97	25	30.34	0.06	0.00	64.28	2.48	2.61	0.27	0.10	0.00	100.11
	26	50.99	0.59	2.10	24.49	1.54	0.94	18.82	0.46	0.72	100.65
	27	53.78	0.21	3.22	21.65	0.90	0.74	16.18	0.94	0.45	98.08
	29	51.03	0.58	2.02	26.89	1.26	0.92	19.63	0.45	0.60	103.38
	30	49.50	0.26	0.61	26.82	3.77	0.95	18.64	0.07	0.27	100.89
	31	50.03	0.28	0.68	26.39	3.58	0.96	18.88	0.14	0.33	101.28
98	41	31.87	0.07	0.61	63.83	1.21	2.05	0.22	0.20	0.22	100.30
	42	31.29	0.04	0.35	63.88	1.16	2.08	0.27	0.34	0.35	99.76
	44	30.71	0.01	0.31	64.83	1.46	2.39	0.24	0.16	0.06	100.17
	48	49.24	0.28	0.48	27.57	3.14	1.07	18.53	0.14	0.28	100.73
	49	48.53	0.32	0.42	32.81	2.00	1.33	15.02	0.15	0.27	100.85
	53	52.92	0.22	3.08	24.13	2.96	0.97	16.22	0.80	0.87	102.17
99	61	32.83	0.22	0.95	66.02	0.98	1.97	0.21	0.16	0.11	103.45
	62	29.91	0.01	-0.08	65.22	1.08	2.05	0.22	0.07	0.00	98.48
	63	33.90	0.00	1.06	65.49	0.91	2.00	0.27	0.27	0.39	104.28
	66	48.76	0.18	0.43	26.06	3.89	1.07	18.48	0.08	0.27	99.23
102	29	32.08	0.00	0.63	65.00	1.20	2.15	0.18	0.22	0.15	101.57
	33	30.93	0.06	0.46	63.22	1.30	2.09	0.66	0.30	0.07	99.09
	40	32.73	0.06	1.04	65.50	1.21	2.23	0.21	0.29	0.29	103.55
	32	51.97	0.33	2.57	27.48	1.74	1.09	15.77	0.47	0.60	102.03
	34	55.05	0.17	3.59	24.90	1.55	0.83	12.77	0.79	0.88	100.52
	37	49.39	0.18	0.66	28.64	2.17	1.00	17.25	0.24	0.37	99.90
	38	51.78	0.35	2.38	27.93	2.07	0.96	16.01	0.42	0.47	102.36
	39	50.08	0.23	0.70	27.91	1.99	0.81	17.74	0.29	0.24	99.99
103	20	50.60	0.54	4.16	26.02	0.80	0.90	15.30	1.66	1.31	101.29
	22	53.96	0.13	6.80	21.48	1.07	0.70	11.34	3.50	1.55	100.54

[a] Total iron reported as FeO, "-" indicates oxide not analyzed

References

Alfano F, Bonadonna C, Volentik ACM, et al. (2011) Tephra stratigraphy and eruptive volume of the May, 2008, Chaitén eruption, Chile. Bull Volcanol 73:613–630. doi: 10.1007/s00445-010-0428-x

Almeev RR, Bolte T, Nash BP, et al. (2012) High-temperature, low-H2O Silicic Magmas of the Yellowstone Hotspot: an Experimental Study of Rhyolite from the Bruneau–Jarbidge Eruptive Center, Central Snake River Plain, USA. J Petrol 53:1837–1866. doi: 10.1093/petrology/egs035

Andersen DJ, Lindsley DH, Davidson PM (1993), QUILF: A Pascal program to assess equilibria among Fe-Mg-Mn-Ti oxides, pyroxenes, olivine, and quartz. Comput Geosci 19:1333-1350

Anderson SW, Stofan ER, Plaut JJ, Crown DA (1998) Block size distributions on silicic lava flow surfaces: Implications for emplacement conditions. Geol Soc Am Bull 110:1258–1267. doi: 10.1130/0016-7606(1998)110<1258:BSDOSL>2.3.CO;2

Atlas, Z.D., Dixon, J.E., Sen, G., Finny, M., and Martin-Del Pozzo, A. (2006) Melt inclusions from Volcán Popocatepetl and Volcán de Colima, Mexico: Melt evolution due to vapor-saturated crystallization during ascent. Journal of Volcanology and Geothermal Research, 153, 221-240.

Bachmann O, Bergantz GW (2004) On the Origin of Crystal-poor Rhyolites: Extracted from Batholithic Crystal Mushes. J Petrol 45:1565–1582. doi: 10.1093/petrology/egh019

Bachmann O, Bergantz GW (2008) Rhyolites and their Source Mushes across Tectonic Settings. J Petrol 49:2277–2285. doi: 10.1093/petrology/egn068

Bachmann O, Dungan MA, Lipman PW (2002) The Fish Canyon Magma Body, San Juan Volcanic Field, Colorado: Rejuvenation and Eruption of an Upper-Crustal Batholith. J Petrol 43:1469–1503. doi: 10.1093/petrology/43.8.1469

Bagdassarov N, Dingwell D (1994) Thermal properties of vesicular rhyolite. J Volcanol Geotherm Res 60:179-191

Barker DS (1970) Compositions of Granophyre, Myrmekite, and Graphic Granite. Geol Soc Am Bull 81:3339–3350. doi: 10.1130/0016-7606(1970)81[3339:COGMAG]2.0.CO;2

Befus KS, Gardner JE, Zinke RW (2012) Analyzing water contents in unexposed glass inclusions in quartz crystals. Am Mineral 97:1898–1904. doi: 10.2138/am.2012.4206

Befus KS, Zinke RW, Jordan JS, et al. (2014a) Pre-eruptive storage conditions and eruption dynamics of a small rhyolite dome: Douglas Knob, Yellowstone volcanic field, USA. Bull Volcanol 76:1–12. doi: 10.1007/s00445-014-0808-8

Behrens H, Tamic N, Holtz F (2004) Determination of the molar absorption coefficient for the infrared absorption band of CO2 in rhyolitic glasses. Am Mineral 89:301-306

Behrens, H., and Schmidt, M.O. (1998) Infrared spectroscopy of hydrous silicic glasses at temperatures up to 600 °C and implications for the incorporation and dynamics of water in glasses. Neues Jahrbuch für Mineralogie, 172, 203-226.

Bell, D.R., Ihinger, P.D., and Rossman, G.R. (1995) Quantative analysis of OH in garnet and pyroxene. American Mineralogist, 80, 465-474.

Bernstein M, Pavez A, Varley N, Whelley, P, Calder ES (2013) Rhyolite lava dome growth styles at Chaiten Volcano, Chile (2008-2009): Interpretation of thermal imagery. Andean Geol 40:295-309

Bindeman IN, Valley JW (2000) Formation of low-δ18O rhyolites after caldera collapse at Yellowstone, Wyoming, USA. Geology 28:719–722. doi: 10.1130/0091-7613(2000)28<719:FOLRAC>2.0.CO;2

Bonnichsen B, Kauffman DF (1987) Physical features of rhyolite lava flows in the Snake River Plain volcanic province, southwestern Idaho. In: Fink JH (ed) The emplacement of silicic domes and lava flows. Geol Soc Am Spec Pap 212:118-145.

Branney MJ, Bonnichsen B, Andrews GDM, et al. (2008) “Snake River (SR)-type” volcanism at the Yellowstone hotspot track: distinctive products from unusual, high-temperature silicic super-eruptions. Bull Volcanol 70:293–314. doi: 10.1007/s00445-007-0140-7

Brugger CR, Hammer JE (2010) Crystallization Kinetics in Continuous Decompression Experiments: Implications for Interpreting Natural Magma Ascent Processes. J Petrol 51:1941–1965. doi: 10.1093/petrology/egq044

Buisson C, Merle O (2002) Experiments on internal strain in lava dome cross sections. Bull Volcanol 64:363-371

Burgisser A, Gardner JE (2004) Experimental constraints on degassing and permeability in volcanic conduit flow. Bull Volcanol 67:42–56. doi: 10.1007/s00445-004-0359-5

Cañón-Tapia E, Castro J (2004) AMS measurements on obsidian from the Inyo Domes, CA: a comparison of magnetic and mineral preferred orientation fabrics. J Volcanol Geotherm Res 134:169–182. doi: 10.1016/j.jvolgeores.2004.01.005

Cardozo N, Allmendinger R (2012) Spherical projections with OSX Stereonet. Comput Geosci. doi: http://dx.doi.org/10.1016/j.cageo.2012.07.021

Carroll MR, Blank JG (1997) The solubility of H2O in phonolitic melts. American Mineralogist 82:549:556.

Castro J, Cashman KV (1999) Constraints on rheology of obsidian lavas based on mesoscopic folds. J Structur Geol 21:807-819

Castro J, Manga M, Cashman K (2002) Dynamics of obsidian flows inferred from microstructures: insights from microlite preferred orientations. Earth Planet Sci Lett 199:211–226. doi: 10.1016/S0012-821X(02)00559-9

Castro JM, Beck P, Tuffen H, et al. (2008) Timescales of spherulite crystallization in obsidian inferred from water concentration profiles. Am Mineral 93:1816–1822. doi: 10.2138/am.2008.2904

Castro JM, Cottrell E, Tuffen H, et al. (2009) Spherulite crystallization induces Fe-redox redistribution in silicic melt. Chem Geol 268:272–280. doi: 10.1016/j.chemgeo.2009.09.006

Castro JM, Dingwell DB (2009) Rapid ascent of rhyolitic magma at Chaitén volcano, Chile. Nature 461:780–783. doi: 10.1038/nature08458

Castro JM, Gardner JE (2008) Did magma ascent rate control the explosive-effusive transition at the Inyo volcanic chain, California? Geology 36:279-282

Castro JM, Mercer C (2004) Microlite textures and volatile contents of obsidian from the Inyo volcanic chain, California. Geophysic Res Lett. doi:10.1029/2004GL020489

Castro JM, Schipper CI, Mueller SP, et al. (2013) Storage and eruption of near-liquidus rhyolite magma at Cordón Caulle, Chile. Bull Volcanol 75:1–17. doi: 10.1007/s00445-013-0702-9

Cathey HE, Nash BP (2009) Pyroxene thermometry of rhyolite lavas of the Bruneau–Jarbidge eruptive center, Central Snake River Plain. J Volcanol Geotherm Res 188:173–185. doi: 10.1016/j.jvolgeores.2009.05.024

Chang W-L, Smith RB, Wicks C, et al. (2007) Accelerated Uplift and Magmatic Intrusion of the Yellowstone Caldera, 2004 to 2006. Science 318:952–956. doi: 10.1126/science.1146842

Chapin CE, Elston WE (1979) Ash-flow Tuffs. Geological Society of America

Christiansen RL (2001) The Quaternary and Pliocene Yellowstone Plateau volcanic field of Wyoming, Idaho, and Montana. USGS Professional Paper 729-G, 120 p

Christiansen RL, Lowenstern JB, Smith RB, Heasler H, Morgan LA, Nathenson M, Mastin LG, Muffler LJP, Robinson JE (2007) Preliminary assessment of volcanic and hydrothermal hazards in Yellowstone National Park and vicinity. USGS Open-file report 2007-1071, 98 p

Clay PL, O'Driscoll B, Gertisser R, et al. (2013) Textural characterization, major and volatile element quantification and Ar–Ar systematics of spherulites in the Rocche Rosse obsidian flow, Lipari, Aeolian Islands: a temperature continuum growth model. Contrib Mineral Petrol 165:373–395. doi: 10.1007/s00410-012-0813-x

Couch S, Sparks RSJ, Carroll MR (2003) The kinetics of degassing-induced crystallization at Soufriere Hills Volcano, Montserrat. J Petrol 44:1477-1502

Davis BK, McPhie J (1996) Spherulites, quench fractures and relict perlite in a Late Devonian rhyolite dyke, Queensland, Australia. J Volcanol Geotherm Res 71:1–11. doi: 10.1016/0377-0273(95)00063-1

Debolt MA, Easteal AJ, Macedo PB, Moynihan CT (1976) Analysis of Structural Relaxation in Glass Using Rate Heating Data. J Am Ceram Soc 59:16–21. doi: 10.1111/j.1151-2916.1976.tb09377.x

Devine, J.D., Gardner, J.E., Brack, H.P., Layne, G.D., and Rutherford, M.J. (1995) Comparison of microanalytical methods for estimating H2O contents of silicic volcanic glasses. American Mineralogist, 80, 319-328.

Dingwell DB (1998) The glass transition in hydrous granitic melts. Phys Earth Planet Inter 107:1–8. doi: 10.1016/S0031-9201(97)00119-2

Dixon, J.E., Stolper, E.M., Holloway, J.R. (1995) An experimental study of water and carbon dioxide solubilities in mid-ocean ridge basaltic liquids. Part 1: Calibration and solubility models. Journal of Petrology, 36, 1607-1631.

Dobson, P.F., Epstein, S., and Stolper, E.M. (1989) Hydrogen isotope fractionation between coexisting vapor and silicate glasses and melts at low pressure. Geochimica et Cosmochimica Acta, 53, 2723-2730.

Eichelberger JC, Carrigan CR, Westrich HR, Price RH (1986) Non-explosive silicic volcanism. Nature 323:598–602. doi: 10.1038/323598a0

Ellis BS, Barry T, Branney MJ, et al. (2010) Petrologic constraints on the development of a large-volume, high temperature, silicic magma system: The Twin Falls eruptive centre, central Snake River Plain. Lithos 120:475–489. doi: 10.1016/j.lithos.2010.09.008

Farrell J, Husen S, Smith RB (2009) Earthquake swarm and b-value characterization of the Yellowstone volcano-tectonic system. J Volcanol Geotherm Res 188:260–276. doi: 10.1016/j.jvolgeores.2009.08.008

Fenn, PM (1977) The nucleation and growth of alkali feldspars from hydrous melts. Can Mineral 15:135-161

Fink J (1980) Surface folding and viscosity of rhyolite flows. Geology 8:250–254. doi: 10.1130/0091-7613(1980)8<250:SFAVOR>2.0.CO;2

Fink JH (1983) Structure and emplacement of a rhyolitic obsidian flow: Little Glass Mountain, Medicine Lake Highland, northern California. Geol Soc Am Bull 94:362–380. doi: 10.1130/0016-7606(1983)94<362:SAEOAR>2.0.CO;2

Fink JH, Griffiths RW (1990) Radial spreading of viscous-gravity currents with solidifying crust. J Fluid Mech 221:485–509. doi: 10.1017/S0022112090003640

Fink JH, Griffiths RW (1998) Morphology, eruption rates, and rheology of lava domes: Insights from laboratory models. J Geophys Res Solid Earth 103:527–545. doi: 10.1029/97JB02838

Fink JH, Griffiths RW (1998) Morphology, eruption rates, and rheology of lava domes; insights from laboratory models. J Geophys Res 103:527-545

Furbish, DJ (1997) Fluid physics in geology: An introduction to fluid motions on Earth's surface and within its crust, New York, 476 p.

Gansecki CA (1998) _40 _Ar/_39_Ar geochronology and pre-eruptive geochemistry of the Yellowstone Plateau volcanic field rhyolites. Stanford

Gansecki CA, Lowenstern JB (1995) Pre-eruptive volatile compositions of the Lava Creek Tuff magma, Yellowstone Plateau Volcanic Field. Tran Am Geophys Union, Eos 76:F665.

Gansecki CA, Mahood GA, McWilliams MO (1996) 40Ar39Ar geochronology of rhyolites erupted following collapse of the Yellowstone caldera, Yellowstone Plateau volcanic field: implications for crustal contamination. Earth Planet Sci Lett 142:91–107. doi: 10.1016/0012-821X(96)00088-X

Gardner JE, Befus KS, Watkins J, et al. (2012) Compositional gradients surrounding spherulites in obsidian and their relationship to spherulite growth and lava cooling. Bull Volcanol 74:1865–1879. doi: 10.1007/s00445-012-0642-9

Gardner JE, Rutherford M, Carey S, Sigurdsson H (1995) Experimental constraints on pre-eruptive water contents and changing magma storage prior to explosive eruptions of Mount St Helens volcano. Bull Volcanol 57:1–17. doi: 10.1007/BF00298703

Gardner JE, Thomas RME, Jaupart C, Tait S (1996) Fragmentation of magma during Plinian volcanic eruptions. Bull Volcanol 58:144–162. doi: 10.1007/s004450050132

Gay NC (1968) The motion of rigid particles embedded in a viscous fluid during pure shear deformation of the fluid. Tectonophys 5:81-88

George, W.O. (1924) The relation of the physical properties of natural glasses to their chemical composition. Journal of Geology, 32, 353-372.

Geschwind C-H, Rutherford MJ (1995) Crystallization of microlites during magma ascent: the fluid mechanics of 1980–1986 eruptions at Mount St Helens. Bull Volcanol 57:356–370. doi: 10.1007/BF00301293

Ghiorso, M.S., and Sack, R.O. (1995) Chemical mass transfer in magmatic processes IV. A revised and internally consistent thermodynamic model for the interpolation and extrapolation of liquid-solid equilibria in magmatic systems at elevated temperatures and pressures. Contributions to Mineralogy and Petrology, 119, 197-212.

Gibson RG, Naney MT (1992) Textural development of mixed, finely porphyritic silicic volcanic rocks, Inyo Domes, eastern California. J Geophys Res 97:4541-4559

Giordano D, Russell JK, Dingwell DB (2008) Viscosity of magmatic liquids: A model. Earth Planet Sci Lett 271:123–134. doi: 10.1016/j.epsl.2008.03.038

Girard G, Stix J (2010) Rapid extraction of discrete magma batches from a large differentiating magma chamber: the Central Plateau Member rhyolites, Yellowstone Caldera, Wyoming. Contrib Mineral Petrol 160:441–465. doi: 10.1007/s00410-009-0487-1

Gonnermann HM, Manga M (2003) Explosive volcanism may not be an inevitable consequence of magma fragmentation. Nature 426:432–435. doi: 10.1038/nature02138

Gonnermann HM, Manga M (2005) Flow banding in obsidian: a record of evolving textural heterogeneity during magma deformation. Earth Planet Sci Let 236:135-147

Gonnermann HM, Manga M (2007) The fluid mechanics inside a volcano. Ann Rev Fluid Mechan 39:321-356

Gottsmann J, Dingwell DB (2001) The cooling of frontal flow ramps: a calorimetric study on the Rocche Rosse rhyolite flow, Lipari, Aeolian Islands, Italy. Terra Nova 13:157–164. doi: 10.1046/j.1365-3121.2001.00332.x

Gottsmann J, Dingwell DB (2002) The thermal history of a spatter-fed lava flow: the 8-ka pantellerite flow of Mayor Island, New Zealand. Bull Volcanol 64:410–422. doi: 10.1007/s00445-002-0220-7

Gregg TKP, Fink JH, Griffiths RW (1998) Formation of multiple fold generations on lava flow surfaces: Influence of strain rate, cooling rate, and lava composition. J Volcanol Geotherm Res 80:281–292. doi: 10.1016/S0377-0273(97)00048-6

Griffiths RW (2000) The Dynamics of Lava Flows. Annu Rev Fluid Mech 32:477–518. doi: 10.1146/annurev.fluid.32.1.477

Griffiths RW, Fink JH (1992) The morphology of lava flows in planetary environments: Predictions from analog experiments. J Geophys Res Solid Earth 97:19739–19748. doi: 10.1029/92JB01953

Gualda GAR, Ghiorso MS, Lemons RV, Carley TL (2012) Rhyolite-MELTS: a modified calibration of MELTS optimized for silica-rich, fluid-bearing magmatic systems. J Petrol 53:875-890

Hammer JE (2008) Experimental studies of the kinetics and energetic of magma crystallization. Rev Mineral Geochem 69:9-59

Hammer JE, Cashman KV, Hoblitt RP, Newman S (1999) Degassing and microlite crystallization during pre-climactic events of the 1991 eruption of Mt. Pinatubo, Philippines. Bull Volcanol 60:355–380. doi: 10.1007/s004450050238

Hammer JE, Cashman KV, Voight B (2000) Magmatic processes revealed by textural and compositional trends in Merapi dome lavas. J Volcanol Geotherm Res 100:165-192

Hammer JE, Rutherford MJ (2002) An experimental study of the kinetics of decompression-induced crystallization in silicic melt. J Geophys Res Solid Earth 107:ECV 8–1–ECV 8–24. doi: 10.1029/2001JB000281

Harker A, (1897) Petrology for students, Cambridge, 334 p.

Harris AJL, Rowland SK (2009) Effusion rate controls on lava flow length and the role of heat loss: a review. In: Thordarson T, Self S, Larsen G, Rowland SK, Hoskuldsson A (eds) Studies in volcanology: the legacy of George Walker. Special Publication of the International Association of Volcanology and Chemistry of the Earth's Interior 2:33–52

Hautmann S, Gottsmann J, Sparks RSJ, et al. (2009) Modeling ground deformation caused by oscillating overpressure in a dyke conduit at Soufrière Hills Volcano, Montserrat. Tectonophysics 471:87–95. doi: 10.1016/j.tecto.2008.10.021

Hervig RL, Dunbar N, Westrich HR, Kyle PR (1989) Pre-eruptive water content of rhyolitic magmas as determined by analyses of melt inclusions in phenocrysts. J Volcanol Geotherm Res 36:293-302

Hess K-U, Cordonnier B, Lavallée Y, Dingwell DB (2008) Viscous heating in rhyolite: An in situ experimental determination. Earth Planet Sci Lett 275:121–126. doi: 10.1016/j.epsl.2008.08.014

Hess, K-U, Dingwell, DB (1996) Viscosities of hydrous leucogranitic melts: A non-Arrhenian model. Am Mineral 81:1297-1300

Hildreth W, (2004) Volcanological perspectives on Long Valley, Mammoth Mountain, and Mono Craters: several contiguous but discrete systems. J Volcanol Geotherm Res 136:169-198

Hildreth W, Halliday AN, Christiansen RL (1991) Isotopic and Chemical Evidence Concerning the Genesis and Contamination of Basaltic and Rhyolitic Magma Beneath the Yellowstone Plateau Volcanic Field. J Petrol 32:63–138. doi: 10.1093/petrology/32.1.63

Honjo N, Bonnichsen B, Leeman WP, Jr JCS (1992) Mineralogy and geothermometry of high-temperature rhyolites from the central and western Snake River Plain. Bull Volcanol 54:220–237. doi: 10.1007/BF00278390

Huber C, Bachmann O, Dufek J (2011) Thermo-mechanical reactivation of locked crystal mushes: Melting-induced internal fracturing and assimilation processes in magmas. Earth Planet Sci Lett 304:443–454. doi: 10.1016/j.epsl.2011.02.022

Huppert HE, Shepherd JB, Haraldur Sigurdsson R, Sparks SJ (1982) On lava dome growth, with application to the 1979 lava extrusion of the soufrière of St. Vincent. J Volcanol Geotherm Res 14:199–222. doi: 10.1016/0377-0273(82)90062-2

Iezzi G, Ventura G (2000) Kinematics of lava flows based on fold analysis. Geophys Res Lett 27:1227–1230. doi: 10.1029/1999GL011279

Ihinger, P.D., Hervig, R.L., and McMillan, P.F. (1994) Analytical methods for volatiles in glasses. In M.R. Carroll and J.R. Holloway, Eds., Volatiles in Magmas, Reviews in Mineralogy, Vol. 30, p. 67-121. Mineralogical Society of America, Chantilly, Virginia.

Jambon A, Semet MP (1978) Lithium diffusion in silicate glasses of albite, orthoclase, and obsidian composition: An ion-microprobe determination. Earth Planet Sci Lett 37:445–450. doi: 10.1016/0012-821X(78)90060-2

Jaupart C, Allégre CJ (1991) Gas content, eruption rate, and instabilities of eruption regime in silicic volcanoes. Earth Planet Sci Let 102:413-429

Jeffery GB (1922) The motion of ellipsoidal particles immersed in a viscous fluid. Proc Roy Soc Lond 102:161-179.

Jellinek AM, DePaolo DJ (2003) A model for the origin of large silicic magma chambers: precursors of caldera-forming eruptions. Bull Volcanol 65:363–381. doi: 10.1007/s00445-003-0277-y

Keith HD, Padden FJ (1963) A Phenomenological Theory of Spherulitic Crystallization. J Appl Phys 34:2409–2421. doi: 10.1063/1.1702757

Keith HD, Padden FJ (1964) Spherulitic Crystallization from the Melt. I. Fractionation and Impurity Segregation and Their Influence on Crystalline Morphology. J Appl Phys 35:1270–1285. doi: 10.1063/1.1713606

Klug C, Cashman KV (1996) Permeability development in vesiculating magmas: implications for fragmentation. Bull Volcanol 58:87–100. doi: 10.1007/s004450050128

Koch-Müller, M., and Rhede, D. (2010) IR absorption coefficients for water in nominally anhydrous high-pressure minerals. American Mineralogist, 95, 770-775.

Lange RL, Carmichael ISE (1990) Thermodynamic properties of silicate liquids with emphasis on density, thermal expansion and compressibility. Rev Mineral Geochem 24:25-64

Lanphere MA, Champion DE, Christiansen RL, et al. (2002) Revised ages for tuffs of the Yellowstone Plateau volcanic field: Assignment of the Huckleberry Ridge Tuff to a new geomagnetic polarity event. Geol Soc Am Bull 114:559–568. doi: 10.1130/0016-7606(2002)114<0559:RAFTOT>2.0.CO;2

Leschik, M., Heide, G., Frischat, G. H., Behrens, H., Wiedenbeck, M., Wagner, N., Heide, K., Beibler, H., and Reinholz, U. (2004) Determinination of H2O and D2O contents in rhyolitic glasses. Physics and Chemistry of Glasses – European Journal of Glass Science and Technology Part B, 45, 238-251.

LeVeque RJ (2002) Finite volume methods for hyperbolic conservation laws. Cambridge University Press, Cambridge, 558 p

Lipman P, Dungan M, Bachmann O (1997) Comagmatic granophyric granite in the Fish Canyon Tuff, Colorado: Implications for magma-chamber processes during a large ash-flow eruption. Geology 25:915–918. doi: 10.1130/0091-7613(1997)025<0915:CGGITF>2.3.CO;2

Lister JR, Kerr RC (1991) Fluid-mechanical models of crack propagation and their application to magma transport in dykes. J Geophys Res 96:10,1049-10,077

Liu Y, Zhang Y, Behrens H (2005) Solubility of H_2O in rhyolitic melts at low pressures and a new empirical model for mixed H_2O-CO_2 solubility in rhyolitic melts. J Volcanol Geotherm Res 143:219-235

Lofgren G (1971a) Experimentally Produced Devitrification Textures in Natural Rhyolitic Glass. Geol Soc Am Bull 82:111–124. doi: 10.1130/0016-7606(1971)82[111:EPDTIN]2.0.CO;2

Lofgren G (1971b) Spherulitic textures in glassy and crystalline rocks. J Geophys Res 76:5635–5648. doi: 10.1029/JB076i023p05635

Lowenstern JB, Clynne MA, Bullen TD (1997) Comagmatic A-type Granophyre and Rhyolite from the Alid Volcanic Center, Eritrea, Northeast Africa. J Petrol 38:1707–1721. doi: 10.1093/petroj/38.12.1707

Lowenstern JB, Smith RB, Hill DP (2006) Monitoring super-volcanoes: geophysical and geochemical signals at Yellowstone and other large caldera systems. Philos Trans R Soc Math Phys Eng Sci 364:2055–2072. doi: 10.1098/rsta.2006.1813

Lowenstern, J.B. (1995) Applications of silicate-melt inclusions to the study of magmatic volatiles. In J.F.H Thompson (Ed.), Magmas, Fluids, and Ore Deposits, Vol. 23, p. 71-99. Mineralogical Association of Canada Short Course.

Malin MC (1980) Lengths of Hawaiian lava flows. Geology 8:306–308. doi: 10.1130/0091-7613(1980)8<306:LOHLF>2.0.CO;2

Manga M (1998) Orientation distribution of microlites in obsidian. J Volcanol Geotherm Res 86:107–115. doi: 10.1016/S0377-0273(98)00084-5

Manley CR (1992) Extended cooling and viscous flow of large, hot rhyolite lavas: implications of numerical modeling results. J Volcanol Geotherm Res 53:27–46. doi: 10.1016/0377-0273(92)90072-L

Manley CR (1996) Physical volcanology of a voluminous rhyolite lava flow: The Badlands lava, Owyhee Plateau, southwestern Idaho. J Volcanol Geotherm Res 71:129–153. doi: 10.1016/0377-0273(95)00066-6

Manley CR, Bacon CR (2000) Rhyolite thermobarometry and the shallowing of the magma reservoir, Coso Volcanic Field, California. J Petrol 41:149-174

Manley CR, Fink JH (1987) Internal textures of rhyolite flows as revealed by research drilling. Geology 15:549–552. doi: 10.1130/0091-7613(1987)15<549:ITORFA>2.0.CO;2

Martel C (2012) Eruption Dynamics Inferred from Microlite Crystallization Experiments: Application to Plinian and Dome-forming Eruptions of Mt. Pelée (Martinique, Lesser Antilles). J Petrol 53:699–725. doi: 10.1093/petrology/egr076

Mastin LG, Ghiorso MS (2001) Adiabatic temperature changes of magma-gas mixtures during ascent and eruption. Contrib Mineral Petrol 141:307-321

McMillan, P.F. (1994) Water solubility and speciation models. In M.R. Carroll and J.R. Holloway, Eds., Volatiles in Magmas, Reviews in Mineralogy, Vol. 30, p. 131-156. Mineralogical Society of America, Chantilly, Virginia.

Melnik O, Sparks RSJ (1999) Nonlinear dynamics of lava dome extrusion. Nature 402:37–41. doi: 10.1038/46950

Merle O (1998) Internal strain within lava flows from analogue modelling. J Volcanol Geotherm Res 81:189–206. doi: 10.1016/S0377-0273(98)00009-2

Miller CD (1985) Holocene eruptions at the Inyo volcanic chain, California: Implications for possible eruptions in Long Valley Caldera. Geology 13:14-17

Morgan GB, London D (2012) Process of granophyre crystallization in the Long Mountain Granite, southern Oklahoma. Geol Soc Am Bull 124:1251–1261. doi: 10.1130/B30569.1

Moynihan CT, Easteal AJ, De BOLT MA, Tucker J (1976) Dependence of the Fictive Temperature of Glass on Cooling Rate. J Am Ceram Soc 59:12–16. doi: 10.1111/j.1151-2916.1976.tb09376.x

Nakada S, Motomura Y (1995) Manner of magma ascent at Unzen Volcano (Japan). Geophys Res Lett 22:567-570

Narayanaswamy OS (1971) A Model of Structural Relaxation in Glass. J Am Ceram Soc 54:491–498. doi: 10.1111/j.1151-2916.1971.tb12186.x

Nesse, W.D. (1991) Introduction to Optical Mineralogy, 335 p., Oxford University Press, New York.

Newman S, Lowenstern JB, (2002) VolatileCalc: a silicate melt-H_2O-CO_2 solution model written in Visual Basic for Excel. Comp Geosci 28:597-604.

Newman S, Stolper EM, Epstein, S (1986) Measurement of water in rhyolitic glasses: Calibration of an infrared spectroscopic technique. Am Mineral 71:1527-1541

Ni H, Zhang Y (2008) H2O diffusion models in rhyolitic melt with new high pressure data. Chem Geol 250:68–78. doi: 10.1016/j.chemgeo.2008.02.011

Nichols, A.R.L., and Wysoczanski, R.J. (2007) Using micro-FTIR spectroscopy to measure volatile contents in small and unexposed inclusions hosted in olivine crystals. Chemical Geology, 242, 371-384.

Nielsen CH, Sigurdsson H (1981) Quantitative methods for electron microprobe analysis of sodium in natural and synthetic glasses. Am Mineral 66:547–552.

Nishikida, K., Nishio, E., and Hannah, R.W. (1995) Selected Applications of Modern FT-IR Techniques, 281 p., Kodansha Ltd., Tokyo.

Nowak M, Cichy SB, Botcharnikov RE, et al. (2011) A new type of high-pressure low-flow metering valve for continuous decompression: First experimental results on degassing of rhyodacitic melts. Am Mineral 96:1373–1380. doi: 10.2138/am.2011.3786

Okumura, S., Nakamura, M., and Nakashima, S. (2003) Determination of molar absorptivity of IR fundamental OH-stretching vibration in rhyolitic glasses. American Mineralogist, 88, 1657-1662.

Pallister JS, Diefenbach AK, Burton WC, et al. (2013) The Chaitén rhyolite lava dome: Eruption sequence, lava dome volumes, rapid effusion rates and source of the rhyolite magma. Andean Geol. doi: 10.5027/andgeoV40n2-a06

Pankhurst MJ, Schaefer BF, Betts PG, et al. (2011) A Mesoproterozoic continental flood rhyolite province, the Gawler Ranges, Australia: the end member example of the Large Igneous Province clan. Solid Earth 2:25–33. doi: 10.5194/se-2-25-2011

Pelton JR, Smith RB (1979) Recent Crustal Uplift in Yellowstone National Park. Science 206:1179–1182. doi: 10.1126/science.206.4423.1179

Petford N, Kerr RC, Lister JR (1993) Dike transport of granitoid magmas. Geology 21:845-848

Proussevitch AA, Sahagian DL (1998) Dynamics and energetics of bubble growth in magmas: analytical formulation and numerical modeling. J Geophys Res 103:18,223-18,251

Pyle DM (1989) The thickness, volume and grainsize of tephra fall deposits. Bull Volcanol 51:1–15. doi: 10.1007/BF01086757

Romine WL, Whittington AG, Nabelek PI, Hofmeister AM (2012) Thermal diffusivity of rhyolitic glasses and melts: effects of temperature, crystals and dissolved water. Bull Volcanol 74:2273–2287. doi: 10.1007/s00445-012-0661-6

Rossman, G.R. (2006) Analytical Methods for Measuring Water in Nominally Anhydrous Minerals. Reviews in Mineralogy and Geochemistry, 62, 1-18.

Rust AC, Manga M, Cashman KV (2003) Determining flow type, shear rate and shear stress in magmas from bubble shapes and orientations. J Volcanol Geotherm Res 122:111–132. doi: 10.1016/S0377-0273(02)00487-0

Rutherford MJ (2008) Magma ascent rates. Rev Mineral Geochem 69:241-271

Rutherford MJ, Gardner JE (2000) Rates of Magma Ascent. In: Sigurdsson H (ed) Encyclopedia of Volcanoes, Academic Press, New York, pp 207-217

Saar MO, Manga M (1999) Permeability-porosity relationship in vesicular basalts. Geophys Res Lett 26:111–114. doi: 10.1029/1998GL900256

Schipper CI, Castro JM, Tuffen H, et al. (2013) Shallow vent architecture during hybrid explosive–effusive activity at Cordón Caulle (Chile, 2011–12): Evidence from direct observations and pyroclast textures. J Volcanol Geotherm Res 262:25–37. doi: 10.1016/j.jvolgeores.2013.06.005

Sieh K, Bursik M (1986) Most recent eruption of the Mono Craters, eastern central California. J Geophys Res Solid Earth 91:12539–12571. doi: 10.1029/JB091iB12p12539

Signorelli, S., Vaggelli, G., and Romano, C. (1999) Pre-eruptive volatile (H_2O, F, Cl, and S) contents of phonolitic magmas feeding the 3550-year old Avellino eruption from Vesuvius, southern Italy. Journal of Volcanology and Geothermal Research, 93, 237-256.

Skirius CM, Peterson JW, Anderson AT (1990) Homogenizing rhyolitic glass inclusions from the Bishop Tuff. Am Mineral 75:1381-1398

Smith JV (2002) Structural analysis of flow-related textures in lavas. Earth-Sci Rev 57:279–297. doi: 10.1016/S0012-8252(01)00081-2

Smith RB, Jordan M, Steinberger B, et al. (2009) Geodynamics of the Yellowstone hotspot and mantle plume: Seismic and GPS imaging, kinematics, and mantle flow. J Volcanol Geotherm Res 188:26–56. doi: 10.1016/j.jvolgeores.2009.08.020

Sparks RSJ (1978) The dynamics of bubble formation and growth in magmas: A review and analysis. J Volcanol Geotherm Res 3:1–37. doi: 10.1016/0377-0273(78)90002-1

Sparks RSJ, Young SR, Barclay J, Calder ES, Cole P, Darroux B, Davies MA, Druitt TH, Harford C, Herd R, James M, Lejeune AM, Loughlin S, Norton G, Skerrit G, Stasiuk MV, Stevens NS, Toothill J, Wadge G, Watts R (1998) Magma production and growth of the lava dome of the Soufriere Hills Volcano, Montserrat, West Indies: November 1995 to December 1997. Geophys Res Lett 25:3421-3424

Spera FJ, Physical Properties of Magma. In: Sigurdsson H (ed) Encyclopedia of Volcanoes, Academic Press, New York, pp 171-190

Stasiuk MV, Barclay J, Carroll MR, et al. (1996) Degassing during magma ascent in the Mule Creek vent (USA). Bull Volcanol 58:117–130. doi: 10.1007/s004450050130

Stasiuk MV, Jaupart C (1997) Lava flow shapes and dimensions as reflections of magma system conditions. J Volcanol Geotherm Res 78:31–50. doi: 10.1016/S0377-0273(97)00002-4

Stelten ME, Cooper KM, Vazquez JA, et al. (2013) Magma mixing and the generation of isotopically juvenile silicic magma at Yellowstone caldera inferred from coupling 238U–230Th ages with trace elements and Hf and O isotopes in zircon and Pb isotopes in sanidine. Contrib Mineral Petrol 166:587–613. doi: 10.1007/s00410-013-0893-2

Stevenson RJ, Briggs RM, Hodder APW (1993) Emplacement history of a low-viscosity, fountain-fed pantelleritic lava flow. J Volcanol Geotherm Res 57:39–56. doi: 10.1016/0377-0273(93)90030-U

Stevenson RJ, Hodder APW, Briggs RM (1994) Rheological estimates of rhyolite lava flows from the Okataina Volcanic Centre, New Zealand. N Z J Geol Geophys 37:211–221. doi: 10.1080/00288306.1994.9514616

Stolper, E. (1982) Water in silicate glasses: An infrared spectroscopic study. Contributions to Mineralogy and Petrology, 81, 1-17.

Swanson DA, Dzurisin D, Holcomb RT, Iwatsubo EY, Chadwick WW, Casadevall TJ, Ewert JW, and Heliker CC (1987) Growth of the lava dome at Mount St. Helens, Washington, (USA), 1981-1983. Geol Soc Am Spec Paper 212:1-16

Swanson SE, Naney MT, Westrich HR, Eichelberger JC (1989) Crystallization history of Obsidian Dome, Inyo Domes, California. Bull Volcanol 51:161-176

Swanson, SE (1977) Relation of nucleation and crystal-growth rate to the development of granitic textures. Am Mineral 62:966-978.

Takeuchi S, Nakashima S, Tomiya A, Shinohara H (2005) Experimental constraints on the low gas permeability of vesicular magma during decompression. Geophys Res Lett 32:n/a–n/a. doi: 10.1029/2005GL022491

Tamic, N., Behrens, H., and Holtz, F. (2001) The solubility of H2O and CO2 in rhyolitic melts in equilibrium with a mixed CO2-H2O fluid phase. Chemical Geology, 174, 333-347.

Till C, Vazquez JA, Boyce JW, Stelton ME (2013) Probing the source and timing of rejuvenation and hybridization in post-caldera rhyolite magmas at Yellowstone caldera, Abstract V53A-2763 presented at 2013 Fall Meeting, AGU, San Francisco, Calif., 9-13 Dec

Tool AQ (1946) Relation Between Inelastic Deformability and Thermal Expansion of Glass in Its Annealing Range*. J Am Ceram Soc 29:240–253. doi: 10.1111/j.1151-2916.1946.tb11592.x

Toramaru A, Noguchi S, Oyoshihara S, Tsune A (2008) MND(microlite number density) water exsolution rate meter. J Volcanol Geotherm Res 175:156–167. doi: 10.1016/j.jvolgeores.2008.03.035

Tuffen H, Castro, JM (2009) The emplacement of an obsidian dyke through thin ice: Hrafntinnuhryggur, Krafla Iceland. J Volcanol Geotherm Res 185:352-366.

Tuffen H, Dingwell D (2005) Fault textures in volcanic conduits: evidence for seismic trigger mechanisms during silicic eruptions. Bull Volcanol 67:370–387. doi: 10.1007/s00445-004-0383-5

Tuffen H, Dingwell DB, Pinkerton H (2003) Repeated fracture and healing of silicic magma generate flow banding and earthquakes? Geology 31:1089–1092. doi: 10.1130/G19777.1

Tuffen H, James MR, Castro JM, Schipper CI (2013) Exceptional mobility of an advancing rhyolitic obsidian flow at Cordon Caulle volcano in Chile. Nat Commun 4:2709. doi: 10.1038/ncomms3709

Tuffen H, Smith R, Sammonds PR (2008) Evidence for seismogenic fracture of silicic magma. Nature 453:511–514. doi: 10.1038/nature06989

Turcotte DL, Schubert G (1982) Geodynamics, New York, pp 1-450.

Valley JW, Bindeman IN, Peck WH (2003) Empirical calibration of oxygen isotope fractionation in zircon. Geochim Cosmochim Acta 67:3257–3266. doi: 10.1016/S0016-7037(03)00090-5

Vazquez JA, Kyriazis SF, Reid MR, et al. (2009) Thermochemical evolution of young rhyolites at Yellowstone: Evidence for a cooling but periodically replenished postcaldera magma reservoir. J Volcanol Geotherm Res 188:186–196. doi: 10.1016/j.jvolgeores.2008.11.030

Ventura G (2004) The strain path and kinematics of lava domes: An example from Lipari (Aeolian Islands, Southern Tyrrhenian Sea, Italy). J Geophys Res 109. doi:10.1029/2003JB002740

Vogel TA, Eichelberger JC, Younker LW, Schraytz BC, Horkowitz JP, Stockman HW, Westrich HR (1989) Petrology and emplacement dynamics of intrusive and extrusive rhyolites of Obsidian Dome, Inyo Craters Volcanic Chain, Eastern California. J Geophys Res 94:17,937-17,956

Walker GPL, Huntingdon AT, Sanders AT, Dinsdale JL (1973) Lengths of Lava Flows [and Discussion]. Philos Trans R Soc Lond Ser Math Phys Sci 274:107–118. doi: 10.1098/rsta.1973.0030

Wark DA, Hildreth W, Spear FS, et al. (2007) Pre-eruption recharge of the Bishop magma system. Geology 35:235–238. doi: 10.1130/G23316A.1

Watkins J, Manga M, Huber C, Martin M (2009) Diffusion-controlled spherulite growth in obsidian inferred from H2O concentration profiles. Contrib Mineral Petrol 157:163–172. doi: 10.1007/s00410-008-0327-8

Watts KE, Bindeman IN, Schmitt AK (2011) Large-volume rhyolite genesis in caldera complexes of the Snake River Plain: Insights from the Kilgore Tuff of the Heise Volcanic Field, Idaho, with comparison to Yellowstone and Bruneau-Jarbridge Rhyolites. J Petrol 52:857-890

Watts KE, Bindeman IN, Schmitt AK (2012) Crystal scale anatomy of a dying supervolcano: an isotope and geochronology study of individual phenocrysts from voluminous rhyolites of the Yellowstone caldera. Contrib Mineral Petrol 164:45–67. doi: 10.1007/s00410-012-0724-x

Webb SL, Dingwell DB (1990) The onset of non-Newtonian rheology of silicate melts. Phys Chem Miner 17:125–132. doi: 10.1007/BF00199663

Wicks CW, Thatcher W, Dzurisin D, Svarc J (2006) Uplift, thermal unrest and magma intrusion at Yellowstone caldera. Nature 440:72–75. doi: 10.1038/nature04507

Wilding MC, Webb SL, Dingwell DB (1995) Evaluation of a relaxation geospeedometer for volcanic glasses. Chem Geol 125:137–148. doi: 10.1016/0009-2541(95)00067-V

Wolff JA, Ellis BS, Ramos FC (2011) Strontium isotopes and magma dynamics: Insights from high-temperature rhyolites. Geology 39:931–934. doi: 10.1130/G32062.1

Wood SH, (1983) Chronology of Late Pleistocene and Holocene volcanics, Long Valley and Mono Basin geothermal areas, eastern California, technical report. US Geol. Surv. Open File Rep. 83:1-76.

Wysoczanski, R., and Tani, K. (2006) Spectroscopic FTIR imagine of water species in silicic volcanic glasses and melt inclusions: An example from the Izu-Bonin arc. Journal of Volcanology and Geothermal Research, 156, 302-314.

Zhang Y, Belcher R, Ihinger PD, Wan L, Xu Z, Newman S (1997) New calibration of infrared measurement of dissolved water in rhyolitic glasses. Geochim Cosmochim Acta 61:3089-3100

Zhang Y, Ni H, Chen Y (2010) Diffusion Data in Silicate Melts. Rev Mineral Geochem 72:311–408. doi: 10.2138/rmg.2010.72.8